

Investigations on Photocatalytic H₂ Generation using Modified TiO₂ and g-C₃N₄ Semiconductors

By

SUSHMA ARJUN RAWOOL

CHEM01201304014

Bhabha Atomic Research Centre, Mumbai

A thesis submitted to the

Board of Studies in Chemical Sciences

In partial fulfillment of requirements

for the Degree of

DOCTOR OF PHILOSOPHY

of

HOMI BHABHA NATIONAL INSTITUTE

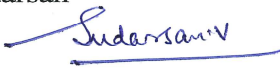


April 2018

Homi Bhabha National Institute

Recommendations of the Viva Voce Committee

As members of the Viva Voce Committee, we certify that we have read the dissertation prepared by **Sushma Arjun Rawool** entitled “**Investigations on photocatalytic H₂ generation using modified TiO₂ and g-C₃N₄ semiconductors**” and recommend that it may be accepted as fulfilling the thesis requirement for the award of Degree of Doctor of Philosophy.

 Chairman - Dr. A. K. Tyagi	Date: 23/04/2018
 Guide / Convener - Dr. Mrinal R. Pai	Date: 23-04-2018
 Examiner - Prof. Raj Ganesh S. Pala	Date: 23/4/18
Member 1- Dr. V. Sudarsan 	Date: 23/4/2018
Member 2- Dr. S. C. Parida 	Date: 23/04/2018
Member 3- Dr. P. A. Hassan 	Date: 23/4/2018

Final approval and acceptance of this thesis is contingent upon the candidate's submission of the final copies of the thesis to HBNI.

I/We hereby certify that I/we have read this thesis prepared under my/our direction and recommend that it may be accepted as fulfilling the thesis requirement.

Date: 23/04/2018

Place: Mumbai



Dr. Mrinal R. Pai

Guide

STATEMENT BY AUTHOR

This dissertation has been submitted in partial fulfillment of requirements for an advanced degree at Homi Bhabha National Institute (HBNI) and is deposited in the Library to be made available to borrowers under rules of the HBNI.

Brief quotations from this dissertation are allowable without special permission, provided that accurate acknowledgement of source is made. Requests for permission for extended quotation from or reproduction of this manuscript in whole or in part may be granted by the Competent Authority of HBNI when in his or her judgment the proposed use of the material is in the interests of scholarship. In all other instances, however, permission must be obtained from the author.



Sushma Arjun Rawool

DECLARATION

I, hereby declare that the investigation presented in the thesis has been carried out by me. The work is original and has not been submitted earlier as a whole or in part for a degree / diploma at this or any other Institution / University.



Sushma Arjun Rawool

List of publications arising from the thesis

Journals

1. “Lab scale optimization of various factors for photocatalytic hydrogen generation over low cost $\text{Cu}_{0.02}\text{Ti}_{0.98}\text{O}_{2-\delta}$ photocatalyst under UV/Visible irradiation and sunlight”, Sushma A. Rawool, Mrinal R. Pai, A. M. Banerjee, R. D. Bapat, Chandrani Nayak and A. K. Tripathi, *International Journal of Hydrogen Energy*, **2018**, *43*, 1271-1284. (Impact factor: 3.582)
2. “*pn* Heterojunctions in $\text{NiO}:\text{TiO}_2$ composites with type-II band alignment assisting sunlight driven photocatalytic H_2 generation”, Sushma A. Rawool, Mrinal R. Pai, Atindra M. Banerjee, Ashok Arya, R. S. Ningthoujam, R. Tewari, Rekha Rao, Bhagyashree Chalke, Pushan Ayyub, A. K. Tripathi and Shyamala R. Bharadwaj, *Applied Catalysis B: Environmental*, **2018**, *221*, 443-458. (Impact factor: 9.446)
3. “A comprehensive study on sunlight driven photocatalytic hydrogen generation using low cost nanocrystalline Cu-Ti oxides”, Mrinal. R. Pai, Atindra. M. Banerjee, Sushma A. Rawool, Anshu Singhal, C. Nayak, Sheryl H. Ehrman, A. K. Tripathi, Shyamala R. Bharadwaj, *Solar Energy Materials and Solar Cells*, **2016**, *154*, 104-120. (Impact factor: 4.784)
4. “Novel carbon nitride photocatalysts decorated with Pt and carbon nanodots for efficient hydrogen generation”, Sushma A. Rawool, M. R. Pai, A. M. Banerjee, A. K. Tripathi, to be communicated.
5. “Effect of different metal deposition on photocatalytic H_2 generation over $\text{g-C}_3\text{N}_4$ ”, Sushma A. Rawool, M. R. Pai, A. M. Banerjee, A. K. Tripathi, to be communicated.
6. “Modification of TiO_2 by carbon for enhanced photocatalytic H_2 generation”, Sushma A. Rawool, M. R. Pai, A. M. Banerjee, A. K. Tripathi, manuscript under preparation.

7. "Comparison of photocatalytic hydrogen yield over TiO₂ prepared by different synthetic procedures", Sushma A. Rawool, M. R. Pai, A. M. Banerjee, A. K. Tripathi, manuscript under preparation.

Symposia/ Conferences

1. "Investigations on photocatalytic properties of C@TiO₂ composites with varying carbon content", Sushma A. Rawool, Mrinal R. Pai, A. M. Banerjee and A. K. Tripathi, presented orally in International Conference on Advanced Nano Materials (ANM-2017), held on 19-21 July 2017 at University of Aveiro, Aveiro, Portugal.
2. "Study on solar photocatalytic H₂ generation using modified TiO₂ and g-C₃N₄ semiconductors", Sushma A. Rawool, Mrinal R. Pai, presented orally in 29th Research Scholar Meet organized by Indian Chemical Society held on 17-18 February 2017 at St. Xavier's College, Mumbai, India, p. 31.
3. "Role of dispersed metal in modifying the photocatalytic properties of graphitic carbon nitride, Pd/g-C₃N₄ and Cu/g-C₃N₄", Sushma A. Rawool, Mrinal R. Pai, A. M. Banerjee and A. K. Tripathi, presented in 7th Asia- Pacific Congress on Catalysis (APCAT-7) held on 17-21 January 2017 at Hotel The Lalit, Mumbai, India.
4. "Photocatalytic properties of co-dispersed Pt and carbon nanodots over g-carbon nitride, Pt/CND/g-C₃N₄ for solar H₂ generation", Sushma A. Rawool, Mrinal R. Pai, A. M. Banerjee, A. K. Tripathi, R. Tewari and S. R. Bharadwaj, presented in 6th Interdisciplinary Symposium on Materials Chemistry (ISMC-2016) held on 6-10 December 2016 at TSH, Anushakti Nagar, Mumbai, India, p.190.
5. "Investigations on the hydrolysis step of copper chlorine thermochemical cycle for hydrogen production", Mrinal R. Pai, D. Sawhney, Sushma A. Rawool, A. M. Banerjee, A. K. Tripathi, presented in 6th Interdisciplinary Symposium on Materials

- Chemistry (ISMC-2016) held on 6-10 December 2016 at TSH, Anushakti Nagar, Mumbai, India, p. 198.*
6. “Metal = Au, Ag and Pt 3% (w/w) dispersed graphitic carbon nitrides (g-C₃N₄) for solar assisted photocatalytic H₂ generation”, Sushma A. Rawool, Tripti Kedia, Mrinal R. Pai, A. M. Banerjee and A. K. Tripathi, presented orally in International Conference on Frontiers at the Chemistry-Allied Sciences Interface (FCASI) held on 25-26 April 2016 at University of Rajasthan, Jaipur, India.
 7. “g-C₃N₄ decorated with Pt and carbon nanodots for photocatalytic H₂ generation”, Sushma A. Rawool, Mrinal R. Pai, A. M. Banerjee and S. R. Bharadwaj, presented orally in International Conference on Sustainable Chemistry and Engineering (SusChemE 2015), held on 8-9 October 2015 at Hotel The Lalit, Mumbai, India, p. 6.
 8. “Photocatalytic H₂ generation over transition metal modified titania supported by DFT calculations. Effect of calcination temperature and ilmenite phase, NiTiO₃ on photoactivity”, Sushma A. Rawool, Mrinal R. Pai, A. M. Banerjee and S. R. Bharadwaj, presented in CATSYMP-2015 held on 6-9 January 2015 at Bhavnagar, India, p. 575.
 9. “Photocatalytic H₂ generation over P-N junctions of NiO-TiO₂ and ternary CuO-NiO-TiO₂ composites under sunlight”, Sushma A. Rawool, Mrinal R. Pai, A. M. Banerjee and S. R. Bharadwaj, presented in 5th Interdisciplinary Symposium on Materials Chemistry (ISMC-2014) held on 9-13 December 2014 at TSH, Anushakti Nagar, Mumbai, India, p. 398.

* Not included in thesis

Workshop/ training

1. DAE-BRNS 1st Workshop on Thermal analysis (Thermawork – 2016) in 20-21 December 2016 at TSH, Anushakti Nagar, Bhabha Atomic Research Centre, Mumbai, India.
2. Global Initiative on Academic Networks (GIAN) course on “Catalysis in Green Chemistry and Environmental Applications”, in 1-10 June 2016 at IIT-Madras, Chennai, India.
3. 2nd National Workshop on Materials Chemistry- Catalytic Materials [NWMC-2013, CAT-MAT] attended in 22-23 November 2013 at TSH, Bhabha Atomic Research Centre, Anushakti Nagar, Mumbai, India.



Sushma Arjun Rawool

Dedicated to....

To my beloved family

ACKNOWLEDGEMENTS

I express my deep and sincere gratitude to my guide, Dr. Mrinal R. Pai for her invaluable guidance, constant encouragement, keen interest, patience and good wishes. Her wide knowledge and logical way of thinking on scientific problems greatly helped me during the work.

I would like to sincerely thank Dr. Shyamala R. Bharadwaj, Former head, FCM&CS for giving me the opportunity to join for PhD and for her constant support, care and encouragement. I am privileged to thank Dr. A. K. Tripathi, Head, HE&CS and Dr. K. I. Priyadarsini, Head, Chemistry Division for their encouragement and support during my research work. I would like to thank Dr. Atindra M. Banerjee for his helpful scientific discussion.

I also thank PhD committee for their constant guidance and their valuable suggestions. I gratefully acknowledge Dr. A. K. Tyagi, Chairperson, Doctoral Committee and Dr. P. A. Hasan, Dr. V. Sudarsan, Dr. S. C. Parida as members of Doctoral Committee for their critical assessment of work and useful comments during progress review and pre-synopsis viva-voce.

I also thank all my collaborators for their guidance and valuable inputs. I sincerely thank Dr. R. Tewari (MSD, BARC), Dr. Pushan Ayyub (TIFR), Ms. Bhagyashree Chalke (TIFR), Mr. Rudhir Bapat (TIFR) for HR-TEM analysis, Dr. Deepa Khushalani (TIFR), Dr. Vivek Polshettiwar (TIFR), Mr. Ayan Maity (TIFR) for N₂ BET surface area analysis, Dr. Ashok Arya (MSD, BARC), for DFT calculations, Dr. D. Bhattacharyaa (AMPD, BARC) for recording EXAFS, Dr. Rekha Rao (SSPD, BARC) for Raman spectroscopy, Dr. Sudarsan (ChD, BARC), for NMR, Dr. Kaustava Bhattacharyya and Dr. Deepak Tyagi (ChD, BARC) for XPS and Analytical Chemistry Division, BARC for analysis of chemical composition.

I also thank to visiting students Bonita G., Sidhangshu Priya, Tripti Kedia, Shailaja, Deepesh and Prasanna Karthick who gave me opportunity to help them during their project work. I would like to thank Mr. Ganesh Mane for technical support. Many thank to Mr. Ashish Nadar for his constant encouragement and support and around in any time of need. I would like to acknowledge Anitha, Ramya, Parvathi and Tapas for their moral support and motivation, which drives me to give my best. I also like to extend my thanks to lab colleagues Dr. Rajini Antony, Rajendra and Nilesh for their support and making the lab environment friendly. Nice and congenial environment provided by all members of my section is also worth mentioning.

Last but not the least I would like to thank my family members and friends for their constant support and encouragement through all phases of my life.

CONTENTS

	Pg No.
SYNOPSIS	xxi
LIST OF FIGURES	xxxii
LIST OF TABLES	xlii
Chapter-1 Introduction	1
1.1 Need for development of renewable and clean fuels	1
1.1.1 Energy crises	1
1.1.2 Generation of green house gases and its impact on environment	2
1.2 A sustainable energy: Solar energy	3
1.3 Solar fuel - Hydrogen	5
1.4 Hydrogen production methods	5
1.4.1 Methods for production of commercial hydrogen	5
1.4.2 Production of H ₂ from renewable source - solar energy and water	6
1.5 Photocatalytic water splitting	8
1.6 Photocatalyst	9
1.7 Processes involved in photocatalytic water splitting	10
1.8 Targets for commercialization of water splitting	11
1.9 Criterion for selection of photocatalyst	12
1.10 Semiconductor as photocatalyst	13
1.10.1 Metal oxides	13
1.10.1.1 TiO ₂	15

1.10.2	Non-oxide photocatalyst	16
1.10.2.1	g-C ₃ N ₄	17
1.10.3	Progress till date.....	18
1.11	Designing modified photocatalyst with improved light absorption properties	21
1.11.1	Cationic or anionic doping.....	21
1.11.2	Dye sensitization.....	23
1.11.3	Recombination is a competing process.....	24
1.11.3.1	Effect of particle size, surface area and crystallinity.....	25
1.11.3.2	Use of sacrificial reagent	27
1.11.3.3	Dispersion of cocatalyst.....	28
1.11.3.4	Formation of heterojunction	29
1.11.3.5	Z- scheme photocatalytic water splitting.....	33
1.12	Optimization of experimental parameters	34
1.13	Global status of pilot plant.....	35
1.14	Aim of the work and future scope	35
Chapter-2 Instrumentation and Experimental Methods		37
2.1	Introduction	37
2.2	Synthesis of catalysts	37
2.2.1	Solid state route.....	38
2.2.2	Sol-gel method.....	38
2.2.3	Thermal decomposition of urea	40

2.2.4	Synthesis of carbon nanodots by top down method.....	42
2.2.5	Photodeposition method.....	43
2.3	Instrumental.....	44
2.3.1	Characterization by using X-ray techniques	44
2.3.1.1	X-ray Diffraction (XRD).....	44
2.3.1.2	X-ray Absorption Spectroscopy (XAS).....	47
2.3.1.3	X-ray Photoelectron Spectroscopy (XPS).....	51
2.3.2	Determination of surface area.....	53
2.3.2.1	N ₂ BET Surface area.....	53
2.3.3	Spectroscopy techniques.....	56
2.3.3.1	Fourier Transform Infrared Spectroscopy (FTIR).....	56
2.3.3.2	Raman Spectroscopy	58
2.3.3.3	Nuclear Magnetic Resonance Spectroscopy (NMR).....	60
2.3.3.4	Diffuse Reflectance Spectroscopy (DRS)	62
2.3.3.5	Photoluminescence (PL).....	64
2.3.4	Electron microscopy techniques	67
2.3.4.1	Scanning Electron Microscopy (SEM).....	67
2.3.4.2	Transmission Electron Microscopy (TEM).....	68
2.3.5	Gas Chromatography (GC).....	70
2.3.6	Thermal analysis techniques.....	73
2.3.6.1	Thermogravimetric Analysis (TGA)	73

2.3.6.2	Differential Thermal Analysis (DTA)	73
2.3.6.3	Evolved Gas Analysis (EGA).....	74
2.3.7	Inductively Coupled Plasma- Optical Emission Spectroscopy (ICP-OES).....	74
2.4	Evaluation of photocatalytic activity.....	74
2.4.1	Experimental conditions	74
2.4.2	Photoreactor	75
2.4.3	Photoirradiator	77
2.4.4	Light sources.....	77
2.4.4.1	UV-visible source	78
2.4.4.2	Visible light source.....	78
2.4.4.3	Sunlight.....	79
2.4.5	Measurement of flux using Si photodiode.....	79
2.4.6	Efficiency calculation	80
2.4.6.1	Apparent Quantum Efficiency (AQE).....	80
2.4.6.2	Solar to Fuel Efficiency (SFE)	81

Chapter-3 Sunlight Driven Photocatalytic Hydrogen Generation over Cu Substituted TiO₂ and Nano-composites of CuO-TiO₂ Powders 82

3.1	Introductions.....	82
3.2	Experimental	84
3.2.1	Synthesis of catalyst/ co-catalyst	84
3.2.2	Characterization	85
3.2.3	Photocatalytic activity.....	87

3.3	Results and discussion.....	87
3.3.1	XRD	87
3.3.2	ICP-OES	91
3.3.3	Crystallite and particle size and morphological features	91
3.3.4	N ₂ BET surface area and porosity.....	93
3.3.5	Raman spectroscopy	95
3.3.6	XAS.....	96
3.3.7	XPS	98
3.3.8	DRS.....	102
3.3.9	Photocatalytic activity.....	103
3.3.9.1	Activity tests under direct sunlight.....	103
3.3.9.2	Activity tests under UV-visible light.....	105
3.4	Mechanism	108
3.5	Conclusion.....	109
Chapter-4 Investigations of Catalytic Properties of <i>pn</i> NiO:TiO₂ Composites: Facilitation of Charge Separation, VBO/CBO Estimation with Type-II Band Alignment at Heterojunctions.....		111
4.1	Introduction	111
4.2	Experimental	113
4.2.1	Synthesis	113
4.2.2	Characterization	115
4.2.3	Photocatalytic activity.....	117

4.2.4	First-Principles theoretical calculations	118
4.3	Results and discussion.....	119
4.3.1	XRD	119
4.3.2	N ₂ -BET surface area and porosity	124
4.3.3	Raman spectroscopy	126
4.3.4	DRS.....	127
4.3.5	Photoluminescence spectroscopy.....	129
4.3.6	Surface morphology.....	133
4.3.7	XPS	138
4.3.8	Photocatalytic activity.....	143
4.4	DFT	148
4.5	Determination of valence band offset (VBO) and conduction band offset (CBO) by XPS	151
4.6	Novelty of work	153
4.7	Conclusion.....	155
Chapter-5 Synthesis, Characterization and Photocatalytic Properties of C@TiO₂ Composites (Carbon = 0.14 - 14.7 Wt %)		
5.1	Introduction	158
5.2	Experimental	160
5.2.1	Synthesis of C@TiO ₂	160
5.2.2	Characterization	160
5.2.3	Photocatalytic activity.....	161

5.3	Results and discussion.....	162
5.3.1	Characterization.....	162
5.3.2	Photocatalytic activity.....	177
5.4	Conclusion.....	179
Chapter-6 Performance of Most Active Photocatalyst, $\text{Cu}_{0.02}\text{Ti}_{0.98}\text{O}_{2-8}$ in Upscaled Photoreactors under Sunlight.....		181
6.1	Introduction.....	181
6.2	Experimental.....	184
6.2.1	Synthesis of $\text{CuTi}(2)$ powder.....	184
6.2.2	$\text{CuTi}(2)/\text{ITO}/\text{PET}$ Films.....	184
6.2.3	Characterization techniques.....	185
6.2.4	Photocatalytic activity.....	186
6.3	Results and discussion.....	187
6.3.1	Characterization.....	187
6.3.2	Photocatalytic activity.....	193
6.3.2.1	Optimization of experimental parameters for evaluation of photocatalytic activity under UV-visible light illumination.....	193
6.3.2.2	Optimization of experimental parameters under sunlight illumination....	197
6.3.3	Replacement of methanol by glycerol.....	205
6.3.3.1	Optimization of catalyst loading in upscaled (2 L capacity) photoreactor by using glycerol as sacrificial reagent.....	206
6.3.4	Comparison of effect of different parameters on H_2 yield.....	207

6.3.5	Comparison of present work with reported results	208
6.4	Conclusion.....	210
Chapter-7 g-C₃N₄ Decorated with Pt and Carbon Nanodots for Photocatalytic H₂ Generation		
212		
7.1	Introduction	212
7.2	Experimental	215
7.2.1	Synthesis of g-C ₃ N ₄ and CND decorated g-C ₃ N ₄	215
7.2.2	Synthesis of Pt/CND/g-C ₃ N ₄ sample.....	215
7.2.3	Characterization	215
7.2.4	Photocatalytic activity.....	217
7.2.4.1	Direct water splitting under UV-visible irradiation.....	217
7.2.4.2	Photocatalytic activity under UV-visible irradiation in presence of sacrificial reagent.....	217
7.2.4.3	Photocatalytic activity under sunlight in presence of sacrificial reagent .	217
7.3	Results and discussion.....	218
7.3.1	XRD	218
7.3.2	FTIR.....	219
7.3.3	¹³ C MAS NMR analysis.....	220
7.3.4	TGA-EGA.....	221
7.3.5	Elemental analysis by CHN analyzer and ICP-OES.....	221
7.3.6	TEM	222
7.3.7	Surface area.....	224

7.3.8	XPS	225
7.3.9	DRS.....	228
7.3.10	Photoluminescence	229
7.3.11	Photocatalytic activity.....	231
7.3.11.1	Direct water splitting under UV-visible illumination.....	231
7.3.11.2	Activity evaluation under UV illumination and sunlight in presence of sacrificial reagent.....	232
7.4	Conclusion.....	238
Chapter- 8 Role of Metal (M = Pt, Pd, Au, Ag and Cu) Dispersion in Improvement of Photocatalytic Properties of g-C₃N₄.....		239
8.1	Introduction.....	239
8.2	Experimental Methods	240
8.2.1	Synthesis of metal/g-C ₃ N ₄ samples	240
8.2.2	Characterization.....	241
8.2.3	Photocatalytic activity.....	242
8.3	Results and discussion.....	242
8.3.1	XRD.....	242
8.3.2	FTIR.....	243
8.3.3	ICP-OES	244
8.3.4	TEM.....	244
8.3.5	DRS.....	246
8.3.6	Photoluminescence spectroscopy.....	247

8.3.7	Photocatalytic activity.....	248
8.3.7.1	Activity under UV-visible illumination.....	248
8.3.7.2	Activity under sunlight illumination.....	249
8.4	Relation between work function of metal and H ₂ yield	250
8.5	Conclusion.....	251
Chapter 9 Conclusion and Scope of the Work in Future		252
References.....		261

SYNOPSIS

Present thesis is focused on modifying the structural, electronic and photocatalytic properties of TiO₂ and graphitic carbon nitride, g-C₃N₄ catalysts, with an aim to develop efficient visible light active catalyst for photocatalytic H₂ generation. Different strategies were adopted to improve the catalytic activity and for those, appropriate synthetic procedures were followed to prepare the modified forms of TiO₂ and g-C₃N₄, various techniques were applied to investigate the morphological and bulk properties of oxides/nitrides and finally photocatalytic hydrogen yield over all samples under different light sources (UV-visible, visible and sunlight) was evaluated. Performance of active photocatalysts was also observed in upscaled photoreactors under sunlight to explore their potential in actual application. Thesis is divided in nine chapters and content of each chapter is summarized below:

Chapter-1 Introduction

Considering limited resources, extensive use of fossil fuels and generation of harmful green house gases, search of alternate clean fuel has become a major research goal. Hydrogen fuel with a calorific value of 141.8 MJ/Kg (~3 times of gasoline), has potential to meet the world's increasing energy demand. Honda and Fujishima [1] in 1972 revolutionized the world about the photosensitized decomposition of water into H₂ and O₂ using an electrochemical cell, led to extensive investigations by researchers worldwide on water splitting processes such as photocatalytic (PWS), photoelectrochemical or electrocatalytic. PWS is a simplest method in which photocatalyst absorbs light falling on it and then utilizes this light energy to split water to produce H₂ and O₂ [1, 2]. This method is very attractive for commercial production of H₂ owing to its simplicity and scope of utilizing renewables such as solar energy and water in presence of suitable photocatalyst. PWS involves three steps (i) absorption of light by semiconductor photocatalyst and generation of electron and hole pair, (ii) separation and migration of charges to active centres on the surface (iii) reduction and

oxidation of water by photogenerated electron and hole to give H₂ and O₂ respectively [3]. Potential of many metal oxides, metal sulphides, niobates, oxynitrides, oxysulphides, titanates etc. as photocatalysts was explored [4-9]. Yet, the required efficiency was not achieved. Main factors which limit the actual application of sunlight driven PWS are low absorption of visible portion of sunlight, high recombination of photogenerated charge carriers and low stability of photocatalyst during reaction [10]. In the present thesis, studies were undertaken to improvise the optical and photocatalytic properties of several photocatalysts; conventionally known UV active TiO₂ and novel organic semiconductor, graphitic carbon nitride (g-C₃N₄). Various strategies such as cationic doping by Cu in TiO₂, composite formation with NiO and CuO inducing *pn* heterojunctions, carbon incorporation in bulk TiO₂ (C@TiO₂) to improve electronic conductivity, surface modification of g-C₃N₄ by dispersing carbon nanodots (CND) and noble metal ions (Pt, Pd, Au, Ag and Cu) were adopted to limit the e⁻/h⁺ recombination reaction and to enhance the photoresponse under visible light illumination. All samples were thoroughly characterized by relevant techniques and their potential for H₂ generation was evaluated under sunlight and UV-visible light in presence of sacrificial reagent. Density functional theory calculations were performed and life time of e⁻/h⁺ from PL decay curves was measured to support the activity trend. In this chapter necessity of H₂ economy, different methods of production of hydrogen, how photocatalytic H₂ generation is advantageous over all other techniques of hydrogen generation and the problems confronted in achieving viable photocatalytic H₂ generation will be addressed. A literature survey of the important results reported by other researchers in the field till date, for the development of photocatalyst will also be reviewed in this chapter. Aim and scope of the investigative studies undertaken are mentioned briefly.

Chapter-2 Instrumentation and Experimental Methods

This chapter describes synthetic procedures adopted to prepare modified TiO₂ and g-C₃N₄ photocatalysts. Techniques used to investigate in detail the structural, electronic and morphological properties of photocatalyst were discussed. Instrumentation and working principle of all the techniques is briefly mentioned in this chapter. These techniques includes X-Ray Diffraction (XRD), Fourier Transform Infrared Spectroscopy (FTIR), Raman Spectroscopy, Extended X-ray Absorption Fine Structure (EXAFS), Nuclear Magnetic Resonance Spectroscopy (NMR), Field Emission Scanning Electron Microscopy (FESEM)-Energy Dispersive X-ray (EDX), Transmission Electron Microscopy- Selected Area Electron Diffraction (TEM-SAED), X-ray Photoelectron Spectroscopy (XPS), N₂ Brunauer-Emmett-Teller (N₂-BET) surface area, Diffuse Reflectance Spectroscopy (DRS), Photoluminescence Spectroscopy (PL) and Thermogravimetry- Differential Thermal Analysis- Evolved Gas Analysis (TG-DTA-EGA). Photocatalytic activity of photocatalyst for H₂ generation was tested by illuminating it under different light sources such as UV-visible light, visible light and sunlight in presence of water and sacrificial reagent [11]. H₂ yield was quantified by using gas chromatography coupled with thermal conductivity detector (TCD). The dependence of H₂ yield on geometrical factors such as illumination area, form of catalyst (powder/films), catalyst concentration and different sacrificial reagents were investigated in up-scaled reactors. Their dimensions, capacities and images of upscaled pyrex reactors are given in this chapter.

Chapter-3 Sunlight Driven Photocatalytic Hydrogen Generation over Cu Substituted TiO₂ and Nano-composites of CuO-TiO₂ Powders

This chapter deals with the effect of cationic substitution over photocatalytic activity of TiO₂. For this a series of Cu doped titania, Cu_xTi_{1-x}O_{2-δ} (x= 0.0, 0.02, 0.06) and also, copper oxide-titanium oxide nanocomposites, xCuO-yTiO₂ (x:y = 1:9, 2:8, 5:5) were

synthesized by sol-gel method and characterized by relevant techniques. These samples were thoroughly characterized by relevant instrumental techniques. The role of Cu ions in enhancement of photocatalytic evolution of H₂ from H₂O-methanol/ glycerol mixtures in both sunlight and UV-visible irradiation over Cu/Ti oxides was investigated. For sunlight assisted photocatalytic H₂ generation maximum activity was found over Cu_{0.02}Ti_{0.98}O_{2-δ} for the doped samples, referred to as CuTi(2), and xCuO-yTiO₂(x:y = 2:8) for the composite samples. Stabilization of anatase phase after incorporation of Cu, lengthening of Ti-O bonds, decrease in co-ordination number around Cu ions and induced oxygen ion vacancies, distortion (σ) in lattice (from EXAFS), increased absorption of light in doped and composite samples as compared to pristine sample, enhanced N₂-BET surface area and microporosity and in situ conversion of Cu⁺² to photocatalytically more active Cu⁺¹ state (revealed by XPS) during illumination results into enhancement of H₂ yield of both doped as well as composite samples.

Chapter-4 Investigations of Catalytic Properties of *pn* NiO:TiO₂ Composites: Facilitation of Charge Separation, VBO/CBO Estimation with Type-II Band Alignment at Heterojunctions

Another strategy adopted to enhance the photocatalytic property of TiO₂ is the formation of *pn* junction at the interface of *p*-type NiO and *n*-type TiO₂ semiconductor. This chapter includes synthesis of nanocomposites, characterization and evaluation of photocatalytic activity under different light sources. NiO-TiO₂ in (1:1) and (0.35:0.65) molar ratios referred as NTC11 and NTC36 respectively, NiTiO₃ and TiO₂ samples were synthesized through sol-gel method. NiO-TiO₂ composite shows presence of NiO and TiO₂ phase along with NiTiO₃ phase. With the emergence of NiTiO₃ phase decrease in photocatalytic activity was observed. As presence of NiTiO₃ may act as a barrier to effective pathway of charge carriers through *pn* junction. Synthesis conditions, calcination temperature

and phase compositions were very critical and played an essential role in determining the overall hydrogen yield. Among all the samples NTC11 has shown maximum H₂ generation. To further improve the activity 1% w/w Pt was loaded over NTC11 which has shown photocatalytic hydrogen yield @ 0.6 l/h/m² with apparent quantum efficiency (AQE) of 5.4 % and solar fuel efficiency (SFE) of 0.8 % under sunlight and 1.4 l/h/m² with AQE of 7.8 % under UV-visible irradiation along with evolution of bubbles was observed. Sustainable H₂ production was observed for 60 h under sunlight illumination over Pt/NTC11 and NTC11. To understand the band alignment at the interface of *p*-type NiO and *n*-type TiO₂, valence band offset (VBO, ΔE_v) and conduction band offset (CBO, ΔE_c) at NiO and TiO₂ heterojunction was calculated. Thus, a composite of *pn* oxides offer lower band gap energy of 2.67 eV as compared to both pure oxides TiO₂ and NiO with effectiveness in charge separation across the *pn* junction leading to efficient improved photocatalyst. Uniform distribution of NiO and TiO₂ in NTC11 seen by HAADF-STEM (High angle annular dark field- scanning transmission electron microscopy), minimum amount of NiTiO₃ phase, change in the band alignment at the interface of heterojunction and enhanced surface area, light absorption properties and life time of charge carriers has shown positive effect on the photocatalytic activity of NTC11.

Chapter-5 Synthesis, Characterization and Photocatalytic Properties of C@TiO₂ Composites (Carbon = 0.14 - 14.7 Wt %)

To overcome the disadvantages of TiO₂, such as limited absorption of sunlight and high rate of e⁻/h⁺ recombination, TiO₂ was decorated with carbon. Incorporation of C has certain advantages such as enhanced absorption of visible light, high adsorptivity, high photocatalytic activity. Hence, it is assumed that C@TiO₂ may be an active photocatalyst for photocatalytic H₂ generation. This chapter deals with synthesis of C@TiO₂ composites by varying carbon content from 0.14- 14.7 wt%, characterization and evaluation of

photocatalytic activity under sunlight and UV-visible light. Samples were synthesized by using ethylene glycol and tetrabutyltitanate to form an organic-inorganic polymer which on calcination in inert atmosphere gives C and TiO₂ composite. For comparison, pristine TiO₂ were also synthesized by annealing the polymers in air at 500°C for 6 h. The bulk properties of composite powders so obtained were characterized using X-ray diffraction (XRD), Fourier transform infrared (FTIR) and Raman spectroscopy. Nature of bonding and local environment around Ti atom was probed using EXAFS. Surface speciation was carried out using X-ray photoelectron spectroscopy (XPS). Carbon content present in each sample was estimated using carbon-sulphur analyser. Thermogravimetry hyphenated with evolved gas analyser (IR detector) was used to characterize the C-TiO₂ composites for their thermal behaviour in air upto 1000°C and identification of gases liberated at different temperatures. All the C-TiO₂ samples shows enhanced light absorption in visible region as compared to pristine TiO₂ sample. Presence of carbon prevents agglomeration of TiO₂ particles evident by the broadening of XRD peak. Structural characterization of carbon was done by using Raman spectroscopy which shows presence of D and G band characteristics of sp² hybridized carbon and graphite like arrangement. Among all the samples maximum activity with H₂ evolution rate of 893 μmol/h/g was observed over C@TiO₂ EG20 having carbon content of 3.8 wt% which is ~ 4 times higher than the rate observed over pristine TiO₂ under UV-Visible illumination. On further increase in carbon content beyond 3.8 wt% decreases in activity was observed as increase in carbon content may blocks the light reaching towards photocatalytically active TiO₂. To further enhance the activity of C@TiO₂ EG20, 1% w/w Pt was photodeposited over the C@TiO₂ EG20 sample. The rate of H₂ generation observed was 7689.5 μmol/h/g and 2721.6 μmol/h/g under UV-Visible and sunlight illumination respectively. Almost constant H₂ evolution was observed after irradiating the sample under sunlight illumination for 32 h. Enhanced photocatalytic activity of C@TiO₂EG20 as

compared to pristine TiO₂ can be attributed to improved light penetration, absorption properties and high surface area.

Chapter-6 Performance of Most Active Photocatalyst, Cu_{0.02}Ti_{0.98}O_{2-δ} in Upscaled Photoreactors under Sunlight.

As mentioned in above chapters TiO₂ was modified by doping with cation like Cu, forming *pn* junction at the interface and composite formation with carbon. Among all the modified TiO₂ photocatalyst, Cu_{0.02}Ti_{0.98}O_{2-δ} (referred as CuTi(2)) was found to be most active under sunlight illumination in absence of cocatalyst. This chapter deals with optimization of experimental parameters and performance evaluation of CuTi(2) for H₂ generation in upscaled reactor under sunlight illumination. Effect of photocatalyst loadings, form of catalyst (powder/films), concentration of sacrificial reagent, replacement of methanol by industrial waste glycerol, role of different configuration of light source with reactor, stirring during the photocatalytic reaction, fluctuations of solar flux at hourly basis and illumination area were studied. The effect of each factor on hydrogen yield was quantified. It was observed that in addition to catalyst loadings and sacrificial reagent, improved dispersion of photocatalyst obtained by stirring the reaction mixture in horizontal geometry resulted in enhanced H₂ yield. With an aim to identify practical materials for pilot plants, 6 mg of CuTi(2) was spread over (30 cm x 0.7 cm) ITO/PET films by Doctor blade technique exhibited enhanced efficiency (3.06 %) as compared to same amount of CuTi(2) powder (1.41 %). Also the experiment was carried out under sunlight in a reactor having capacity of ~2L. The results illustrate that by optimizing operational conditions under sunlight, it is possible to generate H₂ @ 1.167 L/h/m² with apparent quantum efficiency, AQE, of 7.5 % and solar to fuel efficiency, SFE, of 3.9 %. From the above results it is concluded that H₂ at 1 L/h would be evolved photocatalytically over 0.9 m² of CuTi(2) photocatalyst, exposed to sunlight.

Chapter-7 g-C₃N₄ Decorated with Pt and Carbon Nanodots for Photocatalytic H₂ Generation

g-C₃N₄ having a band gap of 2.7 eV, fulfills the required thermodynamic criteria for water splitting. It is a suitable visible light photocatalyst due to its unique two-dimensional structure, excellent chemical stability and tunable electronic structure [12, 13]. However photocatalytic activity of pure g-C₃N₄ is constrained due to high recombination rate of photogenerated electron and hole pair and low utilization of visible light. To modify the photocatalytic properties of g-C₃N₄, it was decorated with Pt metal and carbon nanodots (CND) separately and in combination. Pristine g-C₃N₄ was synthesized by thermal pyrolysis of urea at 550°C for 3h in air. Electrochemical corrosion of graphite rods at 30 V for 120 h was performed, followed by centrifugation and hydrothermal treatment with ammonia to obtain 4-7 nm sized CND. Graphitic nature of g-C₃N₄ and presence of CND was established by relevant techniques. XRD and FTIR spectra were recorded to get insight into structural details. Carbon nanodots (CND) have enhanced the photocatalytic properties of g-C₃N₄ evident by increased photocatalytic H₂ yield under UV-visible and sunlight as compared to pristine sample. Rate of H₂ evolution from pure water as well as in presence of 10% (v/v) triethanolamine (as sacrificial reagent) over different carbon nitride samples under sunlight and UV-visible illumination was evaluated. Pristine g-C₃N₄ has not shown any activity under similar conditions whereas, CND/g-C₃N₄ was found to be active. Total yields of H₂ and O₂ obtained was 132 μmoles/g and 84.6 μmoles/g respectively over CND/g-C₃N₄ (0.67 wt%) for 20 h from direct water splitting. To further enhance the photocatalytic activity Pt was photodeposited over the sample. Highest H₂ yield @ 398.28 μmol/h was observed over Pt/CND/g-C₃N₄ (0.48 wt%) with AQE of 4.8 % and SFE of 2.4 %.

Chapter-8 Role of Metal (M = Pt, Pd, Au, Ag and Cu) Dispersion in Improvement of Photocatalytic Properties of g-C₃N₄.

The properties of g-C₃N₄ can be modified by forming Schottky junctions created by metal/g-C₃N₄ heterostructures. This chapter describes the synthesis, characterization and improvement in photocatalytic properties of g-C₃N₄ after different metals were dispersed on its surface. g-C₃N₄ was synthesized by heating urea at 550°C for 3h. 3% w/w Pt, Ag, Au, Cu and Pd was deposited over g-C₃N₄ by photodeposition method using H₂PtCl₆.6H₂O, AgNO₃, H₂AuCl₄, CuSO₄ and PdCl₂ as metal precursors respectively. Samples were characterized by relevant techniques and photocatalytic activity was evaluated under UV-Visible and sunlight irradiation in presence of water and triethanolamine as sacrificial reagent. DRS spectrum of metal/g-C₃N₄ shows extended absorption in the visible region as compared to pristine sample due to surface plasmon resonance effect (SPR) of metal. Photoluminescence spectra shows presence of metal decreases the recombination of photogenerated charge carrier. g-C₃N₄ has not shown any activity under sunlight irradiation whereas metal deposited sample has shown enhanced H₂ yield. Following order for photocatalytic H₂ generation was observed under sunlight illumination over 80 mg of photocatalyst: Pt/g-C₃N₄ > Pd/g-C₃N₄ > Au/g-C₃N₄ > Ag/g-C₃N₄ > Cu/g-C₃N₄ ~ g-C₃N₄. Under sunlight, H₂ evolution @ 234 μmol/h observed over Pt/g-C₃N₄ as compared to inactive pristine g-C₃N₄. Formation of Schottky barrier assist the separation of photogenerated charge carrier and surface plasmon resonance effect helps in absorption of visible light both these factors results into enhancement of H₂ yield over metal/g-C₃N₄ sample.

Chapter-9 Conclusion and Future Scope

This chapter includes the outcome of all the studies and the scope for the future work. Substitution of transition metal ions at cationic site in TiO₂ lattice and composite formation with TiO₂ or g-C₃N₄ were strategies adopted to enhance the harvesting of visible light and

lowering the rate of recombination reaction. Excess of amount of dopant may acts as a recombination centre hence it is necessary to optimize the dopant concentration. In order to utilize sunlight properly illumination area, proper dispersion of catalyst and proper design of photoreactor is required. Inputs obtained from the present study will be useful to further scale up of sunlight driven photocatalytic H₂ production. All the photocatalysts synthesized here are visible light active as well as stable for long term activity, hence these photocatalyst can be further explore for energy and environment related reactions like conversion of CO₂ into methanol or methane or environmental remediation.

References:

1. M. R. Pai, A. M. Banerjee, A. K. Tripathi, S. R. Bharadwaj, in: S. Banerjee and A. K. Tyagi (Eds.) "Functional Materials: preparations, Processing and Applications", Elsevier, USA, 2012, pp. 579-606.
2. T. Jafari, E. Moharreri, A. S. Amin, R. Miao, W. Song and S. L. Suib, *Molecules* 21(2016) 900.
3. L. Yuan, C. Han, M.-Q. Yang, and Y.-J. Xu, *Inter. Rev. in Physical Chemistry* 35(1) (2016) 1–36.
4. Y. Horiuchi, T. Toyao, M. Takeuchi, M. Matsuoka and M. Anpo, *Phys. Chem. Chem. Phys.* 15 (2013) 13243.
5. S. Y. Tee, K. Y. Win, W. S. Teo, L.-D. Koh, S. Liu, C. P. Teng and M.-Y. Han, *Adv. Sci.* 4 (2017) 1600337.
6. M. Ni, M. K. H. Leung, D.Y.C. Leung and K. Sumathy, *Renewable and Sustainable Energy Reviews* 11 (2007) 401–425.
7. M. R. Pai, A. M. Banerjee and S. R. Bharadwaj, *J. Mater. Res.* 30(21) (2015) 3259-3266.
8. A. M. Banerjee, M. R. Pai, A. Arya and S. R. Bharadwaj, *RSC Adv.* 5 (2015) 61218-61229.
9. M. R. Pai, A. M. Singhal, A. M. Banerjee, R. Tewari, G. K. Dey, A. K. Tyagi and S. R. Bharadwaj, *J. Nanosci. Nanotechnol.* 12 (2012) 1957-1966.
10. A. Kudo and Y. Miseki, *Chem. Soc. Rev.* 38 (2009) 253–278.
11. M. R. Pai, J. Majeed, A. M. Banerjee, A. Arya, S. Bhattacharya, R. Rao and S. R. Bharadwaj, *J. Phys. Chem. C* 116 (2012) 1458-1471.
12. G. Dong, Y. Zhang, Q. Pan and J. Qiu, *Journal of Photochemistry and Photobiology C: Photochemistry Reviews* 20 (2014) 33–50.
13. Z. Zhao, Y. Sun and F. Dong, *Nanoscale* 7 (2015) 15-37.

LIST OF FIGURES

Fig. 1.1 Increase in CO ₂ concentration correlated with rising temperature from 1880 to 2016.	3
Fig. 1.2 Solar irradiance spectrum above atmosphere and at sea level.	3
Fig. 1.3 Harvesting solar energy by photocatalytic water splitting for H ₂ production, storage and fuel cell application.	8
Fig. 1.4 Steps involved during photocatalytic water splitting using semiconductor photocatalyst.	11
Fig. 1.5 Structure of polymeric graphitic C ₃ N ₄	17
Fig. 1.6 (i) Donor level and (ii) acceptor level formed by metal ions doping and (iii) new VB formation by anionic doping.	21
Fig. 1.7 Role of crystallinity and surface area of photocatalyst on photocatalytic activity.	27
Fig. 1.8 Band alignment in different types of heterojunctions (Type I, Type II and Type III) [VB= valence band and CB= conduction band]	30
Fig. 1.9 Band alignment at <i>pn</i> heterojunction.	31
Fig. 1.10 Band alignment at the semiconductor-metal interface. (CB= conduction band, VB=valence band, E _F = Fermi level, ϕ_m and ϕ_s is work function of metal and semiconductor respectively).....	32
Fig. 2.1 Reaction mechanism of thermal pyrolysis of urea into g-C ₃ N ₄ . S is the reaction steps.	42
Fig. 2.2 Schematic diagram of X-ray diffraction.....	44
Fig. 2.3 Normalized X-ray absorption spectra of Cu doped TiO ₂ sample.....	48
Fig. 2.4 Schematic of emission of electron from core level after interaction with X-ray.	52
Fig. 2.5 Classification of physisorption isotherms (IUPAC) [149]	55
Fig. 2.6 Schematic of FTIR instrument.	57

Fig. 2.7 Schematic representation of Raman scattering	59
Fig. 2.8 Specular reflection on smooth surface and diffuse reflection from a rough surface..	63
Fig. 2.9 Typical spectrum of time resolved photoluminescence spectroscopy	66
Fig. 2.10 Schematic of phenomena occurs on interaction of electron beam with sample.....	67
Fig. 2.11 Schematic of gas chromatograph.	70
Fig. 2.12 Photocatalytic H ₂ evolution under direct sunlight in different size of reactors. a. quartz reactor of 81 ml capacity, b. a pyrex cylindrical reactor of ~1 L (990 ml) capacity and c. a beaker type pyrex photoreactor of ~2 L (1963 ml).	76
Fig. 2.13 Pictorial representation of side view of a) vertical geometry: photoreactor and light source both are standing vertical and b) horizontal geometry: photoreactor and light source are in horizontal position.	77
Fig. 2.14 UV-visible emission spectrum of medium pressure mercury vapour lamp.	78
Fig. 2.15 Emission spectrum of visible medium pressure mercury lamp (SAIC, India, 400 W)	79
Fig. 2.16 Typical silicon photodiode spectral response of light meter.	80
Fig. 3.1 A schematic of procedure followed to synthesize Cu _{0.02} Ti _{0.98} O _{2-δ} powder by Sol-Gel route.	85
Fig. 3.2 XRD patterns of different Cu-Ti-O samples synthesized by sol gel calcined at 500 °C for different values of x. Line broadening (δ, FWHM) increases and shift towards lower 2θ angles was observed with increase in Cu content. \$ Brookite, # Anatase TiO ₂ , * Tenorite CuO.....	88
Fig. 3.3 Profile of the XRD patterns of Cu (1-9) composite sample were refined by Rietveld method using GSAS software package. Inset presents the parameters derived for CuTi composites by Rietveld method using GSAS software package.	89

Fig. 3.4 TEM of CuTi(6) nanoparticles (a) as-synthesized (b) calcined at 500 °C. SAED pattern is shown as the inset in respective figures.	92
Fig. 3.5 TEM (a), HRTEM (b) and SAED (c) of $\text{Cu}_x\text{Ti}_{1-x}\text{O}_{2-\delta}$ and CuO -TiO ₂ nanocomposites.....	93
Fig. 3.6 BJH pore size distribution and pore volume curves of CuTi(2). V_{pore} is shown by red and dv/dr by blue curves.....	94
Fig. 3.7 Raman spectra of a) CuTi(6), b) CuTi(1-9), c) CuTi(2-8) and d) CuTi(5-5). Arrow marks indicate the Raman modes due to CuO.	95
Fig. 3.8 Cu K-edge XANES spectra of CuTi(2) sample. Inset shows a derivative plot of the spectrum.....	96
Fig. 3.9 a. Experimental $\chi(r)$ versus r spectrum at Cu K-edge of the CuTi(2) sample along with the best theoretical fits. Open circles are the experimental data fitted with TiO ₂ model as shown by solid continuous line. Inset shows EXAFS fitting results for CuTi(2) photocatalyst assuming that 2 mol % Cu ²⁺ ions are substituted at Ti ⁴⁺ sites in anatase TiO ₂ , b. Experimental $\chi(r)$ versus r spectrum at Ti K-edge of CuTi(2) and pristine TiO ₂	98
Fig. 3.10 a. Overlay of XPS spectra corresponding to Cu -2p _{3/2} and Cu -2p _{1/2} lines for different samples. Deconvolution of Cu -2p _{3/2} peak in b. CuTi(5-5), c. CuTi(2) fresh and d. CuTi(2) used samples.	100
Fig. 3.11 Overlay of XPS spectra corresponding to a. Ti -2p _{3/2} and Ti-2p _{1/2} b. O 1s and c. C 1s lines for different samples. Broad peaks were deconvulated to quantify relatively various oxidation states of an element present in a sample.	102
Fig. 3.12 Diffuse reflectance UV-Vis spectra of doped $\text{Cu}_x\text{Ti}_{1-x}\text{O}_{2-\delta}$ and CuO -TiO ₂ nanocomposite samples a. TiO ₂ , b. CuTi(2), c. CuTi(6), d. CuTi(1-9), e. CuTi(2-8) and f. CuTi(5-5)	103

Fig. 3.13 Time courses of photocatalytic H ₂ generated over a. doped Cu _x Ti _{1-x} O _{2-δ} and b. CuO-TiO ₂ composites under sunlight.....	104
Fig. 3.14 Photocatalytic activity of Cu _x Ti _{1-x} O _{2-δ} and CuO-TiO ₂ composites under UV-visible irradiation.....	105
Fig. 4.1 Schematics of synthesis of NTC11 composite by sol-gel route.....	114
Fig. 4.2 XRD patterns of a. TiO ₂ , b. NiO, c. NTC18, d. NTC36, e. NTC11, f. NTC63, g. NTOsg and h. NTOss calcined at 600 °C. ^A anatase, ^R rutile, ^N NiO and ^{NT} NiTiO ₃	120
Fig. 4.3 Dependence of phase composition of NTC11 on gel drying temperature and calcination conditions. XRD powder patterns of NTC11 obtained after a. drying the gel at 90 °C (LT) and further calcined at 500 °C for 5 h referred as NTC11-LT 500 °C, 5 h, b. drying the gel at 90 °C (LT) and further calcined at 600 °C for 3h referred as NTC11-LT 600 °C, 3h, c. drying the gel at 90 °C (LT) and further calcined at 600 °C for 10 h referred as NTC11-LT 600 °C, 10 h or throughout the manuscript as NTC11 and d. drying the gel at higher temperature of 150 °C (HT) and was calcined at 600 °C for 10 h referred as NTC11-HT 600 °C, 10 h. ^A Anatase phase of TiO ₂ , ^R Rutile phase of TiO ₂ , ^N NiO and ^{NT} NiTiO ₃	122
Fig. 4.4 BJH pore size distribution and pore volume curves of a. TiO ₂ b. NTC36 and c. NTC11. V _{pore} is shown by blue and dv/dr by red curves. Inset shown in ‘a’ is enlarged view.	125
Fig. 4.5 Raman spectra of simple oxides NiO, TiO ₂ compared with their composite binary oxides NTC36, NTC11 and single phase compound oxide, nickel titanate oxide was prepared by solid state route, NTOss. * NiTiO ₃ phase, # anatase phase of TiO ₂	127
Fig. 4.6 Diffuse reflectance UV-visible spectra of a. TiO ₂ , b. NTC36, c. NTC11, d. NTOsg, e. NTOss, f. NiO g. Used NTC11 and h. Used NTC36. Dotted lines (---) are characteristic transitions due to NiTiO ₃ phase.	129

Fig. 4.7 Photoluminescence spectra of different Ni-Ti oxides. #Artefact: instrumental peak due to lamp change at 467 nm.	130
Fig. 4.8 a. Luminescence decay curves of TiO ₂ , NiO, NTC11, NTC36, NTOsg upto 110 ns. b. decay curves of TiO ₂ , NTC11, NTOsg, NTC36 up to 20 ns. Mono-exponential fitting to data of c. TiO ₂ , e. NTC11 up to 20 ns. Tri-exponential fitting to data of d. TiO ₂ , f. NTC11 up to 110 ns.....	131
Fig. 4.9 FESEM images at different accelerating voltages for NTC11(a- b) and NTC36 (c-d). Backscattered image of NTC11 (e) and NTC36 (f). EDX of NTC11 (g) and NTC36 (h). ..	135
Fig. 4.10 TEM, HR-TEM images, SAED pattern and particle size distribution are shown in clockwise direction for (a) NTC11 (b) NTC36 and (c) low (i) and high (iii-iv) magnification STEM-HAADF images of the NTC11 sample along with EELS (ii) of the selected area indicated as positions 1 and 2. Bright and dark contrast in HAADF image arising due to difference in average atomic number corresponds to TiO ₂ and NiO respectively.	138
Fig. 4.11 a. Overlay of XPS spectra corresponding to Ni 2p _{3/2} and Ni 2p _{1/2} lines for different samples. Deconvolution of Ni 2p _{3/2} peak in b. NiO c. NTC36 d. NTC11 and e. used NTC11. ^I and ^{II} are multiplets due to Ni 2p _{3/2}	140
Fig. 4.12 Overlay of XPS spectra corresponding to a. Ti 2p b. O 1s and c. C 1s lines for different samples. Broad peaks were deconvulated to relatively quantify various oxidation states of an element present in a sample. ^I Anatase and ^{II} NiTiO ₃	142
Fig. 4.13 a. H ₂ yield monitored over TiO ₂ , NTC18, NTC36, NTC11, Pt/NTC11, NTC63, NTOsg and NTOss under a. sunlight during 10:00-16:00 h IST, b. UV -Visible irradiation.	144
Fig. 4.14 Recyclability of photocatalytic H ₂ generation over NTC11 and Pt/NTC11 evaluated for 60 h by irradiating the sample under sunlight. (Experimental conditions: 100 mg of photocatalyst was suspended in water + methanol (33 % v/v), evacuated and illuminated	

under sunlight for duration of 6 h in a day during afternoon (10.00-16.00 IST) and H₂ yield was monitored for 10 days with intermittent evacuation after 12 h of irradiation). 145

Fig. 4.15 Visible light activity of NTC11 was established by monitoring H₂ yield for 35 h under medium pressure mercury lamp emitting wavelengths longer than 400 nm ($\lambda_{\text{max}}= 536$ nm). Emission spectrum is shown in inset. Experimental conditions: 100 mg of photocatalyst was suspended in water + methanol (33% v/v), evacuated and illuminated under visible light source for 35 h with intermittent evacuation at regular intervals. 146

Fig. 4.16 Effect of calcination temperature and crystallinity on photocatalytic properties was investigated by evaluating photocatalytic H₂ yield over a NiO and TiO₂ composite in 1:1 composition synthesized under varying heat treatment conditions corresponding to samples shown in Fig. 4.3..... 147

Fig. 4.17 a. Band structure of NiO along high-symmetry L ($\frac{1}{2}, \frac{1}{2}, \frac{1}{2}$), G (0, 0, 0), X (0, 1, 0), W ($\frac{1}{2}, 1, 0$) and K (0, $\frac{3}{4}, \frac{3}{4}$) directions. It can be seen from band gap that there is existence of an indirect band gap of 3 eV. b. Site- and angular momentum-projected partial density of states for NiO showing the valence band to be mainly composed of O - 2*p* and Ni - 3*d* and 4*s*. 150

Fig. 4.18 a. Schematic diagram of band alignment derived at the interface of NiO-TiO₂ semiconductor. b. A pictorial representation of the most probable mechanism proposed for composite, NTC11. 152

Fig. 5.1 TGA-DTA analysis of C@TiO₂EG20 sample in presence of air..... 163

Fig. 5.2 XRD pattern of a. uncalcined C@TiO₂EG20 sample b. C@TiO₂EG (EG= 10, 14, 20, 25, 50, 75, 100) samples calcined in argon atmosphere at 500 °C for 9 h. 164

Fig. 5.3 FTIR spectra of uncalcined and calcined C@TiO₂EG20 sample compared with TiO₂. 165

Fig. 5.4 Raman spectra of TiO₂ and C@TiO₂ samples. 166

Fig. 5.5 Raman spectra of C@TiO ₂ samples shows presence of D and G band.	167
Fig. 5.6 Normalised XANES spectra of TiO ₂ at Ti K-edge along with reference metal foil.	169
Fig. 5.7 Normalised EXAFS spectra of a. Ti metal, b. TiO ₂ , c. C@TiO ₂ EG14, d. C@TiO ₂ EG20, e. C@TiO ₂ EG50, f. C@TiO ₂ EG100 at Ti K-edge along with reference Ti metal.....	170
Fig. 5.8 Fourier transformed EXAFS spectra of TiO ₂ at Ti K-edge (Scatter points) and theoretical fit (Solid line) (a) pristine TiO ₂ , (b) C@TiO ₂ EG14, (c) C@TiO ₂ EG20, (d) C@TiO ₂ EG50 and (e) C@TiO ₂ EG100.	171
Fig. 5.9 N ₂ -BET isotherms of a. TiO ₂ and b. C@TiO ₂ EG20 sample with pore size distribution (shown in inset).	173
Fig. 5.10 Low and high resolution TEM images and SAED pattern of a. TiO ₂ , b. C@TiO ₂ EG20 c.C@TiO ₂ EG100 samples	174
Fig. 5.11 Light absorption properties of C@TiO ₂ samples as a function of carbon content recorded using DRS	175
Fig. 5.12 High resolution spectra of a. C 1s, b. Ti 2p and c. O 1s of TiO ₂ and C@TiO ₂ samples.....	176
Fig. 5.13 H ₂ yield generated over TiO ₂ and C@TiO ₂ samples under a. UV-Visible and b. sunlight illumination.	178
Fig. 5.14 Sustained H ₂ generation over Pt C@TiO ₂ EG20 sample observed under sunlight for 32 h.....	179
Fig. 6.1 a. XRD pattern of CuTi(2) synthesized in two different batches BI and BII, b. Experimental $\chi(r)$ versus r spectrum at Cu K edge of the CuTi(2)-BI and CuTi(2)-BII samples along with the best theoretical fits. Round circles are the experimental data fitted with TiO ₂ model as shown by solid continuous line. Inset shows XANES spectra of CuTi(2)-BI and CuTi(2)-BII samples obtained from both the batches recorded for Cu K-edge, c. XPS spectra	

recorded of Cu 2*p*, Ti 2*p* and O 1*s* for CuTi(2)-BI and BII samples, d. diffuse UV-visible reflectance spectra (DRS) of CuTi(2) of BI and BII samples with pristine TiO₂, e. photoluminescence spectra of CuTi(2)-BI and BII along with TiO₂ recorded by exciting the sample at 285 nm and excitation spectra is given as inset. * artefact at 467 nm. 189

Fig. 6.2 FESEM images of CuTi(2) prepared from batch (a) BI (b) BII (c) Back scattered image of CuTi(2)BII, along with EDX of (d) CuTi(2)-BI and (e) CuTi(2)-BII. 191

Fig. 6.3 Low and high resolution TEM images of (a) CuTi(2)-BI and (b) CuTi(2)-BII. Particle sizes are marked with yellow circles. Fringe width of 0.35 nm corresponds to anatase (*d*₁₀₁) TiO₂ phase. 191

Fig. 6.4 Variation of hydrogen yield with change in a. photocatalyst loadings, (Experimental conditions: Reaction mixture containing constant water to methanol ratio (33% v/v, 15 ml) with suspended photocatalyst in different amounts evacuated and irradiated under UV-visible light in a photoreactor of 81 ml capacity providing an illumination area of 20 cm²), b. concentration of sacrificial reagent, methanol in water (v/v) evolved over CuTi(2) under UV-visible light. (Experimental conditions: 0.1 g of CuTi(2) photocatalyst suspended in reaction mixture containing varying concentration of water to methanol (total volume = 15 ml), evacuated and irradiated under UV-visible light in a photoreactor of 81 ml capacity providing an illumination area of 20 cm²). 194

Fig. 6.5 Role of different configurations in determining photocatalytic hydrogen yield. Pictorial representation of side view of a) Vertical geometry: Photoreactor and light source both are standing vertical and b) horizontal geometry: Photoreactor and light source are in horizontal position. Role of stirring for proper dispersion of photocatalyst in both geometries on hydrogen yield is also shown. (Experimental conditions: 0.1 g of photocatalyst was suspended in aqueous methanol solution (33 %, 15 ml), evacuated and irradiated under UV-visible light in respective geometries. The flux of radiation was recorded using silicon

photodiode luxmeter in individual geometry to calculate the AQE achieved in both configurations).197

Fig. 6.6 Rate of hydrogen generation was monitored as a function of hourly fluctuations in solar flux during day time during 10:40 to 17:40 IST. Day-1 is bright sunny day and day-2 is a relatively cloudy day. (Experimental conditions: 0.1 g of CuTi(2) photocatalyst was suspended in aqueous methanol solution (33 %, 15 ml), evacuated and irradiated under direct sunlight. Rate of hydrogen evolved per hour was plotted as a function of solar flux. The solar flux was recorded using silicon photodiode luxmeter). 199

Fig. 6.7 Dependence of AQE of CuTi(2) photocatalyst on various factors such as 1. Concentration of CuTi(2) photocatalyst (0.1- 4 g/L) was optimized for a given reaction volume and illumination area (141 cm²). 2. Effect of different forms, powder or films on photoactivity was investigated by comparing H₂ yield over 25 mg of CuTi(2) powder with same amount of photocatalyst dispersed over ITO/PET films (illumination area over films = 0.7cm x 30 cm x 4 Nos = 84 cm²). 3. Effect of glycerol as sacrificial reagent on H₂ yield. Experiments were performed in a large sized reactor (~1 L) over CuTi(2) photocatalyst suspended in 250 ml of water + methanol (33 %) purged with argon gas and irradiated under direct sunlight. Experiment with Water + glycerol (15 %) was also performed. Blank ITO/PET films did not show any photocatalytic H₂ evolution.200

Fig. 6.8 Optimization of catalyst loadings in upscaled photoreactors under sunlight using constant concentration of methanol and glycerol as sacrificial reagents. (Experimental conditions: Different loadings of CuTi(2) was dispersed into ~255 ml of water + sacrificial reagent (methanol (33% v/v, 2:1 v/v) and glycerol (15%, 5:1 v/v) solution, purged with argon gas and irradiated under sunlight in upscaled reactor of 2L capacity with illumination area of 172 cm²).204

Fig. 6.9 Comparison of photocatalytic H ₂ yield observed using glycerol and methanol as sacrificial reagents over Pt/CuTi(6) photocatalyst.....	206
Fig. 6.10 A bar graph presenting relative standard deviation calculated in hydrogen yield by varying different factors.....	208
Fig. 7.1 Powder XRD patterns of a. CND/g-C ₃ N ₄ b. Pt/CND/g-C ₃ N ₄ samples.	218
Fig. 7.2 FTIR spectrum of g-C ₃ N ₄ and CND/g-C ₃ N ₄ samples. Inset shows the vibration in the region of 1200-1800 cm ⁻¹ arises due to stretching modes of CN heterocycle.	219
Fig. 7.3 a. NMR spectrum of g-C ₃ N ₄ , CND/g-C ₃ N ₄ -0.48, CND/g-C ₃ N ₄ -0.62 and CND/g-C ₃ N ₄ -0.75, b. thermogram of g-C ₃ N ₄ and CND/g-C ₃ N ₄ -0.67 recorded till 1000 °C in air. ...	220
Fig. 7.4 Low and high resolution TEM images of a. g-C ₃ N ₄ , b. CND/g-C ₃ N ₄ -0.67 and c. Pt/g-C ₃ N ₄	223
Fig. 7.5 Cumulative pore volume and pore size distribution of a. g-C ₃ N ₄ , b. CND/g-C ₃ N ₄ -0.48 and c. CND/g-C ₃ N ₄ -0.62 samples.....	224
Fig. 7.6 a. Overlay of XPS spectra corresponding to a. C1s , b. N1s, c. O1s and d. Pt 4f. ...	226
Fig. 7.7 Light absorption spectra of CND and -NH ₂ modified CND	228
Fig. 7.8 DRS spectra of a. CND/g-C ₃ N ₄ and b. Pt/CND/g-C ₃ N ₄	229
Fig. 7.9 Photoluminescence spectra of a. CND/g-C ₃ N ₄ and b. Pt/CND/g-C ₃ N ₄ samples.	229
Fig. 7.10 Decay spectra of a. g-C ₃ N ₄ , b. CND/g-C ₃ N ₄ -0.67 and c. Pt/CND/g-C ₃ N ₄ -0.48....	230
Fig. 7.11 Photocatalytic activity evaluation of g-C ₃ N ₄ and CND/g-C ₃ N ₄ under UV-visible irradiation in a. absence and b. presence of triethanolamine. (Experimental conditions: 50 mg of photocatalyst dispersed into water or aqueous triethanolamine solution (15 % v/v) and solution was evacuated, irradiated under UV-Visible light).....	233
Fig. 7.12 Photocatalytic activity evaluation of Pt/g-C ₃ N ₄ and Pt/CND/g-C ₃ N ₄ under UV-Visible light. (Experimental conditions: 50 mg of photocatalyst dispersed into water and	

triethanolamine solution (15 % v/v) and mixture was evacuated and irradiated under UV-visible light)	234
Fig. 7.13 Photocatalytic activity evaluation over a. Pt/g-C ₃ N ₄ and Pt/CND/g-C ₃ N ₄ under sunlight and b. Pt/CND/g-C ₃ N ₄ -0.48 under visible light. (Experimental conditions: 80 mg of photocatalyst dispersed into 150 ml of solution of water and triethanolamine (15 % v/v) and this solution was purged with argon gas and irradiated under sunlight from 11:00 to 15:00 IST or visible light).....	235
Fig. 8.1 a. XRD pattern and b. FTIR spectra of g-C ₃ N ₄ and metal/g-C ₃ N ₄ samples.....	243
Fig. 8.2 a. Low, high resolution TEM images and SAED pattern of a. Pt/g-C ₃ N ₄ , b. Pd/g-C ₃ N ₄ . c. Au/g-C ₃ N ₄ and d. EDX line scanning of Au/g-C ₃ N ₄	245
Fig. 8.3 a. UV-Visible DRS and b. photoluminescence spectra of g-C ₃ N ₄ and metal/g-C ₃ N ₄ samples.....	246
Fig. 8.4 Biexponential fitting of decay curve of a. g-C ₃ N ₄ and b. Pt/g-C ₃ N ₄	247
Fig. 8.5 Photocatalytic H ₂ generation evaluated over g-C ₃ N ₄ and metal/g-C ₃ N ₄ under a. UV-Visible (Experimental condition: 50 mg of sample dispersed in 15 ml of water + triethanolamine solution (10 % v/v), evacuated and irradiated under UV-Visible lamp (400 W medium pressure Hg lamp)) and b. sunlight illumination (Experimental condition: 80 mg of sample dispersed in 150 ml of water + triethanolamine solution (10 % v/v), purged with argon gas and irradiated under sunlight from 11:00 to 15:00 IST).....	249
Fig. 9.1 Photocatalytic H ₂ generation expressed in terms of L/h/m ² and AQE of the system evaluated in presence of Pt as cocatalyst and sacrificial reagent and under sunlight illumination.....	259

LIST OF TABLES

Table 1.1 List of methods for commercial production of H ₂	6
Table 1.2 Properties of TiO ₂ polymorph [64]	15
Table 1.3 H ₂ yield over different photocatalyst systems.....	19
Table 1.4 Photoinduced reaction in the bulk and surface of TiO ₂ semiconductor and their timescale.	24
Table 3.1 Abbreviations, lattice parameters and phase identification of Cu _x Ti _{1-x} O _{2-δ} samples.	90
Table 3.2 Elemental analysis of Cu and Ti present in representative doped and composite sample evaluated by ICP-OES technique.	91
Table 3.3 Crystallite size, particle size, N ₂ - BET surface area and porosity of Cu _x Ti _{1-x} O _{2-δ} and xCuO:yTiO ₂ nanocomposites.....	94
Table 3.4 Elemental compositions derived from XPS study of fresh and used doped and composite samples.	99
Table 3.5 Typical values of H ₂ yield (μmol/h) obtained photocatalytically over CuTi(x) samples irradiated under different light source and conditions.	106
Table 4.1 Nominal compositions, abbreviations, weight fraction of anatase/rutile and crystallite size calculated using Scherrer equation in different samples is listed below	124
Table 4.2 Particle size, surface area and porosity of oxides.	125
Table 4.3 Band gap calculated for different Ni/Ti oxides using Kubelka-Munk function. ...	128
Table 4.4 Parameters derived from fitting of decay profile (upto 110 ns) of different samples using tri-exponential decay equation.	132
Table 4.5 Bulk elemental analysis of Ni, Ti and Pt for different composites using EDX and ICP-OES compared with calculated values.	135

Table 4.6 Binding energy values derived from XPS study of TiO ₂ , NiO, NiTiO ₃ , fresh and used composite Ni-Ti oxides.	138
Table 4.7 Elemental compositions derived from XPS study of fresh and used composite Ni-Ti oxides.....	141
Table 4.8 Typical values of photocatalytic H ₂ yield, apparent quantum efficiencies (AQE) and solar fuel efficiency (SFE), obtained over different Ni-Ti oxides irradiated under different conditions.	145
Table 4.9 Comparison of present study with literature reports on various Ni-Ti-O systems for photocatalytic H ₂ evolution under stated experimental conditions.....	154
Table 5.1 C and TiO ₂ content determined in C@TiO ₂ composite samples by ICP-OES and CHN analysis	162
Table 5.2 Ratio of I _D /I _G in C@TiO ₂ samples	167
Table 5.3 Bond distances, co-ordination number and disorder factor (σ^2) of C@TiO ₂ samples	172
Table 5.4 Crystallite size, surface area, pore size and volume of C@TiO ₂ samples	172
Table 5.5 Elemental compositions derived from XPS study of C@TiO ₂ composite samples.	177
Table 6.1 Consistency of morphological and bulk properties of Cu _{0.02} Ti _{0.98} O _{2-δ} , CuTi(2)-BI and BII nanopowders obtained from two different batches synthesized by sol-gel route.	192
Table 6.2 Flux of sunlight at different hours during months of May and October in Mumbai.	198
Table 6.3 Variation of H ₂ yield with increase in illumination area.....	202
Table 6.4 Comparison of present study with literature reports on various Cu-Ti-O systems for photocatalytic H ₂ evolution under given experimental conditions.	209
Table 7.1 Characteristic vibrations of g-C ₃ N ₄ and CND/g-C ₃ N ₄ samples.....	219

Table 7.2 Carbon, nitrogen, hydrogen content by CHN analysis.	222
Table 7.3 Band gap, surface area, pore volume and pore size distribution of CND/g-C ₃ N ₄	224
Table 7.4 Elemental compositions derived from XPS study of g-C ₃ N ₄ and CND/g-C ₃ N ₄ and Pt/CND/g-C ₃ N ₄	227
Table 7.5 Parameters derived from fitting of decay profile (upto 100 ns) of different samples using bi-exponential fitting decay equation CND/g-C ₃ N ₄	231
Table 7.6 H ₂ yield, AQE and SFE obtained under different conditions using Pt/CND/g-C ₃ N ₄ samples.....	235
Table 7.7 Comparison of present study with literature reports on various CND/g-C ₃ N ₄ system for photocatalytic H ₂ evolution under stated experimental conditions.....	236
Table 8.1 Metal content of g-C ₃ N ₄ and metal/g-C ₃ N ₄ sample.	244
Table 8.2 Lifetime measurement by biexponential fitting (upto 100 ns).....	248
Table 8.3 H ₂ yield, AQE and SFE calculated over different metal/g-C ₃ N ₄ samples with different irradiation sources	250

Chapter-1

Introduction

Energy and environment are two important factors which are of concern to human civilization in near future. World's energy demand is increasing with rise in industrialization. Even today fossil fuels are major source of energy which is non renewable. Their limited resources as well as its negative impact on environment after its combustion forces the scientific community to search for a sustainable energy and technology based on it. The main theme of the thesis is the development of a suitable photocatalyst for the production of hydrogen from renewable sources such as solar energy and water.

In this chapter, the thrust for the development of renewable and clean fuels and adverse effects of conventional non-renewable energy sources, different ways to utilize solar energy- which is the most abundant source of energy on earth - and conversion of solar energy into carbon free fuel such as hydrogen is introduced. The different methods for hydrogen generation by using solar energy and how photocatalytic water splitting is most promising approach for commercializing hydrogen production are described briefly in this chapter. Role of heterogeneous catalyst in the water splitting reaction, problems encountered during the reaction and the review of research done till date to bring the water splitting reaction into reality is also revealed here.

1.1 Need for development of renewable and clean fuels

1.1.1 Energy crises

Energy is a backbone of growing economy. According to BP Energy Outlook the global consumption of energy is 13147 Mtoe (million tonnes of oil equivalent) in 2015 and

increases to 17157 Mtoe in 2035 [1]. India is the second largest energy consumer in Asia and world's third largest oil consuming country after US and China. BP energy outlook predicts that by 2035 India's energy consumption is set to grow 4.2 % per year by 2035 which is faster than the major economies in the world. Growing economy and exploding population are the reasons behind the rapid increase in energy demand. In India, most of the energy is derived from fossil fuels and it is predicted that its dominance will increase in future. To satisfy the energy requirement, India is importing fossil fuels. In 2013, it imported 255.3 Mtoe of primary energy which shares for 42.9 % of total primary energy consumption. It is predicted that by 2030, total energy imports may become 53 % of primary energy consumption [2]. Thus growing country like India needs to focus on development of renewable and nonconventional sources which can fulfil its need for energy.

1.1.2 Generation of green house gases and its impact on environment

Pollution and global warming caused due to burning of fossil fuels is a major concern as its partial or complete combustion generates harmful and toxic gases CO, CO₂, SO₂, NO_x, C_xH_y etc. Combustion of coal and natural gasses produces 430 and 190 g of CO₂/kWh [3]. Human activity generates 6 billion tons of CO₂ annually [4]. At the time of industrial revolution in 1750, CO₂ concentration in the atmosphere was 280 ppm which has increased to 404 ppm in 2017 [5]. CO₂ is known as GHG (green house gas) as it absorbs and emits radiations in the thermal infrared region. Recently it is predicted that if the CO₂ generation by burning of fossil fuel continues with the present rate, then global warming will rise to 2 °C by 2036, crossing a threshold which will affect the ecosystem, biodiversity and living of people. To evade this threshold CO₂ concentration must be below 405 ppm [6]. Fig. 1.1 shows how global temperature increases with increase in CO₂ concentration [7].

Therefore it is needed to replace fossil fuels with sustainable, renewable and environment friendly fuel to overcome the scarcity of fossil fuel and its harmful impact on environment after its burning.

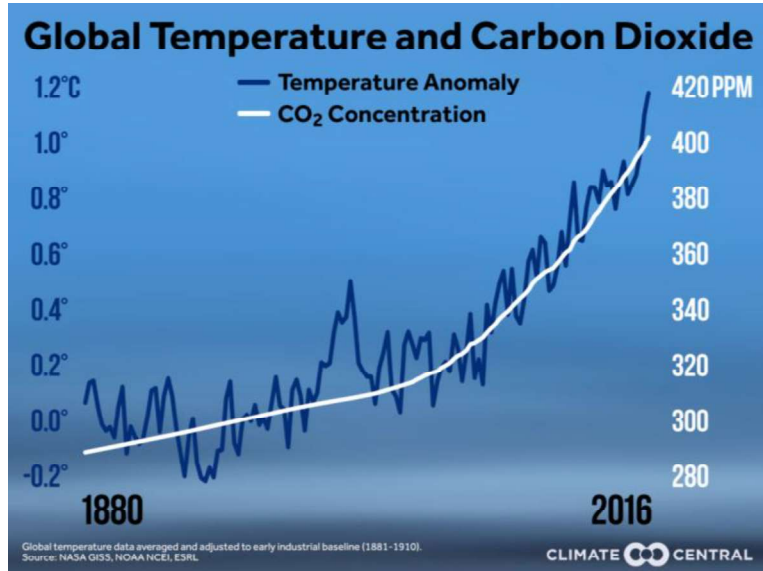


Fig. 1.1 Increase in CO₂ concentration correlated with rising temperature from 1880 to 2016.

1.2 A sustainable energy: Solar energy

Sunlight is a primary source of energy on the earth and it is free, abundantly available and renewable. Fig. 1.2 shows solar irradiance spectrum [8]. Sunlight consist of ~4 % UV region, 45-48 % of visible light and remaining is IR region.

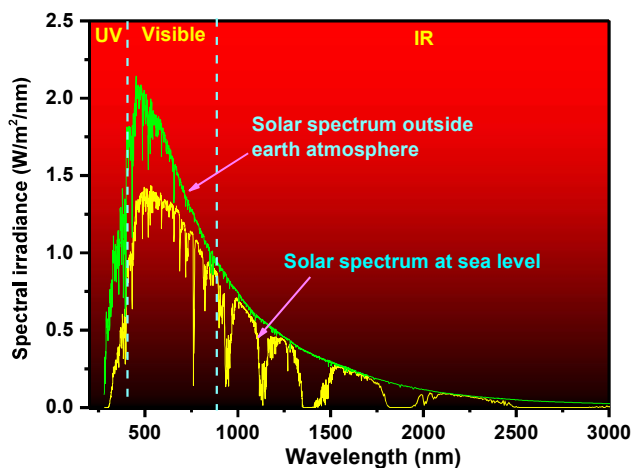


Fig. 1.2 Solar irradiance spectrum above atmosphere and at sea level.

Solar energy can be converted to thermal and electrical energy using clean technology to minimize the GHG (green house gases) emission. Solar energy falling on the Earth is 130,000 TW which is approximately four orders of magnitude of current world's energy demand [9]. Even utilization of all the energy falling on the earth only for half an hour can satisfy the world's one year energy requirement [10]. The International Energy Agency proposed that solar energy could be “a third of the global final energy demand after 2060, while CO₂ emissions would be reduced to very low levels” [11].

India is a tropical country and sunlight is available in abundant amount around 9 months in a year. The utilization of solar energy efficiently can satisfy India's growing energy demand. India receives 200 MW/km² (megawatt per kilometre square) average intensity of solar light [12]. If 0.04 x 10⁶ km² area is used then available solar energy will be 8 x 10⁶ MW equal to 5909 Mtoe (million tonnes of oil equivalent) per year [12] which is far more than the total primary energy consumption of India which was 723.9 Mtoe in 2016 [13]. Hence solar energy is a viable option to reduce dependence on fossil fuels and global warming.

However, sunlight is intermittent in nature. Its availability depends on time, season and geographical position. There are many ways to harvest solar light. One of them is by photovoltaic cell which converts radiant energy into electricity. Currently photovoltaic cells with 46 % efficiencies were developed [14]. But the energy produced by PV cells is expensive as compared to that from the petroleum products as well as its transport to remote area is difficult [15]. Therefore, it is advantageous to store this light energy into some chemical form such as hydrogen, which can be used as a readily available fuel for vehicle and other appliances.

1.3 Solar fuel - Hydrogen

Photosynthesis is a natural process by which plants harvest sunlight and convert it into chemical energy such as carbohydrates. Similarly, solar energy can be converted into chemical energy like hydrogen. H₂ has a high calorific value (141.8 kJ/g) compared to other fuels such as gasoline (40 kJ/g). Therefore, it is an attractive and clean fuel compared to other fuels as after combustion it gives only water. It is most abundant element on the earth in the form of water, biomass etc. It does not occur in pure form in nature therefore it need to be produced from compounds containing hydrogen. Hence, it is an energy carrier or storage medium and not an energy source as a coal. H₂ gas can be stored and transported. With the help of fuel cell it can be burned to give electricity which can be utilized to run automobiles. H₂ can also be utilized in modern chemical industry for Haber process, space application, recycling of CO₂ in Fischer-Tropsch reaction, production of methanol etc. [16]. About 9 million tons of hydrogen per year is produced by US hydrogen industry to use for chemical production, petroleum refining and electrical applications [17]. In India, H₂ is produced commercially for use in fertilizer industry, oil refineries and chemical industry. H₂ can be a boon to India which is immensely dependent on imported petroleum products to satisfy its energy need.

1.4 Hydrogen production methods

1.4.1 Methods for production of commercial hydrogen

96 % of world's H₂ production is from fossil fuels and 4 % by electrolysis of water. Commercially H₂ is produced by application of heat through steam reforming or coal gasification of fossil fuel and listed in Table 1.1. Cost of H₂ production using fossil fuel is \$0.75/kg for steam reforming, \$0.92/kg for coal gasification and \$0.85/kg for plasma arc decomposition [18]. However, these processes use non renewable sources as well as produce

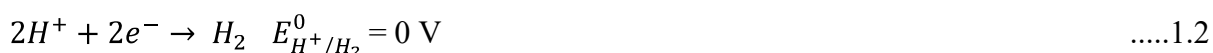
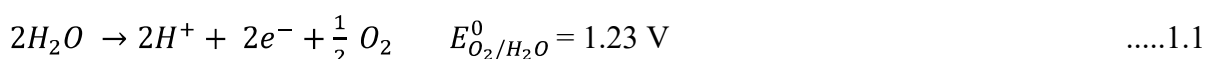
CO₂. The scarcity of fossil fuels will make the production of H₂ more expensive in near future. Also H₂ can be produced by electrolysis of water but this is an expensive way of hydrogen production as the energy required for its production is more than that could have been generated after its burning. Hence from environmental perspective, it will be beneficial to produce hydrogen from renewable energy sources.

Table 1.1 List of methods for commercial production of H₂

Sr No.	H ₂ production route	Process
1	Steam reforming	Fossil fuel reacts with steam at high temperature to give hydrogen; $CH_4 + H_2O \rightarrow CO + 3H_2$
2	Coal gassification	Fossil fuel reacts with controlled amount of oxygen gas and steam to give hydrogen; $3C + O_2 + H_2O \rightarrow 3CO + H_2$
3	Plasma arc decomposition	Cleaned natural gas is passed through plasma arc to generate H ₂ and carbon soot
4	Electrolysis of water	Direct current is used to split water into O ₂ and H ₂ (electrochemical reaction)

1.4.2 Production of H₂ from renewable source - solar energy and water

Water can be a source of H₂ as a molecule of water contains two atoms of hydrogen and one atom of oxygen. It can be split using following equation:



Overall reaction:



Number of electron (n) involved in the reaction is two. Therefore, change in Gibbs free energy required can be given as follows:

$$\Delta G^0 = -nF\Delta E^0 = 237 \text{ kJ/mol} \quad \dots 1.4$$

Equation 1.4 deduced that splitting of water is accompanied with positive change in Gibbs free energy. Hence energy needs to be supplied as it is an endothermic reaction at 298 K. To split water, temperature greater than 2500 K is required at atmospheric pressure [19]. This energy required to break water can be extracted from solar light. Following are the methods which can be used to split water using solar energy.

- a. Thermochemical water splitting [20]: It involves series of chemical reaction above the room temperature to split water into H_2 and O_2 .
- b. Photobiological water splitting [21]: It categorises into two groups one is organic biophotolysis it involves decomposition of organic waste to give H_2 and CO_2 . Other method is water biophotolysis in this bacteria and green algae splits water into H_2 and O_2 with the help of special enzyme in presence of light.
- c. Photocatalytic water splitting (PC) [22]: Splits water using solar energy harvested by powdered photocatalyst to produce H_2 .
- d. Photoelectrochemical water splitting (PEC) [23]: Solar energy absorbed by photoresponsive cathode or anode or both is utilized to bring electrolysis of water.

Among all these techniques PC has gain much attraction as this requires only water, solar light and powdered photocatalyst to convert solar energy into chemical energy. Using this process water can be split at room temperature to produce H_2 . Only drawback PC suffers is that the H_2 and O_2 produce in a single chamber. The mixture can be explosive if not separated. Hence, need to design a reactor where H_2 and O_2 will get separate once they formed. The cost of separation lowers the overall efficiency of water splitting process [24]. Nonetheless PC can be used for commercial solar hydrogen production - a promising way to achieve hydrogen economy.

In hydrogen economy, it was envisioned that hydrogen can be a prospective candidate to replace fossil fuels. H_2 can be produced by photocatalytic water splitting using solar

energy absorbed by photocatalyst and stored into hydrogen storage material. This stored H₂ can be taken to the required site for its utilization or feed into fuel cell to produce electricity. The product water can be recycled back to give hydrogen by employing solar energy. This is a clean way of conversion of solar energy into chemical form which can be further converted into electricity or can be used as fuel. Fig. 1.3 shows the overall process of conversion of solar energy into chemical energy such as H₂ which is a renewable and storable energy carrier.

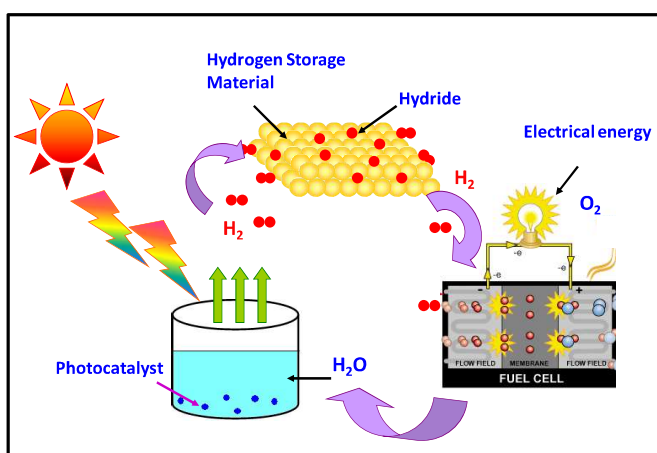


Fig. 1.3 Harvesting solar energy by photocatalytic water splitting for H₂ production, storage and fuel cell application.

1.5 Photocatalytic water splitting

Photocatalytic water splitting is a chemical reaction to split water into H₂ and O₂ using solar energy captured by a photocatalyst. This reaction is similar to photosynthesis by green plants hence referred as artificial photosynthesis [22]. Bard referred photocatalytic water splitting reaction using solar energy as “holy grail” [25].

In 1874 the concept of solar splitting of water into H₂ and O₂ was envisaged by Verne [26] who referred water as future coal. In 1912 Ciamicin [27] proposed the use of solar energy for various photochemical reactions such as catalytic conversion of water and CO₂ into oxygen and methane and other endo-energetic processes. First time in 1968, light assisted oxygen evolution was reported over semiconductor n-type TiO₂ (rutile) electrode by

Boddy [28]. After this in 1972 Fujishima and Honda first time demonstrated water splitting by shining light on n- type TiO_2 (rutile) electrode [29]. When light shines on TiO_2 electrode, electrons and holes are produced. These electrons travels to the Pt counter electrode and reduce water to produce H_2 . The holes on the TiO_2 electrode oxidized water to give O_2 .

1.6 Photocatalyst

Catalyst enhances the rate of reaction by lowering the activation energy of reaction. The modern definition of a catalyst is “A catalyst is a substance that allows a chemical reaction to attain equilibrium faster without itself being permanently involved”. Catalytic reactions plays important role in many industrial as well as natural processes. Catalyst technology is backbone of chemical industries as around 90 % of chemical reactions in industries depend on the catalyst. In many metabolic processes of plants and animals, catalyst is playing an important role. Catalyst can be classified as homogeneous catalyst and heterogeneous catalyst. Homogeneous catalysis is the process where phase of reactant and catalyst is the same whereas in heterogeneous catalysis, catalyst and reactant are in different phases and reaction takes place at the interface of two phases [30].

Photocatalyst plays key role in photocatalytic reactions. It is composed of two words “photo” and “catalyst”. The difference between photocatalyst and thermal catalyst is that former is activated by absorption of photon whereas latter is activated by heat energy [31]. Chlorophyll in plant is an example of natural photocatalyst. It absorbs light and converts water and carbon dioxide into O_2 and glucose. IUPAC defined photocatalyst as “Catalyst able to produce, upon absorption of light, chemical transformations of the reaction partners. The excited state of the photocatalyst repeatedly interacts with the reaction partners forming reaction intermediates and regenerates itself after each cycle of such interactions” [32].

Photocatalytic water splitting can be performed using homogeneous as well as heterogeneous catalyst. Heterogeneous catalyst is advantageous as compared to homogeneous

catalyst. As in heterogeneous photocatalysis separation and reuse of catalyst is easy and cheap as compared to homogeneous catalysis. Also energy is consumed to recover homogeneous catalyst from the reaction medium or it may get deactivate during recovery process. Heterogeneous photocatalysts are thermally stable whereas most of the homogeneous photocatalysts are thermally unstable. Also oxidation of water to give oxygen is a $4e^-$ process which is difficult in homogenous catalysis [22]. In last 4 decades many books as well as review articles are published on water splitting using heterogeneous catalyst [16,24,33–39].

Semiconductors are potential photocatalyst because of their suitable optical and electronic properties. In semiconductors valence band is completely filled while conduction band is partially filled or completely empty band. This valence band and conduction band is well separated by the forbidden gap called band gap. Some external energy like light, thermal etc equal to or greater than band gap energy is needed to promote the electron from valence band to conduction band by leaving a hole in the valence band. This band gap energy is different for different semiconductors. Hence semiconductors are useful for trapping of light/thermal energy. The electrons and holes generated can be utilized further to reduce and oxidize water respectively. This redox reaction is similar to electrolysis. Thus powdered semiconductor photocatalyst is a miniature photoelectrochemical cell as each particle acts as a tiny electrochemical cell [24]. The detailed procedure of water splitting using semiconductor photocatalyst is described below.

1.7 Processes involved in photocatalytic water splitting

The steps involved during photocatalytic water splitting are shown in Fig. 1.4. The first step is absorption of light by the semiconductor photocatalyst to produce e^-/h^+ pairs. When the light possessing energy greater than the band gap falls on semiconductor, electrons from the valence band get excited to the conduction band by leaving behind a hole in valence

band. The second step is the separation and migration of photogenerated e^-/h^+ to the surface active sites. The electron and hole should not recombine back to release energy in the form of unproductive heat or photons. Third step is reduction of water by electron to H_2 and oxidation of water by hole to O_2 .

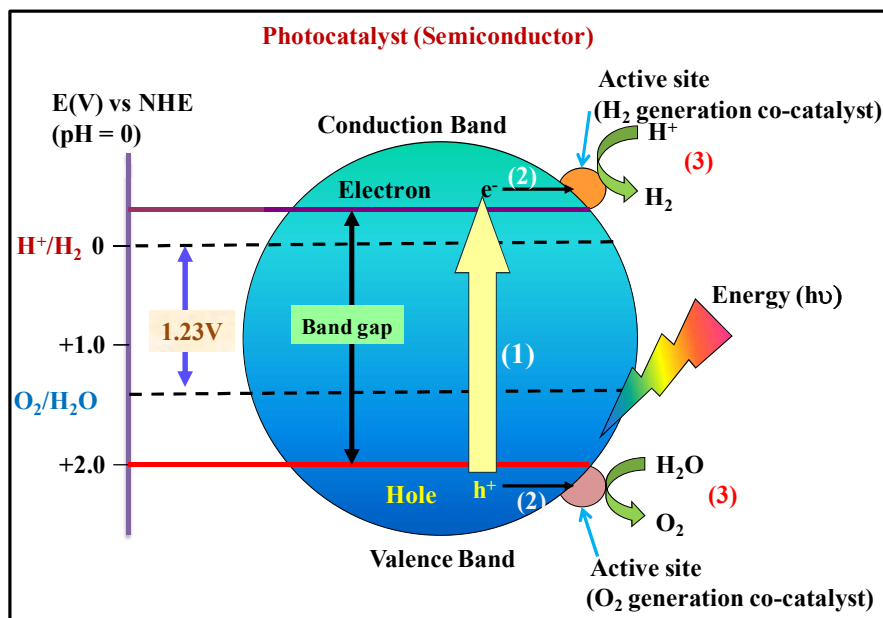


Fig. 1.4 Steps involved during photocatalytic water splitting using semiconductor photocatalyst.

1.8 Targets for commercialization of water splitting

Apparent quantum efficiency (AQE, η): If experimental parameters such as type of light source, reaction cell are different then it is difficult to compare the H_2 yield from lab to lab. Hence, determination of quantum efficiency is important. Quantum efficiency is a ratio of number of electrons produced to the number of photons absorbed by the system. However, it is difficult to determine the number of photons absorbed by the photocatalyst but it is possible to determine the number of photons falling on it by luxmeter. Hence the determined quantum efficiency is the apparent quantum efficiency (AQE, η) [40]. AQE is always smaller than the real QE because it takes into account only the incident photons which are higher in number than the absorbed photons. AQE (η) is calculated by using following equation.

$$\eta(\%) = \frac{2 \times \text{Number of } H_2 \text{ molecules evolved}}{N} \times 100 \quad \dots 1.5$$

Where, N is number of photons falling on the system.

Solar to fuel efficiency (SFE): Another way to calculate efficiency of photocatalyst for the solar water splitting reaction is given by solar to fuel efficiency (SFE) in sunlight is calculated using following formula:

$$SFE = \frac{r_{H_2} \times \Delta H}{P_{sun} \times S} \times 100 \quad \dots 1.6$$

Where r_{H_2} is the rate of hydrogen generation ($\mu\text{mol/h}$), P_{sun} energy flux of solar light (W/m^2) measured as mentioned above and S is the area of the reactor (m^2).

For practical application, target is 30 % AQE at 600 nm which corresponds to 5% of solar energy conversion [22]. With the achievement of SFE of 5 % solar photocatalytic H_2 generation can be produced at the cost of \$2.3/kg which can fulfil the targets of U.S. Department of Energy (DOE) to generate H_2 at the cost of \$2 to \$4/kg [41]. SFE of 10 % can provide H_2 at the cost of \$1.63/kg which is comparable to the cost of gasoline [42].

1.9 Criterion for selection of photocatalyst

Photocatalyst should satisfy the following criterion for practical application.

a. Semiconductor photocatalyst must satisfy the thermodynamic criterion for water splitting. The bottom of the conduction band must be more negative than the reduction potential of water (0 V vs. NHE at pH= 0) and top of the valence band must be more positive than the oxidation potential of water (1.23 V vs. NHE at pH= 0). Therefore, the minimum band gap required to bring the overall water splitting is 1.23 eV which corresponds to the wavelength ~ 1100 nm. However, there is a barrier that electron need to overcome during the charge transfer process between photocatalyst and water molecules. Hence, energy greater than 1.23 eV is needed to drive the reaction. A photocatalyst having a band gap around 2 eV is preferred. This energy corresponds to wavelength in visible region. Hence, it is possible to carry out reaction using solar energy.

b. Photocatalyst must be active under sunlight for practical application. As mentioned above sunlight consists of ~4 % UV region and ~45-48 % of visible light. The band gap must be below 3 eV for the utilization of sunlight spectrum efficiently.

c. To increase the efficiency of reaction, electron and hole pair transfer rate must be faster than the rate of recombination.

d. Photocatalyst must be stable towards light during the reaction and it should not undergo photocorrosion.

e. It should not promote back reactions on the surface. Surface back reaction occurs over the photocatalyst surface where H₂, O₂ and intermediates formed during the reaction may recombine back to give water.

From the above discussion it is important to design a photocatalyst with maximum visible light absorption, low rate of recombination and long term photostability for the reaction.

1.10 Semiconductor as photocatalyst

Many semiconductors have been investigated for their ability to split water under light illumination. Around 190 phases were tested as potential photocatalyst till date [39,43]. Metal oxides, metal sulfides, metal nitrides, metal oxynitrides and metal-free catalysts are promising catalytic systems for photocatalytic water splitting.

1.10.1 Metal oxides

Transition metal oxides are semiconductors and are well known for their catalytic and semiconducting properties. They are stable due to high electronegativity of oxygen atom. Based on metal electronic configuration, transition metal oxides are classified as metal ions with d⁰ and d¹⁰ electronic configuration.

In metal oxides valence band mainly consist of oxygen 2p orbital. Hence the upper level of valence band is located around 3 V (vs NHE, at pH= 0) for most of the metal oxides.

To split water the lower level of conduction band has to be more negative than the H^+/H_2 (0 V vs NHE, at pH=0) level. Hence most of the metal oxides has band gap more than 3 eV [44].

If alkali (Li, Na, K, Rb, Cs), alkaline earth (Be, Mg, Ca, Sr, Ba) and some lanthanide (La, Nd, Sm, Pr) ions are used as a component of the photocatalyst, then they merely build the crystal structure and do not directly contribute to the band formation e.g. A site cations in ABO_3 perovskite [22].

In d^0 electronic configuration, outermost empty d orbitals of metal cation mainly construct conduction band. Oxides having d^0 metal cation includes TiO_2 , ZrO_2 , WO_3 , Ta_2O_5 , Nb_2O_5 oxides [22]. Perovskites like $SrTiO_3$ [45], $NaTaO_3$ [46] and layered perovskites such as $A_2La_2Ti_3O_{10}$ (A = K, Rb, Cs) [47], $Ba_5Nb_4O_{15}$ [48] shows pure water splitting activity in presence of NiO, some hexatitanates with rectangular tunnel structure such as $A_2Ti_6O_{13}$ (A = Na, K, Rb, Cs) [49] shows decomposition of water in presence of RuO_2 . Layered structure such as $K_4Nb_6O_{17}$ [50] and $K_2La_2Ti_3O_{10}$ [51] shows high activity as this layered structure provides different sites for H_2 and O_2 evolution and thus helps in preventing back reaction on the surface [52].

In d^{10} electronic configuration, hybridized orbitals of empty *s* and *p* orbitals of metal cation predominantly forms conduction band. In d^{10} metal oxides conduction band is composed of mainly *sp* hybridized orbitals with large dispersion. This offers high mobility to photogenerated electron in the conduction band and thus useful for photocatalytic reactions [53]. d^{10} metal oxides includes In_2O_3 , Ga_2O_3 , GeO_2 , SnO_2 , Sb_2O_5 , ZnO [22,54,55]. Among them ZnO and In_2O_3 are well known photocatalyst but they are not active for water splitting due to photocorrosion and low conduction band level respectively [22]. Different kinds of indates, gallates, germanate, antimonates and stannates were studied for water splitting reaction [56–62].

Except the d^0 and d^{10} metal oxides, photocatalytic activity of some of the transition metals were also evaluated. CoO (d^7 electronic configuration) nanoparticles synthesized by two different methods femtosecond laser ablation and ball milling. This nanoparticles exhibited pure water splitting with SFE conversion efficiency of 5 %, without loading of cocatalyst. But the stability of CoO nanoparticle was poor is the major drawback as it becomes deactivated after one hour of illumination [63]. Various other conventional semiconductors such as Fe_2O_3 and $BiVO_4$ have been examined with their ability to modify visible light response of photocatalyst. However, they show conduction band level lower than reduction potential of water hence incapable for hydrogen generation.

1.10.1.1 TiO_2

Among metal oxides TiO_2 is a promising catalyst for commercial production of H_2 . As many metal oxides shows slight solubility in water, some ternary oxides shows poor stability due to leaching of alkali and alkaline earth component into reaction media and sulphides shows poor stability as they undergo photocorrosion during the reaction [34]. Excellent stability of TiO_2 is one of the reasons for its extensive use as photocatalyst. Along with stability it shows suitable optical and electronic properties, stable to wide range of pH, non-toxic and low cost. It exists in three phases: brookite (orthorhombic), anatase (tetragonal) and rutile (tetragonal) phase and their properties are tabulated in Table 1.2.

Table 1.2 Properties of TiO_2 polymorph [64]

Properties	Rutile	Anatase	Brookite
Crystal structure	tetragonal	tetragonal	Orthorhombic
Lattice constant (\AA)	$a = 4.5936$ $c = 2.9587$	$a = 3.784$ $c = 9.515$	$a = 9.184$ $b = 5.447$ $c = 5.154$
Space group	P42/mnm	I41/amd	Pbca
Molecule (cell)	2	2	4
Volume/ molecule (\AA^3)	31.2160	34.061	32.172
Density (g/cm^3)	4.13	3.79	3.99

Ti–O bond length (Å)	1.949 (4) 1.980 (2)	1.937(4) 1.965(2)	1.87–2.04
O–Ti–O bond angle	81.2° 90.0°	77.7° 92.6°	77.0°–105°
Band gap	3.02	3.2	2.96

In anatase TiO₂, the distortion of the TiO₆ octahedron is more as compared to rutile phase. Distorted and open structures are more flexible for the transfer of electron. The electronic properties of TiO₂ are well studied where distorted tetragonal lattice imparts favourable photocatalytic properties to anatase TiO₂ [65]. Anatase phase is most active than the rutile phase because of more negative conduction band edge position, lower rate of charge recombination, lower capacity to adsorb oxygen and higher degree of hydroxylation [66,67].

Although having favourable properties for water splitting, its photocatalytic activity is low in sunlight due to inability to absorb visible light and the fast recombination of photogenerated electron and hole pair. Different methods were adopted to improve the photocatalytic activity of TiO₂ are discussed later.

As explained above most of the metal oxides have band gap more than 3 eV hence rendered it unfit for splitting of water under sunlight illumination. Low electron-hole pair mobility and their poor lifetime constrain the activity of metal oxides [42]. Therefore, there is a need to develop a visible light active photocatalyst.

1.10.2 Non-oxide photocatalyst

To overcome the limitations of oxide material, non oxides like sulphides, nitrides were proposed as their valence band is composed of S 3*p* and N 2*p* orbital which are higher in energy as compared to their analogues metal oxide. These include oxynitrides, oxysulphides, sulphides, nitrides of metal having d⁰ and d¹⁰ electronic configuration.

CdS [68], ZnS [69] and CdSe [70] are studied as photocatalyst for H₂ generation. CdS is visible light active catalyst and shows absorption upto 520 nm. But its major drawback is

self oxidation by holes during irradiation. In this S^{2-} in CdS gets oxidized by photogenerated hole results into elution of Cd^{2+} as shown in equation.



Metal oxynitrides shows lower band gap and may show properties of both oxides and nitrides. Metal oxynitride such as TaON [71], $(Ga_{(1-x)}Zn_x)(O_{(1-x)}N_x)$ [72] were studied for splitting of water.

$2p$ orbital of nitrogen has higher energy in nitrides as compared to the analogous orbitals of oxygen in metal oxide [73]. Nitrides such as Ge_3N_4 [74], Ta_3N_5 [75], $g-C_3N_4$ [76] are studied as photocatalyst. Usually nitrides suffer from poor stability and they cannot be used for long term photocatalytic activity [77].

1.10.2.1 $g-C_3N_4$

Among all nitrides, graphitic carbon nitride ($g-C_3N_4$) has attracted much attention as it composed of extremely abundant elements such as C and N, tunable electronic structure, and nontoxic with proven stability both thermally and in solutions of pH 1–14 [78]. $g-C_3N_4$ is an organic polymer of carbon and nitrogen having tri-s-triazine as a repeating unit. These rings are connected each other by sp^3 hybridized N atom to form a 2D layer structure as shown in Fig. 1.5.

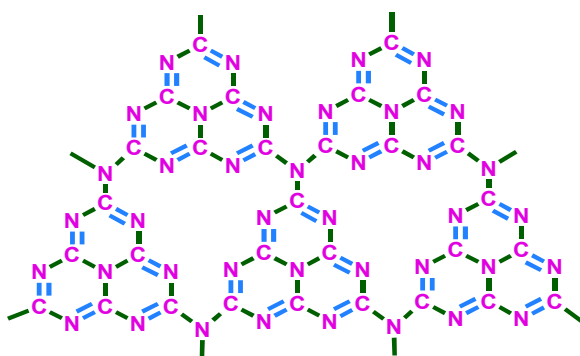


Fig. 1.5 Structure of polymeric graphitic C_3N_4

g-C₃N₄ satisfies the thermodynamic criterion required for water splitting and lower band gap (2.7 eV) compared to TiO₂ (3.2 eV). Hence it is a promising photocatalyst for visible light reactions. Wang et al [76] first demonstrate the photocatalytic properties of g-C₃N₄. They performed the DFT calculation to evaluate the structure of g-C₃N₄ and found that valence band is predominantly composed of nitrogen *p_z* orbitals whereas carbon *p_z* orbitals constitute conduction band. This implies that the nitrogen is the preferred sites for the oxidation of water whereas carbon atom offers reduction sites to produce H₂ [76].

This polymer can be synthesized by polycondensation or pyrolysis of nitrogen rich precursors like cyanamide [76], dicyandiamide [79], melamine [80], thiourea [81], urea [82,83]. The physical and chemical properties of g-C₃N₄ depend on the type of precursor and reaction conditions. Martin et al [78] has reported the highest photocatalytic H₂ evolution over g-C₃N₄ (H₂ @ 20,000 μmol/h over Pt/g-C₃N₄ in presence of sacrificial reagent) synthesized from urea as compared to that synthesized from other precursor like dicyandiamide and thiourea. Experimental as well as DFT calculations revealed that the increase in degree of polymerization and decrease in proton concentration results into enhancement of H₂ production rate.

Although having suitable properties as photocatalyst it suffers from poor activity due to high recombination of electron and hole pair and low surface area with medium band gap [78,84].

1.10.3 Progress till date

Many photocatalytic systems were tested for photocatalytic water splitting till date and they are listed in Table 1.3. Still the required efficiency for water splitting is not achieved for commercialization.

Table 1.3 H₂ yield over different photocatalyst systems

Sr no	Photocatalyst	Co-catalyst	Light source	Reaction conditions	H ₂ yield	AQE/SFE
1	(Ga _(1-x) Zn _x) (N _(1-x) O _x) [85]	Rh _{2-y} Cr _y O ₃	450 W High pressure Hg lamp with aq NaNO ₂ as filter($\lambda > 400$ nm)	300 mg photocatalyst dispersed in 370 ml of aqueous H ₂ SO ₄ , pH adjusted to 4.5	H ₂ : 800 μ mol/h O ₂ : 400 μ mol/h	AQE 5.9 % at 420-440 nm
2	CdS [68]	Pt-PdS	300 W Xe-lamp	300 mg of photocatalysts powder suspended in 200 mL of 0.5 M Na ₂ S-0.5 M Na ₂ SO ₃ solution	8.77 mmol/h	AQE 93 %
3	Black TiO ₂ [86]	Pt	Solar simulator	20 mg photocatalyst dispersed in 1:1 water :methanol solution	10 mmol/h/g	SFE 24 %
4	CoO [63]	No cocatalyst	Solar simulator	25 mg photocatalyst dispersed in water	20 ml in 30 min	SFE 5 %
5	Carbon/TiO ₂ / Carbon nanotube [87]	Pt	Solar simulator	10 mg photocatalyst dispersed in 120 ml of 1:1 water :ethanol solution,	37.6 mmol/h/g	AQE= 95 % at $\lambda < 340$ nm & 1.5 % at 430 nm
6	Carbon dots/g-C ₃ N ₄ [88]	No cocatalyst	300 W Xe-lamp with cut off filter ($\lambda > 420$ nm)	80 mg photocatalyst dispersed in 150 ml water	H ₂ : 45.2 μ mol/h O ₂ : 22.1 μ mol/h	SFE 2 % AQE 16 %

7	La/NaTaO ₃ [52]	NiO	400 W High pressure Hg lamp	1 g of catalyst dispersed in 390 ml of pure water	H ₂ : 19.8 mmol/h O ₂ : 9.7 mmol/h	AQE 56 % (at 270 nm)
8	Hf doped (Na, K)TaO ₃ [89]	No cocatalyst	350 W High pressure Hg lamp	0.1 g dispersed in 350 ml pure water	H ₂ : 4.96 mmol/h O ₂ : 2.46 mmol/h	Not given
		No cocatalyst	350 W High pressure Hg lamp	0.1 g dispersed in 300 ml pure water + 50 ml of methanol	25.6 mmol/h	Not given
9	ZrO ₂ -TaON and WO ₃ [90]	Pt	300 W Xe lamp	100 mg of Pt/WO ₃ and 50 mg of Pt/ ZrO ₂ /TaON; 100 ml (0.5 mM) NaI	H ₂ : 7.5 μmol/h O ₂ : 3.8 μmol/h	AQE 6.3 %
10	LaMg _x Ta _{1-x} O _{1+3x} N _{2-3x} [91]	Pt	300 W Xe lamp	0.2 g in 250 ml 10 vol % methanol solution	H ₂ : 62.5 μmol/5h	Not given
11	BiVO ₄ :In,Mo [92]	RuO ₂	500 W Hg arc lamp	0.3 g of photocatalyst in 100 ml of water	H ₂ : 17 μmol/h	AQE 3.2 % (at 420- 800 nm)
12	PS II and Ru/SrTiO ₃ :Rh [93]	Ru	Xe lamp with a long-pass filter (λ < 420 nm) and 250 mWcm ⁻² power density.	Ru/SrTiO ₃ :Rh (0.1 g), PSII (1 mg chlorophyll) and Fe(CN) ₆ ³⁻ (5 mM) dispersed in 100 ml of buffer solution (50 mM sodium phosphates, 15 mM NaCl, pH 6.0)	H ₂ : 2489 mol H ₂ / mol of PS II/ h O ₂ : 1334 mol H ₂ / mol of PS II/ h	Not given
13	GaN:Mg/ InGaN:Mg [94]	Rh/Cr ₂ O ₃	300 W Xe lamp	0.48 mg sample deposited over 3 cm ² glass plate and immersed in water	H ₂ : 3.46 mol/h/g O ₂ : 1.69 mol/h/g	AQE: 12.3 % (400- 475 nm), SFE: 1.8 %

1.11 Designing modified photocatalyst with improved light absorption properties

As explained above the problem with the transition metal oxides like TiO_2 , Ta_2O_5 , Nb_2O_5 , SrTiO_3 etc are large band gap material. Therefore cannot able to utilize the solar light. Different strategies adopted to utilize major portion of sunlight i.e. visible region by band gap engineering.

1.11.1 Cationic or anionic doping

One of the methods to modify the band gap of metal oxides in order to absorb in the visible region is by cation or anion doping. Dopant is a foreign element which replace the crystal lattice point of the host material [22]. Cationic dopants create impurity levels in the band gap by modifying the electronic structure of semiconductor. These levels may be donor level above the valence band or the acceptor level below the CB [95]. Thus helps in overall reduction of band gap as shown in Fig. 1.6.

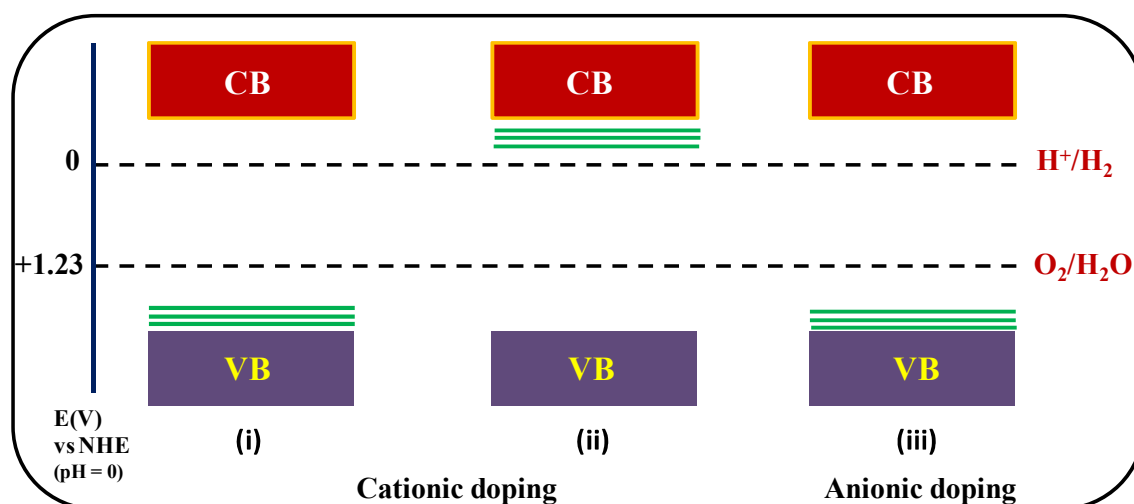


Fig. 1.6 (i) Donor level and (ii) acceptor level formed by metal ions doping and (iii) new VB formation by anionic doping.

Synthesis route, ionic size and amount of dopant, electronegativity and oxidation state of both host and dopant atoms affect the physico-chemical and photocatalytic properties of doped titanium dioxide [96]. Doping of various transition metals with partly filled d orbital and rare earth ions into d^0 and d^{10} material is an effective way to reduce the band gap of

material [55,97]. Transition metals Cu, Ni, Fe and Cr doped TiO₂ shows enhancement in photocatalytic activity of TiO₂ [98–100]. Zalas et al [101] synthesized platinized lanthanide doped TiO₂ photocatalyst and found maximum activity for photocatalytic H₂ generation over 0.5 mol % Gd, Eu, Yb, or Ho doped TiO₂. NiO (0.2 wt %)/ NaTaO₃:La(2 %) shows high activity for pure water splitting with AQE of 56 % at 270 nm which is nine times higher than the undoped NiO/NaTaO₃. La doping decreases the crystal size and shows characteristic ordered surface nanosteps. H₂ evolution takes place over the ultrafine NiO loaded on edge of the nanostep whereas O₂ evolution occurred at the groove of the ordered nanostep structure. Increased crystallinity with decreased particle size and presence of separate H₂ and O₂ evolution sites on the catalyst surface results into enhancement of H₂ yield [52].

Although doping enhances light absorption properties but its excess amount acts as a recombination centres. Hence, small amount of dopant loading is preferred to balance the recombination and light absorption properties. Also the cationic doping creates discrete impurity levels hence disadvantageous for migration of photogenerated holes [95].

Self doping of TiO₂ evades the introduction of unfavourable recombination centre and the thermal stability associated with dopant [38]. Zuo et al [102] reported the high stability, improved light absorption and enhanced photocatalytic activity over Ti³⁺ self doped TiO₂ under visible light illumination. Presence of Ti³⁺ or oxygen vacancy forms defects band below the conduction band minimum and its width depends on the concentration of Ti³⁺ or oxygen vacancy and thus helps in absorption of visible light by narrowing the band gap.

In many cases doping with single element creates charge imbalance which leads to the formation of charge recombination centres. By co-doping charge imbalance can be compensated which suppresses the formation of charge recombination centres and maintaining visible light absorption property. Hence co-doping is an efficient way to improve the photocatalytic activity. Rh and Sb co-doped in SrTiO₃ shows enhanced activity for H₂ and

O₂ generation in presence of respective sacrificial reagent and Pt as cocatalyst. Only doping with Rh shows presence of both +3 and +4 oxidation state. Rh in +4 state acts as recombination centre. But when doped with Sb, restrict the oxidation state of Rh as +3. Maximum H₂ generation was observed over the codoped sample when the ratio of Sb/Rh = 1 in presence of methanol and Pt. Whereas maximum O₂ evolution was observed when the ratio of Sb/Rh = 1.5 in presence of AgNO₃ [103]. Also codoping of C and S in SrTiO₃ shows shift of absorption band edge from 400 to 700 nm and thus enhances the photocatalytic oxidation of 2-propanol under visible light as compared to pristine SrTiO₃ [104].

In case of anionic dopant, (like B, N, C, P and S) *p* orbital of dopant mixes with the 2*p* oxygen state to form valence band (Fig. 1.6). This results into shift of the valence band edge upward thus help in the lowering of band gap to utilize visible region. Anionic doping is more effective as compared to cationic doping as it forms few recombination centres. Hong et al [105] synthesized the sulphur doped mesoporous g-C₃N₄ and proposed the replacement of carbon by sulphur and lowering down the conduction band by 0.25 eV. This narrowing of band gap resulted into increasing light absorption in visible region. S doped mesoporous g-C₃N₄ is 30 times more active than the pristine g-C₃N₄ for photocatalytic H₂ evolution reaction.

1.11.2 Dye sensitization

This is an effective technique for visible light harvesting. Organic dye can be used as a photosensitizer. Dye absorbs light and get excited to the excited state (dye*). This dye in excited state injects electron into conduction band of semiconductor and get converted into radical cation (dye⁺). LUMO (lowest unoccupied molecular orbital) level of the dye and conduction band of semiconductor must be proper for efficient transfer of electron. This electron in the conduction band of semiconductor reduces water to give H₂ whereas the cation radical of dye (dye⁺) reacts with electron donor sacrificial reagent to regenerate back. Proper

design of dye and semiconductor is required to inhibit charge trapping and recombination to enhance the product yield [4]. Most commonly studied metal free dyes are Eosin-Y, acriflavin, Eosin Blue, Rhodamine B, Rose Bengal, fluorescein. Also dyes like ruthenium (II) complex, polypyridine complexes, alizarine, phthalocyanine, and metalloporphyrins having metals at the centres such as Pt(II), Co(II), Zn(II), and Cr(III) are well studied [4,55,95,97,106]. Self degradation of dye is the major problem to be addressed [106].

1.11.3 Recombination is a competing process

Photocatalytic processes inside the bulk and surface of the semiconductor takes place in the range of femtosecond to second. Table 1.4 listed the photoinduced reactions in TiO₂ semiconductor with their corresponding time scale. Charge transfer process takes longer time from picoseconds to millisecond than the recombination or trapping of charges (femtosecond to picosecond time scales). Recombination of free and shallow trap related charges takes place in picoseconds to nanosecond time scale whereas deep trap related charges recombines at a relatively longer time scale than the nanosecond [107,108]. In order to enhance photocatalytic activity, it is important to slow down the recombination and accelerate the electron and hole transfer process.

Table 1.4 Photoinduced reaction in the bulk and surface of TiO₂ semiconductor and their timescale.

A. Photoinduced reactions in the bulk of semiconductor		Time scale
i) Generation		
$TiO_2 \rightarrow e_{hot}^- + h_{hot}^+$		fs
ii) Trapping reaction		
Surface:	$h_{VB}^+ \rightarrow h_{shallow}^+$	50-170 fs
	$h_{VB}^+ \rightarrow h_{deep}^+$	200 fs
Bulk:	$e_{CB}^- \rightarrow e_{shallow}^-$	100- 260 fs
	$e_{CB}^- \rightarrow e_{trap}^-$	50 ps
iii) Recombination reaction		
Surface:	$e_{tr_{shallow}}^- + h_{tr_{shallow}}^+ \rightarrow recombination$	1-10 ps

Bulk:	$e_{tr_{deep}}^- + h_{tr_{deep}}^+ \rightarrow recombination$	> 20 ps
B. Photoinduced charge transfer processes on semiconductor surface		
	$h_{trap}^+ + CH_3OH \rightarrow CH_3O\cdot + H^+$	300 ps
	$e_{trap}^- + Pt \rightarrow e^-[Pt]$	10 ps
	$2e^- + 2H^+ \rightarrow H_2$	10- 900 μ s
	$h^+ + 2H_2O \rightarrow 4H^+ + O_2$	> 100 ms

1.11.3.1 Effect of particle size, surface area and crystallinity

Nanoparticles offer high surface to volume ratio. Surface is important to perform the heterogeneous reaction whereas volume is necessary to generate and separate electron and hole pair formed after absorption of light. Surface area of nanoparticle will be large hence more number of active sites leading to more adsorption of water molecules on the surface and hence enhances the yield of the reaction. But at the same time defect sites will also increase as the surface is also a type of defect where growth of the crystal terminates. These defect sites acts as electron-hole pair recombination centre hence lower down the activity. Due to small size nanoparticles, photogenerated carriers will have to travel a short distance to reach the surface where oxidation and reduction of water will take place. Li et al [109] synthesized hollow nanosphere, solid nanosphere and nanorods of CdS photocatalyst and compared their activity for photocatalytic H₂ evolution under visible light illumination. Maximum yield was observed over solid nanosphere as compared to hollow nanospheres and nanorods. They found that solid nanosphere is beneficial for faster charge migration to the surface active sites and suppression of recombination of charge carrier in bulk. However, in case of small size nanoparticles electron and hole are confined to small space may lead to increase in recombination probability. Hence there is a need to optimize between surface area and particle size by selecting proper size of photocatalyst [22].

Also the quantum size effect shown by nanoparticles can be exploited to enhance water splitting reaction. Band gap energy of nanoparticle increases with decrease in particle size. Hence by changing the size of semiconductor one can modify band gap energies, optical properties and redox potential of electron and hole. Frame et al found that the nanoribbons of CdSe possessing band gap 2.7 eV is active for H₂ generation in presence of sacrificial reagent whereas bulk CdSe having band gap of 1.7 eV is not active. The increase in band gap in nanoparticle of CdSe is a result of quantum size confinement i.e. which is the broadening of band gap with decrease in particle size. Because of this conduction band minima is elevated in CdSe nanoparticles (−0.55 V, NHE, pH = 7) as compared to bulk CdSe (−0.10 V, NHE, pH = 7). Hence electron in CdSe nanoparticle is more reducing (around 0.45 V) as compared to that in bulk [24].

At the interface of semiconductor and electrolyte charge transfer takes place till the Fermi level becomes equal to the redox potential of electrolyte. This is the base of the photocatalyst liquid junction [110]. At equilibrium a space charge layer is formed at the interface results into the bending of the energy levels. Usually the thickness of space charge layer is of the order of 1-10³ nm. This space charge layer helps in separation of photogenerated charge carriers. But in case of nanoparticles band bending decreases with decrease in particle size. Dimension of crystal if comparable to depletion layer limits the effective e⁻/h⁺ separation at the interface [111]. Therefore it is important to optimize the particle size.

In similar way crystallinity is also playing an important role. The crystalline sample will have lesser number of defects hence lesser recombination centres. Fig. 1.7 shows how the photocatalytic activity varies with the change in calcination temperature. Kong et al [112] studied the effect of defects on photocatalytic activity and concluded that decrease in ratio of bulk defects to surface defects in TiO₂ nanocrystals enhances the charge separation which

results in enhancement of photocatalytic efficiency. They also show that calcining TiO₂ at higher temperature can eliminate lattice strain in TiO₂ by reducing defects.

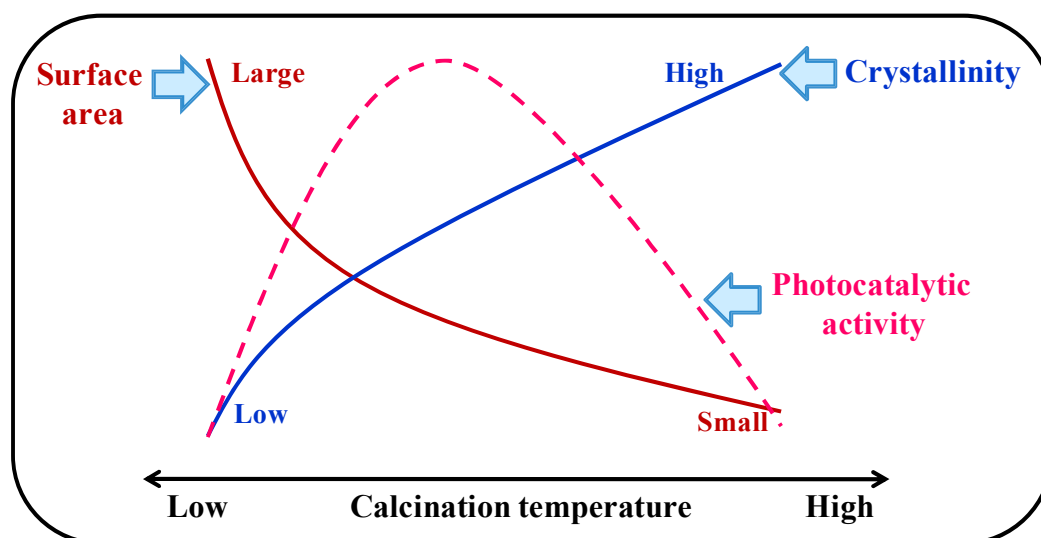


Fig. 1.7 Role of crystallinity and surface area of photocatalyst on photocatalytic activity.

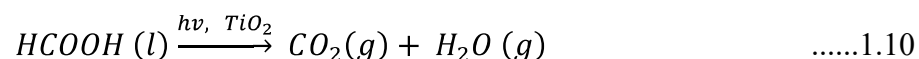
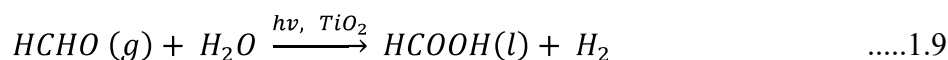
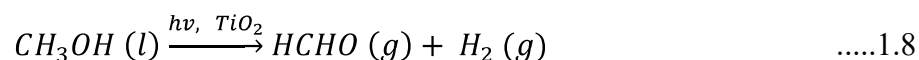
1.11.3.2 Use of sacrificial reagent

Recombination reaction competes with photocatalytic water splitting and affects efficiency of reaction adversely. To minimize the recombination reaction of e^-/h^+ pair, photocatalytic water splitting was studied in presence of electron donor or acceptor reagents. These additives act as either oxidizing agent or reducing agent which get reduced by electron or oxidized by hole respectively. Purely the reaction then on consumption to maintain the inflow of photogenerated electrons therefore refers as sacrificial reagent. Presence of sacrificial reagent also solves the issues related to back reaction of H₂ and O₂ and also addresses safety considerations related to H₂ and O₂ gas separation [113]. The only drawback of addition of sacrificial reagent is that it get consumed during the reaction hence there is need to add sacrificial reagent to continue the reaction [114].

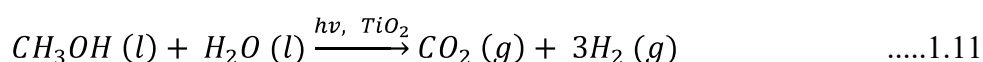
The sacrificial reagent can be classified as inorganic and organic electron donors. Most commonly used sacrificial reagents to scavenge holes are alcohols, amines, sulphite

salts. Methanol which is used as sacrificial electron donor also contributes in H₂ generation.

Following is the mechanism for methanol degradation [113]:



Overall reaction:



Oxidation potential of methanol is 0.02 V which is lower than the oxidation potential of water [114]. Methanol first get oxidized to form formaldehyde which on further oxidation gives formic acid which on subsequent oxidation gives CO₂ and H₂ as final product. During oxidation of methanol, hydroxymethyl radical is formed which injects electron into the conduction band of TiO₂ semiconductor it is called as current doubling effect [115].

Formic acid, glucose, oxalic acid, glycerol, chloroacetic acid, triethanolamine etc. were also used as sacrificial reagent by other researchers [55,76]. Thus, for commercialization, cheap sacrificial reagent such as glycerol which is a byproduct of biodiesel or any other organic compound with insignificant economic value can be used. In chapter 6, attempt was made to replace methanol with glycerol for economically viable production of H₂.

Ag⁺ or Fe³⁺ ions used as sacrificial electron acceptor to carry out photocatalytic O₂ evolution reaction as both the ions gets reduced by scavenging photogenerated electrons.

1.11.3.3 Dispersion of cocatalyst

Co-catalyst dispersed on the surface of photocatalyst provides active sites for reduction or oxidation of reaction and helps in reduction of activation barrier for the reaction. It also prevents back reaction of water formation on the catalyst surface.

Noble metals such as Ru, Rh, Pd, Pt, Au, Ag transition metal oxides like NiO, RuO₂, Rh_{2-y}Cr_yO₃ and transition metal sulphide such as MoS₂ are used as cocatalysts for hydrogen generation reaction, while noble metal oxides like RuO₂ and IrO₂ are used as cocatalysts for the oxygen evolution reaction [22]. RuO₂ is found to be active for both reduction and oxidation of water. Carbon compounds such as graphene, carbon dots etc also used as cocatalyst due to electronic conductivity imparted by pi-conjugated system.

Maeda et al [116] demonstrated that loading of two different co-catalysts for H₂ and O₂ evolution was beneficial for overall water splitting. Pure water splitting under visible light illumination was achieved over gallium and zinc nitrogen oxide (Ga_(1-x)Zn_x)(N_(1-x)O_x) photocatalyst modified with cocatalyst viz. nanoparticles of Rh/Cr₂O₃ core-shell and Mn₃O₄ as a H₂ and O₂ evolution site respectively. Back reaction over the Rh metal is prevented by the presence of amorphous Cr₂O₃ shell as it is permeable to proton and evolved H₂ molecules and not to O₂ molecules.

1.11.3.4 Formation of heterojunction

Different types of heterojunctions and their band alignment is as depicted in Fig. 1.8. Consider there are two different semiconductors A and B (either *p*-type or *n*-type). In type I heterojunction, conduction band (CB) of semiconductor B is above the semiconductor A and the valence band (VB) of semiconductor B is below that of semiconductor A. In this kind of heterojunction, band alignment is such that electron and hole will accumulate on semiconductor A after light illumination. In type II heterojunction, both valence and conduction band of semiconductor A is lower than that of semiconductor B. Here, electrons will move from higher CB of semiconductor B to that of A and holes will move from lower VB of semiconductor A to that of semiconductor B. This band alignment results into efficient separation of photogenerated charge carriers and enhanced photocatalytic activity. Type III is similar to that of Type II except the difference between VB and CB positions of two different

semiconductors is comparatively high as shown in Fig. 1.8. This band alignment provides better driving force for the transfer of charge carriers [117].

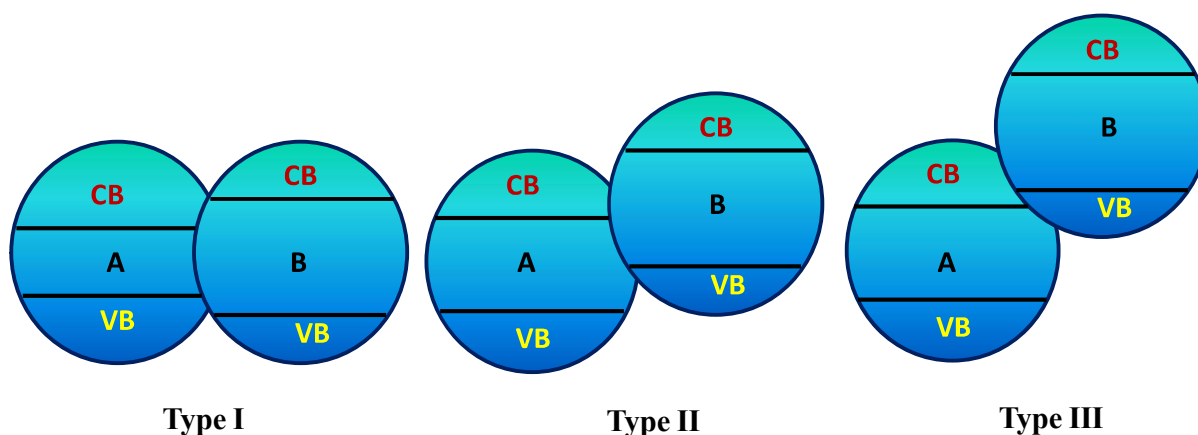


Fig. 1.8 Band alignment in different types of heterojunctions (Type I, Type II and Type III) [VB= valence band and CB= conduction band]

Among solid-solid interfaces following heterojunctions has gained much interest. They are as follows (i) semiconductor- semiconductor heterojunction (ii) semiconductor- metal heterojunction and (iii) semiconductor- carbon heterojunction.

(i) Semiconductor-semiconductor heterojunction

When *p*-type semiconductor comes in contact with *n*-type semiconductor, transfer of charge takes place till their Fermi level becomes equal. As a result of this charge transfer, space charge region is created at the interface. A combination of *p* and *n*-type oxides in a composite sample induces *pn* junctions and a generalized proposed mechanism of charge separation over these two oxides is shown in Fig. 1.9. At the interface band bending will take place as a result of formation of space charge region. The re-distribution of charge in the space charge region induces an electric field. This induced electric field at the *pn* junction helps in the separation of photogenerated electron and hole pair hence longer lifetime of charge carrier which results into enhancement of photocatalytic activity. *pn* junction offers several advantages such as faster charge transfer to the catalyst, reduces the recombination rate hence increased life time of charge carrier, effective separation of charges result into

separation of oxidation and reduction reaction in nanospace [118]. All these advantages results into enhancement of activity.

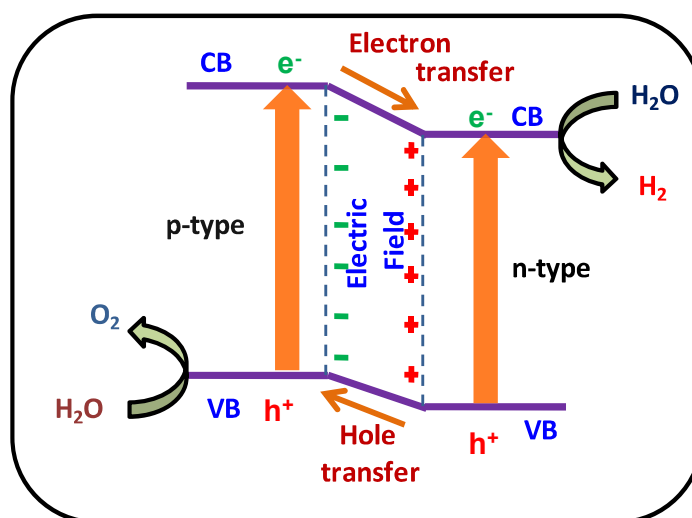


Fig. 1.9 Band alignment at *pn* heterojunction

TiO₂ is well known for its photocatalytic activity and it behaves as *n*-type semiconductor due to loss of lattice oxygen. A combination of *p* and *n*-type oxides in a composite sample induces *pn* junctions at the interface. *n*-type TiO₂ can be coupled with *p*-type NiO [119], Cu₂O [120], Co₃O₄ [121] to construct efficient heterostructured photocatalysts for different photocatalytic reactions. Similarly Meng et al [122] studied *p*-type MoS₂/ *n*-type nitrogen doped reduced graphene oxide nanoscale *pn* junction. The photoelectrochemical studies revealed that nanoscale *pn* junction greatly enhances the charge generation and suppresses the charge recombination, resulting into enhancement of solar H₂ generation in presence of ethanol.

(ii) Semiconductor- metal heterojunction

Noble metals such as Pt, Ag, Au, Cu, Ru and Pd can be loaded over the surface of semiconductor photocatalyst. When semiconductor comes in contact with metal, Schottky barrier (space-charge separation region) forms at the interface. If the work function of metal (ϕ_m) is higher than *n*-type semiconductor then electron will flow from semiconductor to metal. The transfer of charge continues till the Fermi level (E_f) equilibrates as shown in Fig.

1.10. This results into formation of Schottky barrier as excess of negative and positive charge accumulate on the metal and semiconductor respectively [118]. This Schottky barrier helps in the separation of photogenerated charge carrier thus enhances photocatalytic activity. If the metal has lower work function than the semiconductor then the electron will flow from metal to semiconductor.

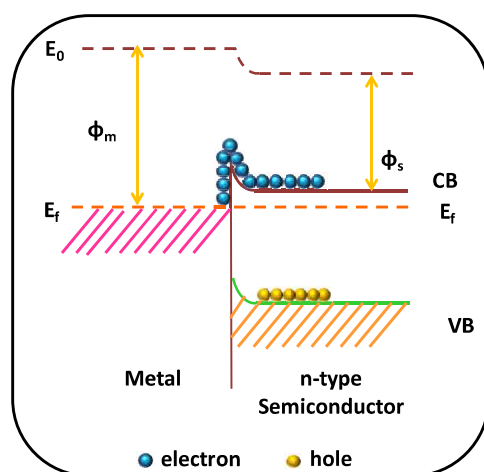


Fig. 1.10 Band alignment at the semiconductor-metal interface. (CB= conduction band, VB= valence band, E_f = Fermi level, ϕ_m and ϕ_s is work function of metal and semiconductor respectively)

Along with the formation of metal –semiconductor heterojunction, metal shows surface plasmon resonance (SPR) effect which helps in harvesting visible light. Surface plasmon resonance is the collective oscillation of conduction band electrons in a metal particle stimulated by the electromagnetic field of incident light [123]. When a light falls on a spherical metal nanoparticle having wavelength greater than the size of the particle, redistribution of charge density takes place. This result into generation of coulombic restoring force and the charge density oscillates coherently in phase with the light falling on it, called SPR. It is also known as localized surface plasmon resonance (LSPR) [123]. Particle size, shape, interparticle interactions and local dielectric environment affects the resonance frequency [124]. Zhang et al [125] found that with increase in the edge length of Ag nanocube, resonance frequency shifted to visible region.

(iii) Semiconductor- carbon heterojunction

This kind of junction is similar to metal-semiconductor junction. Different types of carbon species activated carbon, graphene, carbon dots, carbon nanotubes, fullerene, graphene oxide are used for formation of carbon-semiconductor heterojunction [118,126]. Carbon shows conductivity similar to metal, high surface area, high electron mobility and easy transfer of electron from semiconductor to carbon. Semiconductor-carbon composite shows enhancement of photocatalytic activity due to enhanced light absorption, efficient separation of charge carrier thus prolongs its life time, acts as cocatalyst by providing active sites for photocatalytic reactions. Li et al [127] reported 1.12 mmol/h H₂ generation over Pt(0.5 wt%)/ graphene (1.0 wt%)-CdS composite under visible light illumination in presence of lactic acid which is ~ 4.87 times higher than CdS nanoparticle under similar condition. High photocatalytic H₂ generation credited to the role of graphene as electron collector and transporter thus resulting into enhancement of lifetime of charge carriers. Also it enhances the light absorption properties of composite. Similarly Zhao et al [87] synthesized carbon/TiO₂/carbon nanotube composite in which TiO₂ nanotube sandwiched between two thin tubes of carbon with graphitic nature and observed maximum H₂ generation @ 37.6 mmol/h/g by irradiating the composite under solar simulator with AM 1.5G filter in presence of Pt and ethanol as cocatalyst and sacrificial reagent and attributed high activity to the synergistic effect between carbon and TiO₂ in enhancing the charge carrier separation and increased solar absorption.

1.11.3.5 Z- scheme photocatalytic water splitting

Z- scheme photocatalytic water splitting employs two semiconductors with appropriate band position such that one will generate H₂ and at other semiconductor oxidation will takes place. This concept was proposed to overcome the drawback of simultaneous evolution of H₂ and O₂. Recently, Wang et al [128] developed a catalyst where powdered hydrogen evolution

photocatalyst SrTiO₃:La, Rh and oxygen evolution photocatalyst BiVO₄:Mo were embedded into conducting carbon thin film (SrTiO₃:La,Rh/C/BiVO₄:Mo sheet) and reported Z-scheme photocatalytic water splitting with solar-to-hydrogen energy conversion efficiency of 1.2 % at 331 K and 10 kPa. It was revealed that the photocatalyst sheet is more efficient for pure water splitting than the conventional powdered photocatalyst and PEC as it suppressed the H⁺ and OH⁻ concentration overpotential and IR drop between hydrogen evolution photocatalyst and oxygen evolution photocatalyst.

1.12 Optimization of experimental parameters

Along with the improvement of light absorption properties of photocatalyst by structural modification, it is also important to monitor the effect of experimental parameters such as light source, reaction cell or photoreactor, amount of catalyst loaded, amount and type of sacrificial reagent, configuration of lamp and photoreactor etc. on photocatalytic activity of the photocatalyst. Sreethawong et al [129] varied the amount of photocatalyst and H₂ yield was monitored. It was observed that initially H₂ yield increases with increase in photocatalyst amount and decreases on further addition of photocatalyst. This indicates that it is important to optimize the amount of photocatalyst. Active sites increases with increase in concentration of photocatalyst but at higher loading of photocatalyst penetration of light is masked resulting into decrease in photocatalytic activity.

Amount and type of sacrificial reagent also plays an important role. Lalitha et al [130] found that with increase in amount of sacrificial reagent, H₂ yield increases initially upto certain optimum amount but on further increase in its concentration photocatalytic activity decreases. At low concentration of methanol, rate of H₂ production is low as the slow mass transfer of methanol from solution to the photocatalyst surface affects the reaction. However, at high concentration, methanol blocks the surface active sites resulting into lower adsorption

of water molecules on the surface thus deteriorating the photocatalytic activity [130]. Hence optimum amount of sacrificial reagent is required to derive highest H₂ yield.

Stirring of solution during photocatalytic reaction provides good dispersion of photocatalyst as it does not allow photocatalyst particles to settle down during the reaction in the solution. Thus stirring offers efficient utilization of photons falling on the system. With change in the intensity of light rate of H₂ generation can be varied.

1.13 Global status of pilot plant

Although photocatalyst development is in R&D stage however there are few attempts towards only demonstration of degradation of pollutants and production of H₂ at pilot plant using direct solar light.

In Germany, pilot plant is constructed for the solar photocatalytic treatment of biologically pretreated industrial wastewater for reuse of water in the production process [131]. Villa et al [132] has studied the simultaneous photocatalytic hydrogen production and degradation of organic pollutant under direct solar light at pilot-plant scale using compound parabolic collector (CPC). The experiment was carried out over two different photocatalyst N doped TiO₂ and CdS-ZnS using Pt as cocatalyst in presence of formic acid, glycerol and waste water as sacrificial reagent. Maximum H₂ generation of 4.8×10^4 μmol over Pt/(N-TiO₂) in presence of aqueous solution of 0.05 M formic acid after 5 h of illumination under sunlight was observed. Jing et al also demonstrated pilot plant set up by using CPC under sunlight illumination [133].

1.14 Aim of the work and future scope

Photocatalytic water splitting holds the promise for future hydrogen economy but the challenge involved is to bring this process into reality. Many photocatalysts were tested for pure water splitting but the low stability and limited absorption of visible light limits its use

for practical application. From the above discussion it is concluded that development of a photocatalyst with high efficiency, stable and cost effective is a main concern for bulk production of solar hydrogen.

In the present thesis, studies were undertaken to improvise the optical and photocatalytic properties of several photocatalysts; conventionally known UV active TiO_2 and novel organic semiconductor, $\text{g-C}_3\text{N}_4$. Various strategies such as cationic doping by Cu in TiO_2 , composite formation with NiO and CuO inducing *pn* heterojunctions, carbon incorporation in bulk TiO_2 to improve electronic conductivity, surface modification of $\text{g-C}_3\text{N}_4$ by dispersing carbon nanodots (CND) and noble metal ions (Pt, Pd, Au, Ag and Cu) were adopted to limit the e^-/h^+ recombination reaction and to enhance the photoresponse under visible light illumination. All samples were thoroughly characterized by relevant techniques and their potential for H_2 generation was evaluated under sunlight and UV-visible light in presence of sacrificial reagent. Density functional theory calculations were performed and life time of e^-/h^+ from PL decay curves was measured to support the activity trend. Parameters such as illumination area, catalyst concentration, form of catalyst (powder/films) and amount of sacrificial reagents were optimized for maximum H_2 yield. Performance of the screened photocatalysts was also tested in up-scaled photoreactors (vol = 0.5, 1 and 2 L)..

Instrumentation and Experimental Methods

2.1 Introduction

This chapter includes the experimental techniques used for synthesis of TiO₂ and g-C₃N₄, characterization and evaluation of photocatalytic activities for H₂ generation. The samples were synthesized by various methods such as solid state route, sol-gel and thermal decomposition. These samples were well characterized by various techniques to get insight into surface and bulk properties. These techniques includes X-Ray Diffraction (XRD), X-ray Absorption Spectroscopy (XAS), X-ray Photoelectron Spectroscopy (XPS), N₂ Brunauer-Emmett-Teller (N₂-BET) surface area, Fourier Transform Infrared Spectroscopy (FTIR), Raman Spectroscopy, Nuclear Magnetic Resonance Spectroscopy (NMR), Diffuse Reflectance Spectroscopy (DRS), Photoluminescence Spectroscopy (PL), Scanning Electron Microscopy (SEM)- Energy Dispersive X-ray (EDX), Transmission Electron Microscopy- Selected Area Electron Diffraction (TEM-SAED), Gas Chromatography (GC), Thermogravimetric Analysis- Differential Thermal Analysis- Evolved Gas Analysis (TGA-DTA-EGA) and Inductively Coupled Plasma- Optical Emission Spectroscopy (ICP-OES).

Brief descriptions on general principles of these techniques are given in following sections. Experimental setup required to carry out experiments for H₂ generation was also discussed in details.

2.2 Synthesis of catalysts

Fundamental basis of synthesis methods adopted for preparation of photocatalyst are mentioned below. Further detailed synthesis is included in respective chapters.

2.2.1 Solid state route

Solid state reaction is a traditional way adapted for the synthesis of polycrystalline mixed metal oxides. Two or more metal oxides or its salts such as carbonates, nitrates etc are mixed thoroughly and heated to a higher temperature to obtain the final product. In such kind of reactions sample mixing is playing an important role. Normally solid do not react with each other hence it is necessary to carry out reaction at higher temperature. The first step for the solid state synthesis is to mix the respective metal oxides or their salts in appropriate proportion. Then grind the powder for about one hour or more till it become homogeneous. Grinding time plays a crucial role in achieving homogeneity in final product [134]. More the grinding time better is the homogeneity in the final product. The pellet of this powder was formed by applying pressure up to 1.5 tonnes in hydraulic press. These pellets were then heated at the desired temperature to form the product.

Good crystallinity and homogeneity in sample preparation are advantages of this method provided grinding and mixing must be done properly. However, the demerit of the synthesis route is the formation of product with large particles having size in the range of micrometer and low surface area as results of sintering and grain growth at higher temperature.

Using this method NiTiO_3 was synthesized from NiO and TiO_2 . Synthesis procedure is explained in brief in chapter 4.

2.2.2 Sol-gel method

One of the most commonly used methods for synthesis of metal oxide is sol gel method. Dispersion of colloidal particles in the range of 1 nm to 1mm in liquid is known as sol from which a polymeric network called as gel can be formed [135]. Sol-gel methods are classified on the basis of gel drying temperature. If the gel is dried at room temperature then

it is called as aerogel. If drying of gel is carried out above room temperature then it is called as sol-gel and as xerogel if it is dried in vacuum.

Commonly metal alkoxides are used as precursors in sol-gel synthesis because they readily react with water. Sol-gel chemistry can be described by following reactions:

(i) Hydrolysis



(ii) Condensation reaction



Where, *MOR* is metal alkoxide.

First metal salt (*MOR*) get hydrolyzed and then undergo condensation reaction to form polymeric network called as gel. After this gel formation solvent was decanted or gel was centrifuged. Final product obtained was calcined further at high temperature to form metal oxide.

Concentration of precursor, pH of solution, gelation, drying process, calcination temperature and rate of cooling are the parameters which affects the particle size in the product. The role of gel drying temperature in preventing the formation of NiTiO₃ phase in the composite of NiO and TiO₂ and its affect on the photocatalytic activity is explained in detail in chapter 4.

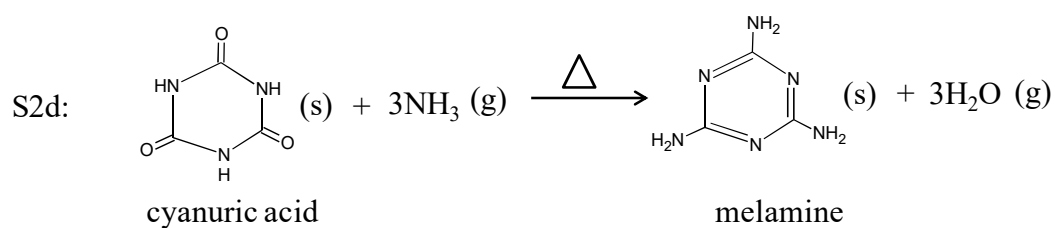
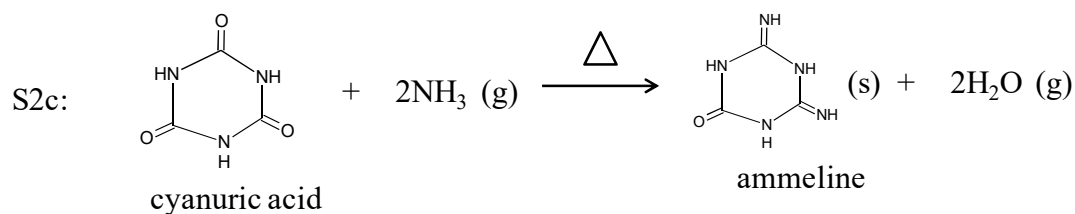
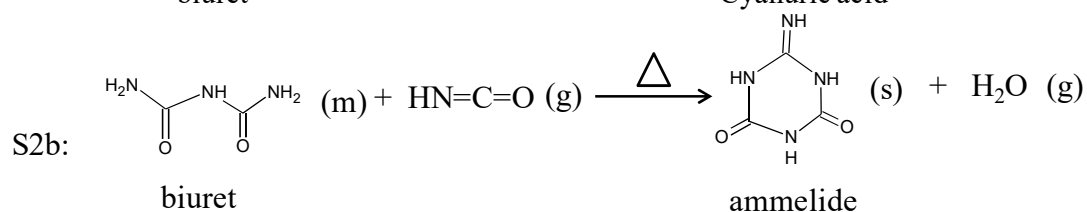
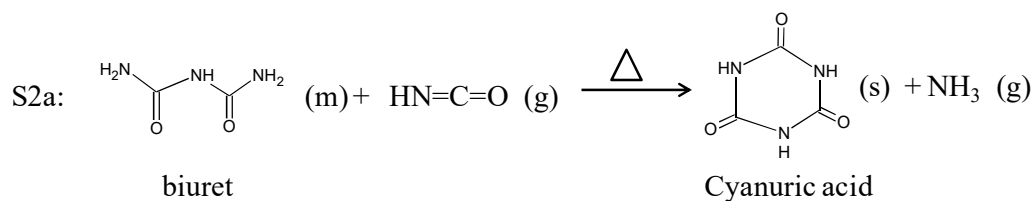
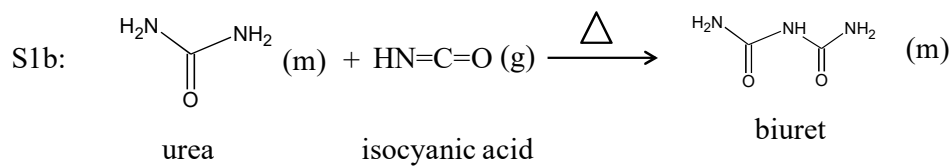
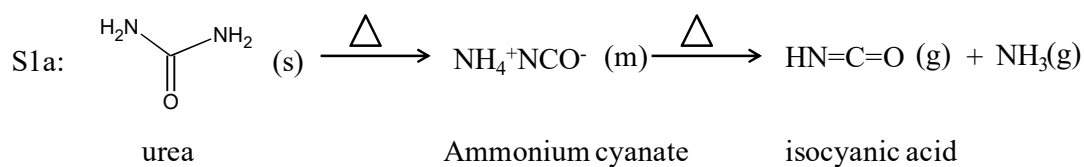
The advantage of sol-gel method over conventional solid state reaction is homogeneous formation of product as precursors are mixed at molecular level in the solution. This route is an effective and easy method for the incorporation of guest into the lattice of host (matrix). Lower processing temperature helps to form the product with high surface area and pore size [136]. By using this method Cu was doped into TiO₂ matrix and CuO and TiO₂ composite was synthesized. Brief discussion of synthesis is given in chapter 3. Same method

also used to prepare different composite of NiO -TiO₂ and C@TiO₂ composite and their synthesis procedure is explained in brief in chapter 4 and 5 respectively.

2.2.3 Thermal decomposition of urea

As mentioned in Chapter 1, g-C₃N₄ can be synthesized by using different precursors such as dicyanamide, thioacetamide, melamine, urea. Here, g-C₃N₄ was synthesized by thermal decomposition of urea [83]. Possible mechanism during thermal pyrolysis of urea is given in Fig. 2.1 [83]. Urea decomposes to give isocyanic acid. Isocyanic acid reacts with intact urea to give biuret. Biuret further produces cyanuric acid, ammelide and ammeline. Cyanuric acid on reaction with ammonia produces melamine and ammeline. This melamine and ammeline reacts to give melam. Melem is produced from melam. This melem on polymerization gives melon which on further polymerization gives graphitic carbon nitride (g-C₃N₄).

In this work, reaction is carried out in a crucible covered with lid. In absence of lid no formation of product was observed. In open crucible, the gases generated after pyrolysis escaped the system without taking part in further reaction and the pyrolysis-generated intermediates decomposes at higher temperature instead of polymerization hence no product observed. But if the reaction is carried out in a covered crucible then the formation of g-C₃N₄ was observed [83]. This implies that the retainable self-supporting atmosphere in covered crucible is important to force the pyrolysis-generated intermediates to polymerize into g-C₃N₄ [83]. In Chapter 7 and 8, g-C₃N₄ was synthesized by heating urea at 550 °C at a heating rate of 5 °C/min in a covered crucible and heating was carried out in a muffle furnace which was placed in a fume hood.



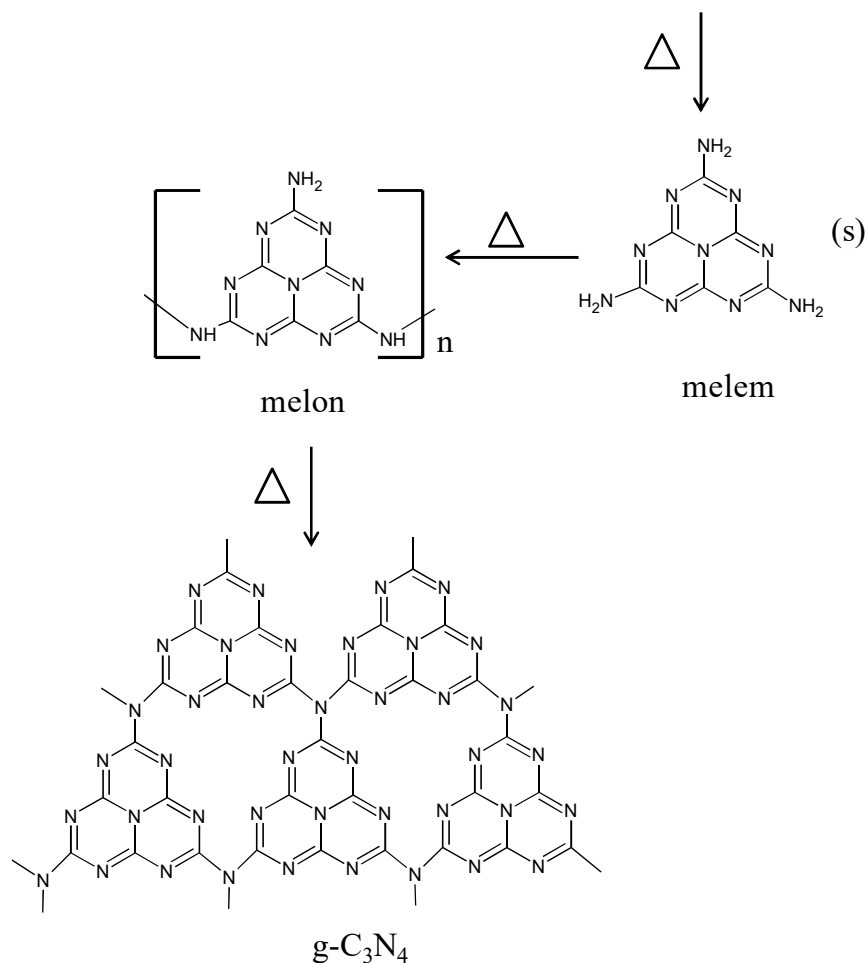
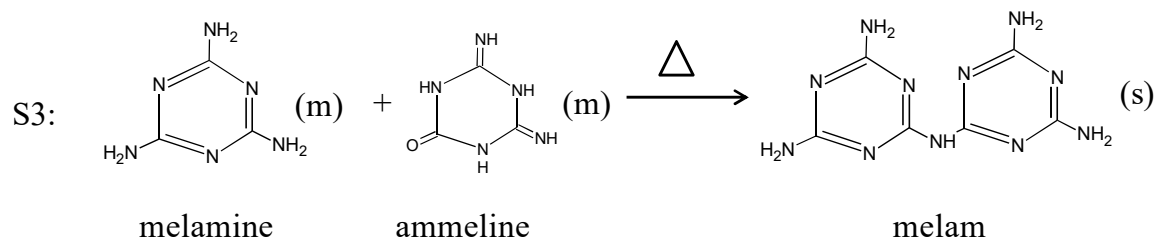
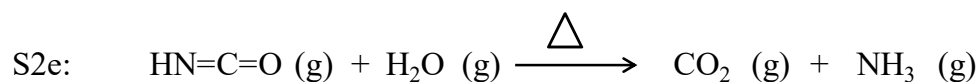


Fig. 2.1 Reaction mechanism of thermal pyrolysis of urea into $\text{g-C}_3\text{N}_4$. S is the reaction steps.

2.2.4 Synthesis of carbon nanodots by top down method

Carbon nanodots (CND) can be synthesized from top down and bottom up methods [137]. In top down methods graphite rod or powder, carbon nanotubes are used as starting material and subjected to harsh conditions like arc discharge method, laser ablation, electrochemical methods etc. Whereas in bottom up methods CNDs are synthesized from

small molecules like glucose, fructose etc. by applying external energy sources like heating, ultrasonication, microwave assisted methods. In chapter 7, carbon nanodots (CND) were synthesized by top down method by subjecting electrochemical oxidation of graphite rod. Synthesis of CND by electrochemical oxidation method is simple and do not require purification step. In this, two graphite rods were immersed in water and a DC potential of 30 V was applied between two graphite rods with continuous stirring. One graphite rod acts as cathode and other as anode. Hydroxyl and oxygen radicals are produced as a result of oxidation of water at the anode. These radicals oxidizes graphite rod to produce sheets of graphene [137]. After 120 h of electrolysis, dark brown solution appeared which was filtered and the filtrate obtained was centrifuged at 15000 rpm for 1h. Finally obtained solution was water soluble CND. Further surface of CND were functionalized with amino group by heating CND solution with NH₃ in an autoclave at 150 °C for 7 h.

2.2.5 Photodeposition method

Photodeposition is a process for the deposition of metal on semiconductor by illuminating aqueous solution of metal salt and semiconductor. As mentioned in Chapter 1, photodeposition method is most beneficial as it allow metal particles to get deposit on the active centres of the surface. A generalized equation for reduction of a metal ion Mⁿ⁺ by photodeposition is



Metal ion gets reduced on the surface of substrate by photogenerated electrons produced after absorption of light by the substrate. In this process substrate was dispersed in water and ethanol and platinum salt. This solution was purged to remove any dissolved gases which may hamper the photocatalytic activity and irradiated under UV-Visible light source.

In Chapter 3, 4, 5 and 7, Pt was photodeposited over semiconductor to enhance the activity. In Chapter 8, metal like Pt, Pd, Au, Ag and Cu were loaded over g-C₃N₄ by

photodeposition method and the role of metal for the enhancement of photocatalytic activity was studied.

2.3 Instrumental

Structural, morphological and bulk properties of synthesized product were done by relevant techniques and their working principle is described below.

2.3.1 Characterization by using X-ray techniques

2.3.1.1 X-ray Diffraction (XRD)

Powder X-ray diffraction technique is well known for determination of phase, phase purity, crystallinity, crystal structure and crystallite size of synthesized material. Crystal consists of well-defined array of atoms, ions or molecules. Wavelength of X-rays in the range of 0.5 to 2 Å is similar to the spacing between planes in crystal lattice. Therefore, lattice diffracts X-rays. Interaction of X-rays reflected by a set of parallel planes satisfying Bragg's condition lead to constructive interference only at a particular angle. Bragg's condition for occurrence of such diffraction is given as follows:

$$n\lambda = 2d \sin\theta \quad \dots\dots 2.4$$

Where n is the order of diffraction, λ is the wavelength of X-ray source (Å), d is spacing between the lattice (Å) and θ is the glancing angle (called as Bragg's angle). Fig. 2.2 shows schematic representation of X-ray diffraction from the atomic plane.

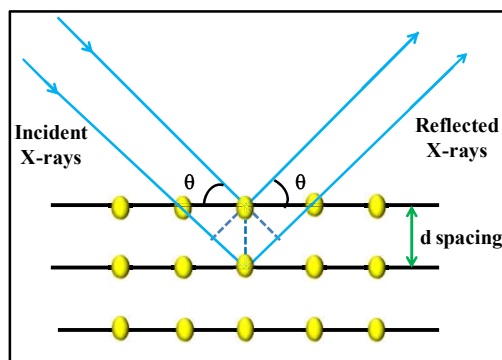


Fig. 2.2 Schematic diagram of X-ray diffraction

A typical X-ray diffractometer consists of three basic elements: X-ray tube, sample holder and X-ray detector. X-rays are generated in a Coolidge tube. In this tube, electrons generated by thermionic effect of tungsten wire are accelerated towards target by applying high voltage. These electrons impinge on target usually Cu metal to produce characteristic X-ray spectra. These spectra consist of a continuous radiation with wavelength higher than a certain lower limiting value and several intense spikes, K_{α} and K_{β} which are characteristic of the target elements. K_{α} consists of $K_{\alpha 1}$ which has a slightly shorter wavelength and twice the intensity as $K_{\alpha 2}$. The background and β -radiations are filtered using β -filters (if Z is the atomic number of target element then $(Z-1)$ element is used as filter) to produce monochromatic X-rays. Monochromatic radiations are used for diffraction experiments. The details of the X-ray production and the typical X-ray spectra are explained in several monographs [138,139]. $K_{\alpha 1}$ and $K_{\alpha 2}$ are nearly close in wavelength hence weighted average of the two is used, for Cu K_{α} radiation = 1.5418 Å is used. The beam of X-rays is passed through the collimator and divergence slits and then allowed to fall on the sample. Powder sample was spread in a rectangular area over glass slide with the help of a binder like collodion or grease or wax. X-ray diffracted from the sample is passed through the collimator slits, divergence, receiving slits, monochromator and finally falls on detector. For detection of X-ray, gas filled or scintillation counters are commonly used. These tubes can be either proportional counter or Geiger-Muller counter in which gas gets ionised after absorption of X-ray. The ions formed after ionization are migrated towards the respective electrodes to generate current which is proportional to number of photons arriving at the detector. Diffracted rays were detected at different angles by changing the position of detector. The output is obtained as plot of the intensity of diffracted X-rays (Y-axis) against angle (X-axis). The peak in the plot corresponds to the set of parallel planes having inter-planar spacing d_{hkl} . A set of d values are characteristics of a particular sample hence XRD is used as fingerprint for the crystalline

sample. The absolute intensity of peak depends on the source intensity and counting time in addition to the nature and distribution of atoms in the unit cell.

In this work, powder XRD patterns were recorded on a Philips diffractometer (model PW 1710), equipped with a graphite monochromator and Ni-filtered Cu-K α radiation. Bragg-Brentano diffractometer is commonly used geometry for diffraction. In general a short time scan in the two-theta (2θ) range of 10 ° to 70 ° is sufficient for the identification of a well crystalline inorganic material. However, low symmetry samples and samples with low crystallinity may need a slow scan. Data was collected in the 2θ ranges at 10 ° to 70 ° with a step width of 0.02 ° and time 1.25 sec. The scan time was optimized for getting good intensity peaks. Prior to data collections, the goniometer needs to be properly aligned for correct zero position. After the proper alignment, the instrument has to be calibrated with standard known materials for the accurate peak position. Usually silicon is used for calibration. The silicon peak positions are adjusted by the correct angle and set angle command or by applying the zero settings to the diffractometer. Subsequently data was collected from the sample. By comparing the observed diffraction pattern with JCPDS (Joint Committee on Powder Diffraction Standards, 1974) files available for reported crystalline samples, fingerprinting of sample materials is normally done. The refinements are usually done by a least square method. The computer software used for this purpose was “Powder-X” [140]. In the case of Cu doped TiO $_2$ system, the observed diffraction pattern was refined using the Riedvelt method [141]. The unit cell parameters are made free to adjust in the best way to fit the observed experimental data.

The broadening of an X-ray peak can occur due to smaller crystallite size or lattice strains arises due to displacements of the unit cells about their normal positions. The two aspects are briefly described below. Crystallite size can be determined from the broadening of

the peak using Scherrer's formula, if the crystal thickness is less than $\sim 2000 \text{ \AA}$. Scherrer's formula given as follows:

$$B(2\theta) = \frac{K\lambda}{L \cos \theta} \quad \dots 2.5$$

where, L is the thickness of the crystal (\AA), λ the X-ray wavelength measured in angstrom (\AA) units and θ (in radians) the Bragg angle, K is the Scherrer constant, generally taken as 0.9 for spherical crystals with cubic symmetry. The line broadening, B(2 θ), is measured from the peak width at half the peak height (FWHM).

$$B(2\theta)^2 = B_M^2 - B_S^2 \quad \dots 2.6$$

Where, B_M is measured peak width at half peak height of the sample (radians) and B_S is corresponding width of a peak of a standard material (radians).

Lattice strain develops due to displacements of the unit cells about their normal positions. Dislocations, domain boundaries, grain-surface relaxation etc. give rise to lattice strain. In nanocrystalline materials microstrains are very common. The peak broadening due to microstrain (ϵ) will be given by following formula:

$$B(2\theta) = 4\epsilon \frac{\sin \theta}{\cos \theta} \quad \dots 2.7$$

From the broadening of the XRD peak both crystallite size and microstrain can be determined by combining equation 2.5 and 2.7.

$$B(2\theta) = \frac{0.9\lambda}{L \cos \theta} + 4\epsilon \frac{\sin \theta}{\cos \theta} \quad \dots 2.8$$

Plotting B(2 θ) vs $\sin \theta$ can get both crystallite size and microstrain.

2.3.1.2 X-ray Absorption Spectroscopy (XAS)

Absorption of X-ray by sample can also provide information regarding chemical composition and structure of the sample. X-ray Absorption Spectroscopy (XAS) includes Extended X-Ray Absorption Fine Structure (EXAFS) and X-ray Absorption Near Edge

Structure (XANES) [142]. In this, X-rays shines on the sample and the intensity of transmitted X-ray is measured. The number of X-rays that are transmitted through a sample (I_t) is equal to the number of X-rays falls on the sample (I_0) multiplied by a decreasing exponential that depends on the type of atoms in the sample, the absorption coefficient (μ), and the thickness of the sample (x).

$$I_t = I_0 e^{-\mu x} \quad \dots 2.9$$

The absorption coefficient can be obtained as follows:

$$\mu = \frac{-\ln(I_t/I_0)}{x} \quad \dots 2.10$$

Absorption of X-rays takes place when the energy of incident X-ray matches to that of the binding energy of an atom in the sample. This results into appearance of absorption edge in the spectrum. Gases, liquid and solid samples can be analyzed by XAS as X-rays are highly penetrating. Elemental concentration up to few ppm can be detected by the XAS because of the brilliance of the synchrotron X-ray radiation source. XAS is element selective as every element has a set of unique absorption edges which corresponding to different binding energies of its electrons. Typical XAS spectra is shown in Fig. 2.3.

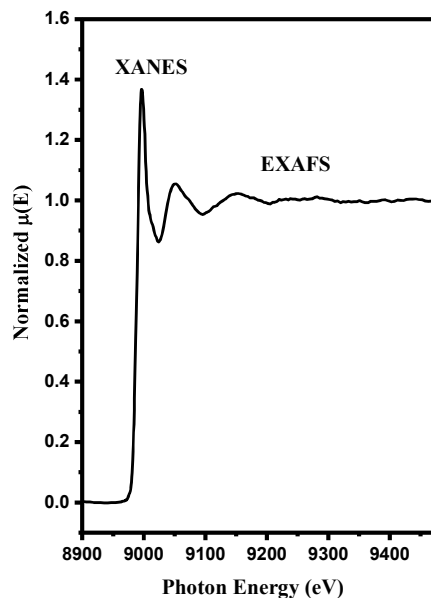


Fig. 2.3 Normalized X-ray absorption spectra of Cu doped TiO_2 sample.

An X-ray absorption spectrum is generally divided into following sections [143]:

- i) pre-edge (energy of incident photon (E) less than adsorption edge (E_0))
- ii) X-ray absorption near edge structure (XANES): where the energy of the incident X-ray beam is $E = E_0 \pm 10$ eV
- iii) Near Edge X-ray Absorption Fine Structure (NEXAFS), in the region between 10 eV up to 50 eV above the edge
- iv) Extended X-ray absorption fine structure (EXAFS), which starts approximately from 50 eV and continues up to 1000 eV above the edge

The pre-edge appears as a result of transition of electron from core level to the unfilled or half filled orbitals. This pre-edge gives information about covalency and electronic structure. In the XANES region, the absorption peaks due to transitions of core electrons to non-bound levels with close energy occurs. A rise of absorption is observed in this region because of the high probability of the transition to occur. XANES gives information about the oxidation state of the absorbing atom as well as co-ordination chemistry (e.g. octahedral, tetrahedral co-ordination). The ejected photoelectrons have low kinetic energy in NEXAFS and strong multiple scattering by the first and even higher coordinating shells dominates in this region. Whereas in EXAFS region, photoelectrons have high kinetic energy and in this region single scattering by the nearest neighbouring atoms normally dominates. The wavelength of the ejected photoelectron is dependent on the energy and phase of the backscattered wave which exists at the central atom. The wavelength changes with the change in the energy of the incident photon. The phase and amplitude of the backscattered wave are dependent on the type of atom involving in the backscattering and the distance between the backscattering atom and the central atom. The scattering depends on the atomic species hence it is possible to obtain information related to the chemical coordination environment of the original absorbing atom (central atom) by analyzing these EXAFS data.

XAS measurements in Chapter 3 on Cu doped TiO₂ samples at the Cu K edge and in Chapter 5 on C@TiO₂ samples at Ti K edge were carried out in fluorescence mode at the Scanning EXAFS Beamline (BL-9) at the INDUS-2 Synchrotron Source (2.5 GeV, 100 mA) at the Raja Ramanna Centre for Advanced Technology (RRCAT), Indore, India [144]. The beam line uses a double crystal monochromator (DCM) in the photon energy range of 4-25 KeV with a resolution of 10⁴ at 10 KeV. A 1.5 m horizontal pre-mirror with meridional cylindrical curvature is used prior to the DCM for collimation of the beam and higher harmonic rejection. The second crystal of the DCM is a saggital cylinder with radius of curvature in the range 1.28-12.91 meters which provides horizontal focusing to the beam. For measurements in the fluorescence mode, the sample is placed at 45° to the incident X-ray beam and the fluorescence signal I_f is detected using a Si drift detector placed at 90° to the incident X-ray beam. An ionization chamber detector is used prior to the sample to measure the incident X-ray flux and the absorbance of the sample is obtained as a function of energy by scanning the monochromator over the specified energy range.

In order to take care of the oscillations in the absorption spectra, the energy dependent absorption coefficient $\mu(E)$ has been converted to absorption function $\chi(E)$ defined as follows [145]:

$$\chi(E) = \frac{\mu(E) - \mu_0(E)}{\Delta\mu_0(E_0)} \quad \dots 2.11$$

Where E_0 absorption edge energy, $\mu_0(E_0)$ is the bare atom background and $\Delta\mu_0(E_0)$ is the step in the $\mu(E)$ value at the absorption edge. After converting the energy scale to the photoelectron wave number scale (k) as defined by,

$$k = \sqrt{\frac{2m(E - E_0)}{\hbar^2}} \quad \dots 2.12$$

The energy dependent absorption coefficient $\chi(E)$ has been converted to the wave number dependent absorption coefficient $\chi(k)$, where m is the electron mass. Finally, $\chi(k)$ is

weighted by k^2 to amplify the oscillation at high k . The functions $\chi(k)k^2$ are Fourier transformed in r space to generate the $\chi(r)$ versus r (or FT-EXAFS) spectra in terms of the real distances from the centre of the absorbing atom. It should be mentioned here that a set of EXAFS data analysis program available within the IFEFFIT software package [146] have been used for reduction and fitting of the experimental EXAFS data. This includes data reduction and Fourier transform to derive the $\chi(r)$ versus r spectra from the absorption spectra, generation of the theoretical EXAFS spectra starting from an assumed crystallographic structure and finally fitting of the experimental data with the theoretical spectra using the FEFF 6.0 code for Cu doped TiO₂ and ARTEMIS software for C@TiO₂ samples. The bond distances and disorder (Debye-Waller) factors (σ^2), which give the mean-square fluctuations in the distances, have been used as fitting parameters.

2.3.1.3 X-ray Photoelectron Spectroscopy (XPS)

XPS is widely used technique to determine the elemental composition, empirical formula, oxidation state of the elements on the surface. XPS is also known as Electron Spectroscopy for Chemical Analysis (ESCA). In XPS, Al K α (8.3386 Å or 1486.6 eV) or Mg K α (9.89 Å or 1253.6 eV) X-rays are used as X-ray source. When the X-ray falls on the sample, electron from core level gets ejected as shown in Fig. 2.4. Kinetic energy of these electrons gets detected by the detector. XPS requires ultra-high vacuum (UHV) conditions. By this technique all the elements above Lithium (atomic number 3) can be detected.

From the measured kinetic energy (KE) of the ejected electron, binding energy (BE) of the electron can be evaluated by using the following formula:

$$KE = h\nu - BE - \phi \quad \text{.....2.13}$$

Where $h\nu$ is the energy of incident photon, ϕ is the work function of spectrometer.

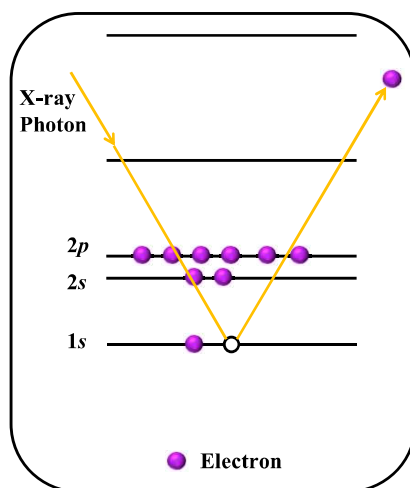


Fig. 2.4 Schematic of emission of electron from core level after interaction with X-ray.

A typical plot of XPS spectra is number of electrons get detected against the binding energy. Elemental identification is possible as each element produces a characteristic set of XPS peaks at characteristic binding energy values [147]. These peaks observed in XPS correspond to the electron configuration of electrons within the atoms, 1s, 2s, 2p, 3s, etc. The amount of electron detected i.e. the area under the peak is proportional to the concentration of that element on the surface. The shape of peak and binding energy value slightly changed with the chemical site of the electron emitting atom. Hence XPS can also provide chemical bonding information. As X-rays can penetrate 1-5 μm of the material, the electrons generated deeper inside may recaptured or trapped within the material hence will not able to come out of the surface. XPS detects only those electrons which have escaped into the vacuum of the instrument. Thus the electron ejected from 0-10 nm thickness of the sample are get detected in XPS. It is non destructive technique but very sensitive to surface contamination hence sometimes in situ surface cleaning is required using an ion gun.

XPS experiments were recorded on an electron spectrometer (SPECS, Surface Nano Analysis GmbH, Germany) using Mg- K_{α} X-rays ($h\nu=1253.6$ eV) as the primary source of radiation with an overall energy resolution of the instrument of about 0.7 eV. The appropriate

corrections for charging effects were made with the help of a C 1s signal appearing at 284.5 eV.

2.3.2 Determination of surface area

2.3.2.1 N₂ BET Surface area

In the field of heterogeneous catalysis, surface area of catalyst is an important factor because the reaction occurs on the surface of the catalyst. Generally surface area and pore size is measured by adsorption and desorption techniques. The commonly used method for determination of surface area is BET (Brunauer-Emmett-Teller) method [148]. It involves following equation known as BET equation which assumes formation of monolayer of gas molecules over the surface.

$$\frac{p}{v(p_0 - p)} = \frac{1}{v_m C} + \frac{C-1}{v_m C} \left(\frac{p}{p_0}\right) \quad \dots 2.14$$

Where, p is Adsorption equilibrium pressure, p_0 is saturation vapour pressure of adsorbate at the adsorption temperature, v_m is volume of adsorbate required for mono layer coverage, v is volume of adsorbate adsorbed at equilibrium pressure p , C is Constant related exponentially to the heat of adsorption in the first layer (q_1) and heat of liquefaction of adsorbate (q_L); $C = e^{(q_1 - q_L)/RT}$.

A plot of $p/(p_0 - p)v$ against relative pressure p/p_0 gives a straight line. From the slope $s = (C-1)/v_m C$ and intercept $I = 1/v_m C$, v_m can be calculated as follows:

$$v_m = \frac{1}{s+I} \quad \dots 2.15$$

By knowing v_m and cross sectional area of adsorbate molecule, the value of specific surface area of sample can be derived. Thus, specific surface area (S) in m²/g is given by,

$$S = \frac{v_m N_A A_m}{W \times 22414} \times 10^{-20} \quad \dots 2.16$$

where, N_A = Avogadro's number, v_m = Monolayer volume in ml at STP, W = Weight of the catalyst sample (g), A_m = Mean cross sectional area occupied by adsorbate molecule which is 16.2 \AA^2 for nitrogen at 77 K.

At higher p/p_0 values complexity associated with multilayer adsorption and/or pore condensation may arise therefore generally data over a range of $p/p_0 = 0.05- 0.3$ is taken. Adsorption isotherm is obtained by measuring quantity of adsorbed gas over a range of relative pressures at constant temperature. By lowering relative pressure, quantities of gas removed from the sample is measured to obtain desorption isotherm. Information regarding surface area and porosity can be obtained by constructing an isotherm. IUPAC classified isotherms into six types as follows (Fig. 2.5) [149].

Type I or Langmuir isotherms are concave to the p/p_0 axis and the amount of adsorbate approaches a limiting value as p/p_0 approaches 1. Type I physisorption isotherms are exhibited by microporous solids having relatively small external surfaces, for example, activated carbons and molecular sieve zeolites. The limiting uptake of adsorbate is governed by the accessible micropore volume rather than by the internal surface area.

Type II isotherms are the normal form of isotherm obtained with a nonporous or macroporous adsorbent. This type of isotherm represents unrestricted monolayer-multilayer adsorption. Point B, the start of the linear central section of the isotherm, is usually taken to indicate the relative pressure at which monolayer coverage is complete.

Type III isotherm are convex to the p/p_0 axis over its entire range. Type III isotherm are rarely encountered. A well-known example is the adsorption of water vapor on nonporous carbons. The absence of a distinct point B on type III isotherm is caused by stronger adsorbate-adsorbate than adsorbate-adsorbent interactions.

Type IV isotherm is exhibited by mesoporous solids. The steep slope at relatively higher pressure indicates capillary condensation at mesopores. The initial part of the type IV isotherm follows the same path as the type II.

Type V isotherm is not common and corresponding to type III except that pores in the mesopore range are present.

Type VI isotherm corresponds to stepwise multilayer adsorption on a uniform non-porous surface. The step-height signifies the monolayer capacity for each adsorbed layer and in the simplest case, remains almost constant for two or three adsorbed layers.

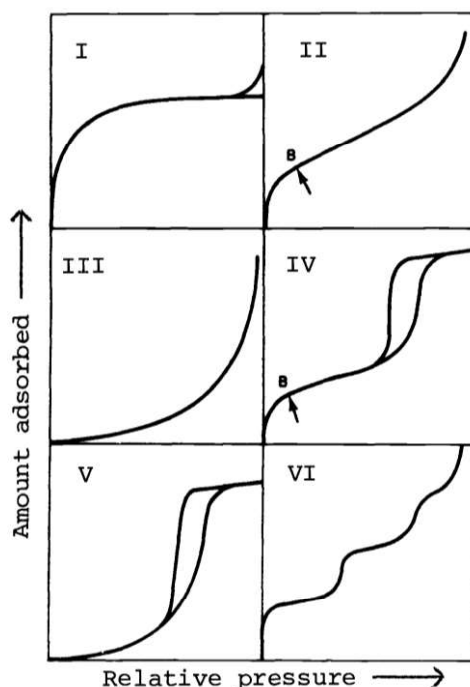


Fig. 2.5 Classification of physisorption isotherms (IUPAC) [149]

Monolayer formation of gas molecules on the surface is used to determine the specific surface area, while the principle of capillary condensation can be applied to assess the presence of pores, pore volume and pore size distribution. Following conventions are given by IUPAC on pore sizes: Micropores: pore widths < 2 nm, Mesopores: 2 nm $<$ pore widths < 50 nm, Macropores: pore widths > 50 nm.

For determination of surface area of samples, Micromeritics ASAP 2020 V3.01 H analyzer was used. Before determination of surface area, samples were subjected to a pre-treatment at 300 °C for ~ 5 h under vacuum with a liquid N₂ trap to remove impurities such as moisture. From desorption curve data, pore size distribution were done by using BJH pore size distribution curve.

2.3.3 Spectroscopy techniques

2.3.3.1 Fourier Transform Infrared Spectroscopy (FTIR)

FTIR is used for the determination of structure or the vibration mode of the sample. Infrared region of electromagnetic spectrum covers the range from 1 to 1000 microns (in terms of wavelength). This range divides into three regions; Near IR (12500 – 4000 cm⁻¹), Mid IR (4000 – 200 cm⁻¹) and Far IR (200 – 10 cm⁻¹). Infrared region 1300-900 cm⁻¹ is referred as fingerprint region [150].

The atoms in molecules are not stationary and are considered as point masses which held together by Hooke's law. By classical mechanics, it can be shown that displacements of masses from their mean positions are always the sum of displacements due to a particular set of vibrations. In the set of vibrations if the masses are in phase and their motion is such that the centre of gravity of the molecule remains unaltered then these vibrations are known as fundamental modes of the molecule. Vibrations are classified as stretching and bending vibrations. Bending vibrations are further sub classified as wagging, rocking, twisting, or scissoring. Along with fundamental modes a large number of vibrational absorptions overtones (multiple of fundamental modes, 2v or 3v etc), combination tones (v₁ + v₂, v₃ + v₄ etc.) and difference tones (v₁ - v₂, v₅ - v₆ etc) can also be observed in a typical infrared absorbance spectrum [151]. Only those vibrations which results in the change in dipole moment of molecule show absorption in IR region [152]. Some of the vibrations may not

result into change in dipole moment, hence IR inactive. Intensity of absorption band is determined by the magnitude of the change in dipole moment.

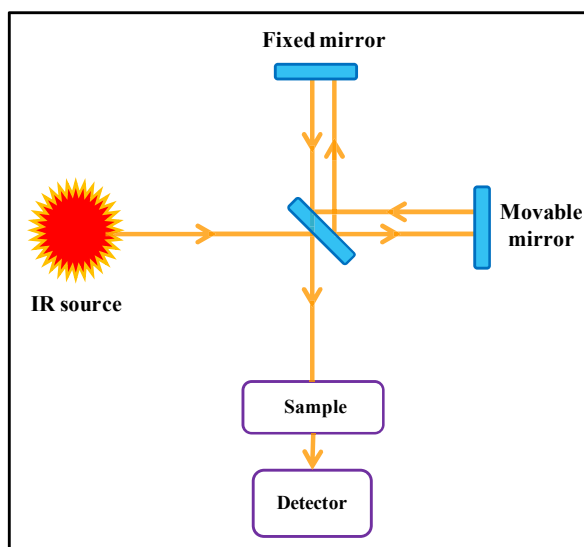


Fig. 2.6 Schematic of FTIR instrument.

Fig. 2.6 represents typical ray diagram of instrument. Light from IR source is collimated by a collimator mirror and introduced into Michelson interferometer. This interferometer consists of a beam splitter, fixed and moving mirror. Beam splitter splits the beam into two equal halves. One part falls on a fixed mirror whereas other part falls on a moving mirror. The path difference between two beams is introduced by the movement of moving mirror which results into generation of different interferograms consisting of different combination of wavelengths. Signal to noise ratio is very high. Mirror is moved by a motor. He-Ne laser is used for the alignment of the moving mirror and to measure the path difference precisely. Scan time and resolution is determined by its movement. Light from the source after collimation passed through the interferometer and finally falls on the sample. The transmitted light is allowed to fall on the detector. The two main types of detectors, thermal and photonic (photodetectors) are used. For the present studies, DTGS (deuterated triglyceride sulphate) type detector was used. The interferogram obtained is in time domain and can be converted to frequency domain by mathematical treatment called Fourier

transformation. This gives a spectrum of change in intensity with respect to wavenumber. 60 scans were recorded for a sample to obtain spectra of high signal to noise ratio.

FTIR spectra of the all the samples were recorded in the mid IR region (4000-400 cm^{-1}) of the samples, at a resolution of 4 cm^{-1} . For this purpose about 150 mg of dry KBr was mixed with an amount (~2.5 mg) of the sample and grounded properly to reduce the particle size to less than 5 μm in diameter, otherwise large particles scatter the IR beam and cause a slope baseline of spectrum. The mixture was then pressed into a transparent, thin pellet at 5 tons/ cm^2 . Opaque pellets give poor spectra, because little IR passes through them. Also white spots in a pellet indicate that the powder is not ground well enough or dispersed properly in the pellets. Hence KBr pellet must be thin and transparent. These pellets were used for IR spectral measurements. FTIR measurements were carried out on Bomem (MB 102) spectrometer.

2.3.3.2 Raman Spectroscopy

Raman spectroscopy is a spectroscopic technique used to study vibrational, rotational and low-frequency modes in a system. In Raman spectroscopy technique, molecules scattered monochromatic light incident on it. Only 0.01% of incident light gets scattered by molecule hence intense energy source like laser is required. Three different lines are observed in Raman spectrum, i.e. Stokes line, anti-Stokes line and Rayleigh scattering [150]. When light impinges on sample, molecule gets excited from the ground state to the virtual state as shown in Fig. 2.7. Rayleigh scattering occurs when the molecule is in ground state and excited to the virtual state and relaxed to the same ground state. When the molecule from the ground state excited to the virtual state and come back to the excited state of the ground state, then it is called as Stokes Raman scattering. If the molecule is already present in the excited state of ground state and relaxed by coming to the ground state, then it is called as anti-Stokes Raman

scattering. Intensity of anti-Stokes line is poor as compared to Stokes line as few molecules are present in the excited state of the ground state.

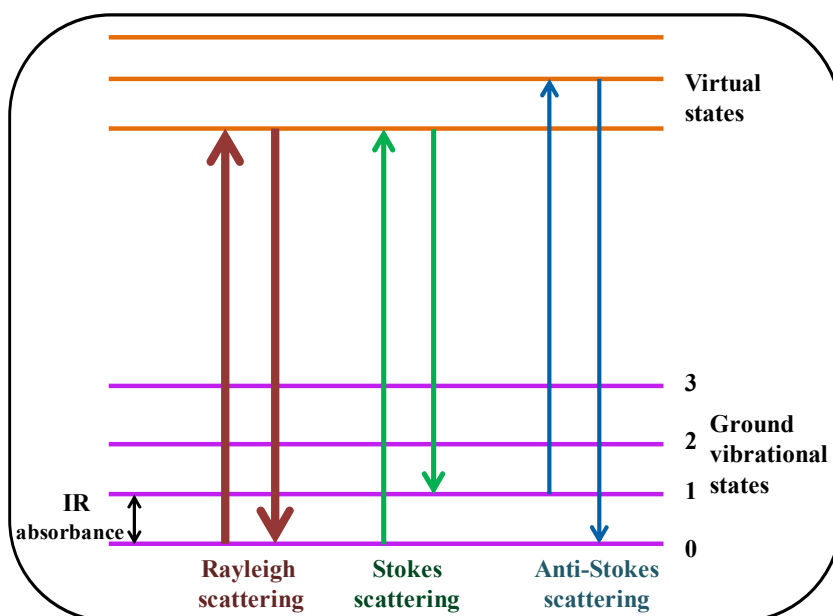


Fig. 2.7 Schematic representation of Raman scattering

For the molecule to show Raman effect there must be a change in the polarizability – the deformation of electron cloud with respect to vibrational coordinate. Intensity of Raman scattering depends on the amount of polarizability change.

Generally, a laser beam falls on the sample and the scattered light is collected and sends through the monochromator. Wavelengths near to incident light as a result of Rayleigh scattering are filtered out and remaining wavelengths are allowed to pass through detector. In this thesis work, Raman spectra were recorded using 532 nm lines from a diode Nd: YAG laser (power 15 mW) focused to a spot size of $\sim 20 \mu\text{m}$. The scattered light was analyzed using an indigenously built 0.9 m single monochromator, coupled with a super notch filter and detected by a cooled charge couple device (CCD, Andor Technology). A resolution limited line width of 3 cm^{-1} was achieved at entrance slit width of $50 \mu\text{m}$.

2.3.3.3 Nuclear Magnetic Resonance Spectroscopy (NMR)

NMR gives structural information and chemical environment around a particular nucleus in a molecule. Nuclei with odd atomic number have nuclear spin. A nucleus is a charged particle in motion hence it will develop a magnetic field. ^1H and ^{13}C has nuclear spin of $1/2$ hence behave as a tiny bar magnet. They are oriented randomly in absence of magnetic field. When the magnetic field is applied they orient themselves line up parallel to the applied field, either spin aligned or spin opposed. The most populated state is low energy state where the nucleus has spin aligned in the direction of magnetic field. By applying the energy it is possible to transfer the nucleus to higher energy level. The energy difference between the two levels falls in the range of radiofrequency.

2.3.3.3.1 Chemical shift

Applied magnetic field induces an electronic orbital angular momentum which results into the generation of small magnetic field. Because of this generated magnetic field the actual magnetic field felt by the nucleus is different from that of the applied. Hence different nuclei absorbs in different region which depends on their electronic environment around them. Chemical shift (δ) of nucleus is defined as the difference between resonance frequencies of sample to that of standard and is given as follows

$$\delta = \frac{\nu - \nu^0}{\nu^0} \times 10^6 \quad \dots\dots 2.17$$

Where, ν and ν^0 are the resonance frequencies of sample and standard respectively.

2.3.3.3.2 Magic Angle Spinning Nuclear Magnetic Resonance (MAS NMR)

Molecular motion averages out anisotropic effects and dipolar interactions in solution NMR spectroscopy. This is not the case with solid state NMR spectroscopy hence broadening in NMR spectra of solid is observed. This broadening is a result of following interactions (i)

magnetic interactions of nuclei with the electron cloud present in its surrounding, (ii) magnetic dipole– dipole interactions between nuclei and (iii) interactions between electric quadrupole moment and electric field gradient in the surrounding. Broadening arises because of these interactions make NMR spectra unsuitable to get useful information. By using some experimental strategies, it is possible to average out these interactions in solid state NMR. One of the techniques is magic angle spinning nuclear magnetic resonance (MAS NMR) technique.

In this technique powder sample is rotated at high speed at an angle of 54.7° (magic angle) to applied magnetic field. This helps in reducing the line broadening which appears due to the above mentioned interactions. As all these interactions contains the angular term of $(3\cos^2\theta-1)$ which becomes zero at $\theta = 54.7^\circ$. This makes solid state NMR simple as a result of reduction of line broadening. Hence individual chemical environments can be correlated with corresponding chemical shift values obtained from these samples [153,154].

Although, MAS is an efficient technique employed for getting high resolution NMR patterns from solid samples, in many cases, due to spinning, sidebands, which are mirror images of the isotropic peak and spread from the isotropic peak by integer multiples of the spinning frequency, appear along with the central isotropic peak for nuclei having wide range of chemical shift values. The central isotropic peak can be identified by varying the spinning speeds and observing the consistency of line positions as the positions of isotropic peaks do not shift with change in spinning frequencies. For nuclei having a nuclear spin value $\frac{1}{2}$, sideband pattern is a measure of the chemical shift anisotropy and valuable information regarding the symmetry of the electronic environment around a probe nuclei can be obtained from the intensity distribution of sidebands. However, in the presence of large number of isotropic peaks, the number of sidebands also increases, and there can be overlap between the sidebands and isotropic peaks, which makes the MAS NMR pattern complicated.

In Chapter 7, ^{13}C MAS NMR spectra of g- C_3N_4 recorded on AVANCE 400 MHz machine with a ^{13}C basic frequency of 100.57 MHz.

2.3.3.4 Diffuse Reflectance Spectroscopy (DRS)

UV-Visible diffused reflectance spectroscopy used for characterization of optical and electronic properties of different solid materials. The band gap of powdered material can be determined by using UV-Visible Diffuse Reflectance Spectroscopy. This method is also useful to get information about oxidation state and co-ordination environment around transition metal.

Semiconductors which are used as photocatalyst shows band gap in the range of near IR, visible and UV-Visible region. Band gap of semiconductor is either of direct band gap or indirect band gap. Minima of the conduction band and maxima of the valence band are characterized by crystal momentum (k-vector) in the Brillouin zone. The material can be characterized as the direct band gap if the momentum of electrons and holes is alike in both conduction and valence band. In case of indirect band gap, momentum of electrons and holes is different in both conduction and valence band. Radiative recombination is fast in direct band gap material whereas it is very slow in case of indirect band gap material.

When light falls on the powder sample, it gets reflected in all direction as a result of different powder shapes. Light undergoes diffuse or specular reflection when it falls on the powder surface. Specular reflections are mirror like reflection of waves from a smooth surface whereas in diffused reflection incident light scattered in different angles and not at the same angle as in specular reflection as shown in Fig. 2.8. In diffused reflection light get reflected in all direction on the rough surface as a result of multiple reflections at microscopic irregularities such as grain boundaries inside the material.

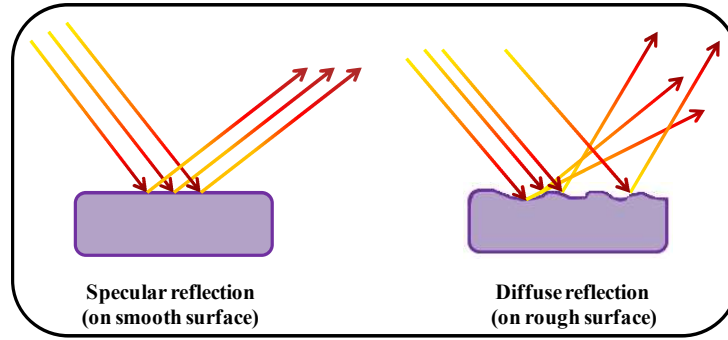


Fig. 2.8 Specular reflection on smooth surface and diffuse reflection from a rough surface

If powder absorbs light falling on it then the scattered light will have low intensity than the incident light. The wavelength of light at which powder do not show absorbance will show strong scattered light intensity than the wavelength at which powder absorbs.

DRS instruments consist of UV-Visible spectrophotometer with an integrating sphere. This integrating sphere collects the diffused light from the sample and not the specular signal hence Kubelka Munk (K-M) theory can be applied. Kubelka Munk (K-M) function related to the absorption coefficient and scattering coefficient by following equation [147].

$$f(R_{\infty}) = \frac{(1-R_{\infty})^2}{2R_{\infty}} = \frac{K}{S} \quad \dots\dots 2.18$$

Where $R_{\infty} = \frac{R_{Sample}}{R_{Standard}}$, $f(R_{\infty})$ is Kubelka Munk (K-M) function, K = absorption coefficient and S = scattering coefficient. R_{∞} can be measured from reflectance spectra and hence K-M function can be calculated using equation 2.18.

Band gap of semiconductor can be determined using following equation.

$$\sqrt[n]{h\nu f(R_{\infty})} = A(h\nu - E_g) \quad \dots\dots 2.19$$

Where $f(R_{\infty})$ is Kubelka Munk function, h is Planck's constant (6.634×10^{-34} Js), ν is frequency of vibration (s^{-1}), E_g band gap (eV), A is proportional constant. The value of n denotes the nature of transition i.e. $n=1/2$ and $3/2$ for direct allowed and forbidden transition respectively and $n= 2$ and 3 for indirect allowed and forbidden transition respectively.

$\ln(f(R_\infty)h\nu)$ against $\ln(h\nu-E_g)$ can be plotted by taking approximate value of E_g . The slope of the straight line near to band edge will give the value of n [155]. By substituting the value of n in equation, $\sqrt[n]{h\nu f(R_\infty)}$ against $h\nu$ is plotted. The intercept on X- axis gives the band gap value of the semiconductor.

An optical characteristic of all samples studied in this thesis was recorded using spectrophotometer of JASCO model V-530 (Japan) with an integrating sphere attachment. Samples were scanned in range of 200-800 nm at the scanning speed of 200 nmmin⁻¹. BaSO₄ was used as standard for recording spectra in reflectance mode.

2.3.3.5 Photoluminescence (PL)

Excitation of sample by photon is called as photoluminescence. In photoluminescence, sample absorbs light falling on it and then re-emits.

2.3.3.5.1 Steady State Photoluminescence Spectroscopy

In steady state photoluminescence spectroscopy, sample on excitation of light, electron get excited to the allowed excited state. These electrons may get de-excited by emission of light (radiative process) or by non radiative process. The energy of emitted light depends on the energy difference between ground state and excited state and not on the incident light. Localized defects or impurity levels contributes to the radiative transitions hence the analysis of PL spectrum can give information regarding the defects or impurities. Their concentration can be determined from the magnitude of the PL signal.

The light from the source passed through the monochromator and then falls on the sample. A portion of incident light gets absorbed by the sample and it gets transferred to the excited state. Some of the excited state molecule radiates energy in the form of photon and comes to the ground state. In all directions fluorescent light is emitted. A part of the fluorescence light passed through the monochromator and arrives at detector. The detector is

placed 90 °C to the incident light to avoid the risk of incident or transmitted light arriving the detector. Many light sources such as laser, photodiodes and lamp like Xenon arc, mercury vapour lamp are used. Photomultiplier tube (PMT) is the most commonly used detector.

Absorption spectrum deals with the transition from ground state to the excited state whereas photoluminescence deals with transition from excited to ground state. Excitation spectrum can be obtained by plotting/ measuring intensity of emitted light versus excitation wavelength. This spectrum looks similar to the absorption spectrum. The wavelength at which maximum absorption takes place is used as excitation wavelength to get emission spectrum having more intense emission at longer wavelength.

Emission spectra of all samples studied in this thesis are obtained by using Edinburgh Instruments' FLSP 920 system equipped with a 450 W Xe lamp having a Peltier element cooled red sensitive Hamamatsu R955 PMT was used to record PL with a resolution of 3 nm at room temperature. All emission spectra were corrected for the detector response and excitation spectra for the lamp profile.

2.3.3.5.2 Time Resolved Photoluminescence Spectroscopy (TRPL)

Time resolved photoluminescence spectroscopy (TRPL) is useful to get information about recombination of lifetime of electron and hole pair generated after absorption of light. The average time molecule spends in the excited state before returning to the ground state is referred to as lifetime of excited state. The decay of excited state to the ground state can be given as follow:

$$I(t) = I_0 e^{-t/\tau} \quad \dots\dots 2.20$$

Where $I(t)$ is intensity at time t , I_0 is the intensity at time zero, τ is the lifetime. Lifetime is defined as the time required to drop the intensity by $1/e$ or 37 %. Typical decay spectrum is shown in Fig. 2.9.

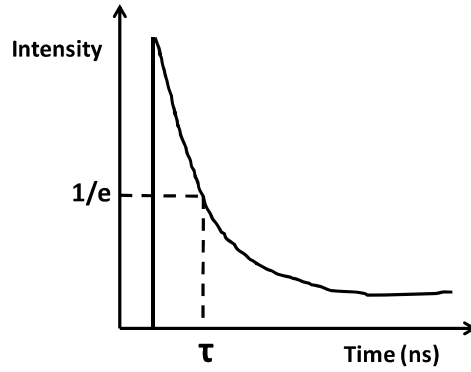


Fig. 2.9 Typical spectrum of time resolved photoluminescence spectroscopy

In terms of rate constant lifetime can be given by following formula [156].

$$\tau = \frac{1}{k_{nr} + k_r} \quad \dots 2.21$$

Where, k_r and k_{nr} is the radiative and nonradiative decay rate respectively. The radiative lifetime is the inverse of radiative decay rate.

In steady-state photoluminescence spectroscopy sample is illuminated with continuous light source whereas in TRPL sample is excited by short pulses of light and measures the emitted light at definite time intervals after excitation by pulse. By using both time correlated single photon counting (TCSPC) and multichannel scaling (MCS) mode lifetime measurements can be done. The PL emission intensity obtained as a function of time is then fitted to exponential model to get lifetime of charge carrier.

This technique is useful to get more insight about lifetime of charge carrier in photocatalyst. More the charge carrier lifetime better is the photocatalytic activity of the sample. In Chapter 4, lifetime enhancement of charge carrier is evaluated in *pn* heterojunction NiO-TiO₂ nanocomposite. In this chapter, life time measurements were carried out using TCSPC spectrometer (Horiba Jobin Yvon, U.K.). The samples were excited by light pulses from a diode laser source ($\lambda = 267$ nm, repetition rate of 1 MHz for all samples containing TiO₂ and $\lambda = 339$ nm for pure NiO with instrumental response function (IRF) < 0.75 ns), and the fluorescence was detected using a PMT (Photomultiplier tube)-based

detection module (model TBX4). Also in Chapter 6 and 7, lifetime improvement of g-C₃N₄ using CND and metal were studied in detail. In both chapters lifetime measurements were carried out by using Edinburgh Instruments FLSP 920 system equipped with a nanosecond hydrogen flash lamp as the excitation source and employing TCSPC technique.

2.3.4 Electron microscopy techniques

2.3.4.1 Scanning Electron Microscopy (SEM)

When electron beam strikes the matter, mainly three phenomena occurs are (i) emission of secondary electron, (ii) back scattering of electrons, (iii) transmission of electrons.

Emissions of characteristic X-rays, cathode luminescence and absorption of electrons also occur during the interaction of primary electrons with the matter. All the phenomena are shown in Fig. 2.10.

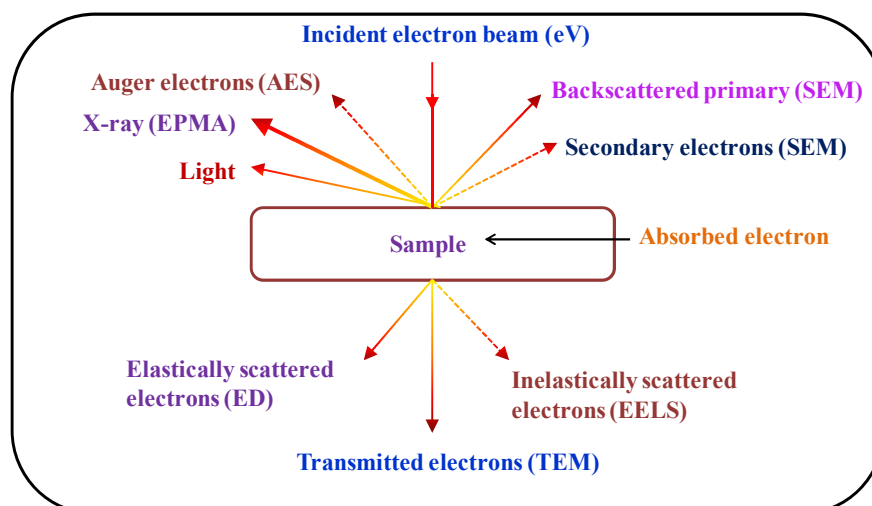


Fig. 2.10 Schematic of phenomena occurs on interaction of electron beam with sample.

In SEM, secondary and back scattered electrons are used to make image. In this technique, beam of electrons is focused on the sample [157]. The electrons reflected from the surface i.e. backscattered electrons and secondary electrons are detected and fed to a synchronously scanned CRT as an intensity-modulating signal and thus displays a specimen

image on the CRT screen. Image magnification is determined by the CRT raster width divided by the electron probe scanning width. A wide range of magnification can be used, the best achievable resolution being about 2 nm. Scanning microscope is made up of (i) electron optical system, (ii) specimen stage, (iii) display and recording system and (iv) vacuum system. If the sample is not conducting then it must be coated with gold or graphite in order to avoid built up of charge on the surface. It gives useful information about surface morphology, particle size, magnetic domains, surface defects etc.

In electron microscopy, elements present in the sample also emit characteristics X-rays of that element as a result of interaction of electron beam with the sample. These X-rays are detected by the silicon-lithium detector. This can give both qualitative and quantitative analysis of the elements (having atomic number greater than 11) present in the sample. This technique is known as energy dispersive analysis of X-ray (EDS or EDAX).

In this thesis microstructure of metal oxides is studied by using SEM. In Chapter 4 and Chapter 6, SEM was recorded using a Zeiss Gemini Plus field emission scanning electron microscope operated at 5 kV.

2.3.4.2 Transmission Electron Microscopy (TEM)

TEM uses high energy electron beam which transmitted through the sample to form image and analyze the microstructure with atomic scale resolution. As mentioned above after interaction of electrons with material, some electron gets transmitted or diffracted from the sample. These electrons can be utilized in TEM microscopy.

A ray of electron produces by heating a pin-shaped cathode heated up by passing the current. A high voltage under ultra-high vacuum accelerates the electrons to the anode. The accelerated ray of electrons passes a drill-hole at the bottom of the anode. The lens-systems consist of electronic coils generating an electromagnetic field. A condenser first focuses the ray and then it allows the ray to pass through the object. The object consists of a thin (< 200

nm), electron transparent, carbon film on which the powder particles were dispersed. After passing through the object, the transmitted electrons are collected by an objective. Thereby an image is formed, which is subsequently enlarged by an additional lens system. The images can be visualized by focusing the transmitted electrons to a plane where imaging devices such as charge couple device CCD camera and/or fluorescence screen are placed.

The transmission electron microscopes operated at the voltage as high as 200 kV with a magnification of 3,00000 X is routinely used at present. To resolve the finest possible details in the sample, it is advantageous to use high voltage to give the shortest possible wavelength illumination, an objective lens with very low aberrations and a microscope with extremely high mechanical and electrical stabilities. High resolution needs both high instrumental resolving power and high image contrast. This technique is termed as high-resolution transmission electron microscopy (HR-TEM) [158].

The wavelengths used in imaging microscopy are five orders magnitude smaller than the visible light wavelength. This means the nearly infinite resolution. But the resolution is limited to 1-2 Å due to aberrations inherent to electromagnetic lenses. In addition to imaging mode, diffraction mode is also useful which is known as selected area electron diffraction. In this, an interference pattern formed between the transmitted and diffracted beams is used and it gives information about crystalline structure, as well as defects such as planar and line defects, grain boundaries, interfaces, etc. Bright and dark field imaging in combination with electron diffraction gives valuable information regarding morphology, crystal phases, and defects in a material. Also composition of sample at the microscale can be determined by recording the EELS or EDX spectra.

This technique is used to study morphological features like shape, size, size distribution and extent of aggregation. Also, the metal dispersion was analysed in metal/g-C₃N₄ sample using this technique. The samples were prepared by ultrasonication of the finely

ground samples in ethanol and then dispersing on a carbon film supported on a copper grid. FEI-Tecnai G-20 microscope operating at 200 kV was used for HR-TEM images.

2.3.5 Gas Chromatography (GC)

Gas chromatography is one of the separating techniques used for the separation and quantification of volatile or gaseous component [150]. Basic component of gas chromatography is column which is stationary phase, carrier gas which is a mobile phase and detector.

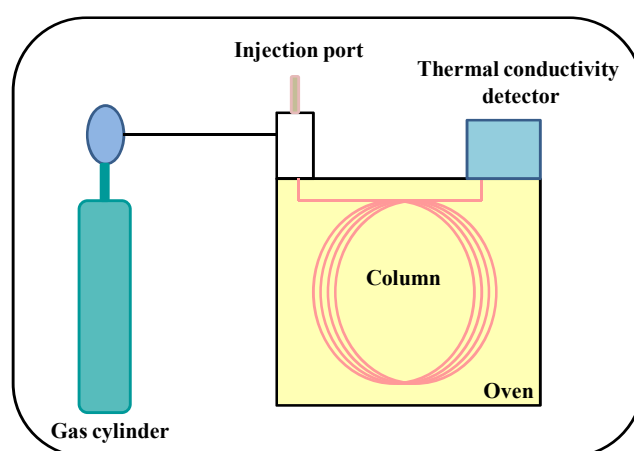


Fig. 2.11 Schematic of gas chromatograph.

As shown in Fig. 2.11 a flow of gas (mobile phase, carrier gas) is passed through a narrow tube known as column. A known volume of the sample or analyte is injected into the injection port by a microsyringe. When the carrier gas carries the analyte molecules through the column, adsorption of the analyte molecules takes place either onto the column walls or onto packing materials in the column. The rate at which the molecules progress along the column depends on the strength of adsorption, which in turn depends on the type of molecule and on the stationary phase materials. Since each type of molecule has a different rate of progression, the various components of the analyte mixture are separated as they progress along the column and reach the end of the column at different times (retention time). Generally, substances are identified (qualitatively) by the order in which they elute from the

column and by the retention time of the analyte in the column. Other parameters that can be used to alter the order or time of retention time are the carrier gas flow rate and temperature of the column. Quantitative analysis of component is also possible by comparing peak area of known amount of standard to that of the component. Columns are classified on the basis of tubing dimensions and packing material. Packed columns and capillary columns are two types of columns. Packed columns are 1.5- 10 m in length and 2- 4 mm internal diameter and typically made up of stainless steel. While capillary columns have internal diameter in the range of 0.1- 0.5 mm and length can be varies from 10- 100 m. The inner column walls are coated with the active materials (wall coated open tubular (WCOT) column), some columns are quasi solid filled with many parallel micropores (porus layer open tubular (PLOT) columns). Most capillary columns are made of fused-silica with a polyimide outer coating. These columns are flexible, so a very long column can be wound into a small coil. Columns are selected on the basis of the type of packing material, film thickness of stationary phase, column length and column diameter. Column is housed in an oven and its temperature can be precisely controlled electronically. Molecular adsorption and the rate of progression along the column is temperature dependant hence a careful control of the column temperature is required. Better separation can be achieved by reducing the temperature but it can result in very long elution time. In some cases temperature is ramped either continuously or in steps to provide the required separation. This is referred to as a temperature program. The flow rate can be varied by using electronic pressure control during the analysis which helps in faster run times while keeping acceptable levels of separation. Column temperature always has to be high than the injection port temperature to avoid any condensation/ deposition of analyte into the column.

The choice of carrier gas (mobile phase) is important. Most commonly used carrier gases are Ar, He, N₂, H₂ and air. The selection of carrier gas depends on the detector being

used. Sometimes its selection depends on the sample matrix too. Also purity of carrier gas is depends on the detector type used for analysis. Typically, purities of 99.995% or above are used. Carrier gas flow rate affects the analysis in similar as that of temperature. Higher the flow rate faster is the analysis but lower the separation between analytes. Thus, while selecting flow rate one need to balance between type of separation and time required for analysis. In modern GCs flow rate is electronically controlled.

A number of detectors are used in gas chromatography. The most common are the flame ionization detector (FID) and the thermal conductivity detector (TCD). Both are sensitive to a wide range of components and both work over a wide range of concentrations. While TCDs are essentially universal and can be used to detect any component other than the carrier gas (as long as the thermal conductivities of component is different from that of the carrier gas at detector temperature). TCD relies on the thermal conductivity of solute passing around a tungsten- rhenium filament through which current flows. Generally N₂ or He is used as carrier gas due to their relatively high thermal conductivity which helps to keep the filament cool and maintain uniform resistivity and electrical efficiency of filament. When the components with the mobile phase elute from the column, thermal conductivity decreases. This decrease in thermal conductivity causes rise in filament temperature and resistivity resulting in fluctuations in voltage. Detector sensitivity is proportional to filament current and inversely proportional to the temperature of that detector and flow rate of the carrier gas. H₂ has relatively high thermal conductivity. For H₂ detection, He or N₂ can not be used as carrier gas as they have relatively high thermal conductivity. Hence Ar as carrier gas which has relatively low thermal conductivity is recommended for better sensitivity.

FIDs are sensitive primarily to hydrocarbons and are more sensitive to them than TCD. However, FID cannot detect water. Both detectors are also quite robust. Since TCD is

non-destructive, it can be operated in-series before an FID (destructive), thus providing complementary detection of the same components.

In this work, GC is used for separation and quantification of gaseous mixture produced after photocatalytic reaction. In chapter 3, 4 and 6, a gas chromatograph of model Michro-1100, Netel, India equipped with a thermal conductivity detector (TCD), a molecular sieve column with argon as the carrier gas was employed in the isothermal temperature mode at 50 °C oven temperature. While in chapter 5, 7 and 8, a gas chromatograph of model GC 2010 plus, Schimadzu, Japan equipped with a Carboxen column (0.32 mm ID, 30 m length) was employed in the isothermal temperature mode at 35 °C oven temperature.

2.3.6 Thermal analysis techniques

Thermal analytical methods are important to investigate phase changes, decomposition and chemical changes by heating the sample.

2.3.6.1 Thermogravimetric Analysis (TGA)

Thermogravimetric analysis (TGA) is a technique which measures the change in weight with respect to time or temperature. Loss in weight occurs during heating as a result of evolution of water/ volatile content (such as O₂, CO₂ etc.) while gain in weight can occur in case of oxidation or adsorption of gases. Also thermal stability of compound can be determined using this technique.

2.3.6.2 Differential Thermal Analysis (DTA)

In DTA, sample and thermally inert reference like Al₂O₃ are heated at a controlled uniform heating rate in a furnace. Temperature difference between sample and reference is recorded. This difference in temperature is plotted against time or temperature. Exothermic or endothermic reactions can be detected with respect to inert reference. Exothermic reactions shows upward peak whereas downward peak is due to endothermic reactions. DTA data also

provides information about transformations such as glass transitions, crystallization, melting and sublimation. Area under the DTA peak gives the enthalpy change and it is unaffected by the heat capacity of the sample.

2.3.6.3 Evolved Gas Analysis (EGA)

Evolved gas analysis (EGA) involves analysis of gases evolved during heating of the sample. Coupling of TGA or DSC technique with different analytical methods such as FTIR, mass spectrometer, gas chromatography or optical in-situ evolved gas analysis can be used.

In chapter 5, gases evolved during heating of C@TiO₂ sample in presence of air were determined by using TGA coupled EGA. Thermal stability of g-C₃N₄ was evaluated by using TGA and mentioned in Chapter 7.

2.3.7 Inductively Coupled Plasma- Optical Emission Spectroscopy (ICP-OES)

ICP-OES is an analytical technique used for the detection and quantification of chemical elements. It is a type of emission spectroscopy which uses the inductively coupled plasma to produce excited atoms and ions that emit electromagnetic radiation at wavelengths characteristic of a particular element. From the intensity of emitted light, concentration of metal ion in the sample can be determined.

The elemental analysis of Cu, Ni, Ti, Pt, Pd, Au and Ag present in the samples were done using ICP-OES (JobinVyon JY 2000, France) after microwave digestion of sample in concentrated HNO₃-HCl (aqua regia).

2.4 Evaluation of photocatalytic activity

2.4.1 Experimental conditions

The potential of the catalyst synthesized in this study was evaluated for H₂ generation. For this, a particular amount of sample was dispersed in a solution of water and sacrificial

reagent. The resultant solution was evacuated before irradiation to provide air free conditions as oxygen acts as an electron scavenger and, on photo-adsorption, blocks the active sites for the reaction. This evacuated solution was irradiated under different light sources.

As mentioned in Chapter 1 presence of sacrificial reagent is important to reduce the recombination of electron-hole pair recombination. In case of TiO_2 and $\text{g-C}_3\text{N}_4$ system methanol and triethanolamine was used as sacrificial reagent respectively. The reactor assembly used in the reaction and emission spectra of different sources are explained below in brief.

2.4.2 Photoreactor

Two different types of photoreactors of different geometry were used to carry out the reaction. Photographs of these photoreactors were given in Fig. 2.12a, b and c. A rectangular quartz photoreactor having a capacity of 81 ml ($10 \times 2.1 \times 2.1 \text{ cm}^3$) is shown in Fig. 2.12a. The illumination area of this reactor is 20 cm^2 .



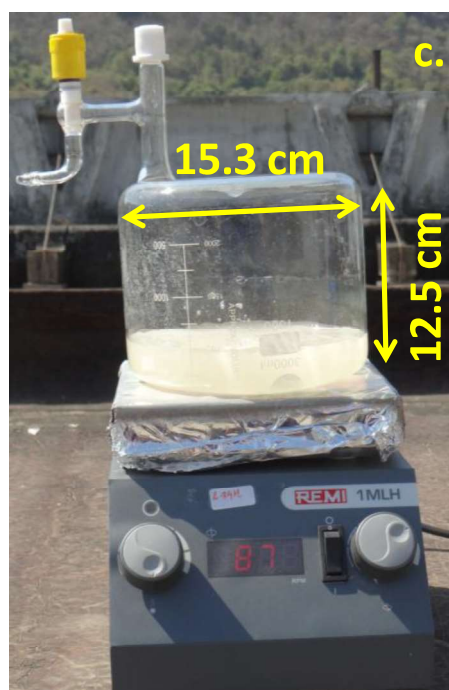
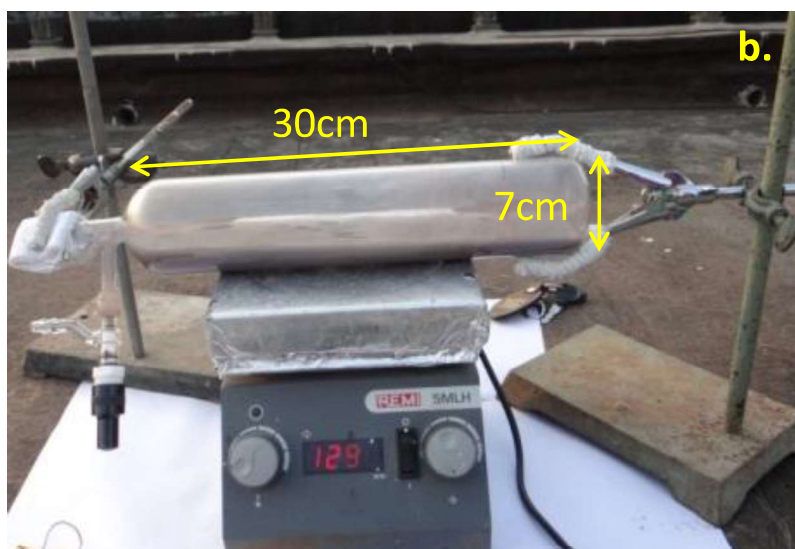


Fig. 2.12 Photocatalytic H₂ evolution under direct sunlight in different size of reactors. a. quartz reactor of 81 ml capacity, b. a pyrex cylindrical reactor of ~1 L (990 ml) capacity and c. a beaker type pyrex photoreactor of ~2 L (1963 ml).

To scale up the reaction under sunlight different reactors with different volume and geometry were constructed. Fig. 2.12b shows the tubular pyrex photoreactor of ~ 1L (990 ml) capacity having width of 30 cm and height of 7 cm with illumination area of 141 cm². Another reactor with higher illumination area and different geometry were made. Fig. 2.12c shows the circular pyrex photoreactor of ~2 L (1963 ml) capacity having width of 15.3 cm and height of 12.5 cm with illumination area of 172 cm². All the photoreactors are equipped

with sampling port to withdraw the reaction product by using microsyringe and Young's valve to purge the reaction solution with inert gas like argon or evacuate the solution before irradiation. The solution in 1 L reactor or 2 L reactor is difficult to evacuate. Hence purging with inert gas is preferred to remove any dissolved gases.

2.4.3 Photoirradiator

Horizontal and vertical photoirradiator assembly is shown in Fig. 2.13. Lamp and reactor was kept parallel in both assemblies. The lamp is surrounded with water circulation jacket to absorb IR irradiation.

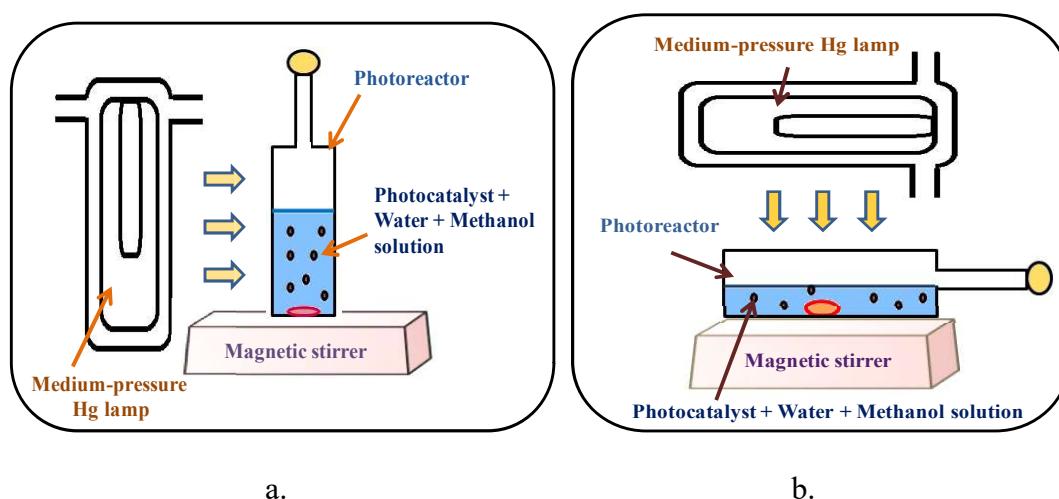


Fig. 2.13 Pictorial representation of side view of a) vertical geometry: photoreactor and light source both are standing vertical and b) horizontal geometry: photoreactor and light source are in horizontal position.

All the reactions were carried out in horizontal assembly as this geometry helps to provide better illumination area as compared to the vertical assembly. In Chapter 6, the different experimental parameters and effect of different assembly on evaluation of photocatalytic activity were studied in details.

2.4.4 Light sources

Photocatalytic reaction was evaluated under different light sources and they are described in details below.

2.4.4.1 UV-visible source

For UV-visible irradiation, medium pressure mercury vapour lamp was used. The emission spectrum of UV-visible lamp is given in Fig. 2.14. To carry out UV-visible reaction, 81 ml reactor was used whose details are given above.

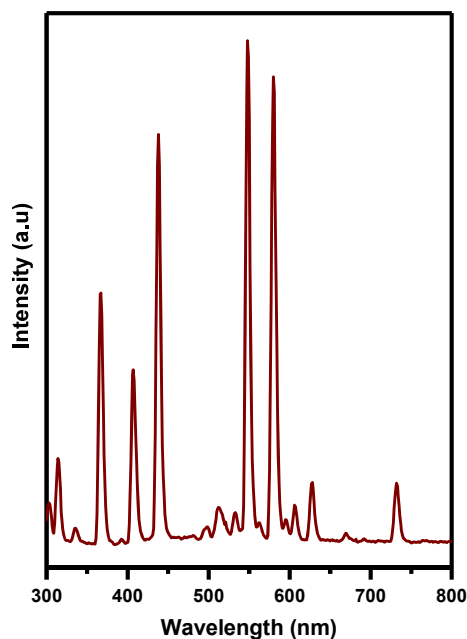


Fig. 2.14 UV-visible emission spectrum of medium pressure mercury vapour lamp.

2.4.4.2 Visible light source

Experiments were carried out by using visible light source, to eliminate the UV light and measure the photoresponse of catalyst for H₂ generation in visible light. Here 400 W medium-pressure Hg lamp, SAIC, India was used as visible light source. The emission spectrum of visible lamp is shown in Fig. 2.15. The emission spectrum of visible light source with wavelengths greater than 400 nm, $\lambda_{\text{max}} = 536$ nm. Horizontal assembly is used in this experiments which is explained above by replacing UV lamp with visible light source.

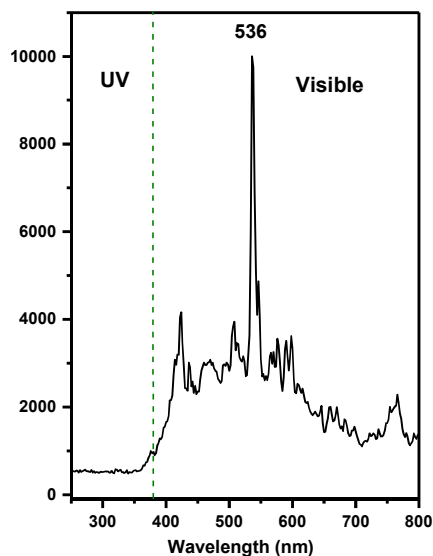


Fig. 2.15 Emission spectrum of visible medium pressure mercury lamp (SAIC, India, 400 W)

2.4.4.3 Sunlight

To check the feasibility of catalyst for practical application experiments were carried out under actual sunlight irradiation. The experiments were performed on the terrace of our institute. Sunlight consists of ~4 % UV, 45-48 % visible and remaining is infrared portion of light. The solar spectrum is given in Chapter 1 in Fig. 1.2.

In sunlight all the three reactors were used to evaluate photocatalytic activity of the catalyst. Sunlight is not constant it varies through a year. The effect of flux variation on H₂ generation was studied in detail during different months and mentioned in Chapter 6. The effect of cloudy and sunny day on H₂ yield was also monitored and included in Chapter 6. Also the illumination hours were optimized during a day and found that illumination during 11:00 to 15:00 IST is more effective.

2.4.5 Measurement of flux using Si photodiode

The flux of sunlight, UV-Visible lamp and visible lamp were measured using a silicon photodiode based light meter LX 1108, Lutron Electronic. Fig. 2.16 shows spectral response of silicon photodiode used in light meter.

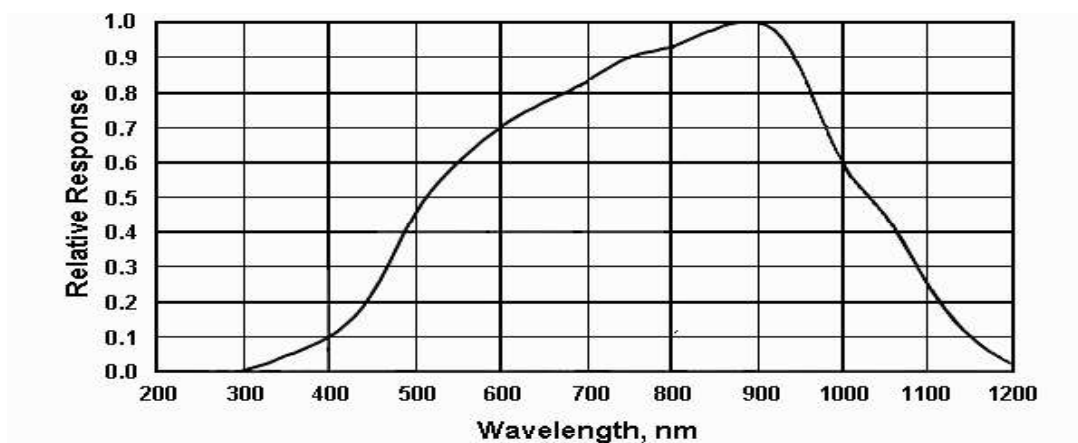


Fig. 2.16 Typical silicon photodiode spectral response of light meter.

Solar flux was measured daily in the peak hours and the average recorded during 11.00-15.00 IST were used for AQE and SFE measurement. Day to day flux variations of sunlight were recorded using a light meter. The lux of UV-visible and visible light source was measured by placing lux meter near the photo reactor. The number of photons falling on the reaction cell or flux of UV-Visible medium pressure mercury lamp was determined to be 19×10^4 Lux in horizontal geometry irradiation of UV-visible photoirradiator. Flux of visible lamp was determined to be 9.84×10^4 Lux.

The H_2 yield quantified by using GC equipped with TCD detector and lux of light source measured is used for the determination of efficiency of reaction.

2.4.6 Efficiency calculation

2.4.6.1 Apparent Quantum Efficiency (AQE)

Emission spectrum of medium-pressure mercury lamp was recorded in the wavelength range of 200-800 nm as shown in Fig. 2.14 and 2.15. For polychromatic light, energy of a single photon was considered as the weighted average energy (E_a) of all the photons in the range of 300-600 nm. For this, contribution of photon of each wavelength λ_i (i varying from 300-600 nm) towards the total energy was calculated as

$$E_i(\lambda_i) = \frac{I_{\lambda_i}}{I_{tot}} \times \frac{hc}{\lambda_i} \quad \dots\dots 2.22$$

$$E_a = \sum_{300}^{600} E_i(\lambda_i) \quad \dots 2.23$$

Total light intensity incident at the sample position in horizontal geometry was measured using a calibrated lux meter as mentioned above. It was also corrected for the reactor surface area exposed to light, assuming uniform intensity distribution, over the powder dispersed in the solution of water and sacrificial reagent. The fraction of light intensity in the wavelength region between 300 to 600 nm only was considered for the calculation of quantum efficiency as the absorption of light above 600 nm was negligible. The incident light intensity in the range of 300-600 nm (E_m) was obtained by multiplying the total incident intensity with the ratio of the area in 300 - 600 nm range to the total area of the emission profile. Finally the apparent quantum efficiency (η) is given by following expression

$$\eta (\%) = \frac{2 \times H_2 \text{ yield}}{N} \times 100 \quad \dots 2.24$$

Where, $N = \frac{E_m}{E_a}$

Similarly AQE was also calculated for the photocatalytic reaction performed under sunlight using flux values. The average flux values measured in the interval of one hour during time window of 11.00-15.00 IST were taken for efficiency measurement.

2.4.6.2 Solar to Fuel Efficiency (SFE)

Solar to Fuel (SFE) energy conversion efficiency in sunlight was calculated by using following formula:

$$SFE = \frac{rH_2 \times \Delta H}{P_{sun} \times S} \times 100 \quad \dots 2.25$$



Where rH_2 is the rate of hydrogen generation ($\mu\text{mol/h}$), P_{sun} energy flux of solar light (W/m^2) measured as mentioned above and S is the area of the reactor (m^2).

**Sunlight Driven Photocatalytic Hydrogen Generation over
Cu Substituted TiO₂ and Nano-composites of CuO-TiO₂
Powders**

3.1 Introduction

As discussed in the introduction chapter, TiO₂ is an attractive material as photocatalyst owing to its optical and electronic properties, high resistance to photocorrosion, stable to wide range of pH, non-toxic and low cost. Despite of having these properties high recombination rate as well as its band gap of 3.2 eV restricts its use for sunlight application. There are many strategies for the improvement of visible light response hence photocatalytic activity of TiO₂ [159–164]. One of the effective methods is band gap engineering by doping with cation. The cationic dopants add impurity levels in the conduction band of TiO₂ modifying its electronic structure. These defects and dopants create sub-band states in the band gap of TiO₂ and shift the absorption edge of TiO₂ towards the visible region, thus enhancing the visible light photoactivity.

The advantages of transition metal ions is attributed to their behaviour as electron scavengers via $M^{n+} + e^-_{cb} \rightarrow M^{(n-1)+}$ where $M^{n+} = Cu^{2+}, Mn^{3+}, Fe^{3+}$. Cu has been considered to be important owing to the narrow band gap energies of its oxides (cupric oxide, CuO possesses 1.4 eV and cuprous oxide, Cu₂O possesses 2.2 eV) and their high light absorption coefficients [165–170]. As a p-type semiconductor with narrow band gap, cupric oxide has found use in a wide range of applications. Nanocrystalline CuO exhibits improved optical, electronic and catalytic properties that differ from those of bulk CuO [170,171]. Hara et al. [172] introduced Cu₂O powder as a p-type visible light photocatalyst that unlike electrodes

does not photodegrade for overall water splitting. Since then, copper oxide has been considered as a potential photocatalyst and has been extensively studied. The absorption of visible light by Cu_2O or CuO greatly extends the wavelength range of TiO_2 when coupled; therefore further enhancing the efficiency of solar energy usage. Cu doping can also effectively reduce the wide band gap of TiO_2 by creating defects and d-band states of Cu in TiO_2 and can also act as active trap centres of electrons to reduce carrier re-combination [173]. Cu-doped TiO_2 or CuO/TiO_2 composites serve as an efficient photocatalytic material in the degradation of gas phase alcohols [174], 4-nitrophenol [175], acid orange [176], low concentration of mercury [177], SO_2 and NO removal etc. [178]. Wang et al. [179] have reported that the Cu-doped TiO_2 thin films exhibited enhanced photocatalytic activity compared to the reference TiO_2 thin film, for the degradation of methylene blue (MB) solution under simulated solar-driven irradiation. Cu-doped TiO_2 / graphene composites can also effectively photodegrade methyl orange (MO), and show an excellent photocatalytic enhancement over pure TiO_2 [180]. The role of surface/ interfacial Cu^{2+} sites in the photocatalytic activity of coupled $\text{CuO}-\text{TiO}_2$ nanocomposites is emphasized by Li et al. [181]. Recently, Singhal et al reported the photocatalytic H_2 generation over Cu_2O oxides prepared by various simple one pot synthetic routes using inexpensive precursors [182]. Photocatalytic properties determined by the combined effect of the surface area, porosity and crystallinity of the Cu_2O nanocrystals achieved with different synthetic routes were discussed.

In the present chapter we will discuss investigations on TiO_2 , a series of doped $\text{Cu}_x\text{Ti}_{1-x}\text{O}_{2-\delta}$ ($x= 0.0, 0.02, 0.06$) and composites, $x\text{CuO}:y\text{TiO}_2$ ($x:y= 1:9, 2:8, 5:5$) and compared their activities for photocatalytic H_2 generation under sunlight and UV-visible light in identical conditions. Structural, electronic, optical and surface properties were characterized by relevant techniques. The role of Cu ions as a dopant or as a composite in

enhancing the photocatalytic properties of TiO₂ was investigated by ex-situ characterization of both fresh and used catalysts. Apparent quantum efficiency (AQE) and solar to fuel efficiency (SFE) of the photocatalysts under different conditions were calculated.

3.2 Experimental

3.2.1 Synthesis of catalyst/ co-catalyst

Nanoparticles of TiO₂ and doped Cu_xTi_{1-x}O_{2-δ} (x= 0.0, 0.02, 0.06) and composites, xCuO:yTiO₂ (x:y= 1:9, 2:8, 5:5) with nominal compositions were synthesized through sol-gel method by mixing reactants in appropriate stoichiometry as depicted by following equation:



Cupric acetate trihydrate (>99 %, SDFCL, s d fine-chem Ltd), titanium tetraisopropoxide (TTIP, 97 %, Aldrich) and propan-2-ol (AR>99.5 %, SDFCL, s d fine-chem Ltd) were used as received. For 2 mol% Cu doped TiO₂, 30 ml of propan-2-ol and 7.2 ml of TTIP was mixed to prepare solution A. Another solution referred as B containing 0.0908 g of cupric acetate dissolved in 10 ml distilled water was also prepared. Solution A was added drop wise to the solution B under constant stirring till a gel was formed. The gel was left overnight undisturbed for nucleation to take place. After nucleation, the gel was heated at 50 °C, stirred and was vacuum dried for ~1 h to remove the moisture from the sample. The dried sample was heated in oven at 100 °C for ~1 h. Further, the sample was calcined at 500 °C for 5 h at a heating rate of 2 °C min⁻¹ in air to ensure the uniformity and the completion of the reaction. The typical synthesis route of 2 mol% Cu doped TiO₂ oxide (Cu_{0.02}Ti_{0.98}O_{2-δ}) is shown in Fig. 3.1. Remaining samples were synthesized by varying amount of copper. Depending on Cu content, white to brownish-black to black coloured photocatalyst powders were obtained.

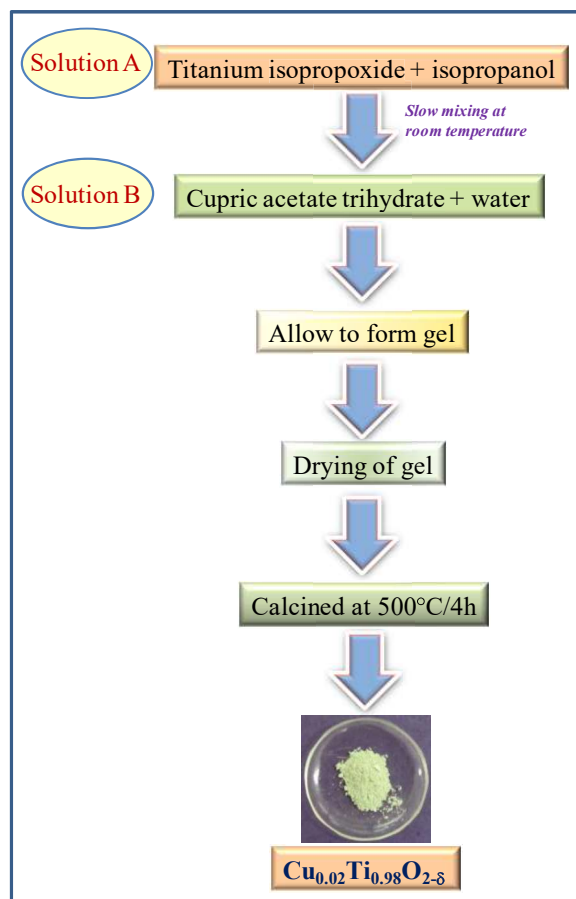


Fig. 3.1 A schematic of procedure followed to synthesize $\text{Cu}_{0.02}\text{Ti}_{0.98}\text{O}_{2-\delta}$ powder by sol-gel route.

To further improve the photocatalytic hydrogen production, Pt as cocatalyst (~1 % by weight) was loaded on the $\text{Cu}_x\text{Ti}_{1-x}\text{O}_{2-\delta}$ ($x= 0.02$ and 0.06) samples, by the photo-deposition method. For this purpose, 0.1 g of the catalyst was mixed with 25 ml of water, 5 ml of ethanol and 2.5 ml of chloroplatinic acid hexahydrate ($\text{H}_2\text{PtCl}_6 \cdot 6\text{H}_2\text{O}$, 0.002 M). The resulting reaction mixture was evacuated in a quartz cell and then irradiated under medium-pressure mercury lamp (Hg, Ace Glass Inc., 450W) for about 3 h. After irradiation, the solution was washed with ethanol, filtered and the residue was dried in an oven at 100 °C.

3.2.2 Characterization

Cu-Ti samples were characterized by relevant techniques which are explained in detail in Chapter 2. Powder XRD patterns were recorded on a Philips diffractometer (model PW 1710), equipped with a graphite monochromator and Ni-filtered $\text{Cu-K}\alpha$ radiation. The

crystallite size was calculated from the XRD line width using the Scherrer equation. The profiles of the XRD patterns were refined by the Rietveld method using GSAS software package. The background of the diffraction data was modelled by linear interpolation of selected points to create a smooth varying background pattern. The profile was fitted with Pseudo-Voigt function with one asymmetry and high and low broadening parameters. The scale, unit cell parameters and profile parameters were refined to match the observed and calculated intensity of the diffraction data. N₂- BET surface area was measured with a Quantachrome Autosorb-1 analyser using nitrogen as the adsorbing gas. The elemental analysis of Cu and Ti present in the oxide samples was evaluated using ICP-OES (*JobinVyon* JY 2000, France). Raman spectra were recorded using 532 nm lines from a diode Nd: YAG laser (power 15 mW) focused to a spot size of ~20 μm. The scattered light was analyzed using an indigenously built 0.9 m single monochromator, coupled with a super notch filter and detected by a cooled charge couple device (CCD, Andor Technology). A resolution limited line width of 3 cm⁻¹ was achieved at entrance slit width of 50 μm. The band gap of all semiconductor oxide samples was estimated by recording their diffuse reflectance UV-visible spectra using a spectrophotometer of JASCO model V-530, Japan, scanned in the range of 200-1000 nm at the scanning speed of 200 nmmin⁻¹. High resolution TEM /SAED images were recorded on FEI-*Tecnai* G-20 microscope operating at 200 kV. EXAFS measurements of the Cu doped TiO₂ samples at the Cu *K* edge were carried out in fluorescence mode at the Scanning EXAFS Beamline (BL-9) at the INDUS-2 Synchrotron Source (2.5 GeV, 100 mA) at the Raja Ramanna Centre for Advanced Technology (RRCAT), Indore, India [144–146]. The beam line uses a double crystal monochromator (DCM) in the photon energy range of 4-25 KeV with a resolution of 10⁴ at 10 KeV. XPS experiments were recorded on an electron spectrometer (SPECS, Surface Nano Analysis GmbH, Germany) using Mg- K_α X-rays (hν=1253.6 eV) as the primary source of radiation with an overall energy resolution of the

instrument of about 0.7 eV. The appropriate corrections for charging effects were made with the help of a C 1s signal appearing at 284.5 eV.

3.2.3 Photocatalytic activity

Photocatalytic activity of all the samples were evaluated under sunlight and UV-visible light as mentioned in chapter 2. In this, 100 mg of photocatalyst was dispersed in water and methanol solution (33 % v/v) and solution was evacuated and illuminated under UV-visible light source (450 W medium pressure Hg lamp). H₂ generated was monitored after every 2 h of interval by using gas chromatography equipped with TCD. In similar way H₂ production activity of the catalyst was evaluated by irradiating the reaction mixture under sunlight illumination from 11:00 – 15:00 IST. Evolution of H₂ bubbles were observed during sunlight illumination. By using the lightmeter flux value of UV lamp as well as variation of flux in a day was measured during the illumination time in sunlight. These flux values were used to calculate AQE and SFE by using formula mentioned in Chapter 2.

3.3 Results and discussion

3.3.1 XRD

XRD patterns of nanosized TiO₂, CuO, Cu_xTi_{1-x}O_{2-δ} as a function of x synthesized by sol-gel route are shown in Fig. 3.2. The XRD pattern of the undoped sample shown in curve a, coincides with that of anatase, TiO₂ (JCPDS No: 21-1272). It crystallizes in the tetragonal space group with $a = 3.785(1) \text{ \AA}$, $c = 9.501(1) \text{ \AA}$, cell volume = $136.13(1) \text{ \AA}^3$ and $Z = 4$. An additional weak line at 30.8° corresponding to hkl_{90} of brookite phase (JCPDS 29-1360) was observed. hkl_{100} of brookite coincides with hkl_{100} of anatase phase. Curve g matches with tenorite CuO (JCPDS card No. 05-0661) having monoclinic phase with $a = 4.684 \text{ \AA}$, $b = 3.425 \text{ \AA}$, $c = 5.129 \text{ \AA}$, cell volume = 81.16 \AA^3 . XRD patterns of Cu²⁺ substituted TiO₂ are represented in the curves b to f. XRD patterns shown in curves b-c reveal that aliovalent

substitution of Cu^{2+} ions in TiO_2 has resulted in single-phase compositions with TiO_2 phase referred as doped samples. While, in subsequent samples having Cu content ($\geq 10\%$), the presence of additional weak reflections at $2\theta = 35.5^\circ, 38.7^\circ, 48.7^\circ$, marked as * in their XRD patterns (curves d-f) was observed. These were identified and attributed to the monoclinic CuO phase (JCPDS card No. 05-0661). The XRD lines due to the CuO phase are prominently observed in $\text{CuTi}(5-5)$. Thus, $\text{Cu}^{2+} \geq 10\%$ has resulted in mixed phased samples comprised of TiO_2 and CuO.

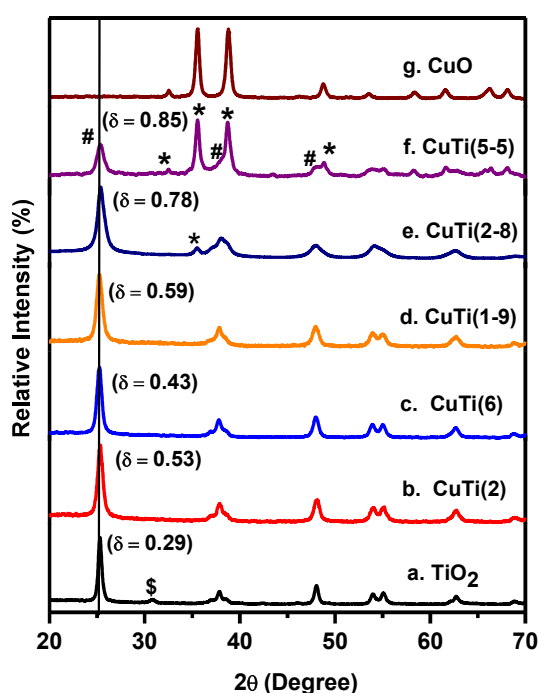


Fig. 3.2 XRD patterns of different Cu-Ti-O samples synthesized by sol gel calcined at 500°C for different values of x. Line broadening (δ , FWHM) increases and shift towards lower 2θ angles was observed with increase in Cu content. \$ Brookite, # Anatase TiO_2 , * Tenorite CuO.

In this chapter, the biphasic oxide samples composed of CuO and TiO_2 phases are referred as composite sample viz; $\text{CuTi}(1-9)$, $\text{CuTi}(2-8)$ and $\text{CuTi}(5-5)$. The number in parentheses indicates the nominal composition of CuO and TiO_2 in each sample. The nominal compositions, extent of substitution (x), phases identified and the lattice parameters indexed by Rietveld refinement for the various Cu substituted samples along with their abbreviations are given in Table 3.1. XRD profiles of composite samples were refined by Rietveld method.

CuTi(1-9) could not be fitted for CuO due to low counts (Fig. 3.3). However, lattice parameters could be generated for TiO₂ in CuTi(1-9) as given in Table 3.1.

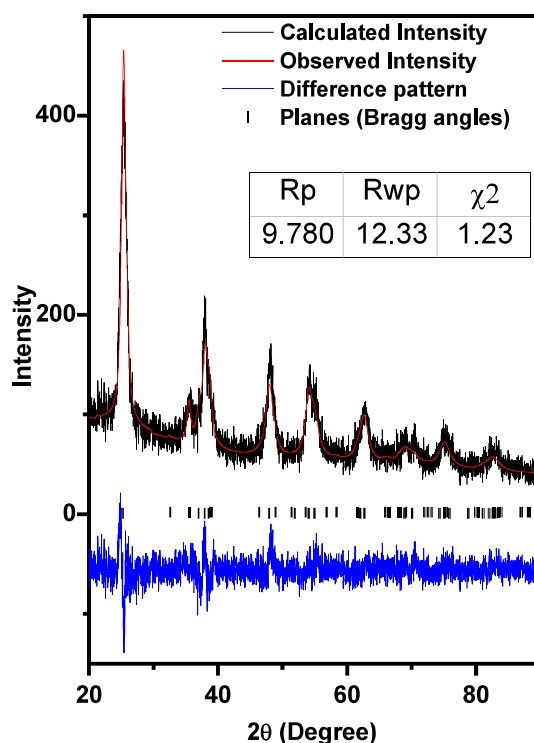


Fig. 3.3 Profile of the XRD patterns of Cu (1-9) composite sample were refined by Rietveld method using GSAS software package. Inset presents the parameters derived for CuTi composites by Rietveld method using GSAS software package.

Rietveld refined curves along with difference patterns were generated for other composite oxides also CuTi(2-8) and CuTi(5-5). All observed XRD reflections have a good fit with the calculated pattern in CuTi(2-8) and CuTi(5-5) samples. The lattice parameters generated for both the phases CuO and TiO₂ present in CuTi(2-8) and CuTi(5-5) are listed in Table 3.1. The vertical lines in these figures represent the Bragg angles at which planes due to both the phases appear. Using this software, each phase was quantified in its respective composite sample by considering the individual reflections of both TiO₂ and CuO lines. The amount of individual phases, CuO and TiO₂ (wt % and mole %) present in each composite sample are given in Table 3.1. The possibility of incorporation of CuO in TiO₂ lattice cannot be ruled out in the composite samples. From XRD results it is evident that TiO₂ lattice can

tolerate Cu upto 10 %. This explains that why the calculated wt % values are lower than expected in both the composite samples, CuTi(2-8) and CuTi(5-5). Molecular weight of CuO and TiO₂ are nearly same 79.54 g/mol and 79.88 g/mol respectively, therefore its wt % and mol % ratio are identical Table 3.1.

Table 3.1 Abbreviations, lattice parameters and phase identification of Cu_xTi_{1-x}O_{2-δ} samples.

Nominal Composition	Abbreviation	Phase identified by XRD	a (Å°) obtained by Rietveld refinement for TiO ₂	b (Å)	c (Å)	Volume (Å) ³	Wt (%) of CuO: TiO ₂
			a (Å°) Obtained by Rietveld refinement for CuO				
TiO ₂	TiO ₂	Tetragonal TiO ₂	3.785(1)		9.501 (1)	136.13 (1)	
Cu _{0.02} Ti _{0.98} O _{2-δ}	CuTi(2) Doped	Tetragonal TiO ₂ single phase	3.785(1)		9.508 (1)	136.23 (3)	
Cu _{0.06} Ti _{0.94} O _{2-δ}	CuTi(6) Doped	Tetragonal TiO ₂ single phase	3.785(1)		9.511 (2)	136.28 (4)	
Cu _{0.1} Ti _{0.9} O _{2-δ}	CuTi (1-9) Compo site	Biphasic CuO and TiO ₂ (1:9 molar ratio)	3.785(1)		9.490 (2)	135.95 (3)	*
Cu _{0.2} Ti _{0.8} O _{2-δ}	CuTi (2-8) Compo site	Biphasic CuO and TiO ₂ (2:8 molar ratio)	3.798 (1)		9.489 (3)	136.90 (6)	8: 92
			4.678(2)	3.422(1)	5.130 (1), β = 99.35	81.04 (2)	
Cu _{0.5} Ti _{0.5} O _{2-δ}	CuTi (5-5) Compo site	Biphasic CuO and TiO ₂ (5:5 molar ratio)	3.784(1)		9.474(6),	135.63 (9)	39: 61
			4.678(1)	3.422 (1)	5.130 (1) β=99.3 4(2)	81.04 (2)	

* The Counts due to CuO are too low to be quantified.

3.3.2 ICP-OES

Further, chemical composition is confirmed using the ICP-OES technique as shown in Table 3.2. The experimental values are in agreement with the calculated values within experimental error.

Table 3.2 Elemental analysis of Cu and Ti present in representative doped and composite sample evaluated by ICP-OES technique.

S. No.	Sample	Nominal composition	Experimental values (wt %)	Calculated values (wt %)
1.	CuTi(2) Doped	$\text{Cu}_{0.02}\text{Ti}_{0.98}\text{O}_{2-\delta}$	Cu= 2, Ti= 54	Cu= 1.59, Ti= 58.74
2.	CuTi(2-8) composite	$\text{Cu}_{0.2}\text{Ti}_{0.8}\text{O}_{2-\delta}$	Cu= 16, Ti= 44	Cu= 15.92, Ti= 47.99

3.3.3 Crystallite and particle size and morphological features

The incorporation of a larger cation, Cu^{2+} (0.73 Å) in place of relatively smaller sized cation ($\text{Ti}^{4+} = 0.68$ Å) has resulted in morphological and bulk modifications. With the increase of the copper content, line broadening (δ , FWHM) accompanied with decrease in intensity of the 101_{100%} peak was observed. The presence of amorphous CuO is indicated. Choudhury et al [173] have reported similar effect during their investigations on pristine and 2 %, 4 %, and 6 % Cu doped TiO_2 . They showed that increase in broadening and lowering in intensity of diffraction peak in XRD pattern were due to increase in the fraction of the amorphous grain boundary, containing many of the structural defects and degradation of structural quality or loss of crystallinity of TiO_2 on Cu doping respectively. The crystallite sizes calculated using Scherrer equation is listed in Table 3.3. The morphological characteristics of Cu/Ti/O nanoparticles have been investigated by transmission electron microscopy (TEM). A representative low resolution image of as-synthesized and calcined CuTi(6) sample is shown in Fig. 3.4(a-b). Particles having amorphous centre surrounded by crystalline boundaries indicating short range ordering were observed in the TEM image of as-synthesized CuTi(6) sample. Diffuse rings shown in the selected area electron diffraction pattern (SAED) confirms the nano-crystalline nature of the sample Fig. 3.4a. Whereas,

distinct lattice fringes indicative of long range ordering appeared inside the crystallites of hexagonal morphology (marked by red outline) for calcined sample (Fig. 3.4b). Well defined rings with dotted SAED pattern were observed for the crystalline CuTi(6) sample.

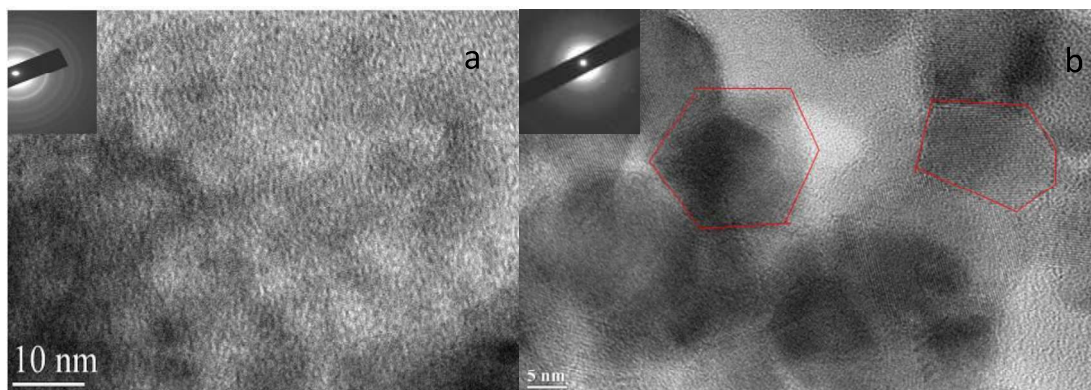


Fig. 3.4 TEM of CuTi(6) nanoparticles (a) as-synthesized (b) calcined at 500 °C. SAED pattern is shown as the inset in respective figures.

Representative low and high resolution TEM images with SAED patterns of all calcined samples are shown in Fig. 3.5. Cu doping in TiO₂, has decreased the crystallite and particle size considerably in agreement with other reports [183]. Due to lack of any stabilizing surfactants, the particles are agglomerated but it is still possible to determine the diameters of the particles Table 3.3, which are in the range 7-15 nm for doped and 4-9 nm for composite samples. A single particle with distinguishable grain boundaries and clear lattice fringes could be discerned within agglomerate as seen in their high-resolution images. TiO₂, CuTi(2) and CuTi(6) (Fig. 3.5) have non spherical particles with similar morphology. All rings in the SAED pattern in TiO₂, CuTi(2) and CuTi(6) samples were indexed for anatase TiO₂. Both tenorite CuO and anatase TiO₂ phase coexist in the particles of CuTi(2-8) and CuTi(5-5) confirmed by SAED pattern (Fig. 3.5).

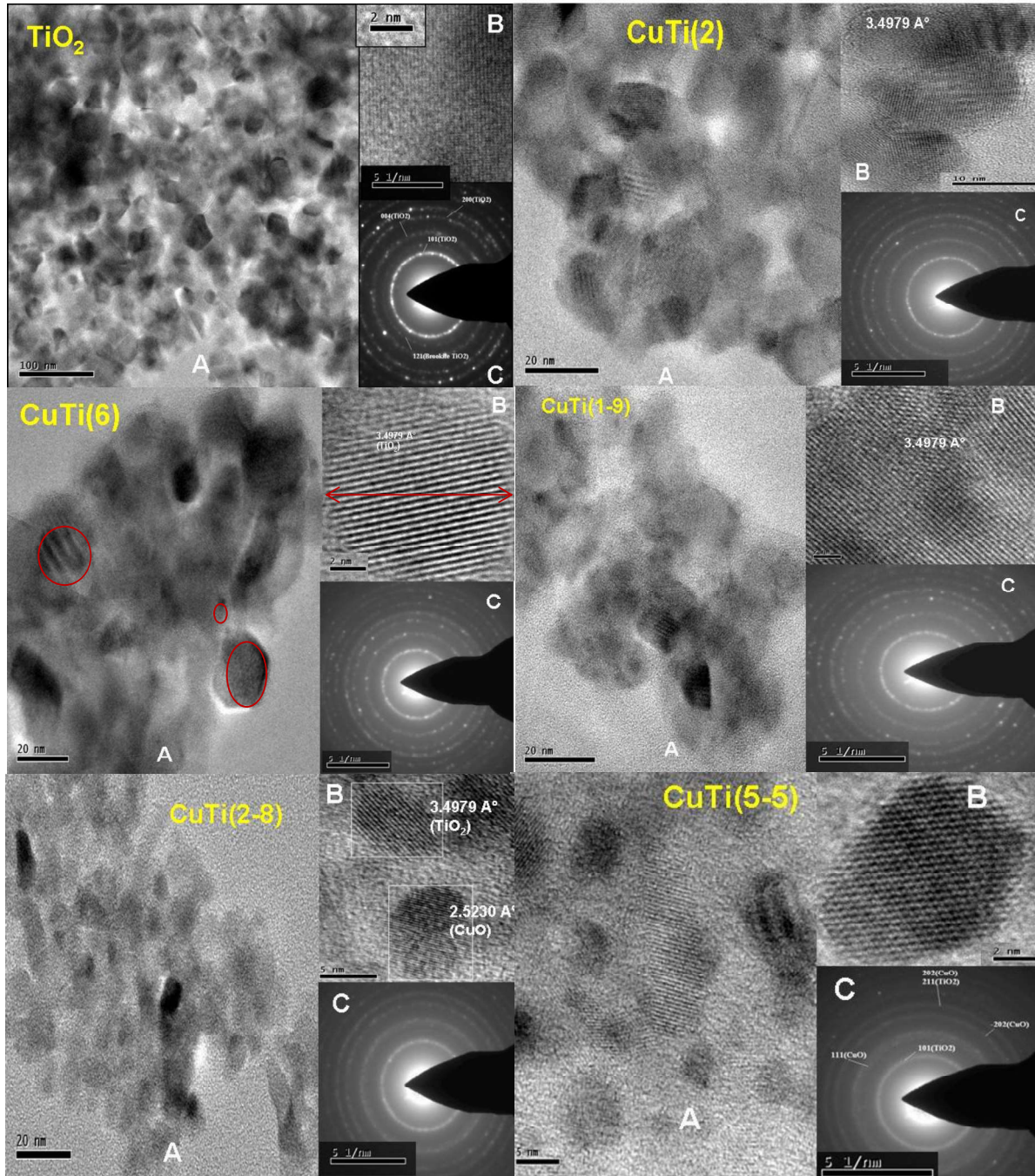


Fig. 3.5 TEM (a), HRTEM (b) and SAED (c) of $\text{Cu}_x\text{Ti}_{1-x}\text{O}_{2-\delta}$ and $\text{CuO}-\text{TiO}_2$ nanocomposites.

3.3.4 N_2 BET surface area and porosity

N_2 BET surface areas, mesopore cumulative pore volumes and mean pore size diameter for some of the representative samples are listed in Table 3.3.

Table 3.3 Crystallite size, particle size, N₂- BET surface area and porosity of Cu_xTi_{1-x}O_{2-δ} and xCuO:yTiO₂ nanocomposites.

Sample	Crystallite size (nm) of samples calcined at 500 °C estimated by Scherrer equation	Particle size from TEM (nm)	Specific surface area (m ² /g)	BJH pore size distribution	Pore volume (cm ³ /g)
TiO ₂	20.1	15-30	42	mesoporous (in all ranges upto 100 Å)	0.1
CuTi(2)	12.6	7-14	73.16	microporous and mesoporous (in all ranges upto 100 Å)	0.071
CuTi(6)	14.2	7-15	61.54	Mesoporous (in range of 10-30 Å and 90-80 Å)	0.064
CuTi(1-9)	11.2	4-15	-	-	-
CuTi(2-8)	7.4	4-9	-	-	-
CuTi(5-5)	9.8	3.5-8	73.08	Mesoporous (in range of 40-60 Å)	0.184

Both Cu doped and composites have shown enhanced surface area as compared to TiO₂ (42 m²/g). Cu doping upto 2 % resulted in formation of both micropores and mesopores of varying sizes Fig. 3.6.

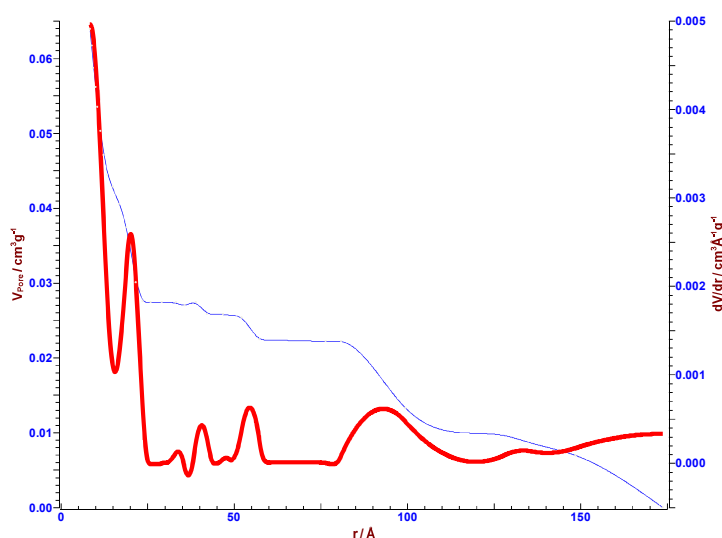


Fig. 3.6 BJH pore size distribution and pore volume curves of CuTi(2). V_{pore} is shown by red and dV/dr by blue curves.

With increase in copper content from 2 to 6 %, BET surface area decreased from $\sim 73 \text{ m}^2\text{g}^{-1}$ to $\sim 61 \text{ m}^2\text{g}^{-1}$ due to blockage of the micropores by the copper oxide clusters formed over the titania surface. This is evident by decrease in cumulative pore volume from $0.071 \text{ cm}^3\text{g}^{-1}$ to $0.064 \text{ cm}^3\text{g}^{-1}$ in CuTi(2) and CuTi(6) respectively. In case of the composite CuTi(5-5) sample, a large proportion of pores of size 40-60 Å were formed and pore volume increased to $0.18 \text{ cm}^3\text{g}^{-1}$.

3.3.5 Raman spectroscopy

Raman spectra of $\text{Cu}_x\text{Ti}_{1-x}\text{O}_{2-\delta}$ as a function of x synthesized by the sol-gel route are shown in Fig. 3.7. Raman bands at 151, 200, 394, 515 and 636 cm^{-1} corresponding to $E_g(1)$, $E_g(2)$, $B_{1g}(1)$, $A_{1g}+B_{1g}(2)$ and $E_g(3)$ vibrational modes of anatase TiO_2 [184,185] are seen for all CuO- TiO_2 oxides.

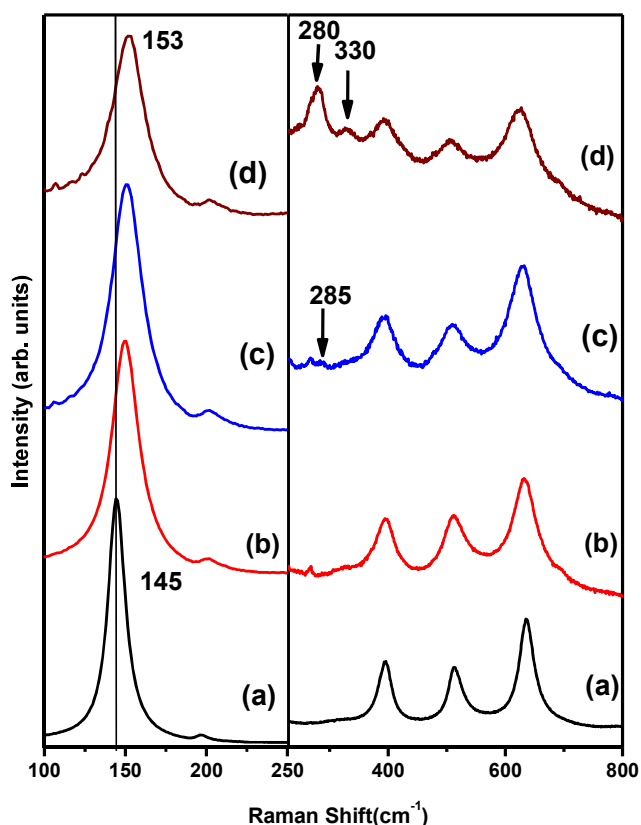


Fig. 3.7 Raman spectra of a) CuTi(6), b) CuTi(1-9), c) CuTi(2-8) and d) CuTi(5-5). Arrow marks indicate the Raman modes due to CuO.

The compositions with CuO upto 6 % show only the modes of TiO₂. There are no signatures of CuO in the lower compositions as the Raman scattering cross section of CuO is very low compared to that of anatase TiO₂. Weak Raman features due to CuO were observed in CuTi(2-8) nanocomposite whereas, CuTi(5-5) shows prominent Raman bands at 280 and 330 cm⁻¹ due to A_g and B_g(1) modes of nanocrystalline CuO, respectively [186,187]. A considerable increase in FWHM and the frequency of the E_g(1) mode of TiO₂ is attributed to increased nanocrystallinity of the samples with an increase in Cu content also evident by TEM studies.

3.3.6 XAS

Consequences of Cu²⁺ substitution at Ti⁴⁺ sites on local environment around metal ions were probed using X-ray Absorption Near Edge Spectroscopy (XANES). XANES spectrum for sol-gel synthesized CuTi(2) photocatalyst is shown in Fig. 3.8.

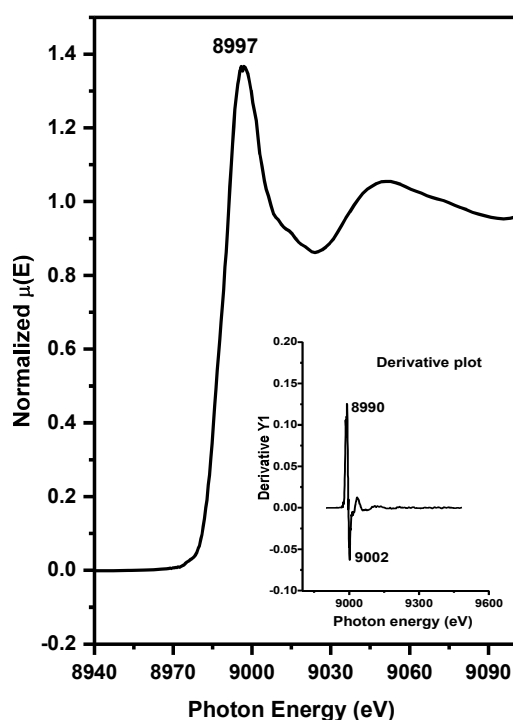


Fig. 3.8 Cu K-edge XANES spectra of CuTi(2) sample. Inset shows a derivative plot of the spectrum.

The spectrum exhibits absorption edges corresponding to $1s \rightarrow 4p$ electric dipole allowed transitions in the Cu K-edge. The first peak maxima position in the derivative spectrum (shown as inset in Fig. 3.8) is considered as the absorption energy. Thus, the absorption energy of the CuTi(2) sample is 8990 eV. XANES spectrum shows a strong intense peak at 8997 eV that is attributed to existence of Cu(II) species [188]. Unlike the spectra of reported Cu₂O and CuO, presence of pre-edge is not observed in the sample which indicates a symmetric environment around Cu cations [188,189]. It also suggests that free CuO or Cu₂O is not present in the sample and Cu is occupying the symmetrical octahedral Ti sites in TiO₂ lattice.

The $\chi(r)$ versus r plots generated (Fourier transform range $k = 2.0-9.0 \text{ \AA}^{-1}$) for all the samples from the $\mu(E)$ versus E spectra following the methodology described in Chapter 2. The experimental $\chi(r)$ versus r spectra of the Cu doped TiO₂ samples have been fitted with theoretical spectra assuming Cu cation replaces Ti cation in the TiO₂ anatase structure. The lattice parameters and space group etc. for the anatase TiO₂ structure are obtained from the reported values in the literature [190]. The spectra have been fitted from 1-2 Å with a Cu-O shell at 1.94 Å ($\times 6$). The fitting results show that the CuTi(2) is indeed a single phase TiO₂ with Cu ions replacing Ti atoms in the TiO₂ matrix. The bond length, coordination number and distortion (σ) in lattice were obtained as a result of the best fitting and have been mentioned in inset of Fig. 3.9a. The ionic radius of Cu²⁺ in six co-ordinations is 0.73 Å while that of Ti⁴⁺ is 0.68 Å. This suggests that if Cu²⁺ replaces Ti⁴⁺ in the TiO₂ lattice, the resulting Cu-O bond length would be more than that of Ti-O bond length. However, as can be seen from Fig. 3.9a, the Cu-O bond lengths in the samples are less than the theoretical Cu-O or Ti-O bond lengths of 1.94 Å. This is also evident from Ti K edge EXAFS spectrum (Fig. 3.9b) which shows that the peak in the radial distribution function ($\chi(r)$ versus r) at Ti sites appears at higher r value in case of CuTi(2) (1.36 Å) compared to pure TiO₂ sample of 1.23 Å. This

indicates Ti-O bond length increases on Cu doping as compared to the undoped sample. Shortening of Cu-O bonds suggests that Cu might have been incorporated into TiO₂ lattice as Cu³⁺ since Cu³⁺ has a lower ionic radius of 0.54 Å in octahedral coordination. However, characterization by XPS described in next paragraph does not support the existence of Cu in the +3 state on the surface. Oxygen coordination is less than nominal value of 6 in the neighbourhood of Cu (inset inside Fig. 3.9a) indicating creation of oxygen vacancies to maintain the charge balance. Presence of substitution-induced disorder/defects in lattice is reflected by relatively higher values of σ^2 (0.006).

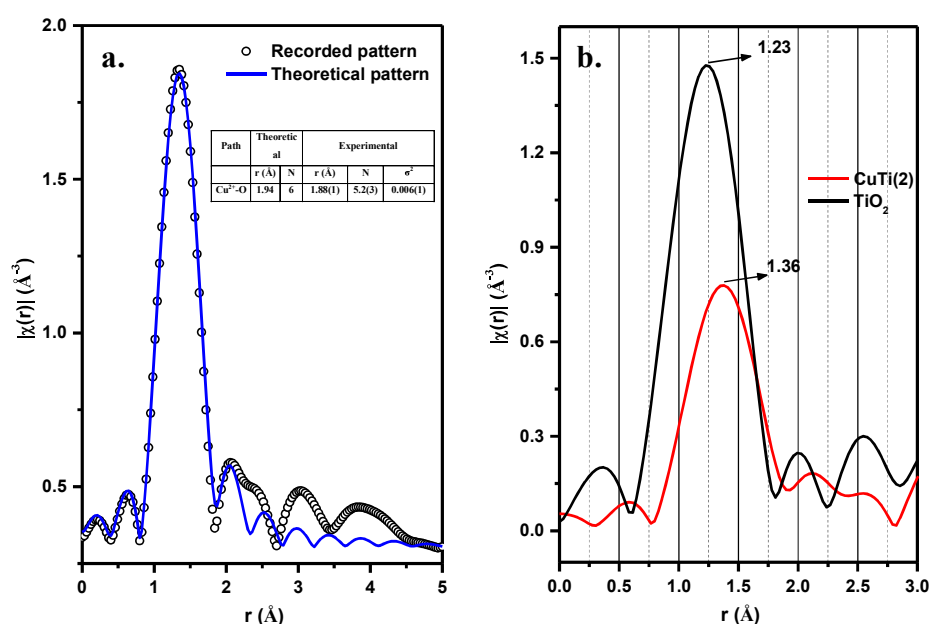


Fig. 3.9 a. Experimental $\chi(r)$ versus r spectrum at Cu K-edge of the CuTi(2) sample along with the best theoretical fits. Open circles are the experimental data fitted with TiO₂ model as shown by solid continuous line. Inset shows EXAFS fitting results for CuTi(2) photocatalyst assuming that 2 mol % Cu²⁺ ions are substituted at Ti⁴⁺ sites in anatase TiO₂, b. Experimental $\chi(r)$ versus r spectrum at Ti K-edge of CuTi(2) and pristine TiO₂.

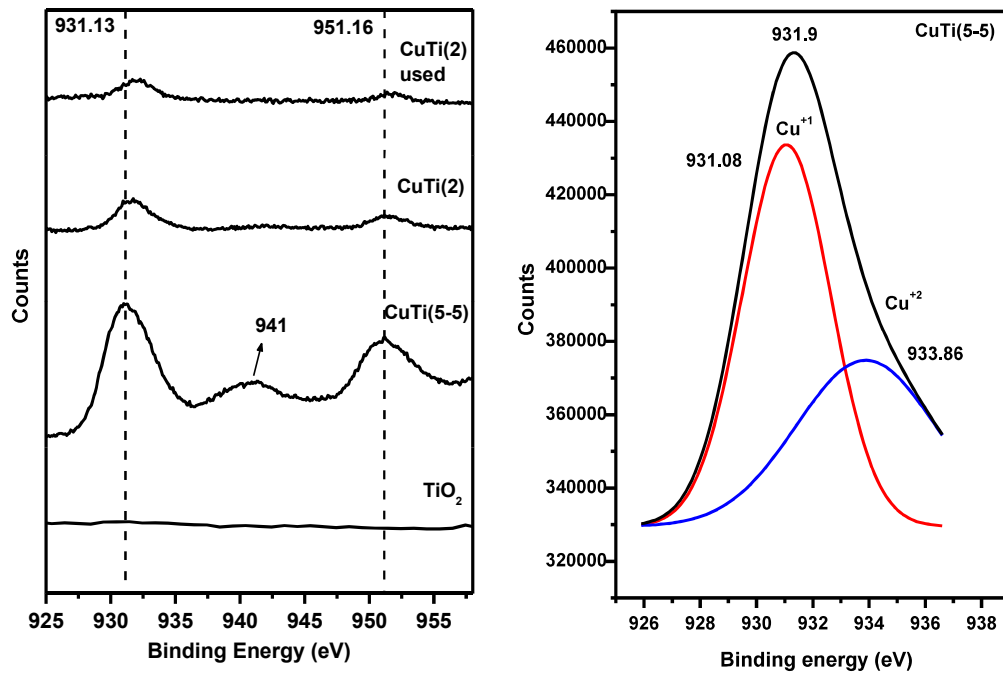
3.3.7 XPS

X-ray photoelectron spectra of TiO₂, fresh and used CuTi(2), CuTi(5-5) were recorded to explain the variations in oxidation states of Cu and Ti metal ions and O speciation (O²⁻ and OH⁻) in samples before and after the photocatalytic reaction. Cu-2p_{3/2} and Cu-2p_{1/2} lines along with satellites appear in the region of 925-960 eV and exhibits a progressive peak

shift towards higher binding energy with increase in oxidation state from Cu metal to Cu₂O and CuO [190]. In the present study, as expected there is no peak in this region (925-960 eV) of survey scan of TiO₂ sample. While in CuTi(2) and CuTi(5-5), XPS peak due to Cu -2p_{3/2} and Cu -2p_{1/2} were observed at ~ 931.9 and 951.8 eV respectively along with weak satellite peak at 941.9 eV (Fig. 3.10a). 931.9 eV peak can be deconvoluted into peaks ca. 931.6 and 934.2 eV (Fig. 3.10b-d). These values of binding energies agree well with monovalent and divalent copper respectively [191]. The significant difference for the divalent copper line is a considerably larger line width (a factor of 2) and also a very intense satellite whereas both the mono- and trivalent copper compounds show only weak satellites [191]. These satellites have been attributed to shake-up transitions by ligand-to-metal 3d charge transfer. This charge transfer cannot occur in Cu⁺¹ compounds and metallic Cu because of their completely filled 3d shells. Thus, binding energies of deconvoluted peaks and weakly intense satellite peak confirms that copper exists majorly in the +1 state and to some extent in the +2 state on the surface of both the CuTi(2) and CuTi(5-5) oxides. The intensity of the Cu 2p peak increases with increase in Cu content. However, the relative ratio of Cu⁺¹/Cu⁺² is higher in CuTi(2) as compared to CuTi(5-5) sample (Table 3.4). The higher concentration of Cu⁺² species on the CuTi(5-5) surface originated most probably from the bulk CuO present in the composite oxide. The absence of Cu⁺² in used CuTi(2) sample (Fig. 3.10d) will be discussed after the photoactivity results.

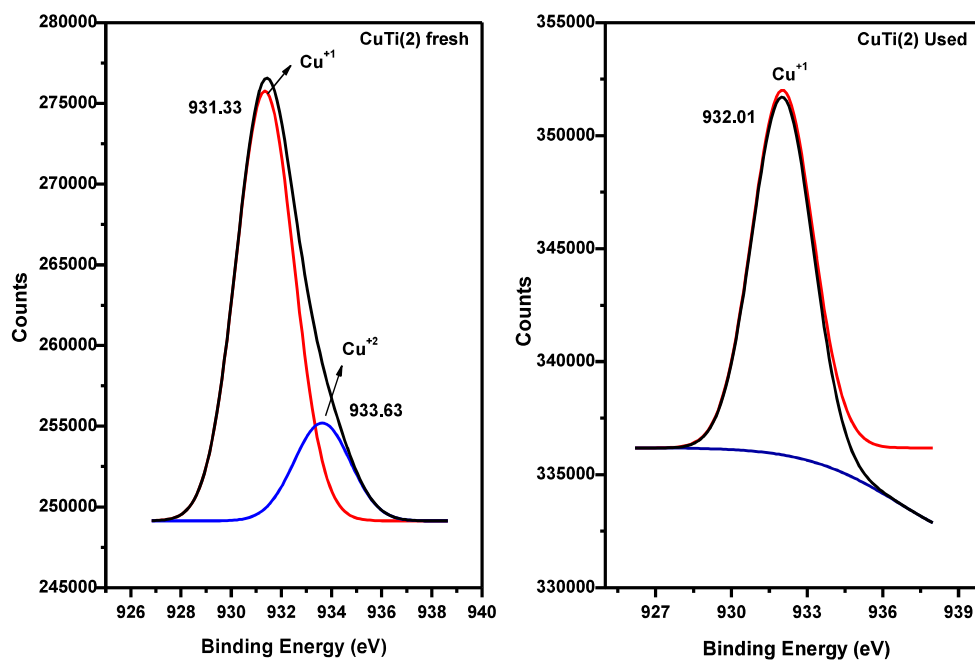
Table 3.4 Elemental compositions derived from XPS study of fresh and used doped and composite samples.

S. No.	Photocatalyst	Chemical composition (at %)			Ratio	
		Ti	Cu	O	OH/O ⁻²	Cu ⁺¹ /Cu ⁺²
1	TiO ₂	24.7	0	75.3	0.62	-
2	CuTi(5-5)	19.4	5.4	75.2	1.36	1.4:1
3	CuTi(2)	25.4	0.8	73.8	0.66	4.5:1
4	CuTi(2) used	21.6	0.6	77.7	1.13	No Cu ⁺²



a.

b.



c.

d.

Fig. 3.10 a. Overlay of XPS spectra corresponding to Cu $-2p_{3/2}$ and Cu $-2p_{1/2}$ lines for different samples. Deconvulation of Cu $-2p_{3/2}$ peak in b. CuTi(5-5), c. CuTi(2) fresh and d. CuTi(2) used samples.

BE values in the range of 457.7 to 458.4 eV and 463.4 to 464.2 eV (Fig. 3.11a) for Ti $2p_{3/2}$ and $2p_{1/2}$ respectively, in the range of 528.91 to 529.6 eV (Fig. 3.11b) for O $1s$ and from 284.6 to 284.7 eV (Fig. 3.11c), for C $1s$ core levels for TiO₂, CuTi(5-5), fresh and used CuTi(2) can be seen. These values confirm that Ti is in the +4 state in both TiO₂ and Cu-Ti oxides [192]. O $1s$ peak signal obtained from pristine as well as copper incorporated samples could be resolved in two spectra using a Gaussian fit as shown in Fig. 3.11b to yield a major peak at 529.2 eV and another one at 531.06 eV. The secondary peak was assigned to adsorbed hydroxy species, –OH species present on the surface in addition to bulk oxide (O²⁻) species [192,193]. OH⁻/O²⁻ ratios were derived from area under deconvoluted peaks and the ratios were nearly same 0.62 and 0.66 for both the fresh oxides TiO₂ and CuTi(2) respectively Table 3.4. However, after photocatalytic activity tests, the ratio enhanced to 1.13 in used CuTi(2) photocatalyst. The individual peak areas shows that, the peak area of adsorbed hydroxyl species are almost constant, however, that of O²⁻ has decreased after photocatalytic reaction. Thus, resulting in increase in OH⁻/O²⁻ ratio for the used CuTi(2). pH was monitored before and after 12 h photocatalytic reaction in sunlight. A shift towards acidic side (from 6.63 to 5.4) was observed which may lead to solubilisation of Cu²⁺ ions [194] present on surface to some extent and consequently leads to decrease in O²⁻ ion concentration. Changes towards acidic pH after photocatalytic activity test are due to probable formation of formic acid and carbon dioxide [195]. Carbon $1s$ peak at ~284.5 eV was also observed in all the samples and is shown in Fig. 3.11c. However, in the used CuTi(2) sample, in addition to 284.5 eV another peak appeared at 292.37 eV. The presence of adsorbed species of the type >C=O on the surface of used CuTi(2) sample may be responsible for the appearance of this peak [196] Methanol gets oxidized by h⁺ to acid or aldehyde which might be adsorbed on the surface of the photocatalyst. In all other samples, the carbon $1s$ peak appearing at 284.5 eV was used to provide BE shift correction in their spectra.

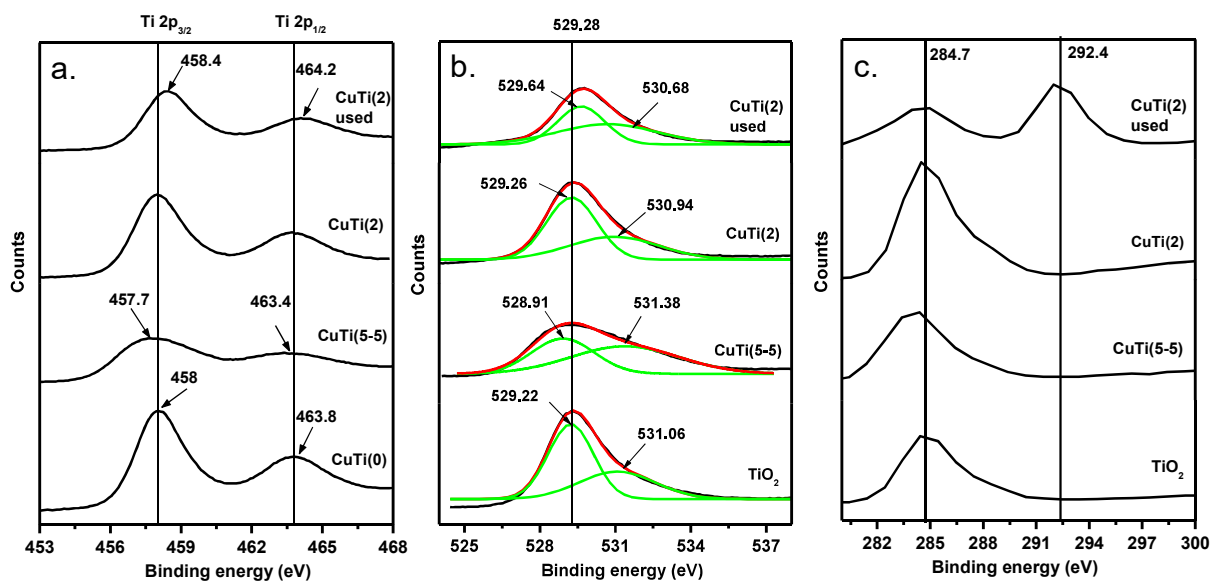


Fig. 3.11 Overlay of XPS spectra corresponding to a. Ti $-2p_{3/2}$ and Ti $-2p_{1/2}$ b. O $1s$ and c. C $1s$ lines for different samples. Broad peaks were deconvoluted to quantify relatively various oxidation states of an element present in a sample.

3.3.8 DRS

TiO₂ is a white coloured oxide; with increasing Cu content, the colour changes from white to yellow to green in single phasic doped samples whereas the colour varies from dark green in CuTi(1-9) to black in CuTi(2-8) and CuTi(5-5) in case of composite samples Fig. 3.12. The light absorption properties of Cu_xTi_{1-x}O_{2-δ} (x= 0.0, 0.02 and 0.06) and composite of xCuO:yTiO₂ (x:y=1:9, 2:8, 5:5) were monitored by recording the UV-visible diffuse reflectance spectra shown in Fig. 3.12. The spectrum of TiO₂ falls in range of 300 to 500 nm with an absorption peak in the UV region at 388 nm with an optical band gap of 3.2 eV. When doped with copper into TiO₂, a considerable shift of the peak towards the visible range occurred for all the samples with a broad band between 500 and 700 nm with λ_{\max} at ~566 nm (Fig. 3.12b and c) and progressively λ_{\max} shifts to ~600 nm in CuTi(1-9) oxide (Fig. 3.12d). This absorption band at ~566 nm is attributed to the presence of Cu¹⁺ clusters in partially reduced CuO matrix, evident by XPS also [197]. However, the absorption band with λ_{\max} at ~600 nm observed in CuTi(1-9) oxide (Fig. 3.12d) indicates the crystalline and

bulk CuO are in octahedral symmetry [198]. DRS spectra of composite samples (curves e-f) are quite different from the doped samples (a-d). The spectrum of a composite sample is a result of an overlap of the band structures of both the TiO₂ and CuO oxides. Thus, it can be inferred that incorporation of transition metal ions such as copper was effective for visible light response and can play a significant role in enhancing the hydrogen evolution [173] using solar energy economically.

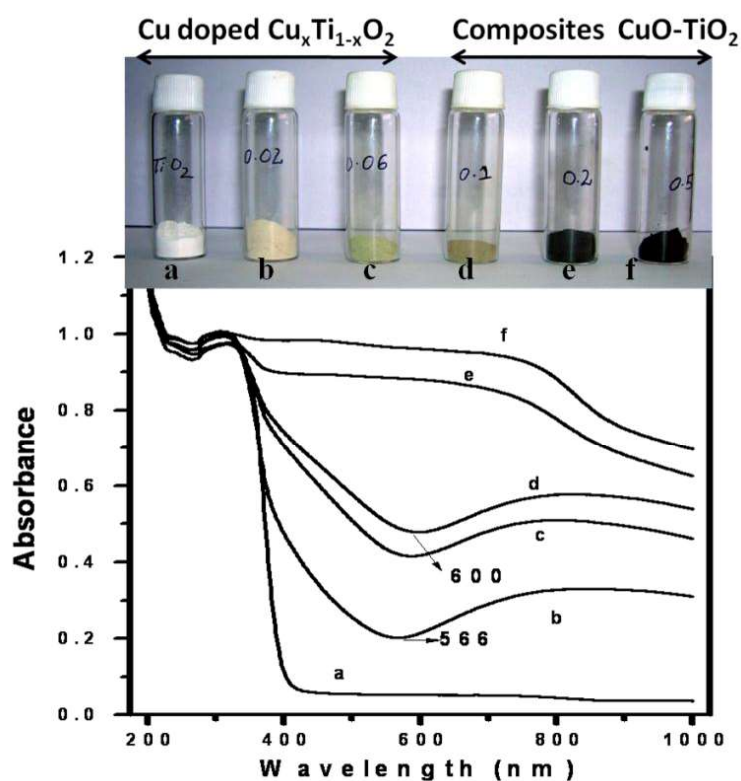


Fig. 3.12 Diffuse reflectance UV-Vis spectra of doped $\text{Cu}_x\text{Ti}_{1-x}\text{O}_{2-\delta}$ and $\text{CuO}-\text{TiO}_2$ nanocomposite samples a. TiO_2 , b. $\text{CuTi}(2)$, c. $\text{CuTi}(6)$, d. $\text{CuTi}(1-9)$, e. $\text{CuTi}(2-8)$ and f. $\text{CuTi}(5-5)$

3.3.9 Photocatalytic activity

3.3.9.1 Activity tests under direct sunlight

Various photocatalytic activity tests were performed over pristine TiO₂, Cu doped $\text{Cu}_x\text{Ti}_{1-x}\text{O}_{2-\delta}$ ($x= 0.0, 0.02, 0.06$) and composite $x\text{CuO}:y\text{TiO}_2$ ($x:y= 1:9, 2:8, 5:5$) samples to monitor the photocatalytic H₂ yield under different light sources and cocatalyst (Table 3.5).

Hydrogen bubbles were observed during irradiation in sunlight. The time dependent photocatalytic H₂ yield under sunlight for 12 h is plotted and shown in Fig. 3.13. The samples suspended in water-methanol mixture were irradiated in intense sunlight of daytime for 6 h each for two days. All samples were found to be active. There was no increase in H₂ yield during dark period.

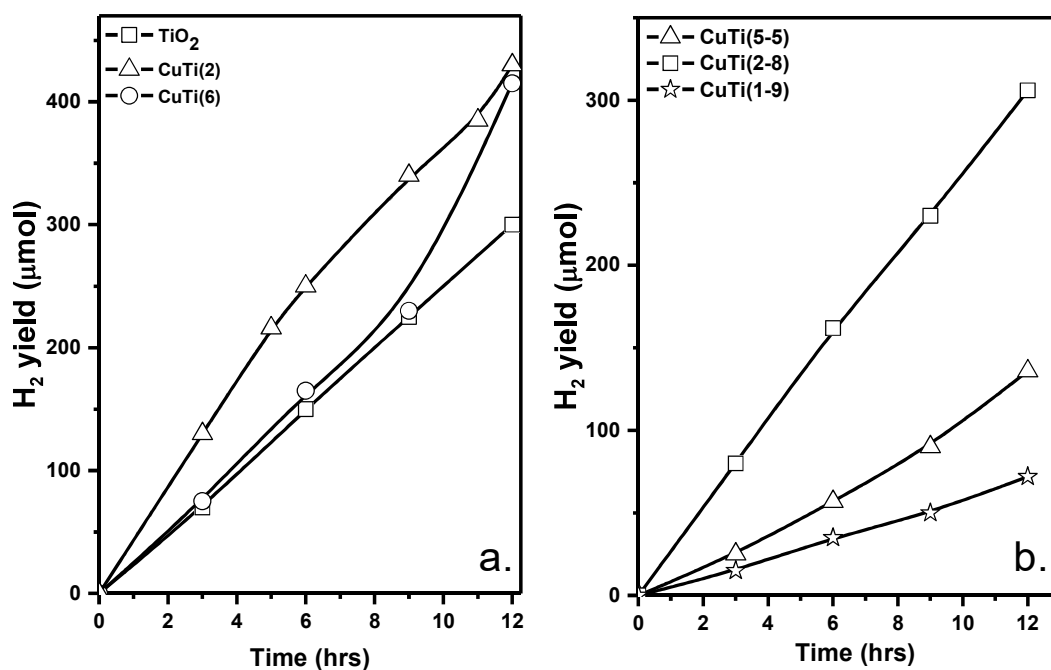


Fig. 3.13 Time courses of photocatalytic H₂ generated over a. doped Cu_xTi_{1-x}O_{2-δ} and b. CuO-TiO₂ composites under sunlight.

Maximum yield of photocatalytic hydrogen was obtained over 0.1 g of CuTi(2) sample ca. 430 μmoles in 12 h (rate of H₂ evolution = 36.0 μmol/h) as shown in Fig. 3.13a. In other words, 9.6 ml of H₂ was generated in the 81 ml capacity photoreactor suggesting that more than ~10 % v/v photocatalytic H₂ was generated in 12 h over CuTi(2) sample under sunlight. Among composite samples, maximum hydrogen yield of ~306 μmoles in 12 h was found to be generated over 0.1 g of the CuTi(2-8) sample (rate of H₂ evolution = 25.5 μmol/h) as shown in Fig. 3.13b. The decreasing order of catalytic activity is as follows: CuTi(2) > CuTi(6) > CuTi(2-8) > TiO₂ > CuTi(5-5) > CuTi(1-9) under sunlight. Although, photoresponse in the visible region increased with increase in Cu ion content, photocatalytic

hydrogen yield was not enhanced with increasing Cu content. Probable reasons to explain this are discussed later. The maximum AQE achieved was 3.6 % for the doped CuTi(2) sample and 2.5 % over the nanocomposite of CuTi(2:8) under sunlight (Table 3.5). To further enhance the performance of CuTi(2), 1 %w/w Pt was deposited over its surface. 1(%w/w)Pt/CuTi(2) shows 413.0 $\mu\text{mol/h}$ under UV-Visible light with apparent quantum efficiency of 25.7 % (Table 3.5).

3.3.9.2 Activity tests under UV-visible light

Although AQE calculations take in account of variable solar flux, the photocatalytic activities of Cu doped and composite samples were compared under constant flux UV-visible light (emission spectrum and set-up shown in Chapter 2). The photocatalytic H_2 yield over all samples increased in UV-visible irradiation (Fig. 3.14).

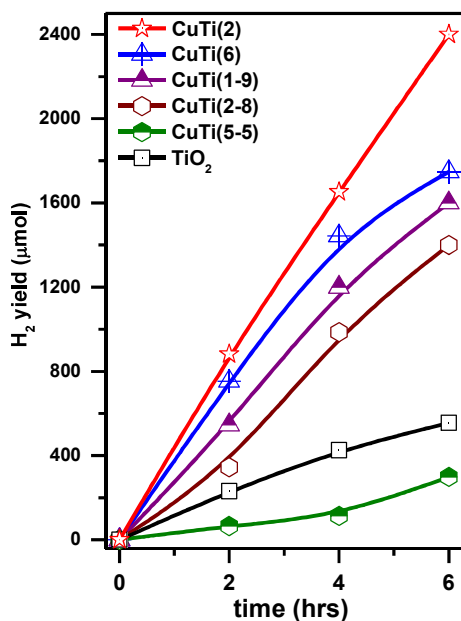


Fig. 3.14 Photocatalytic activity of $\text{Cu}_x\text{Ti}_{1-x}\text{O}_{2-\delta}$ and CuO-TiO₂ composites under UV-visible irradiation.

Among the composite samples, a maximum conversion of 293.5 $\mu\text{mol/h/0.1g}$ with AQE of 18.3 % (Table 3.5) was observed over CuTi(1-9) under UV- visible light as compared to 6 $\mu\text{mol/h/0.1g}$ in sunlight. Use of the CuTi(2) sample resulted in H_2 evolution

rate of 333 $\mu\text{mol/h}/0.1\text{g}$ with AQE of 20.8 % (Table 3.5) under UV-visible illumination as compared to 36 $\mu\text{mol/h}/0.1\text{g}$ in sunlight. Pt was photodeposited as co-catalyst over CuTi(2) to enhance the H_2 yield to 413.0 $\mu\text{mol/h}/0.1\text{g}$ and AQE rise to 25.7 % (Table 3.5). In case of Cu doped TiO_2 samples, the decreasing order of catalytic activity under UV-visible irradiation is almost same as obtained for sunlight. But the order changes in case of composite samples as $\text{CuTi}(1-9) > \text{CuTi}(2-8) > \text{TiO}_2 > \text{CuTi}(5-5)$. This suggests that under UV-visible irradiation, a nanocomposite with higher TiO_2 content shows the maximum H_2 yield. Whereas, under sunlight, both the semiconductor oxides of high and low band gap (TiO_2 , $E_g = 3.2$ eV and CuO , $E_g = 1.4$ eV respectively) should be present in an optimum amount in a nanocomposite to maximize the photocatalytic H_2 yield.

Table 3.5 Typical values of H_2 yield ($\mu\text{mol/h}$) obtained photocatalytically over CuTi(x) samples irradiated under different light source and conditions.

Sample	H_2 yield ($\mu\text{mol/h}$), AQE (η %), SFE (%)		Illumination Area (A) cm^2
	Sunlight	UV-Visible light (medium pressure Hg lamp)	
	0.1 g catalyst + water + methanol (33 % v/v, total volume 15ml) evacuated in reactor of capacity 81 ml irradiated under sunlight	0.1 g catalyst + water + methanol (33 % v/v, total volume 15ml) evacuated in reactor of capacity 81 ml, irradiated under flux of 10^{17} photons/s	
TiO_2	24.9	115.68, $\eta = 7.2$	20
CuTi(2)	36, $\eta = 3.6$	333.3, $\eta = 20.8$	20
CuTi(6)	34.6	291.3, $\eta = 18.2$	20
CuTi(1-9)	6	293.5, $\eta = 18.3$	20
CuTi(2-8)	25.5, $\eta = 2.5$	175.0, $\eta = 10.9$	20
CuTi(5-5)	5.8	50.5, $\eta = 3.1$	20
Pt/CuTi(2)	154.4, $\eta = 5.8$	413.0, $\eta = 25.7$, SFE= 2.2%	20

Cu doped titanium oxides and CuTi(2) in particular, in present study were found to be the most efficient visible light photocatalyst. The photocatalytic activities are governed by enhanced surface area and porosity, light absorption, distorted structure, optimum concentration of defect. Enhanced surface area and porosity generated favoured the

photocatalytic properties of Cu-Ti oxides. Incorporation of Cu in TiO₂ as a solid solution helps in stabilizing the more photocatalytically active anatase phase [199]. EXAFS investigations confirm the bulk substitution of Cu²⁺ at Ti⁴⁺ sites in CuTi(2) accompanied with more lattice distortion as suggested by σ values and lengthening of Ti-O bonds as compared to pristine TiO₂. There is no segregation of CuO or Cu₂O in the doped sample as confirmed by absence of pre-edge absorption in the XANES spectra of CuTi(2). Charge balance and lower coordination number around Cu ions (inset inside Fig. 3.9) suggests generation of O²⁻ ion vacancies. Distorted structures are more open and flexible, favouring charge carrier dynamics and enhancement in H₂ yield [159,200,201]. Another reason of maximum activity of CuTi(2) is attributed to the maximum surface area (73 m²/g) accompanied with microporosity in spite of identical preparation route followed for all the samples. Lower Cu contents have induced favourable morphological characteristics with enhanced surface area. From 2 to 6 % Cu doping, there is a diminution of surface area by 20 %. The micropores are observed only in CuTi(2) sample whereas all other Cu-Ti oxides are devoid of micropores. This may be due to blockage of the pores by the copper oxide clusters formed over the titania surface. Thus, optimum concentration of defects and favourable morphological characteristics, have imparted most favourable photocatalytic properties to the CuTi(2) oxide. However, with increase in Cu content, activity descended. As a result of higher Cu incorporation, more and more defects are generated. It is well reported that defects also acts as recombination centres for photogenerated e⁻ and h⁺. Kudo et al [22] have reported that process of preparation of nanopowders causes simultaneous formation of defects, these defects and grain boundaries acts as recombination centers for the generated electrons and holes, thus decreasing the photoactivity. Thus, inspite of enhanced visible light harvesting properties, the increase in rate of recombination reaction due to increased defect concentration at higher Cu content causes deterioration in photoactivity. Also, Lee et al [202]

have observed similar trend and have reported that with increase in Cu content, decrease in photocatalytic activity over Cu-Ti-O nanofibres was observed. Their results are in agreement with our findings. They found that 6 % Cu incorporated TiO₂ is most active as compared to 9 % and 12 %. They have attributed this trend to two reasons. One is the coverage of the host TiO₂ semiconductor by CuO which might limit the light accessibility thus hampering the initiation of photocatalytic reaction. Secondly, the relatively higher crystalline defects of the anatase TiO₂ due to the higher Cu inclusion could contribute to the overall decrease in the photocatalytic H₂ generation as crystal defects are potential charges recombination centers and lower the photocatalytic activity.

3.4 Mechanism

Surface characterization by XPS suggests the presence of Cu⁺¹ species predominantly along with small amount of Cu²⁺ in both doped and composite samples. Song et al. [203] reported the influence of oxidation state of Cu ion on photoactivity. They suggested that conversion of Cu⁰ to Cu⁺¹ and Cu⁺² progressively leads to a decrease in activity. The existence of Cu²⁺ is considered to be a recombination centre as it gets reduced by *e*⁻ and then oxidized by *h*⁺, thus, facilitating the recombination of *e*⁻ and *h*⁺, which affects the electron economy adversely. Here in the present study, XPS reveals that the ratio of Cu⁺¹/Cu⁺² is more in CuTi(2) than in CuTi(5-5) and only Cu⁺¹ species are present in the used CuTi(2) sample (deconvulated Cu2*p*_{3/2} peaks in Fig. 3.10b-d). The absence of Cu⁺² in used CuTi(2) can be explained by following reactions:



From reduction potentials [204] values, reduction of cupric to cuprous ion is more favourable than water reduction. Other two reduction reactions shown in eq 3.2-3.3 are not possible. Under light illumination, photogenerated *e*⁻ reduces Cu⁺² to Cu⁺¹ at the surface.

Cu₂O formed on the surface with band gap of 2.2 eV, absorbs visible light photons to generate e⁻s which are transferred from CB of Cu₂O to CB of TiO₂ and reduces water molecules to evolve H₂. Also presence of adsorbed >C=O species in used CuTi(2) catalyst (Fig. 3.11c) suggests oxidation of methanol to higher oxidation products on the surface of photocatalyst is taking place. Surface composition of used oxide by XPS shows that its surface is enriched in Cu⁺¹ indicating the predominance of Cu₂O-TiO₂ type of oxides instead of CuO-TiO₂. Colon et al. [199] reported that stabilization of Cu₂O versus CuO induced better photocatalytic results for phenol degradation. Li et al. [205] also reported the improvement in photocatalytic activity on incorporation of Cu₂O into the TiO₂ matrix by an electrochemical method where surface Cu⁺¹ species may act as the photoactive species with improved charge carrier properties and e⁻/h⁺ separation, leading to enhancement in photocatalytic H₂ yield.

3.5 Conclusion

Doped Cu_xTi_{1-x}O_{2-δ} (x= 0.0, 0.02, 0.06) and composites, xCuO:yTiO₂ (x:y = 1:9, 2:8, 5:5) were synthesized by a sol-gel method and characterized by all relevant techniques. 2-6 % Cu doping in TiO₂ resulted in solid solutions with improved photocatalytic properties and in a shift in absorption edge towards visible wavelengths as compared to pristine TiO₂. Dark green to black coloured CuO-TiO₂ composites absorbed light over the whole UV-visible range. Cu_{0.02}Ti_{0.98}O₂ (CuTi(2)) and CuO-TiO₂ in 2:8 mol% ratio (CuTi(2-8)) were the most active formulations among doped and composites. Dispersion of 1% Pt as cocatalyst over CuTi(2) further enhanced activity to 154.4 μmol/h/20cm² or 77200 μmol/h/m² with AQE of 5.8 % under sunlight and 25.7 % in UV-visible light. Investigations over Cu modified titania powders have shown that Cu²⁺ substitution at Ti⁴⁺ sites in TiO₂, stabilized the more photocatalytically active anatase phase, decreased coordination number around the Cu ions, lengthened Ti-O bonds, induced-oxygen ion vacancies and distortion (σ) in lattice (from

EXAFS, XPS). Distorted structures are more open and flexible with improved charge carrier dynamics and favourable photocatalytic properties. Reduction of CuO to photocatalytically more active Cu₂O by photogenerated e^- on surface of composites was evident by the absence of a Cu²⁺ peak in the XPS spectra of used CuTi(2). Based on the above results, TiO₂ modified by Cu²⁺ ions is an efficient low cost visible light photocatalyst that can be targeted for large scale H₂ production under sunlight.

**Investigations of Catalytic Properties of *pn* NiO:TiO₂
Composites: Facilitation of Charge Separation, VBO/CBO
Estimation with Type-II Band Alignment at Heterojunctions**

4.1 Introduction

In chapter 3 improvement of visible light activity of TiO₂ by Cu doping is demonstrated. Amount of Cu was varied from (2- 50 mol %). Enhancement of activity was attributed to the role of Cu in +1 and +2 state. As explained in Chapter 1, commonly used strategies to impede the e^-/h^+ recombination of TiO₂ are forming metal-semiconductor interface where metal acts as electron trap centre, improving crystallinity to reduce defects which otherwise acts as recombination centers and generation of internal electric field through *pn* or polymorph junctions [34]. Among these strategies most effective strategy to reduce recombination rate and enhanced visible light absorption of TiO₂ is by formation of *pn* junction. Studies have revealed that synergistic effects prevail between *p* and *n* type semiconductors in composites leading to important electrical, optical properties and improved separation of photogenerated holes and electrons [206–209]. TiO₂ is well known for its photocatalytic activity and it behaves as *n*-type semiconductor due to loss of lattice oxygen. Nickel oxide (NiO) is a *p*-type semiconductor and it is widely used as hydrogenation catalyst [210], gas sensor [211], its indirect band gap is 3.6 eV [212] still it shows absorbance in visible light due to *d-d* transition. A combination of *p* and *n*-type oxides in a composite sample induces *pn* junctions and a generalized proposed mechanism of charge separation over these two oxides is shown in Fig. 1.9 of Chapter 1.

The effect of *pn* junction can be verified using electric voltammetry where the photocurrent would be enhanced under forward bias in the presence of *pn* film [213,214]. Another novel *pn* junction, $\text{Ag}_3\text{PO}_4/\text{BiPO}_4$ photocatalyst was found to enhance photodegradation of methyl orange as compared to individual oxides, ascribed to highly efficient charge separation of photogenerated electron–hole pairs through *pn* heterojunction [215]. NiO based photocatalysts have applications in photodegradation of dyes and pigments [213,216], photocatalytic reduction of hexavalent chromium, $\text{Cr}_2\text{O}_7^{2-}$ in aqueous solution [119,217], photo-degradation of harmful chemicals such as p-chlorophenol or gaseous acetaldehyde under UV light irradiation [218,219]. In spite of extensive investigations on photodegradation and photoreduction reactions, scanty literature on evaluating the potential of NiO and TiO_2 system as a photocatalyst for H_2 generation is available [100,220–222].

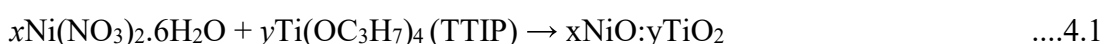
In the present study, efforts were undertaken to prepare almost NiTiO_3 free NiO- TiO_2 composites and after thorough characterization their photocatalytic properties were evaluated in sunlight, visible and UV-visible irradiation for decomposition of water. Nano-composites of NiO- TiO_2 in (1:1) and (0.35:0.65) ratios, NiTiO_3 , TiO_2 and NiO samples were synthesized through sol-gel method at different calcination temperatures. Co-formation of a secondary phase NiTiO_3 and its contribution in photocatalytic activity of NiO- TiO_2 composite is emphasized and supported by DFT calculations. Single phase preparation of NiTiO_3 was also attempted by solid state route by using respective oxides in appropriate quantity. To establish the phase purity/composition, surface morphology, oxidation states, elemental quantification on surface and bulk, optical features, electronic properties, e^-/h^+ recombination profiles, samples were characterized by relevant techniques. Band alignment at heterojunctions of NiO- TiO_2 oxides in composites was proposed here after calculating the valence band offset (ΔE_v) and conduction band offset (ΔE_c). Lifetimes of photoexcited electrons and holes was measured by time-resolved photoluminescence in composites and compared with single

phased oxides, to emphasize the role of *pn* nanojunctions in charge carrier separation. Also, photocatalytic activity was evaluated by monitoring generation of hydrogen from water and methanol mixture in evacuated atmosphere under visible, UV-visible and natural sunlight. Effect of calcination temperature and subsequent formation of NiTiO₃ phase on photocatalytic activity of NiO-TiO₂ nanocomposites was investigated. Sustained H₂ evolution for 60 h under sunlight and 35 h under visible light illumination was observed over most active sample. Apparent quantum efficiency (AQE) and solar fuel efficiencies (SFE) achieved are reported here.

4.2 Experimental

4.2.1 Synthesis

Nanoparticles of oxides TiO₂, NiO, NiTiO₃ and composites, xNiO: yTiO₂ (xmoles: ymoles = 1:1 and 0.35:0.65, abbreviated as NTC11 and NTC36 respectively) were synthesized through sol-gel method by mixing reactants in appropriate stoichiometry as depicted by following equation:



Nickel nitrate hexahydrate, Ni(NO₃)₂·6H₂O (>99% Loba Chemie Pvt. Ltd.), titanium tetraisopropoxide (TTIP, 97 %, Aldrich) and propan-2-ol (AR >99.5 %, SDFCL, s d fine-chem Ltd) were used as received. For typical synthesis of NiO: TiO₂ in 1:1 molar ratio, 3.763 g of Ni(NO₃)₂·6H₂O was dissolved in 50 ml ethanol and 50 ml HNO₃ (5M) to prepare solution A. Another solution referred as B containing 3.85 ml of TTIP and 30 ml of propan-2-ol was also prepared. Solution A was added drop wise to the solution B under constant stirring till a gel was formed. The gel was left overnight undisturbed for nucleation to take place. After nucleation, the gel was heated at two different temperatures viz; 90 °C (LT) and 150 °C (HT) to obtain powder. The as-synthesized powders of composite samples and TiO₂

were further calcined at 500 °C and 600 °C at a heating rate of 5 °C min⁻¹ in air to ensure the uniformity and completion of the reaction. Schematic of synthesis route is shown in Fig. 4.1.

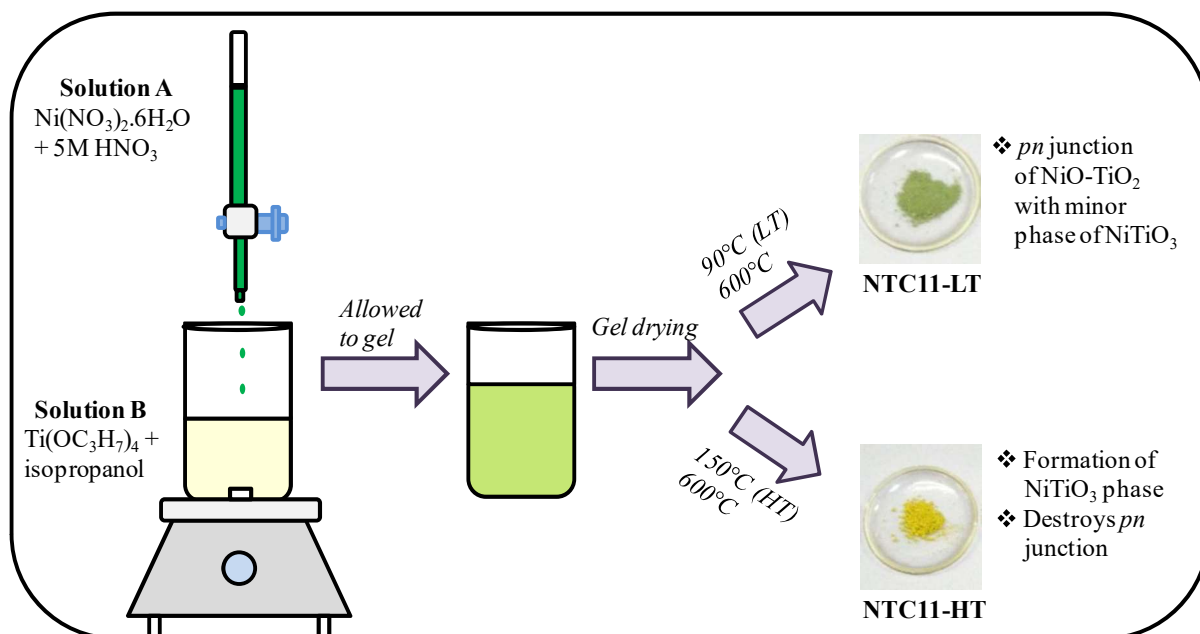


Fig. 4.1 Schematics of synthesis of NTC11 composite by sol-gel route.

Synthesis of single phase NiTiO₃ was attempted by sol-gel and solid state method. The dry powder obtained after sol-gel method in the manner mentioned above was calcined at 600 °C for 10 h and at 850 °C for 5 h to obtain pure NiTiO₃ phase. Equimolar mixtures of NiO and TiO₂ was subjected to grinding of 40 minutes followed by heat treatment of 700 °C for 83 h and further heated to 1000 °C for 78 h for solid state synthesis of NiTiO₃. Sample was grinded at intermediate levels and reaction pathway was monitored by recording powder XRD. Single phase NiTiO₃ oxide prepared by sol-gel and solid state route are abbreviated as NTOsg and NTOss respectively, in the present manuscript. Pure NiTiO₃ was yellow in colour, whereas composite oxides were found to be green in colour. NTC36 is rich in NiTiO₃ phase and therefore has yellow colour unlike green coloured NTC11. A photograph of samples is shown in Fig. 4.1 and Fig. 4.6.

1 % (w/w) Pt was loaded as co-catalyst on NTC11 by photo deposition method. A mixture of 25 ml of water, 5 ml of ethanol and 2.5 ml of H₂PtCl₆·6H₂O (0.002M) was added

to a 100 mg of NTC11. Whole solution was evacuated and irradiated in UV-visible light for 2 h. Then sample was washed to remove chloride ion content and then it was dried in an oven at 100 °C to remove moisture and enhance adhesion of Pt particles on catalyst surface.

4.2.2 Characterization

Powder X-ray diffraction (XRD) patterns were recorded on a Philips diffractometer (model PW 1710), equipped with a graphite monochromator and Ni-filtered Cu-K α radiation using accelerating voltage and current was 35 kV and 20 mA respectively. The crystallite size of different phases was estimated from peak broadening of the diffraction peak of corresponding phase by using Scherrer equation as mentioned in Chapter 2 [223].

Also the weight fraction of anatase is estimated by following formula:

$$f = \frac{100}{(1+1.256I_r / I_a)} \quad \dots 4.2$$

Where f is weight fraction of anatase in sample containing mixture of anatase and rutile phase, I_a & I_r is the intensity of diffraction peak of 101 plane of anatase phase and 110 plane of rutile phase [224] respectively.

XPS experiments were recorded on an electron spectrometer (SPECS, Surface Nano Analysis GmbH, Germany) using Mg-K α X-rays ($h\nu = 1253.6$ eV) as the primary source of radiation with an overall energy resolution of ~ 0.7 eV. The appropriate corrections for charging effects were made with the help of a C $1s$ signal at 284.5 eV. Band offset in the NiO-TiO $_2$ composite was determined by X-ray photoelectron spectroscopy (XPS) using a method given by Kraut et al [225]. Valence band offset (ΔE_v) and conduction band offsets (ΔE_c) at NiO and TiO $_2$ heterojunction was calculated by using the equation 4.3 and 4.4.

$$\Delta E_v = (E_{CL}^{NiO} - E_{VBM}^{NiO}) - (E_{CL}^{TiO_2} - E_{VBM}^{TiO_2}) - \Delta E_{CL} \quad \dots 4.3$$

where E_{CL}^{NiO} and $E_{CL}^{TiO_2}$ are the energy of the NiO and TiO₂ core lines respectively, E_{VBM}^{NiO} and $E_{VBM}^{TiO_2}$ are the energies of the NiO and TiO₂ VBMs respectively. ΔE_{CL} is the energy difference between CL of Ni2p_{3/2} and Ti2p_{3/2} core levels in the NTC11 composite.

The conduction band offset (ΔE_c) was calculated by using following formula:

$$\Delta E_c = (E_{Band\ gap}^{TiO_2} - E_{Band\ gap}^{NiO}) - \Delta E_v \quad \dots 4.4$$

The microstructure was studied using a Zeiss Gemini Plus field emission scanning electron microscope (FESEM) operated at 5 kV. TEM-SAED was recorded on FEI-Tecnai G-20 microscope operating at 200 kV. The source is LaB₆ filament, the HV was at 200 kV. HAADF-STEM (High Angle Annular Dark Field –Scanning Transmission Electron Microscopy) images of NTC11 were recorded using Carl zeiss Libra 200FE TEM microscope. Electron energy loss profile were recorded using incolumn EELS in TEM. N₂-BET surface area was measured with Micromeritics ASAP 2020 V3.01 H analyzer using N₂ as the adsorbing gas. The pore size distribution based on desorption isotherm estimated by using method developed by Barret, Joyner and Halender (BJH) assuming a cylindrical pore model. The elemental analysis of Ni, Ti and Pt present in the oxide samples was evaluated using ICP-OES (*JobinVyon* JY 2000, France). Raman spectra were recorded using 532 nm lines from a diode Nd:YAG laser (power 15 mW) focused to a spot size of ~ 20 μm. The scattered light was analyzed using an indigenously built 0.9 m single monochromator, coupled with a super notch filter and detected by a cooled charge couple device (CCD, Andor Technology). An optical characteristic of all samples was recorded using spectrophotometer of JASCO model V-530 (Japan) with an integrating sphere attachment in scanning range of 200-800 nm at the scanning speed of 200 nmmin⁻¹. Edinburgh Instruments' FLSP 920 system equipped with a 450 W Xe lamp having a Peltier element cooled red sensitive Hamamatsu R955 PMT was used to record PL with a resolution of 3 nm at room temperature. All

emission spectra were corrected for the detector response. Time-resolved fluorescence measurements were carried out using a time-correlated single photon counting (TCSPC) spectrometer (Horiba Jobin Yvon, U.K.). The samples were excited by light pulses from a diode laser source ($\lambda = 267$ nm, repetition rate of 1 MHz for all samples containing TiO₂ and $\lambda = 339$ nm for pure NiO with instrumental response function (IRF) < 0.75 ns), and the fluorescence was detected using a PMT-based detection module (model TBX4).

4.2.3 Photocatalytic activity

Photocatalytic activity of all samples was evaluated under different light illuminations: sunlight, visible and UV-visible light sources as per experimental details given in Chapter 2. For quick reference, photocatalytic activity was evaluated in a rectangular quartz reactor of dimensions (10 x 2.1 x 2.1 cm³, 81 ml, Chapter 2), equipped with a gas sampling port for analysis and an evacuation valve. In all experiments, 0.1 g of catalyst was suspended in water + methanol mixtures (33 % v/v, 15 ml). Reaction mixtures were evacuated before irradiation to provide air free conditions as oxygen acts as an electron scavenger and, on photo-adsorption, blocks the active sites for the reaction [223]. Photocatalysts suspended in water-methanol mixtures were then irradiated under different light sources. In case of experiments under sunlight, samples were photoirradiated for duration of 4-6 hours during the afternoon (10.00-16.00 IST). The evolved H₂ was quantified using a gas chromatograph (model Michro-1100, Netel, India) equipped with a thermal conductivity detector (TCD), a molecular sieve column with argon as the carrier gas was employed in the isothermal temperature mode at 50 °C oven temperature. H₂ bubbles were evolved during sunlight irradiation. The emission spectrum of sunlight, visible light source with wavelengths greater than 400 nm, $\lambda_{\text{max}}=536$ nm (medium-pressure Hg lamp, SAIC, India, 400 W) and UV-Visible light source (medium-pressure Hg lamp, SAIC, India, 400 W) and reaction assembly is shown in Chapter 2. The flux of both sunlight and medium pressure

mercury lamps was measured using a silicon photodiode based light meter LX 1108, Lutron Electronic as mentioned in Chapter 2. Solar flux was measured daily in the peak hours and the average recorded during 11.00-16.00 IST were used for AQE and SFE measurement. Detailed calculations of AQE and SFE are given in Chapter 2.

4.2.4 First-Principles theoretical calculations

Plane-wave based first-principles calculations within the density functional theory (DFT) with projector augmented wave (PAW) [226] potentials using Vienna *Ab-initio* Simulation Package (VASP) code [227] for calculations of ground state electronic properties of NiO (cubic, Fm3m). The PAW potentials used $[2s2p]$ state of O atom, and $[3p3d4s]$ state of Ni atom as valence states. We have used generalized gradient approximation (GGA) for exchange and correlations potential as parameterized by J. P. Perdew, K. Burke and M. Ernzerhof (PBE) [228]. Spin-polarized calculations using GGA+ U_{eff} approach were used, where U_{eff} is the Hubbard parameter and found to be 6.0 eV for NiO. The expansion of electronic wave functions in plane waves was set to a kinetic energy cut-off (E_{cutoff}) of 450 eV for all the structures. The Brillouin-zone was sampled using Monkhorst-Pack k -point mesh [229]. For each structure, optimization was carried out with respect to a k -point mesh and E_{cutoff} to ensure convergence of the total energy to within a precision better than 1 meV/atom. The Methfessel-Paxton technique [230] was used for free energy calculations with a modest smearing of 0.1 eV, which resulted in a very small entropy term (<0.1 meV/atom) in all the cases. The structural relaxations (b/a , c/a ratio and atomic positions) were performed for each structure using the conjugate gradient algorithm until the residual forces on the atom were less than 0.01 eV/Å and stresses in the equilibrium geometry were less than 5×10^{-2} GPa. The total electronic energy and density of states (DOS) calculations were performed using the tetrahedron method with Blöchl corrections [231]. For partial DOS and charge transfer, we have taken Wigner-Seitz radii of Ni and O as 1.32 and 0.92 Å, respectively.

4.3 Results and discussion

4.3.1 XRD

XRD analysis was employed to monitor the progress of synthetic reaction, to identify the crystalline phases present and to determine crystallite size in the final product. XRD powder patterns of the samples calcined at 600 °C are shown in Fig. 4.2. Single phased oxides TiO₂ and NiO prepared under identical conditions are also shown for comparison (Fig. 4.2a and b). As expected TiO₂ calcined at 600°C consisted of both the anatase (A) and rutile (R) phases. XRD lines due to cubic NiO (JCPDS No. 47-1049), tetragonal TiO₂ anatase (JCPDS No. 21-1272) and rutile (JCPDS No. 21-1276) were indexed in the composite samples NTC18, NTC11, NTC36 and NTC63 calcined at 600°C for 10 h. In addition, extra lines appearing at $2\theta = 24.1^\circ, 33.1^\circ, 35.6^\circ, 40.8^\circ, 49.4^\circ, 54.0^\circ, 57.4^\circ$ and 64.1° were also observed in the composite samples. These lines belonged to a secondary phase of NiTiO₃. To evaluate the contribution of NiTiO₃ phase in photocatalytic activity, a pure phase of NiTiO₃ was attempted by synthesized by both sol-gel (sg) and solid state (ss) routes as shown in Fig. 4.2 g-h, respectively. Nickel titanate, NiTiO₃ has a rhombohedral symmetry with lattice parameters $a = b = 5.030$, $c = 13.79 \text{ \AA}$, $\text{vol} = 302.19 \text{ \AA}^3$ (JCPDS Card No. 33-0960). However, preparation by both methods yielded major phase of NiTiO₃ along with NiO and rutile as impurities. There are inherent problems with NiTiO₃ and phase pure product normally is not achieved as reported by many researchers [232,233]. Ruiz-Preciado et al [233] calculated the relative content of impurities (Rutile, NiO) present in each sample prepared by sol –gel and solid state route.

Proportion of secondary phase, NiTiO₃ is higher in NTC36 than observed in NTC11 composite evident by comparing the intensities of XRD lines due to NiTiO₃ phase in curves d and e of Fig. 4.2. A slight peak shift of -0.035° in XRD line at $2\theta = 25.348^\circ$ due to 101 plane of anatase TiO₂ phase was observed for NTC36 oxide as compared to TiO₂ synthesized under

similar conditions as shown in Fig. 4.2. The peak shift may be attributed to the incorporation of Ni ions at Ti site in anatase lattice. NTC18 shows presence of predominately anatase along with minor NiO, NiTiO₃ and rutile phases and whereas NTC63 shows NiO as major phase with NiTiO₃ in substantial amounts, while anatase is in minor phase with insignificant amount of rutile as revealed by the XRD patterns.

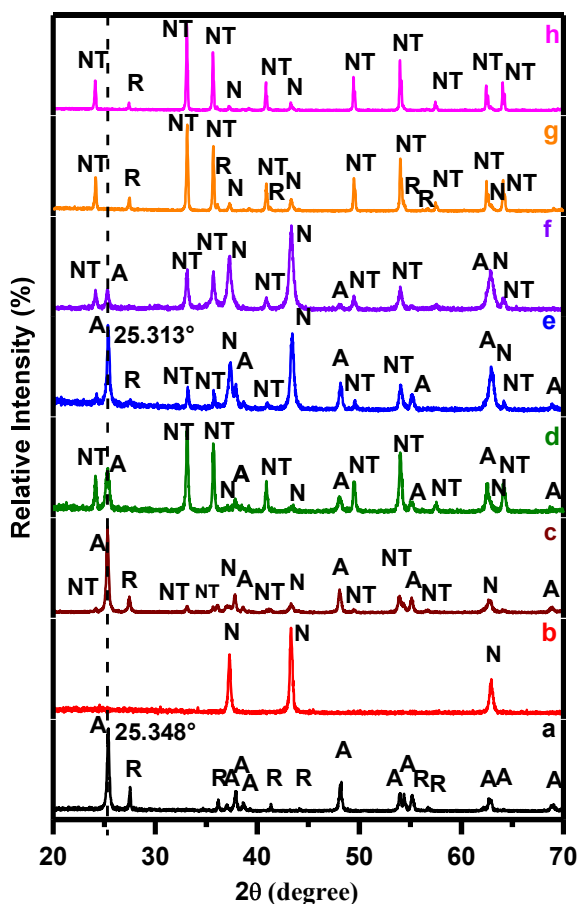


Fig. 4.2 XRD patterns of a. TiO₂, b. NiO, c. NTC18, d. NTC36, e. NTC11, f. NTC63, g. NTOsg and h. NTOss calcined at 600°C. ^A anatase, ^R rutile, ^N NiO and ^{NT} NiTiO₃.

Some authors [201,221] observed that presence of NiTiO₃ as impurity phase, hampers the functioning of *pn* junction of NiO-TiO₂. Co-formation of NiTiO₃ along with nano-junctions is undesirable. Presence of a secondary phase may act as a barrier to effective pathway of charge carriers through *pn* junction. Development of NiTiO₃ phase during preparation of NTC11 depends on gel drying temperature and calcinations as monitored in Fig. 4.3. It is reported that gel drying temperature plays an essential role in determining the

phase composition [234]. Increase in gel drying temperature from 90 °C to 150 °C favours the crystallization of high temperature sintered phase, NiTiO₃ along with small amount of anatase TiO₂, rutile and NiO phases present in the sample, NTC11-HT 600 °C, 10 h (Fig. 4.3d). NTC11 samples obtained after drying the gel at lower temperature, 90 °C and calcining at 500 °C, (referred as NTC11-LT 500 °C, 5 h) yielded anatase rich composition devoid of NiTiO₃ phase (Fig. 4.3a). As calcination temperature increased to 600 °C for 3h duration (sample referred as NTC11-LT 600 °C, 3 h), transformation of anatase to rutile was observed in addition to onset of NiTiO₃ phase (Fig. 4.3b). Further increase in duration to 10 h at 600 °C (referred as NTC11-LT 600 °C, 10 h or NTC11 throughout manuscript), resulted in well crystalline powders composed of anatase TiO₂ and NiO as major phases with weak lines due to NiTiO₃ phase (Fig. 4.3c). Intensity of NiTiO₃ phase in curve c increased at the expense of Rutile and NiO phases (curve b) suggesting that free NiO reacted preferentially with high temperature rutile phase of TiO₂ to form nickel titanate, NiTiO₃. Photocatalytic activities of all these samples calcined under different conditions (Fig. 4.3) were evaluated and discussed later to establish structure-activity correlations. Among all samples NTC11 composite oxide (Fig. 4.3c) was found to be most active. Thus, gel drying temperature of 90 °C and calcination at 600 °C for 10 h are the optimized conditions that offer a well crystalline *pn* nanojunction comprised of NiO and anatase TiO₂ phases (1:1) with minimal amount of NiTiO₃.

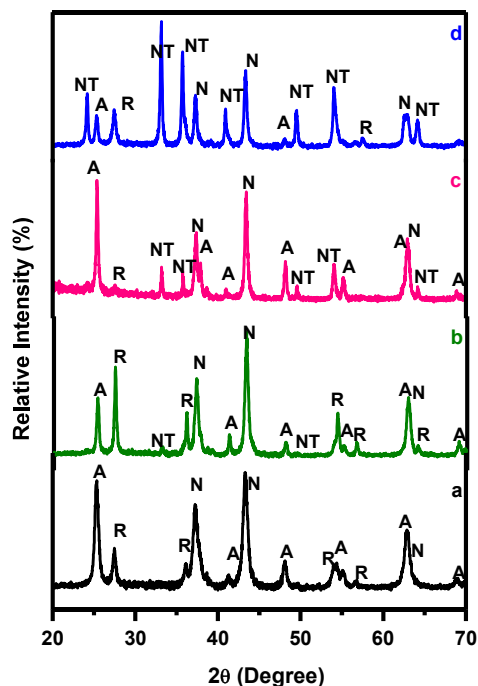


Fig. 4.3 Dependence of phase composition of NTC11 on gel drying temperature and calcination conditions. XRD powder patterns of NTC11 obtained after a. drying the gel at 90 °C (LT) and further calcined at 500 °C for 5 h referred as NTC11-LT 500 °C, 5 h, b. drying the gel at 90 °C (LT) and further calcined at 600 °C for 3h referred as NTC11-LT 600 °C, 3h, c. drying the gel at 90 °C (LT) and further calcined at 600 °C for 10 h referred as NTC11-LT 600 °C, 10 h or throughout the manuscript as NTC11 and d. drying the gel at higher temperature of 150 °C (HT) and was calcined at 600 °C for 10 h referred as NTC11-HT 600 °C, 10 h. ^A Anatase phase of TiO₂, ^R Rutile phase of TiO₂, ^N NiO and ^{NT} NiTiO₃.

The nominal compositions, identification of phases, weight fraction of anatase/rutile and crystallite size estimated from Scherrer equation for different phases present in each sample of Ni-Ti-O oxides along with their abbreviations are given in Table 4.1. The average crystallite size were calculated by Scherrer equation using line width corresponding to *101* plane of anatase TiO₂, *110* plane of rutile TiO₂, *200* plane of NiO and *104* plane of NiTiO₃ phases present in composite and pure oxides. Anatase and NiO crystallites of 20-30 nm, whereas crystallites of 30-45 nm due to NiTiO₃ were present in NTC36 and NTC11 samples as listed in Table 4.1. Increase in crystallite size from 17.9 nm to 43.5 nm with increase in calcination temperature from 500 °C to 600 °C respectively, was observed for pure phase of anatase TiO₂. Also, from Table 4.1 it is revealed that the presence of NiO has restricted the growth of anatase crystals upto ~23 nm in NTC36 and ~31 nm in NTC11 as compared to

large crystallites of ~43 nm observed for pristine TiO₂ calcined at 600 °C. Samples of NiTiO₃, NTOsg and NTOss consisted of highly sintered crystallites with 80-81 nm and 141-143 nm size, respectively (Table 4.1). It is well reported that traditional synthetic procedures yield large NiTiO₃ particles with low surface areas and pore volumes due to inherent problems such as high reaction temperature and heterogeneous solid phase reactions [201,235,236]. The relative ratio of anatase/rutile present in TiO₂ calcined at different temperatures and NiTiO₃ samples prepared by both routes (NTOss and NTOsg) and composite oxides (NTC36, NTC11), were calculated using equation mentioned in experimental section and listed in Table 4.1. The TiO₂ crystallized completely in anatase phase after calcinations at 500 °C; however 25 % of it got transformed into rutile after calcinations at 600 °C as listed in Table 4.1. However the transition of anatase into rutile was inhibited by presence of NiO in NTC36 and NTC11 composite samples, evident by weak peak of rutile phase at $2\theta = 27.4^\circ$, amounting to 13.9 % (Table 4.1). Absence of noticeable rutile peak in NTC36 cannot be explained by above reason of phase transition inhibition as very small amount of free NiO is present in NTC36. The presence of strong XRD lines due to NiTiO₃ phase in NTC36 sample (Fig. 4.2d) without any peaks due to free rutile TiO₂ and NiO phases, suggests a possibility of swiping away of whatever amount of rutile TiO₂ formed preferentially by NiO to react and produce high temperature sintered NiTiO₃ phase at 600 °C. As content of free NiO increases in the composite sample the transition (anatase → rutile) reaction is inhibited and crystallization of derogatory phase NiTiO₃ decreases. Presence of NiO in NTC11 inhibits the transformation of anatase into rutile phase and stabilizes the TiO₂ in anatase phase is in agreement with work reported by other researchers [217,237]. Possibly, slow heating of gel and availability of greater fraction of Ni ions during synthesis of NTC11, restricted the crystallization of adverse phase, NiTiO₃ and liberated the free NiO and TiO₂

phases, in contrast to what was observed in NTC36 where the reaction pathway leads to formation of substantial amounts of NiTiO₃ phase.

Table 4.1 Nominal compositions, abbreviations, weight fraction of anatase/rutile and crystallite size calculated using Scherrer equation in different samples is listed below

Sample	Abbreviation	Weight [#] fraction of Anatase (%)	Weight fraction of Rutile (%)	Crystallite size (nm)*			
				Anatase (<i>hkl</i> ₁₀₁)	Rutile (<i>hkl</i> ₁₁₀)	NiO (<i>hkl</i> ₂₀₀)	NiTiO ₃ (<i>hkl</i> ₁₀₄)
NiO: TiO ₂ (0.35:0.65 molar ratio)	NTC36	100	-	22-23.2	-	\$	44.9
NiO: TiO ₂ (1:1 molar ratio)	NTC11	86.1	13.9	27.5-31.5	\$	23.1-28.7	31.9
NiTiO ₃ sg	NTOsg	-	Minor phase	-	98.6	83.2	80-81
NiTiO ₃ ss	NTOss	-	-	-	-	-	141-143
TiO ₂	TiO ₂ – 500 °C	100	-	17.9	-	-	-
	TiO ₂ – 600 °C	75	25	43.5	68.0	-	-

[#]Using formula expressed by equation no. 4.2 given in experimental section.

*Crystallite size was calculated of individual phases in each sample considering the most intense line of the corresponding phase present in each sample.

[§]Crystallite size was not calculated due to poor intensity of NiO peak (*hkl*₂₀₀) and rutile TiO₂ peak (*hkl*₁₁₀).

4.3.2 N₂-BET surface area and porosity

N₂-BET surface area, mean pore size diameter and cumulative pore volume of pristine TiO₂ is compared with composites of NiO and TiO₂ calcined at 600 °C. The comparative data is listed in Table 4.2. Composite sample, NTC11 and NTC36 have shown enhanced surface area of 29.6 and 19 m²g⁻¹ respectively, and as compared to 10 m²g⁻¹ of TiO₂. The pore size distribution and cumulative pore volumes of both the samples are shown in Fig. 4.4. TiO₂ is microporous with binodal distribution with maximas at 1.8 and 1.9 Å (Fig. 4.4a). However, these micropores coagulate to mesopores on composite formation with NiO. Mesopores in range of 11-150 Å with maxima at ~34 Å in NTC11 and still larger mesopores in range of 50-150 Å with maxima at 90 Å in NTC36 (Fig. 4.4b-c) were observed.

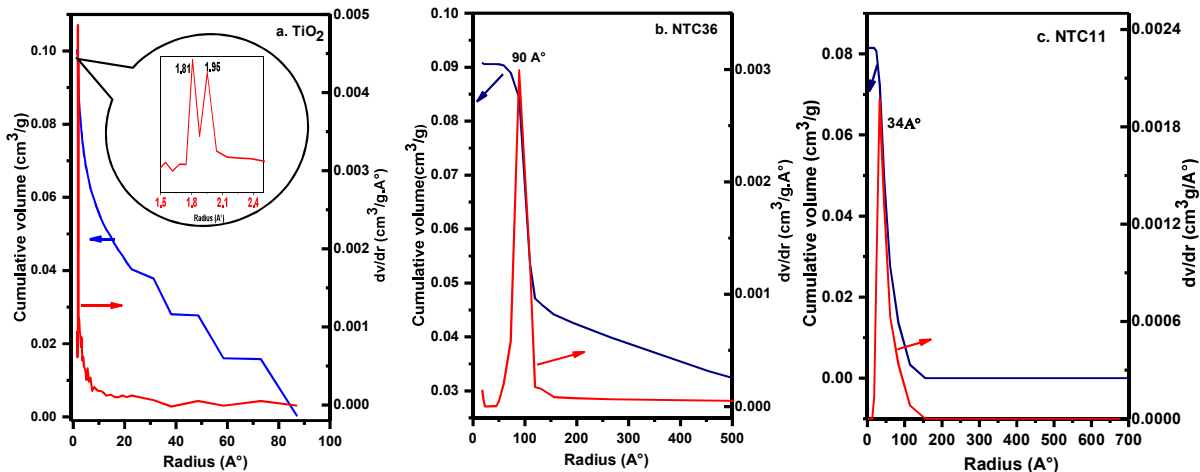


Fig. 4.4 BJH pore size distribution and pore volume curves of a. TiO₂ b. NTC36 and c. NTC11. V_{pore} is shown by blue and dv/dr by red curves. Inset shown in ‘a’ is enlarged view.

A decrease in cumulative pore volume from 0.1005 cm³g⁻¹ (TiO₂) to 0.09 cm³g⁻¹ and 0.08 cm³g⁻¹ in NTC36 and NTC11, respectively was observed (Table 4.2). Calcination temperature plays a very important role in deciding the resultant surface areas and porosity of oxides. Melian et al [221] observed that surface areas of Ni/Ti oxides was between 374-470 m²g⁻¹ was slashed by 74 % when calcined at 400 °C and by 90 % at 550 °C. Similarly, pore volume of samples reduced to 0.1 cm³g⁻¹ from 0.3 cm³g⁻¹ for temperatures above 550 °C. The reduction in surface areas above 500°C coincides with emergence of the high temperature phases such as rutile and NiTiO₃ at the expense of more dispersed forms such as NiO, affecting the morphological properties adversely.

Table 4.2 Particle size, surface area and porosity of oxides.

Sample	Particle size from TEM (nm)	Specific Surface area (N ₂ -BET) (m ² /g)	BJH pore size distribution	Pore Volume (cm ³ /g)
TiO ₂	-	10.24	Microporous binodal narrow distribution with peaks at (1.8 and 1.9 Å)	0.1005
NTC36	36-40 (maxima)	19	Mesopores in range of 50-150 Å with distribution maxima at 90 Å	0.09
NTC11	25-30 (maxima)	29.6	Mesopores in range of 11-150 Å with distribution maxima at 34 Å	0.08

4.3.3 Raman spectroscopy

Fig. 4.5 shows Raman spectra of pure phases TiO_2 , NiO , NiTiO_3 and compared with composite oxides, NTC11 and NTC36. According to factor group analysis, anatase TiO_2 has six Raman active modes predicted by group theory and they appear at 144 (E_g), 197 (E_g), 399 (B_{1g}), 513 (A_{1g}), 519 (B_{1g}) and 639 cm^{-1} (E_g) marked as # in Fig. 4.5 [184]. The two peaks of doublet (513 and 519 cm^{-1}) merges to one peak at 516 cm^{-1} at room temperature [184]. E_g , 144 cm^{-1} is the most intense and sharp vibration mode and others are weak vibrations. The rutile phase of TiO_2 has a weak band $\sim 143 \text{ cm}^{-1}$. Rutile has four Raman active fundamentals, while anatase has six Raman active fundamentals [184]. Thus, the spectrum corresponds to anatase without features of rutile phase. XRD pattern of TiO_2 shows partial conversion of anatase to rutile at 600°C, while in Raman spectrum (Fig. 4.5), modes due to rutile phase are not observed in presence of anatase because of its poor scattering efficiency. Similarly, a Raman profile of other pure oxide, NiO was recorded and shows a characteristic broad band at $\sim 500 \text{ cm}^{-1}$ in Fig. 4.5 [238]. This band originates due to the strong phonon-magnon interaction at nanoparticles surface or some defects, which compete with the magnetic ordering of the nanoparticles [238]. Raman modes of another highly crystalline compound NiTiO_3 are marked as * in Fig. 4.5 appearing at 192, 230, 247, 291, 345, 395, 465, 614, 707 and 757 cm^{-1} [239]. The ten Raman active modes are assigned considering the C_{3i}^2 symmetry and $R\bar{3}$ space group of rhombohedral NiTiO_3 powders. The bands are sharp and intense confirming the highly crystalline nature of NiTiO_3 phase obtained as a result of solid state route calcined at 1000 °C. These were compared with Raman spectra of composite oxides, NTC36 and NTC11. It was observed that characteristic peaks of anatase phase were present in NTC36 and NTC11 composites along with weak peaks of NiTiO_3 phase in agreement with XRD results. However, the most intense mode of NiTiO_3 which appeared at 707 cm^{-1} was not

observed in NTC11 but was present in NTC36. Signature peaks due to NiO or rutile were not observed in Raman spectra of composites due to poor scattering efficiencies of the phase.

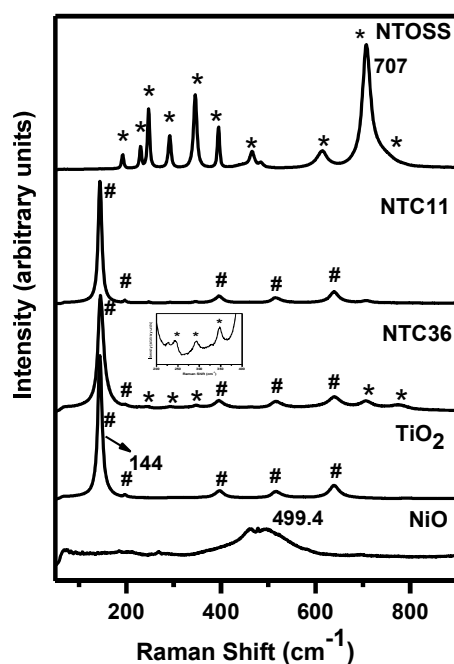


Fig. 4.5 Raman spectra of simple oxides NiO, TiO₂ compared with their composite binary oxides NTC36, NTC11 and single phase compound oxide, nickel titanate oxide was prepared by solid state route, NTO_{ss}. * NiTiO₃ phase, # anatase phase of TiO₂.

4.3.4 DRS

Diffuse reflectance spectrum of white TiO₂ is compared with coloured composite oxides in Fig. 4.6. Here, like coloured oxides have shown similar absorption spectra. Presence of NiO has enhanced light absorption properties of composite samples in visible region. The two composite oxides, NTC11 and NTC36 show disparity in their colours. NTC11 is green colored, however, NTC36 is bright yellow, similar to NTO_{sg} and NTO_{ss} oxides. Excluding TiO₂ (band gap ~3.2 eV), spectra of all other samples shows extended absorption in visible light; along with this a noticeable shift in absorption edge towards higher wavelengths was also observed. Band gap of all samples is calculated considering Ti edge tabulated in Table 4.3.

Table 4.3 Band gap calculated for different Ni/Ti oxides using Kubelka-Munk function.

Sample	Band Gap (eV) Calculated by Ti band edge
TiO ₂	3.20
NTC36	2.82
NTC11	3.18
NTOsg	3.17
NTOss	3.17
NiO	3.60

Band gap of black coloured, NiO is 3.6 eV yet; it shows absorption in visible region because of presence of vacant $3d$ states of Ni above valence band which extends the photoresponse in visible region. DRS of NTC11 appears to be an overlap of absorption spectra of both NiO and TiO₂. The DRS spectra shown in curves b, d, e corresponding to NTC36, NTOsg and NTOss, respectively are similar in nature and sample colour. The peaks at 374, 450, 743 nm and shoulder at 511 nm appearing in these spectra are characteristic peaks of NiTiO₃ phase and are prominent for nickel titanate, NTOsg and NTOss. 374 nm attributed to the $O^{2-} \rightarrow Ti^{4+}$ charge transfer interaction. $Ni^{2+} 3d^8$ band situates between conduction band formed due to $3d$ orbitals of Ti^{4+} and valence band formed due to oxygen $2p$ orbitals [240]. Hence, charge transfer transition $Ni^{2+} \rightarrow Ti^{4+}$ occurs at lower energy compared to $O^{2-} \rightarrow Ti^{4+}$ charge transfer transition. 450 and 511 nm due to the crystal field splitting of $3d^8$ band of Ni^{2+} ions into two sub-bands called the $Ni^{2+} \rightarrow Ti^{4+}$ charge transfer (CT) bands. It also shows absorbance at 743 nm as indicated by its yellow colour [241]. NiO and NiTiO₃, phases were simulated by DFT using VASP software to understand the contribution of valence orbitals of different atoms in valence band and conduction band and to explain the observed absorption properties. DRS of NTC11 and NTC36 samples was also recorded after use in photocatalytic activity tests as shown in curves g and h respectively, revealed that light absorption properties of composites, were unaltered after irradiation and therefore can be reused.

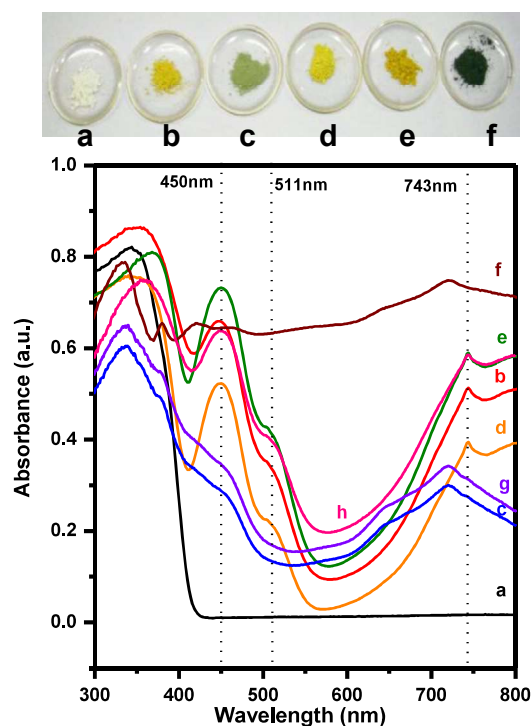


Fig. 4.6 Diffuse reflectance UV-visible spectra of a. TiO_2 , b. NTC36, c. NTC11, d. NTOsg, e. NTOss, f. NiO g. Used NTC11 and h. Used NTC36. Dotted lines (---) are characteristic transitions due to NiTiO_3 phase.

4.3.5 Photoluminescence spectroscopy

Photoluminescence (PL) spectra of Ni/Ti oxides are shown in Fig. 4.7, reveals the course of electron and hole produced after absorption of light. From PL data, TiO_2 shows a broad emission peak in range of 355 to 530 nm with maximum peak at 427 nm recorded at excitation wavelength at 280 nm. This is related to band edge emission and shoulder at 448 nm is associated with defect/trap emission in TiO_2 [242–244]. Peak intensity is found to decrease in all oxides containing Ni ions. Ni acts as a quenching agent. PL spectra of composites NTC11 and NTC36 differ in both peak positions and profiles also. In case of NTC11, there is a broad peak (355-530 nm) with peak maximum at 427 nm corresponding to band edge emission of TiO_2 , followed by weak emissions coinciding with NiO peaks. However, unlike NTC11, the PL profile of NTC36 matches with NiTiO_3 . NiTiO_3 shows a broad emission same as TiO_2 but with a peak maximum shifted from 427 nm to lower wavelength of 412 nm. The peaks at 412 nm and 553 nm were observed in NTC36, NTOsg

and NTOss (marked in Fig. 4.7). In cases of NTC36, NTOsg and NTOss, the half widths at maximum intensity are less than that of TiO₂ or NTC11. NiO shows very poor luminescence at 450, 532, 644 and 666 nm upon photo-excitation at 365 nm as shown in Fig. 4.7.

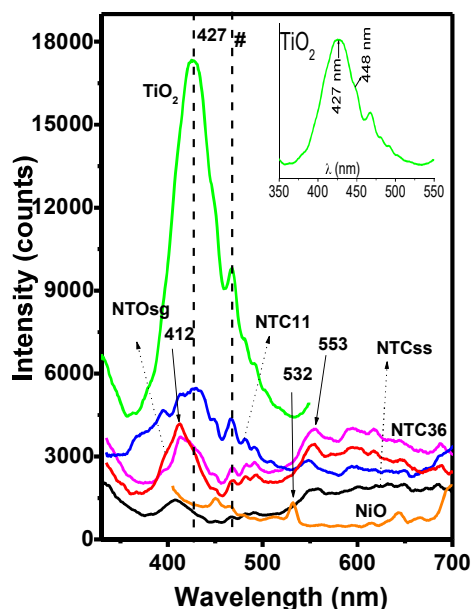


Fig. 4.7 Photoluminescence spectra of different Ni-Ti oxides. #Artefact: instrumental peak due to lamp change at 467 nm.

Maximum activity of NTC11 for production of H₂ is related to broad range of absorption/emission from UV to visible. Preparation route has affected the PL intensity. NTO prepared by sol-gel route has shown intense emission as compared to solid state route prepared oxide. The PL signals attenuate with increasing calcination temperature for both types of NiTiO₃, in good agreement with literature reports [244]. It is also reported that the light absorption also decreases distinctly with increasing calcination temperature. Therefore, it is difficult to reveal the intrinsic change of photoluminescence signals with sintering.

Photoluminescence decay curves of Ni/Ti oxides upto 110 ns are shown in Fig. 4.8a. Excitation and emission wavelengths for all samples except NiO were monitored at 267 nm and 427 nm, respectively. NiO was excited using 339 nm to yield emission at 532 nm. Decay profile of all samples apart from NiO is shown in Fig. 4.8b upto 20 ns. Here, decay data is shown upto 20 ns because about 75 % of decay is completed within 20 ns. Data are fitted

with mono-exponential equation. Typical monoexponential fitting to data of TiO₂ and NTC11 are shown in Fig. 4.8c, e, respectively. Lifetimes of 0.91, 0.90, 0.92, 1.02 and 0.68 ns were observed for TiO₂, NTC11, NTC36, NTOsg and NiO, respectively. NiO gives least value of lifetime among them. Lifetime values of other samples are almost unchanged within error bar of 0.10 ns. 75 % decay takes place within 20 ns, beyond that (25 % decay data) upto 110 ns was fitted with tri-exponential equation. Triexponential fitting of TiO₂ and NTC11 is shown in Fig. 4.8d, f respectively.

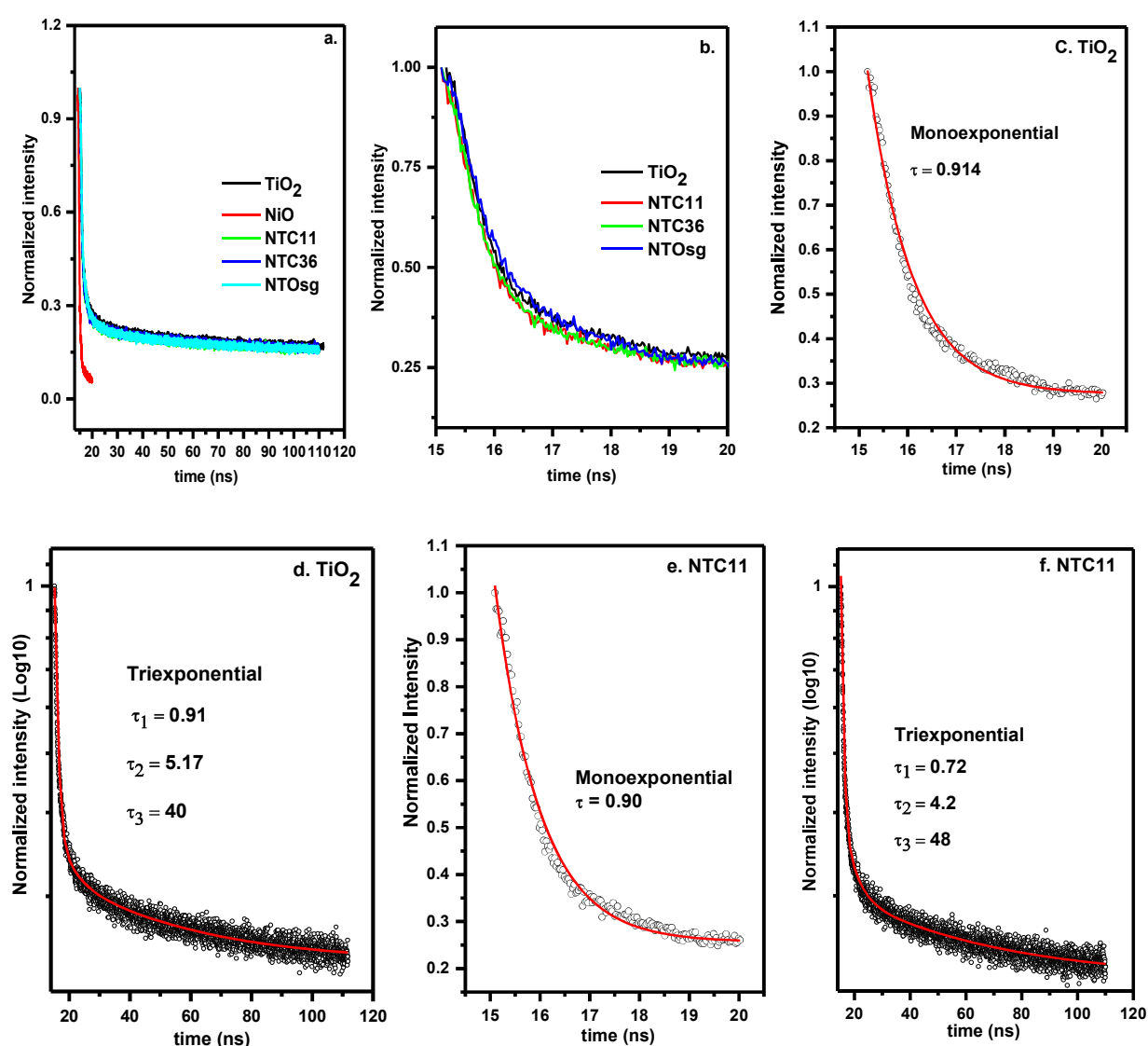


Fig. 4.8 a. Luminescence decay curves of TiO₂, NiO, NTC11, NTC36, NTOsg upto 110 ns. b. decay curves of TiO₂, NTC11, NTOsg, NTC36 up to 20 ns. Mono-exponential fitting to data of c. TiO₂, e. NTC11 up to 20 ns. Tri-exponential fitting to data of d. TiO₂, f. NTC11 up to 110 ns.

Fitting parameters are given in Table 4.4. The shortest lifetime ($\tau_1 < 1$ ns) is related to the band-band edge e^-/h^+ recombination [243]. The medium lifetime ($\tau_2 = 4-5$ ns) will be related to the presence of self-trap below conduction or Ti-O charge transfer in TiO_6 unit. The longer component (τ_3) in lifetime (>39 ns) will be related to oxygen defects in particles. The τ_1 contributed about 75% and remaining two components (τ_2, τ_3) contributed about 14 % of decay data. τ_2 has about 98%, whereas τ_3 has 2% contribution in 14% of decay data. Decay is much faster for NiO as compared to others. It is because Ni d^8 electrons are paramagnetic and also NiO is antiferromagnetic [245], which quenched luminescence. Rate of recombination of e^- and h^+ is fast over pure NiO. It is quite obvious that photogenerated e^- recombines with h^+ instantaneously at all three sites (τ_1, τ_2 , and τ_3) of NiO as compared to other samples. Lifetimes of 0.91 ns in TiO_2 is similar to 0.90 in NTC11 suggesting that band edge recombination which is contributing to 75 % decay is governed by presence of TiO_2 and not by NiO despite the fact that free NiO is available in equal proportion as TiO_2 in NTC11. Similarly, τ_2 originating from recombination reaction at self trap states is also same as TiO_2 . However, τ_3 is 39 ns in TiO_2 , 48 ns and 47 ns in NTC11 and NTOsg respectively, and 59 ns in NTC36 much higher than NiO of 11 ns.

Table 4.4 Parameters derived from fitting of decay profile (upto 110 ns) of different samples using tri-exponential decay equation.

Parameters	Samples				
	TiO ₂	NTC11	NTC36	NTOsg	NiO
τ_1 (ns)	0.91	0.72	0.72	0.86	0.5
τ_2 (ns)	5.2	4.2	5.0	4.2	1.0
τ_3 (ns)	39	48	59	47	11
X ² (goodness of fitting)	0.986	0.989	0.989	0.990	0.985

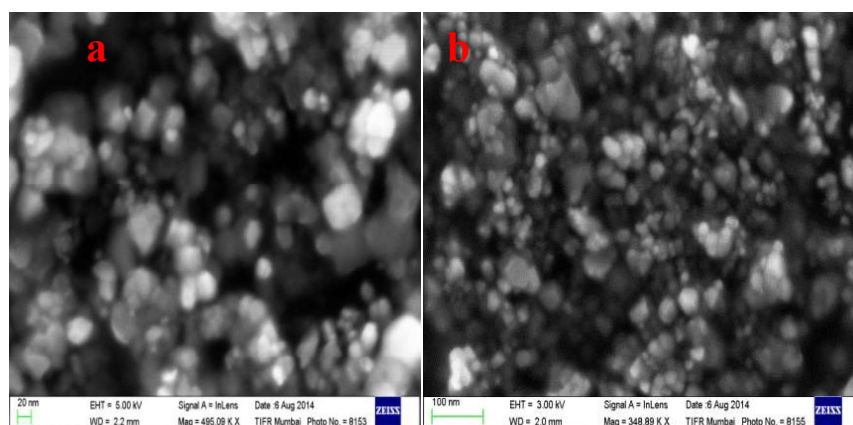
By proportion itself and by characterization results, it is evident that free NiO is substantially present in NTC11 than NTC36. Thus, it is expected that presence of PL quencher in NTC11 composite will enhance the recombination. However, it was observed that lifetime τ_1, τ_2 and τ_3 has increased from 0.5 ns, 1.0 ns and 11 ns observed in pure NiO to

0.72 ns, 4.2 ns and 48 ns in composite NTC11, respectively (Table 4.4). Among the NTC36 and NTC11, τ_1 and τ_2 are comparable; however, τ_3 is higher for NTC36. The recombination reaction at oxygen defects is quantified as τ_3 . This implies NTC11 has more of oxygen vacancies due to multiphasic nature of NTC11 relative to NTC36 in which NiTiO₃ phase predominates. The grain boundary between two phases acts as sites for e^- and h^+ recombination. Thus, more the grain boundaries higher will be the rate of recombination reaction. This implies coexistence of TiO₂ with NiO in any form has helped in delaying the recombination reaction considerably.

4.3.6 Surface morphology

FESEM micrographs along with EDX patterns and backscattered images for composite samples, NTC11 and NTC36 are shown in Fig. 4.9. FESEM images reveal agglomerates, inside which shape and dimensions of particles can be deciphered. Upon comparing Figures it can be noticed that size of the particles in sample NTC11 is more homogeneous as compared to NTC36. From these images, however, it is difficult to distinguish NiO from TiO₂ as all particles exhibits are of similar morphology with particle size varying in the range of ~ 15-20 nm. Distinctly large nearly spherical particles of nearly 50 nm size were observed in NTC36 (highlighted by red outline in Fig. 4.9c-d). The XRD results and crystallite sizes of individual phases estimated by Scherrer equation, listed in Table 4.1 suggests the emergence of highly sintered NiTiO₃ as secondary phase under the stated experimental conditions. This phase is more dominant in the NTC36 composite sample as compared to NTC11. Thus, large particles prominently present in NTC36 (outlined in red) are possibly belonging to NiTiO₃ phase. However, FESEM images of NTC11 are devoid of such large particles. It is known that large particles of NiTiO₃ with poor surface areas and porosity are produced by conventional synthetic routes, due to inherent problems such as high reaction temperature and heterogeneous solid phase reactions [201,235,236]. Lopes et al

[239] reported characterization of NiTiO₃ powders prepared by polymeric precursor method after thermal treatment at different temperatures for 2 h in air atmosphere and investigations by SEM, revealed that the NiTiO₃ powders, heat treated between 600 °C and 1000 °C, present a mean distribution of the particle in the range of 94–306 nm. Backscattered electrons (BSE) from NTC11 and NTC36 samples were imaged and are shown in Fig. 4.9e-f, respectively. BSE are used to detect contrast between areas with different chemical compositions thus can provide information of distribution of different phases. Apparently, NTC11 have shown almost uniform distribution of individual phases present in the sample in concurrence with TEM images. Aggregation or segregation of any phase was not observed in backscattered FESEM image of NTC11. Thus, it appears that NiO and TiO₂ are uniformly distributed in NTC11 without segregation of either phase. NiO and TiO₂ may not be distinguished by BSE due to similar molecular weight. However, backscattered image of NTC36 shows prominence of two phases represented by bright and dark field. EDX patterns show that intensity of peaks due to Ni relative to Ti increases from NTC36 to NTC11 (Fig. 4.9g-h).



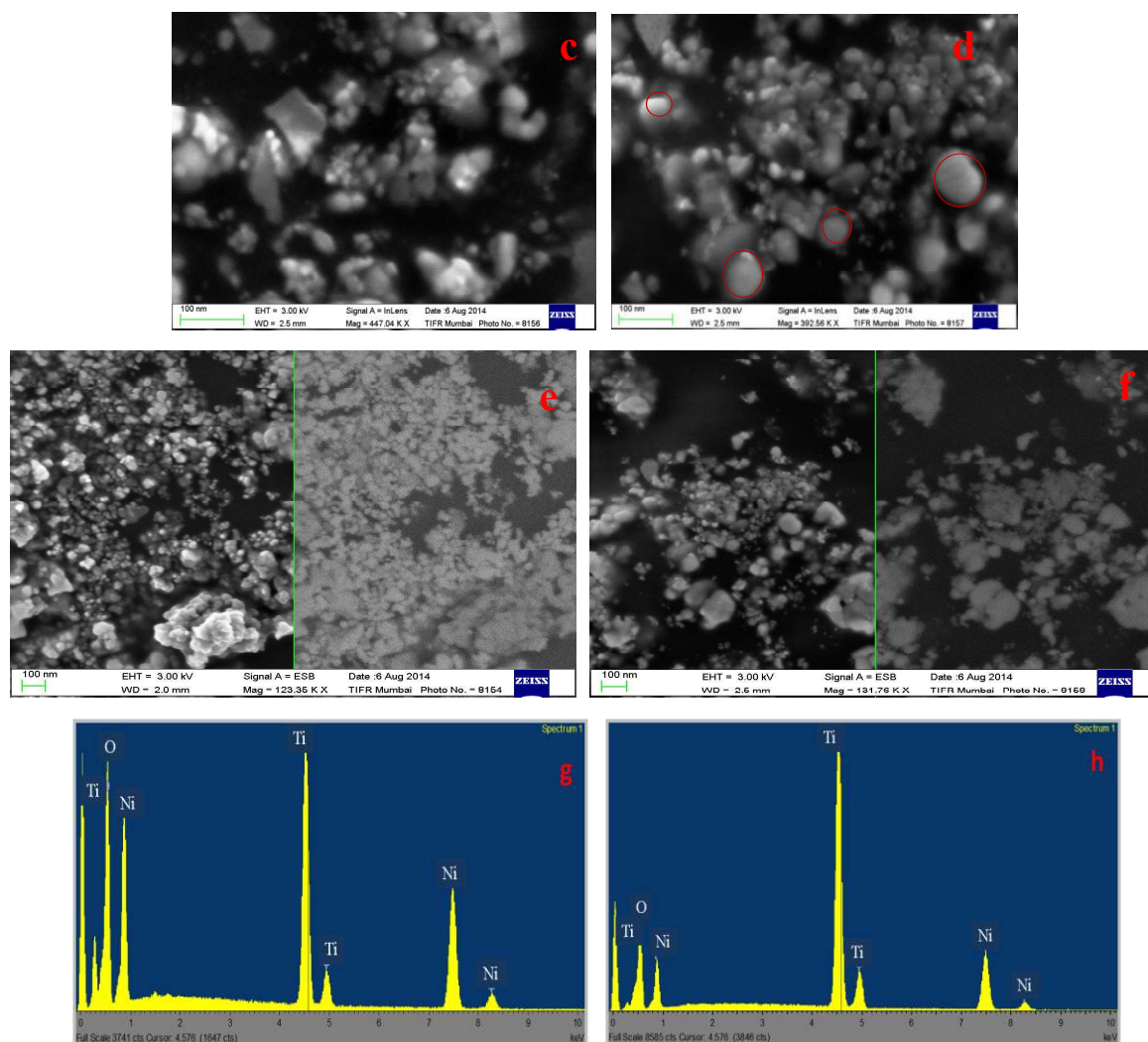


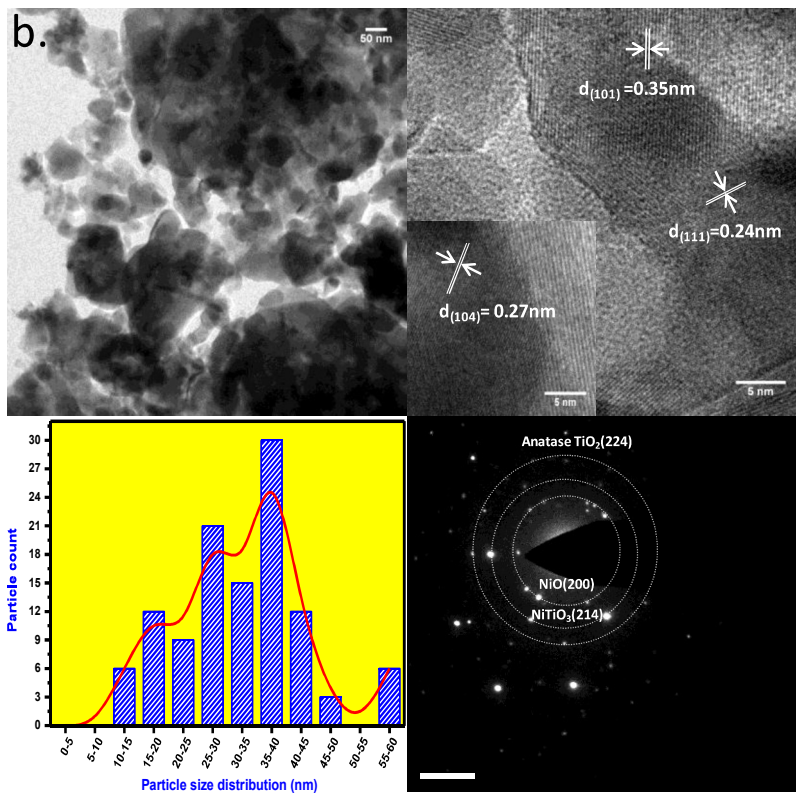
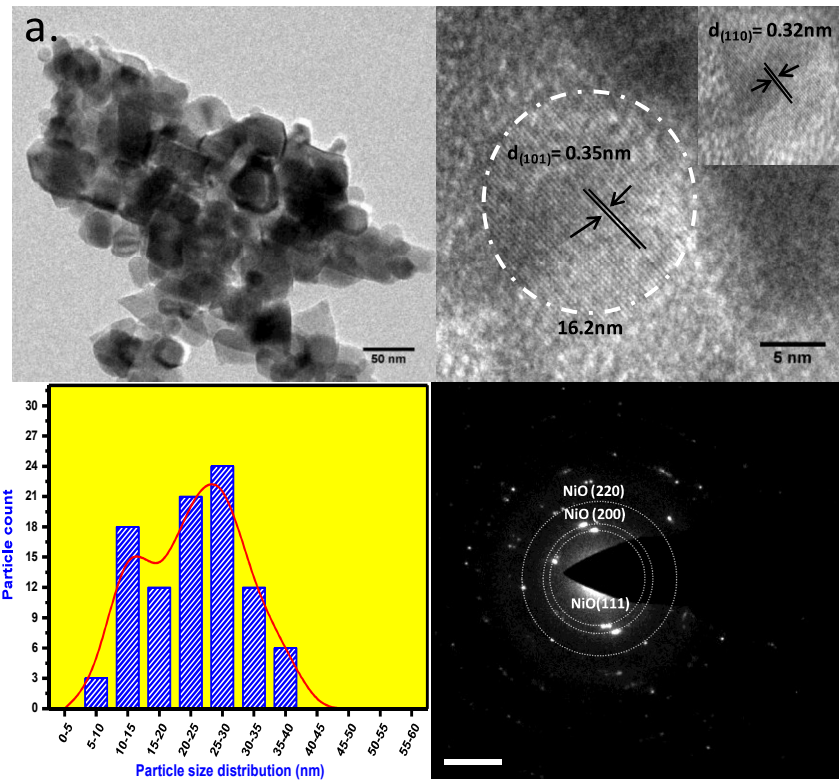
Fig. 4.9 FESEM images at different accelerating voltages for NTC11(a- b) and NTC36 (c-d). Backscattered image of NTC11 (e) and NTC36 (f). EDX of NTC11 (g) and NTC36 (h).

Bulk composition was determined by EDX and ICP-OES and was in agreement within experimental error ($\pm 5\%$) with the calculated values for both the composites in Table 4.5.

Table 4.5 Bulk elemental analysis of Ni, Ti and Pt for different composites using EDX and ICP-OES compared with calculated values.

Sample	ICP-OES (mol %)				EDX (mol %)			Calculated values (mol %)			NiO/TiO ₂
	TiO ₂	NiO	Pt	NiO/TiO ₂	TiO ₂	NiO	NiO/TiO ₂	TiO ₂	NiO	Pt	
Pt(1%w/w)/NTC11			0.3							0.4	
NTC11	50.2	49.85		0.99	50.51	49.49	0.98	50	50		1
NTC36	62.39	33.6		0.54	68.9	31.11	0.45	65	35		0.54

Low and high resolution TEM images with particle size distribution and SAED patterns are shown in Fig. 4.10a and b for NTC11 and NTC36, respectively. Low resolution image shows agglomeration of particles. Faceted particles with proper boundaries could be resolved within agglomerates. HR-TEM images reveal that the material is highly crystalline, as depicted by well defined lattice fringes. A high resolution image of NTC11 reveals lattice fringes with fringe width of 0.35 nm and 0.32 nm belonging to *101* plane of anatase and *110* plane of rutile phase of TiO₂, respectively. Particle size observed from TEM data was similar to the crystallite size obtained from XRD which reveals that each grain corresponds to single crystallite [246]. Particle size distribution (PSD) derived from low resolution image of NTC11 (Fig. 4.10a) suggests maximum number of particles falls in range of 10-30 nm, while distribution shifts towards higher particle size in NTC36 (Fig. 4.10b) with majority of particles more than 30 nm in size. Unlike NTC36, NTC11 comprises of very small particles also, say 5-10 nm and is devoid of very large particles of 50-55 nm. HR-TEM of NTC36 nanoparticles (Fig. 4.10b) shows lattice fringes with d-spacing of 0.35, 0.27 nm and 0.24 nm which corresponds to *101* plane of anatase, *104* plane of NiTiO₃, *111* plane of NiO phase, respectively. Diffused rings with dotted pattern forms SAED of NTC11 and NTC36 revealing nanocrystalline nature of these powders. These patterns were indexed and found to consist of phases in agreement with XRD results. HAADF – STEM images of NTC11 were recorded at low and high magnification (Fig. 4.10c(i-iv)). Bright and dark contrast in HAADF image arises due to difference in average atomic number corresponds to TiO₂ and NiO, respectively. Electron energy loss spectroscopy (EELS) at selected positions from adjacent particles showed presence of peaks due to Ti and Ni, respectively (Fig. 4.10cii). The chemical identification using EELS suggested that NiO and TiO₂ are in close proximity to each other (ciii-civ).



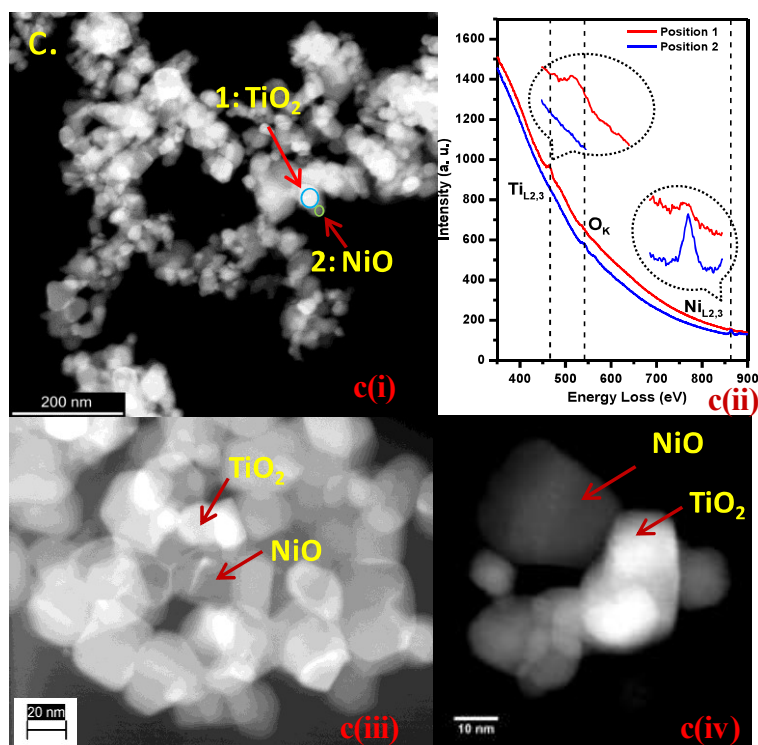


Fig. 4.10 TEM, HR-TEM images, SAED pattern and particle size distribution are shown in clockwise direction for (a) NTC11 (b) NTC36 and (c) low (i) and high (iii-iv) magnification STEM-HAADF images of the NTC11 sample along with EELS (ii) of the selected area indicated as positions 1 and 2. Bright and dark contrast in HAADF image arising due to difference in average atomic number corresponds to TiO_2 and NiO respectively.

4.3.7 XPS

XPS survey spectrum indicates presence of Ni, Ti, O and C elements with photoelectron peaks appearing at binding energies 853 (Ni $2p_{3/2}$), 872 (Ni $2p_{1/2}$), 458 (Ti $2p_{3/2}$), 464 (Ti $2p_{1/2}$), 529 (O $1s$) and 285 eV (C $1s$). Typical binding energy values observed for different elements are tabulated in Table 4.6.

Table 4.6 Binding energy values derived from XPS study of TiO_2 , NiO, NiTiO_3 , fresh and used composite Ni-Ti oxides.

Sample	Binding Energy (eV)							
	O $1s$	Ti $2p_{3/2}$	Ti $2p_{1/2}$	Ni $2p_{3/2}$		Ni $2p_{1/2}$		C $1s$
				Main peak	Satellite peak	Main peak	Satellite peak	
TiO_2	529.27, 530.92	457.98	463.69	-	-	-	-	284.47
NiO	529.22, 531.06, 534.01	-	-	853.81, 855.78	860.92	872.8	879.63	284.53

NTC36	529.12, 531.0	457.53, 459.29	463.55	854.43, 856.20	861.11	872.67	879.60	284.47
NTC11	529.72, 531.53	457.76 459.43	463.84	853.72, 855.56	861.08	872.99	879.94	284.49
NTO sg	530.58,5 31.61	458.65	464.31	856.01	862.20	873.70	880.43	284.50
NTC36 used	529.47, 531.43	458.02, 459.37	463.81	854.79, 855.74	861.39	872.67	879.48	284.53
NTC11 used	529.88, 531.65	457.59, 459.02	463.64	854.20, 855.9	861.40	872.85	880.32	284.48

Fig. 4.11a shows high resolution XPS spectra of Ni ions present in different samples. The XPS spectrum of NiO is quite complex and is deconvoluted to yield peaks at 853.81, 855.78, 860.92 eV in the Ni $2p_{3/2}$ region (Fig. 4.11b) and 872.8 and 879.63 eV for Ni $2p_{1/2}$ region. The first two peaks at 853.81, 855.78 eV are attributed to multiplet splitting of Ni $2p_{3/2}$ [247], 860.92 and 879.63 eV are satellite peaks of Ni $2p_{3/2}$ and Ni $2p_{1/2}$ respectively. The broadening of the main line and the satellite is due to interactions of the central Ni atom with either neighbouring NiO₆ octahedra or with oxygen-deficient defects [248]. The deconvoluted Ni $2p$ XPS spectrum of composite oxides NTC36 and NTC11 is shown in Fig. 4.11c and d respectively, to reveal the multiple peaks due to Ni²⁺, at positions observed for free NiO. The spectrum confirmed the existence of NiO with Ni at +2 oxidation state in composite samples. However, for the NTC11, the first multiplet appears with lower intensity as compared to free NiO. The homogeneous distribution of TiO₂ molecules around NiO in NTC11 has probably affected the multiplet intensity of Ni $2p$. This suggests the co-existence of NiO and TiO₂ in composite material, NTC11. In case of nickel titanate, NTOsg, comparatively a sharp peak at 856.01 eV was observed corresponding to symmetric octahedral environment around Ni ions situated in cubic unit cell of NiTiO₃. The oxidation state of Ni and Ti ions in used NTC11 sample were same as fresh sample, confirming the chemical stability of the composite oxides after photocatalytic activity tests. Ni/Ti ratio is maintained, however, O/M ratio has increased due to adsorption of water molecules, affecting the multiplet intensity (Fig. 4.11d-e).

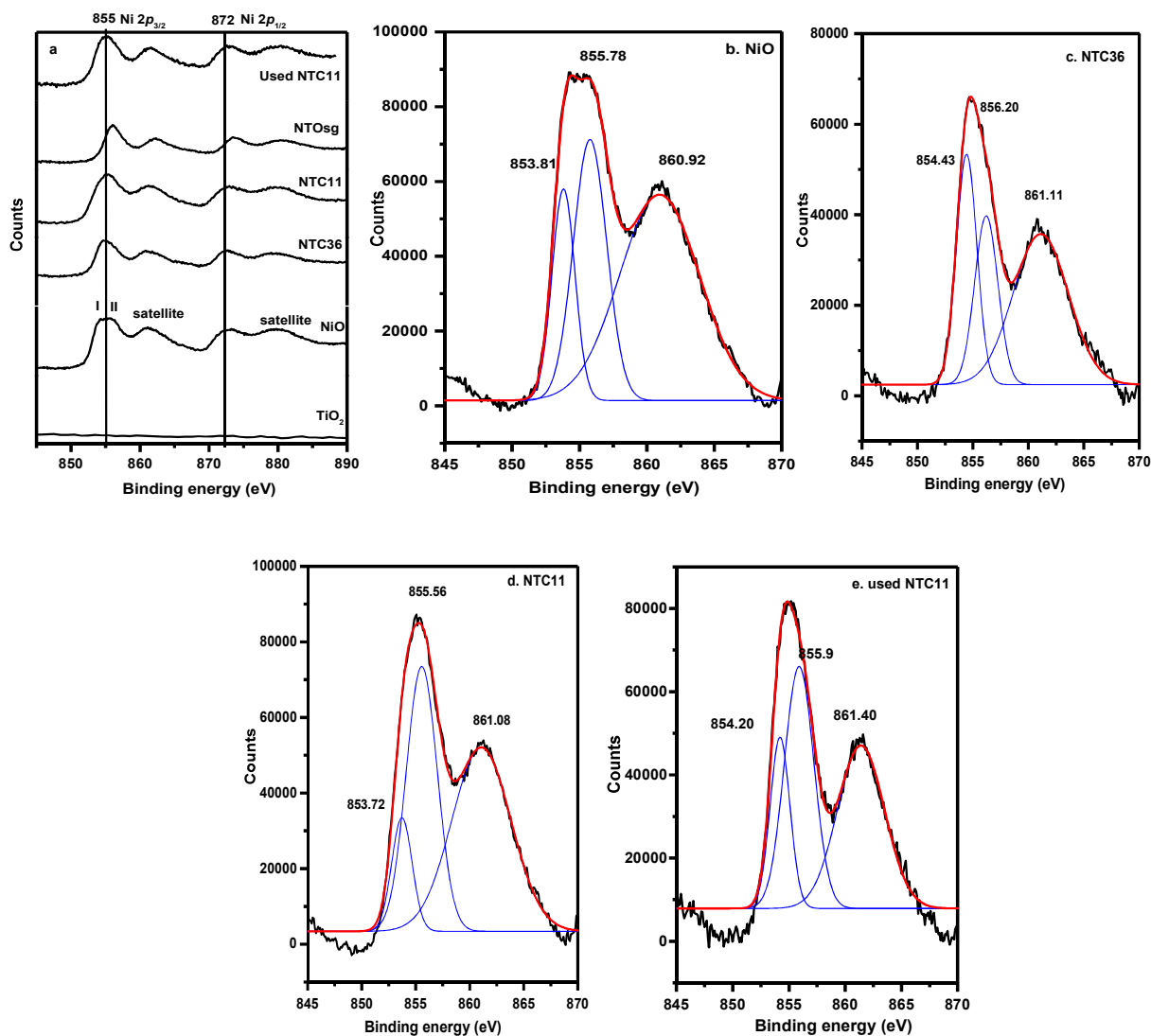


Fig. 4.11 a. Overlay of XPS spectra corresponding to Ni $2p_{3/2}$ and Ni $2p_{1/2}$ lines for different samples. Deconvulation of Ni $2p_{3/2}$ peak in b. NiO c. NTC36 d. NTC11 and e. used NTC11. ^I and ^{II} are multiplets due to Ni $2p_{3/2}$.

BE values in the range of 455.1 to 461.0 and 461.0 to 467.2 eV (Fig. 4.12a) for Ti $2p_{3/2}$ and $2p_{1/2}$ respectively, in the range of 526.9 - 537 eV (Fig. 4.12b) for O1s and from 281.15 - 287.6 eV (Fig. 4.12c) for C 1s core levels for TiO₂, NiO, NTC11 and fresh and used NTC11 can be seen. These values confirm that Ti is in the +4 state in both TiO₂ and Ni-Ti oxides [192]. Ti $2p$ XPS spectrum was deconvulated to reveal the contribution of Ti⁴⁺ ions from different phases as shown in Fig. 4.12a. Ti $2p$ peak shifts by 0.67 eV on crystallization into NiTiO₃ (NTOsg) phase (Fig. 4.12a) as compared to anatase TiO₂ attributed to different local environment experienced by Ti ions in NiTiO₃ lattice [249]. As obvious, the intensity of

Ti $2p$ XPS signal decreased in NTC11 as compared to NTC36 in accordance with the proportion of Ti content present in each sample. As explained above the expected bulk composition of composite oxides, NTC11 and NTC36 were found to be in agreement with the experimental values analysed using ICP-OES results (Table 4.5). However, the elemental composition on surface of individual photocatalysts was derived from XPS (Table 4.7).

Table 4.7 Elemental compositions derived from XPS study of fresh and used composite Ni-Ti oxides.

Sample	Chemical composition (atom %)				
	Ti	Ni	O	[Ni]/[Ti]	[O]/[M] M= Ti+Ni
TiO ₂	24.8	-	75.2	-	3.0
NiO	-	19.92	80.08	-	4.02
NTC36	20.67	5.05	74.27	0.24	2.9
NTC11	11.15	10.61	78.24	0.95	3.6
NTO sg	13.70	7.60	78.70	0.55	3.7
NTC11 used	10.20	9.80	80.0	0.96	4.0

The surface concentration of [Ni]/[Ti] was 0.24 in NTC36, lower than the ideal value 0.54. While, it was found to be 0.95 in case of NTC11 which is in close agreement with the expected value of 1.0. This suggests that surface of NTC36 unlike bulk, is rich in Ti and deficient of Ni ions. For, NTC11, the composite character of bulk is extended upto surface and Ni and Ti metal ions are homogeneously distributed over the surface of NTC11. This explains how the multiplicity of Ni $2p$ spectrum is affected in NTC11. Thus, XPS investigations revealed that surface properties of NTC11 composite oxide are more favourable for the photocatalytic activity as compared to NTC36. The metal ions act as active sites for adsorption of water molecules. For, used NTC11 oxide the ratio is same as fresh sample within experimental error, suggesting that surface composition after photoactivity tests has not varied. Thus, leaching of the Ni or Ti metal ions from the surface of the photocatalyst did not occur during the activity evaluation. O $1s$ peak obtained from pristine

TiO₂, NiO as well as Ni-Ti oxides could be resolved mainly in two spectra using a gaussian fit as shown in Fig. 4.12b to yield a major peak at ~529 eV and another one at ~531 eV. The secondary peak was assigned to –OH⁻ (hydroxy) species present on the surface in addition to bulk oxide (O²⁻) species [192]. In case of NiO, the broad O1s peak is resolved in three peaks at 529.22, 531.06 and 534.01 eV. The additional peak at 534.01 eV observed in NiO spectrum is arising from chemisorbed oxygen containing species from either water, oxygen, CO or CO₂ [250]. The surface concentration of [O]/[Ti] in pristine TiO₂ from Table 4.7 exceeds the ideal value of 2 and in case of NiO also, it is ~4 ideally should have been 1. Thus, indicating that surface is rich in oxygen which can be explained by presence of adsorbed hydroxy species in the form of Ti(OH)₄ linkages where required [O]/[Ti] is 4 on surface of TiO₂. Presence of additional chemisorbed oxygen on surface of NiO explains the exceptionally high observed [O]/[Ni] ratio. Further, increase in [O]/[M] (where M = Ni + Ti) concentration of used NTC11 sample indicated that Ni-Ti-O oxides offers more active sites for adsorption of water molecules.

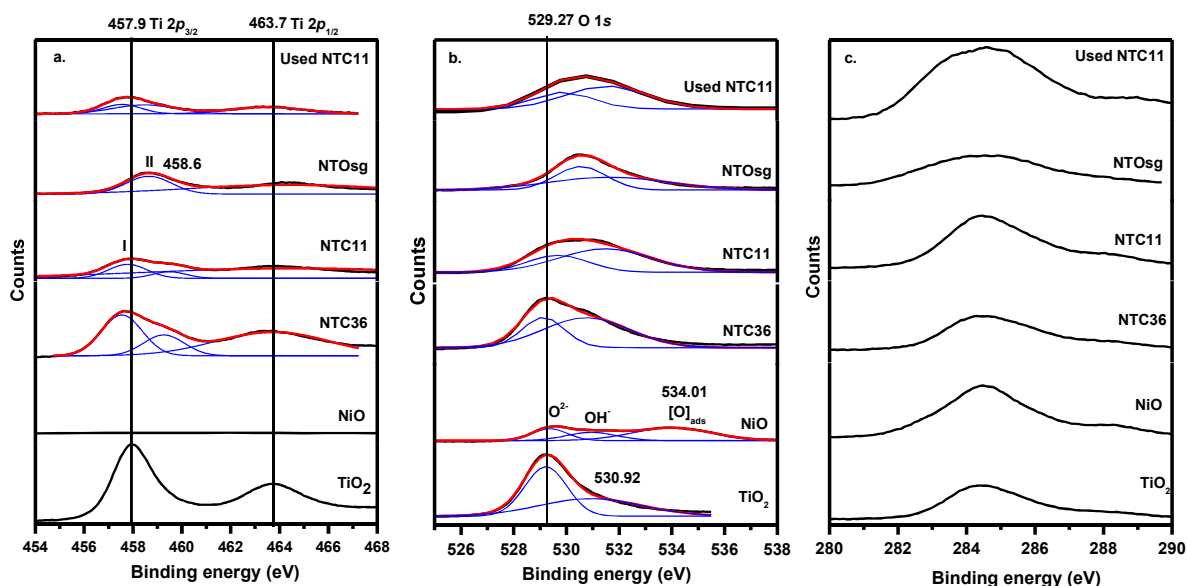


Fig. 4.12 Overlay of XPS spectra corresponding to a. Ti 2p b. O 1s and c. C 1s lines for different samples. Broad peaks were deconvoluted to relatively quantify various oxidation states of an element present in a sample.^I Anatase and ^{II} NiTiO₃.

4.3.8 Photocatalytic activity

Photocatalytic activities of *pn* semiconductors, NTC36 and NTC11 was evaluated under different sources of light (Fig. 4.13-4.16) and compared with individual oxides, NiO, TiO₂ and NiTiO₃. 100 mg of photocatalyst was suspended in a mixture of water and methanol (2:1 v/v), irradiated in sunlight, UV-visible and exclusively visible light source under evacuated conditions. H₂ yield, AQE, SFE achieved over different samples under different light sources and conditions is tabulated in Table 4.8. Fig. 4.13a, b show hydrogen yield in μmol obtained over Ni-Ti oxides in sunlight and medium pressure mercury light source with UV-visible photoemission, respectively. Hydrogen yield increased linearly with irradiation time. No evolution of hydrogen gas was detected in dark. Also evolution of H₂ bubbles was observed in evacuated conditions under sunlight irradiation. Evacuation before irradiation is favorable to get maximum hydrogen yield [223]. The decreasing order of photocatalytic activity of samples calcined at 600 °C in sunlight is as follows: NTC11 (H₂ @ 20.4 $\mu\text{mol/h}$) > NTC18 (H₂ @ 5.17 $\mu\text{mol/h}$) > TiO₂ (H₂ @ 2.5 $\mu\text{mol/h}$) ~ NTC36 (H₂ @ 2.34 $\mu\text{mol/h}$) > NTOsg (H₂ @ 1.52 $\mu\text{mol/h}$) > NTC63 (H₂ @ 1.36 $\mu\text{mol/h}$) > NTOss (H₂ @ 0.22 $\mu\text{mol/h}$) and under UV-visible illumination is as follows: NTC11 (H₂ @ 84 $\mu\text{mol/h}$) > NTC18 (H₂ @ 51.28 $\mu\text{mol/h}$) > TiO₂ (H₂ @ 29.1 $\mu\text{mol/h}$) ~ NTC36 (H₂ @ 24.5 $\mu\text{mol/h}$) > NTOsg (H₂ @ 10 $\mu\text{mol/h}$) > NTOss (H₂ @ 1.8 $\mu\text{mol/h}$) > NTC63 (H₂ @ 0.88 $\mu\text{mol/h}$) > NiO (H₂ @ 0.4 $\mu\text{mol/h}$), respectively. The trend shows that composite, NTC18 consisting of higher proportion of TiO₂ has performed reasonably well, with activity higher than parent TiO₂, but lower than NTC11. However, NiO rich composite, NTC63 has shown NiO like poor activity. Thus, both composites, NTC63 and NTC18 have shown performance, corresponding to the predominant phase. The poor activity of NTC36 is attributed to presence of derogatory, NiTiO₃ phase in dominance in this sample. Thus, ideal composition for exploiting the role of *pn* junctions is 1:1 in present study. Similarly, Parida et al. [251] investigated NiO/Ta₂O₅

composites with varying molar ratio of both the oxides and it was found that 1:3 was most active due to formation of *pn* junctions and minimum hindrance from the secondary phase, NiTa₂O₆ developed.

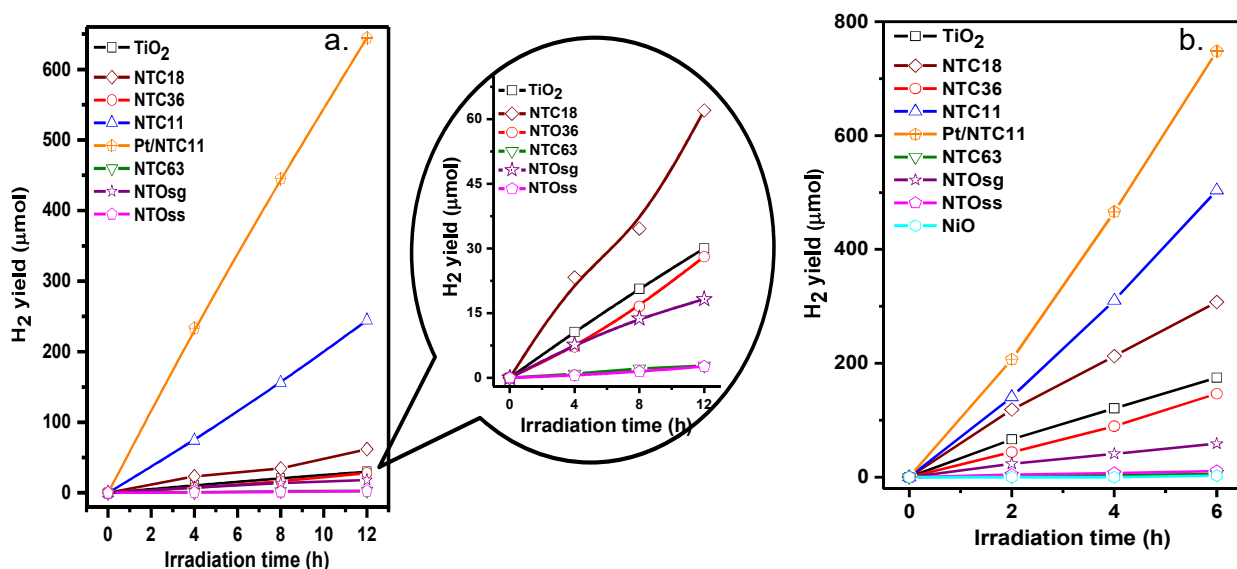


Fig. 4.13 a. H₂ yield monitored over TiO₂, NTC18, NTC36, NTC11, Pt/NTC11, NTC63, NTOsg and NTOss under a. sunlight during 10:00-16:00 h IST, b. UV -visible irradiation.

Composite NTC11 has performed considerably better than individual pure oxides such as nickel titanate and nickel oxide under different light sources. However, photocatalytic activity of NTC36 is poor than TiO₂. Among all these samples, maximum photocatalytic activity was observed for NTC11 with H₂ generation rate of 204 μmol/h/g and 840 μmol/h/g of hydrogen yield with apparent quantum efficiency 2 % and 5.3 % in sunlight and UV-Vis irradiation, respectively. To enhance the hydrogen yield, 1 % (w/w) Pt was loaded as co-catalyst over NTC11 by photodeposition method. Pt provides sites for H⁺ reduction by photogenerated electrons trapped due to schottky barrier. Pt(1 % w/w)/NTC11 photocatalyst liberated H₂ @ 537 μmol/g/h (Fig. 4.13a) with AQE of 5.4 % under sunlight irradiation and 1250 μmol/g/h (Fig. 4.13b) with AQE of 7.8 % (Table 4.8) under UV-visible light irradiation.

Table 4.8 Typical values of photocatalytic H₂ yield, apparent quantum efficiencies (AQE) and solar fuel efficiency (SFE), obtained over different Ni-Ti oxides irradiated under different conditions.

Sample	Activity (μmol/h)			Illumination Area (cm ²)	AQE (η, %) (UV-Visible)	AQE (η, %) (Sunlight)	SFE (%)
	UV-Visible light	Sunlight	Visible light				
NTC36	24.5	2.34	-	20	1.52	0.2	
NTC11	84	20.4	30.56, η = 1.6%	20	5.3	2.0	
NTOsg	10	1.52	-	20	0.61	0.15	
NTOss	1.8	0.22	-	20	0.11	0.02	
1%(w/w) Pt/NTC11	125	53.7	-	20	7.8	5.4	0.8
TiO ₂	29.1	2.5	-	20	1.82	0.25	
NiO	0.4	-	-	20	0.03		

Stability of composite photocatalysts NTC11 and Pt/NTC11 was also established under sunlight for 60 h over same 100 mg of sample (Fig. 4.14).

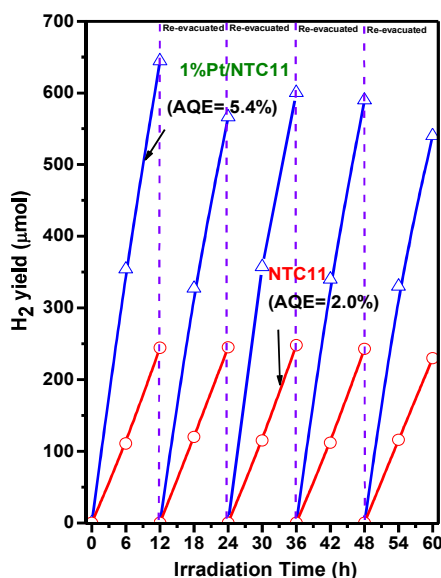


Fig. 4.14 Recyclability of photocatalytic H₂ generation over NTC11 and Pt/NTC11 evaluated for 60 h by irradiating the sample under sunlight. (Experimental conditions: 100 mg of photocatalyst was suspended in water + methanol (33 % v/v), evacuated and illuminated under sunlight for duration of 6 h in a day during afternoon (10.00-16.00 IST) and H₂ yield was monitored for 10 days with intermittent evacuation after 12 h of irradiation).

Linear H₂ evolution was observed over Pt/NTC11 upto 60 h under sunlight at an average rate of 490 μmol/g/h with standard deviation of (+/- 2.7 %). Sustained H₂ evolution without any deterioration in photocatalytic activity was found for 60 h. Methanol which was initially added, sufficed for the complete activity test of 60 h. So, intermittent addition of sacrificial reagent was not required.

Further, to establish the visible light activity exclusively, the performance of NTC11 was also evaluated for 35 h under visible light lamp with λ_{max} at 536 nm without UV emission (inset of Fig. 4.15). H₂ evolution @ 306 μmol/g/h with AQE of 1.6 % was constantly observed for 35 h over NTC11 (Fig. 4.15) under visible light. Thus, visible light activity and stability of NTC11 is established under both sunlight and visible light illumination. XPS results, have established that the *pn* composites retain the chemical and compositional stability on surface after photocatalytic reduction of water to H₂.

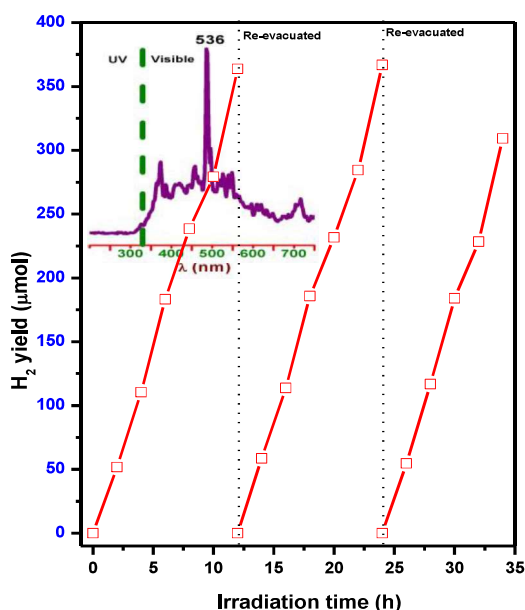


Fig. 4.15 Visible light activity of NTC11 was established by monitoring H₂ yield for 35 h under medium pressure mercury lamp emitting wavelengths longer than 400 nm (λ_{max}= 536 nm). Emission spectrum is shown in inset. Experimental conditions: 100 mg of photocatalyst was suspended in water + methanol (33% v/v), evacuated and illuminated under visible light source for 35 h with intermittent evacuation at regular intervals.

Calcination temperature and phase compositions were very critical and found to determine the overall hydrogen yield. Photocatalytic activities of all the samples prepared with varying heat treatment discussed above (XRD of samples are shown in Fig. 4.3) were evaluated and shown in Fig. 4.16 to establish structure-activity correlations.

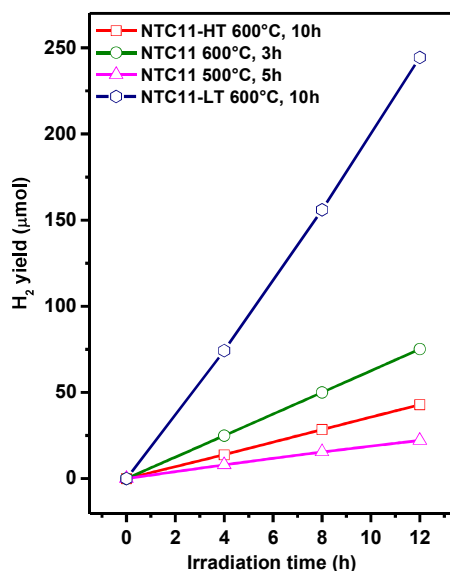


Fig. 4.16 Effect of calcination temperature and crystallinity on photocatalytic properties was investigated by evaluating photocatalytic H₂ yield over a NiO and TiO₂ composite in 1:1 composition synthesized under varying heat treatment conditions corresponding to samples shown in Fig. 4.3.

The decreasing trend in activity was NTC11-LT 600 °C, 10 h > NTC11-LT 600 °C, 3 h > NTC11-HT 600 °C, 10 h > NTC11-LT 500 °C, 5 h. The fall in activity coincides with the appearance of NiTiO₃ phase. To verify the results, a sample of NiTiO₃, synthesized by solid state was tested and found to result in poor photocatalytic H₂ yield @ of 2.2 and 18.0 μmol/g/h in sunlight and UV-visible light irradiation, respectively (Fig. 4.13a and b). NiTiO₃ phase has shown lowest activity among all Ni-Ti oxides under investigation in all conditions. Low activity of NTC11-LT calcined at 500 °C is attributed to poor crystallinity of anatase TiO₂ and cubic NiO phases present in sample (Fig. 4.3a) as compared to the 600 °C calcined sample. From the trend, it is observed that activity increases with increase in crystallinity of the NiO and TiO₂ phases. Thus, both crystallinity and presence of NiTiO₃ phase determined

the overall H₂ yield. Among all samples maximum photocatalytic hydrogen yield was observed over NTC11 or NiO-TiO₂ (1:1) - LT calcined at 600 °C for 10 h with H₂ yield @ 204 μmol/g/h under sunlight (Fig. 4.3c) persistent upto 60 h. Presence of NiTiO₃ phase is minimal in NTC11, and therefore resulted in maximum activity in line with our other results. Thus, gel drying temperature of 90 °C and calcination at 600 °C for 10 h are the optimized conditions that offer a well crystalline *pn* nanojunction comprised of NiO and anatase TiO₂ phases (1:1) with minimal amount of NiTiO₃.

4.4 DFT

It was important to understand the electronic properties and band structure of individual oxides constituting the composites. The electronic properties of TiO₂ are well studied where distorted tetragonal lattice imparts favourable photocatalytic properties to anatase TiO₂ [65]. First principles DFT based band structure calculations were performed on single phase rhombohedral, NiTiO₃ and reported by Banerjee et al [201] which revealed that strong intermixing of Ni -3*d* with O -2*p* orbitals occurred in the valence band of NiTiO₃ and resulted in generation of a pseudo band gap at 1.36 eV. This pseudo band gap might act as hindrance and may contribute in weakening the intensity of electronic transition due to Ni²⁺ → Ti⁴⁺ charge transfer. The highlights of these calculations are mentioned in experimental section. The inactivity of ilmenite NiTiO₃ was also attributed to its structure consisting of a pseudo close packed hexagonal array of O²⁻ ions with two thirds of the octahedral sites of any basal plane occupied by identical cations in an ordered hexagonal net [236]. Owing to this geometry the oscillator strength for the charge transfer transitions, Ni²⁺ → Ti⁴⁺ becomes too weak to have an acceptable photoresponse in visible light.

Since NiO shows spin polarized calculations, the electronic structure of NiO was calculated using VASP code in order to clarify the distribution of valence states of Ni, O atoms near Fermi level and to understand the role of NiO in modifying the photocatalytic

properties and enhancing the visible light activity of *pn* nanocomposites with TiO₂. Fig. 4.17a show calculated band structures of NiO along a few high-symmetry directions; while Fig. 4.17b show total as well as site- and *l*- projected partial density of states (DOS) for NiO. The lowest unoccupied state (LUMO) are found at G -point (0, 0, 0) and X point (0, 1, 0) in the conduction band whereas the highest occupied state (HOMO) are found at point L (½, ½, ½) in the valence band as shown in Fig. 4.17a. The O-2*p* states in the valence band show a sharp peak near the Fermi level representing its localized nature. The strong optical transitions are due to flat bands from valence band to conduction band (shown by arrows in Fig. 4.17a) and these are found along L to G point, W to X point, from G - X to G point and G - X to X point. These transitions from highest occupied (HOMO) states in valence band to the unoccupied states (LUMO) in conduction band are at different k vector and exhibit a consistent band gap of about 3.0 eV. Thus, NiO is an indirect band gap material (Fig. 4.17a). The calculated E_g (band gap) of 3.0 eV is not consistent with the reported optical band gap (3.6 eV) due to limitations of the calculations performed here. The Fig. 4.17b shows the contribution of individual orbitals of Ni and O in formation of valence band and conduction band. Positive and negative *n*(E) corresponds to the majority and minority spin states, respectively. This convention has been used in all other DOS plots (Fig. 4.17b). Since NiO- shows spin polarized calculations, net magnetic moment was found to be 2.0 Bohr magneton. Near E_f, fermi level O-2*p* and Ni-3*d* states dominate show strong hybridization. Ni-4*s* states contributes in the middle region of valence band at around -3 eV where contribution from O-2*p* states is smaller. The position of conduction band is dictated by Ni-3*d* states. The valence band consists of mainly O-2*p*, Ni-4*s* and 3*d* states (Fig. 4.17b), while the conduction band is mainly comprised of Ni-3*d* states. The O 2*p* states contribute considerably to the Density of states near Fermi level, whereas the Ni 3*d* and 4*s* just make the contributions in lower and mid part of valence band, respectively.

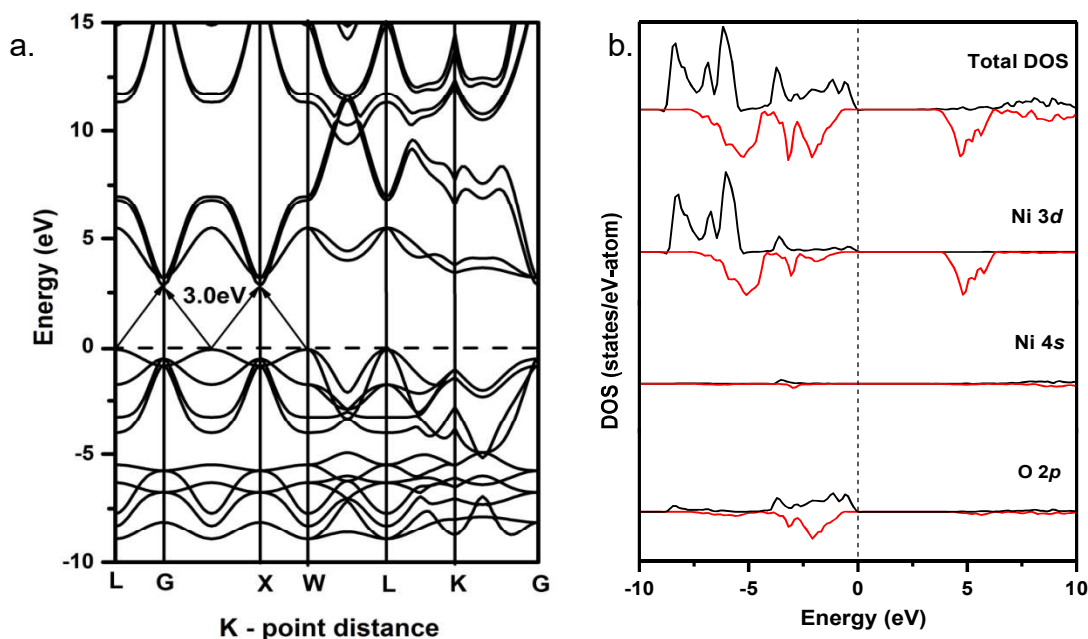


Fig. 4.17 a. Band structure of NiO along high-symmetry L ($\frac{1}{2}, \frac{1}{2}, \frac{1}{2}$), G (0, 0, 0), X (0, 1, 0), W ($\frac{1}{2}, 1, 0$) and K (0, $\frac{3}{4}, \frac{3}{4}$) directions. It can be seen from band gap that there is existence of an indirect band gap of 3 eV. b. Site- and angular momentum-projected partial density of states for NiO showing the valence band to be mainly composed of O - $2p$ and Ni - $3d$ and $4s$.

Band calculations on NiO reveals that the large dispersion of Ni $3d$ and $4s$ states, and the optical indirect transition are in favour of photon energy storage and electron-hole separation to benefit the photocatalytic activity of NiO-TiO₂ composites. The theoretical calculations reveal a net charge transfer of 1.248 electrons from Ni to O ions. The charge transfer properties of NiO lead to longer carrier lifetimes [252,253] facilitating e^-/h^+ separation for higher efficiencies, and its conduction band edge is suitable for driving hydrogen evolution via water splitting [254]. Nickel oxide is an inexpensive yet highly promising candidate for photocatalytic applications. NiO has a rock salt structure, with Ni²⁺ ions anti-ferromagnetically coupled in the [111] direction [255]. The valence band edge (VBE) is composed of O $2p$ and conduction band edge (CBE) of Ni $3d$ character. This makes NiO a charge –transfer (CT) material. CT materials have VBE and CBE of different characters in contrast to Mott-Hubbard type semiconductors in which the VBE and CBE both have Ni $3d$ characters [255]. The large, indirect band gap of NiO has however limited its

functionality as a light absorber. In spite of absorbing light in UV region, the colour of NiO is black which is attributed to the impurity levels created above VBE and below CBE [256–259]. This model study is also useful in understanding the performance of similar photocatalysts.

4.5 Determination of valence band offset (VBO) and conduction band offset (CBO) by XPS

Unfortunately, it is difficult to determine the exact nature of Ni–Ti–O linkages/interactions on surface or bulk, but it may be assumed on the basis of above results that the NiO and TiO₂ phases are in close proximity and it is very likely that *pn* junctions would commence by their interaction in the NTC11 composite. These close interactions of NiO–TiO₂ oxides leading to *pn* heterojunctions, would affect the band structure and electronic structure at the interface and consequently improves visible light absorption and photocatalytic activities of NTC11 composite. Performance of NTC11 composite as photocatalyst would be primarily determined by proper alignment of band levels of *p* and *n* semiconductors at the heterojunction. Valence band offset (ΔE_v) and conduction band offset (ΔE_c) at NiO and TiO₂ heterojunction was calculated using the equation 4.3 and 4.4 and schematically shown in Fig. 4.18a. This method is generally used to establish band offset of film-substrate interface. In order to record the energy of photoelectrons from both film and interface which is lying beneath the film, minimum thickness of film (~2 nm) is required. But in case of composite both the NiO and TiO₂ are in contact with each other and within the analysis depth of the instrument. Hence thickness limitation is not taken into account.

Linear portion of valence band edge was extrapolated to the spectral baseline and the intercept will give the value of VBM energy. Here determination of VBM by linear extrapolation may involve some error but this may not affect the determination of band offset as it involves difference in energy rather than the absolute energy. $E_{VBM}^{TiO_2} = -1.23$ eV and

$E_{VBM}^{NiO} = 2.56$ eV estimated using above mentioned technique. Since, the zero point of the binding energy scale corresponds to the Fermi level (E_F), the position of the E_{VBM}^{NiO} and $E_{VBM}^{TiO_2}$ (valence band maximum) with respect to E_F as expected, was negative (-1.23 eV) for p type NiO and positive (2.56 eV) for n type, TiO_2 semiconductors. The energy difference between the CL and VBM for TiO_2 was 457.01 eV and for NiO was 854.45 eV. ΔE_{CL} was found to be 396.91 eV for NTC11 composite. Using equation 4.3 the calculated value of valence band offset ΔE_v was 0.53 eV. By putting the value for ΔE_v and band gap values of TiO_2 and NiO in equation 4.4, conduction band offset (ΔE_c) was calculated and found to be 0.93 eV.

Based on these calculations, the type-II band alignment was observed in NTC11 as shown in Fig. 4.18a where e^- will be transferred from CB of NiO to CB of TiO_2 and h^+ will flow from VB of TiO_2 to VB of NiO purely driven by the band energetics. A pictorial representation of the most probable mechanism proposed for NTC11 is shown in Fig. 4.18b.

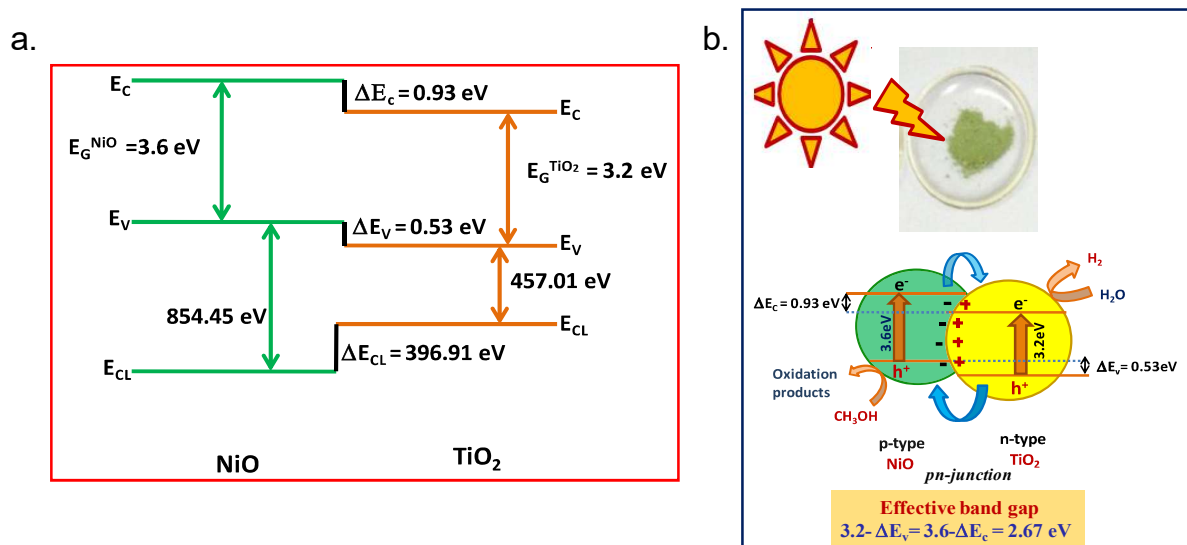


Fig. 4.18 a. Schematic diagram of band alignment derived at the interface of NiO-TiO₂ semiconductor. b. A pictorial representation of the most probable mechanism proposed for composite, NTC11.

The alignment of bands in this new configuration has effectively reduced the forbidden gap to $3.2 - \Delta E_v = 3.6 - \Delta E_c = 2.67$ eV at the pn junctions in the composite oxide. Thus, in present study, a composite of pn oxides offers lower band gap energy of 2.67 eV

with effectiveness in charge separation leading to efficient improved photocatalyst with sustainable H₂ yield for 60 h in sunlight.

In support of this band alignment scheme, time resolved photoluminescence spectra have revealed increased life times of charge carriers due to efficient separation at the heterojunctions induced in NTC11.

4.6 Novelty of work

To review our results, literature reports on Ni-Ti-O systems were surveyed and the most relevant ones for H₂ evolution are listed in Table 4.9. Ni incorporated in TiO₂ in any form whether on surface by impregnation, or coupled with titania as NiO or in form of cationic dopant substituting Ti⁴⁺ in titania lattice, results in enhancement of activity. Dispersion of minor amounts of NiO on TiO₂ surface by wet impregnation is commonly used strategy which has been adopted by most of researchers to enhance the hydrogen yield as there it acts as trap centres for electrons and sites for the photoreduction. Also, these trap centres formed on surface directs the photogenerated electrons to reach surface. Melian et al [221] have modified the catalytic properties of TiO₂ by incorporating Ni and N both at the crystallographic sites of TiO₂ lattice and have reported H₂ yield of 260 μmol/h over 1 g of the most active oxide doped catalyst under fluorescent lamps. However, another approach in which both NiO and TiO₂ in substantial amounts is merged in a composite; offers efficient charge separation, by increasing the life of e^- and h^+ produced during the photoirradiation was entirely different, proceeding via altered mechanisms and had therefore renewed the interest. The improved photocatalytic properties of composites are by virtue of heterojunctions formed at the interfacial contact of dissimilar semiconductors of NiO and TiO₂. Li et al. [222] and Yu et al. [260] have investigated *pn* junctions in bicomponent composites and reported H₂ generation using mesoporous NiO/TiO₂ with 377 μmol/h/g and NiO/rGO/TiO₂ with 240 μmol/h/g respectively. Among all reports, catalysts used in our

studies have shown comparatively better performance in the terms of H₂ yield (Table 4.9), although it is pertinent to mention here that experimental conditions used for activity evaluation are not same. Here, a comprehensive comparison of the composites, NTC11, NTC36 with their component oxides and the secondary pure phase, NiTiO₃ which was found to coexist and was degrading the photocatalytic activity, under identical conditions is reported. The results reported here offer conversion rates under actual sunlight unlike most of the reports showing activity in UV light. With an aim to extend this work to a pilot plant, H₂ yield obtained over 100 mg of photocatalyst are extrapolated to more realistic extrapolation of per illumination area (m²) in addition to per g (Table 4.9). Most active photocatalyst, Pt/NiO-TiO₂ was found to generate photocatalytic H₂ @ of 1250 μmol/h/g or 1.4 L/h/m² with AQE of 7.8 % under UV visible irradiation and 537 μmol/g/h or 0.6 L/h/m² under sunlight with AQE of 5.4 % and SFE of 0.8 %. The Ni-Ti composites were found to be cheap, active and stable photocatalysts and are therefore potential candidates for solar photocatalytic applications.

Table 4.9 Comparison of present study with literature reports on various Ni-Ti-O systems for photocatalytic H₂ evolution under stated experimental conditions.

Author	Photocatalyst	Source of light	H ₂ yield	Reaction conditions	AQE
Dengwei Jing et al [100]	Nickel doped mesoporous TiO ₂	300 W high-pressure Hg lamp	~185 μmol/h	0.3 g photocatalyst suspended in 300 ml of 20 vol % aqueous methanol solution	Not given
Ruixia Liu et al [220]	NiO _x -loaded TiO ₂	500 W high-pressure Hg lamp	900 μmol/h/g	20 mg photocatalyst suspended in a mixture of 10 ml water and 2 ml glycerol and irradiation carried out at 50 °C	Not given
E. Pulido Melián et al [221]	TiO ₂ modified with different Ni/Ti molar ratios (0.015, 0.030, 0.045) and constant Ni/N ratio	A set of two Solarium Philips HB175 lamps, each equipped with four 15 W Philips CLEO	260.76 μmol/h	Photocatalyst (concentration of 1 g/L) suspended in 200 ml of aqueous suspension containing 25 % methanol and pH adjusted to 5 by	Not given

	equal to 1.5	florescent tubes		using NaOH solution	
Lingling Li et al [222]	Mesoporous NiO/TiO ₂ bicomponent composite nanofibers	300 W Xenon lamp	377 $\mu\text{mol/h/g}$	50 mg of photocatalyst suspended in 80 ml aqueous methanol solution (methanol 25 vol%)	1.7%
Sreethawong et al [246]	NiO-loaded TiO ₂ photocatalyst synthesized by Single-step sol-gel (SSSG) and incipient wetness impregnation (IWI) method	300 W high-pressure Hg lamp	SSSG NiO/TiO ₂ with 1.5 wt% NiO loading: 162.6 $\mu\text{mol/h}$ IWI NiO/TiO ₂ with 1 wt% NiO loading: 117.4 $\mu\text{mol/h}$	0.2 g photocatalyst suspended in 200 mL of distilled water, 20 ml of methanol	Not given
Xin Yu et al [260]	NiO/rGO/TiO ₂ p-n hetero-structured coaxial nanocable	Commercial solar simulator (300 W) equipped with a Xenon lamp	240 $\mu\text{mol/h/g}$	50 mg photocatalyst dispersed in 80 ml of distilled water and 20 ml of methanol	Not given
Present work	NTC11	400 W UV-visible medium pressure Hg lamp	840 $\mu\text{mol/h/g}$ or 940.5 ml/h/m ²	100 mg photocatalyst suspended in a mixture of 10 ml water and 5 ml methanol	5.3
		Direct Sunlight	204 $\mu\text{mol/h/g}$ or 228.5 ml/h/m ²		2.0
	Pt/NTC11	400 W UV-visible medium pressure Hg lamp	1250 $\mu\text{mol/h/g}$ or 1400.0 ml/h/m ²	100 mg photocatalyst suspended in a mixture of 10 ml water and 5 ml methanol. Evaluated for 60 h	7.8
		Direct Sunlight	537 $\mu\text{mol/h/g}$ or 601.7 ml/h/m ²		5.4

4.7 Conclusion

In the present study, the nanocrystalline composites of NiO and TiO₂ oxides in four different compositions were synthesized, with an objective to create the interfacial contact between diverse semiconductors; *p* and *n* type so that electric field is induced within catalysts particles, leading to efficient separation of charge carriers, e^- and h^+ which are generated during the photocatalytic process. Further, to accentuate the role of *pn* heterojunctions in

composites, the photocatalytic properties of these composites; NTC11 and NTC36 were investigated in detail for H₂ evolution reaction and compared with the pure oxides, NiO, TiO₂ and NiTiO₃ prepared under identical conditions. It was found that among all samples, NTC11 was distinctly most active and repetitive cycles yielded reproducible H₂ yields for 60 h under sunlight confirming its photostability under prolonged exposure. Formation of *pn* nanojunctions in NTC11 evident by enhanced life times of charge carriers monitored by time resolved photoluminescence. Uniform distribution of NiO and TiO₂ nanoparticles with Ni/Ti in ratio of 0.99 and 0.95 at bulk and surface, respectively was found in NTC11 sample. It shows presence of monodisperse, nanosized faceted particles, having higher surface area, better porosity and pore volume. Phase identification by XRD revealed the formation of desired composite where, crystalline NiO and TiO₂ phases appear with minimal NiTiO₃ phase. The presence of impurity ilmenite phase, NiTiO₃, more prominent in NTC36 than NTC11, will however, disrupt the *pn* junctions formed in the composite oxides, and may interrupt in the swift drive of charge carriers across the junctions. The crystal and electronic structure of NiTiO₃ are responsible for its poor activity. First principles calculations by density functional theory over pure NiO revealed it's electronic and band structure that helped in understanding its behavior as PL quencher and its contribution in visible light absorption of composites. Valence band offset (ΔE_v) and conduction band offset (ΔE_c) at NiO and TiO₂ heterojunction in NTC11 was calculated and found to be 0.53 eV and 0.93 eV, respectively. Type-II band alignment was derived at the interface and the effective forbidden gap was deduced to be $3.2(E_{g, TiO_2}) - \Delta E_v = 3.6(E_{g, NiO}) - \Delta E_c = 2.67$ eV. Thus, a composite of *pn* oxides offers lower band gap energy of 2.67 eV as compared to both pure oxides TiO₂ and NiO with effectiveness in charge separation across the *pn* junction leading to efficient improved photocatalyst. This study demonstrates the benefit of designing of *pn* junction from low cost and earth abundant NiO and TiO₂ for enhancing the photocatalytic H₂ evolution

activity by tendering lower band gap energy and facilitating charge separation. Thus, NiO and TiO₂ in 1:1 ratio devoid of derogatory effect of NiTiO₃ phase are active, cheap and stable photocatalyst which can be projected as potential photocatalysts for actual large scale solar applications.

Synthesis, Characterization and Photocatalytic Properties of C@TiO₂ Composites (Carbon = 0.14 - 14.7 Wt %)

5.1 Introduction

As discussed in introduction chapter, carbon- semiconductor heterojunction formation is one of the effective way to reduce recombination of electron and hole pair as well as to enhance light absorption properties of semiconductor like TiO₂. Carbon in different forms offers several advantages such as electronic conductor due to sp² hybridized carbon, high surface area, acts as cocatalyst, enhances light absorption properties [118]. These properties of carbon make it a promising candidate for modifying photocatalytic activity of TiO₂. There are many approaches to incorporate carbon doping [261,262], dispersion in different forms [263] and coating [264,265].

Yang et al [266] synthesized TiO₂-carbon hybrid nanomaterials by heating oleylamine wrapped TiO₂ nanosheets in inert atmosphere for photocatalytic H₂ evolution. These hybrid nanomaterials exhibit higher and stable photocatalytic H₂ generation than pure TiO₂ nanoparticles. Parayil et al [267] found enhanced H₂ yield over C modified TiO₂ with an optimum carbon loading of 3.62 %. Zhao et al [87] synthesized TiO₂ nanotube sandwiched between two thin tubes of graphitic carbon and has shown enhanced H₂ production at the rate of 37.6 mmol/h/g by illuminating the photocatalyst under solar simulator in presence of Pt as cocatalyst and ethanol as sacrificial reagent. The high activity of the composite attributed to the synergistic effect between carbon and TiO₂ for enhancing the charge carrier separation and increased light absorption.

There are several studies investigated application of C-TiO₂ composite for oxidation of organic contaminants. Zhang et al [264] coated carbon on TiO₂ hollow spheres which has shown enhanced light absorption for degradation of Rhodamine B and found that formation of Ti-O-C bond is beneficial for the charge transfer between TiO₂ and Carbon. Nawi et al [268] revealed that optimum thickness of carbon coating should be 0.68 nm for photocatalytic degradation reaction. Hybridization of graphitic carbon with TiO₂ shows enhancement in photocatalytic activity due to favoured electronic interactions at the interface investigated by the electrochemical studies [265,269]. Although extensive literature is available on photocatalytic activity of carbon modified TiO₂. However, the specific site where carbon incorporated in TiO₂ is yet to be revealed.

In the present study, carbon decorated sample was synthesized by sol-gel method. Ethylene glycol was used as carbon precursor. Ethylene glycol is selected as precursor as it is a cross linking reagent also, it polymerizes with titanium precursor and forms organic-inorganic polymer. This polymer after calcination in inert atmosphere forms carbon@TiO₂ composite. C-TiO₂ composite are reported in literature using various carbon sources such as glucose [270], sucrose [262,267], oleylamine [266], cyclohexane [271] etc.

Till date there are no reports to the best of our knowledge, on application of C-TiO₂ nanocomposite using ethylene glycol and titanium tetrabutoxide for photocatalytic H₂ generation under sunlight. To establish the phase purity/composition, surface morphology, oxidation states, elemental quantification, optical features, electronic properties, samples were characterized by XRD, FTIR, Raman spectroscopy, XPS, XAS (EXAFS/ XANES), HR-TEM, CHN analysis, ICP-OES and DRS. Also, photocatalytic activity was evaluated by monitoring generation of hydrogen from aqueous methanol (33 % v/v) in evacuated atmosphere under UV-visible and natural sunlight. H₂ evolution for 32 h under sunlight

illumination was evaluated over most active sample. Apparent quantum efficiency (AQE) achieved is reported here.

5.2 Experimental

5.2.1 Synthesis of C@TiO₂

8.5 ml of tetrabutyltitanate (TBT) was poured to 10.5 ml of ethylene glycol (EG) along with stirring till it solidifies. A solution containing 2.7 ml water + 170 ml acetone was added drop wise to the above mixture. Finally the gel was centrifuged, washed with water and ethanol several times and dried at 80 °C to obtain white colloidal organic–inorganic polymer. This polymer was calcined in an argon atmosphere at 500 °C for 9 h at a heating rate of 2 °C/min, to obtain homogeneous C@TiO₂ nanocomposites. In a similar way, a series of samples were prepared by varying the amount of EG from 14, 20, 25, 50, 75 and 100 ml and abbreviated as C@TiO₂ followed by the amount of ethylene glycol added. For comparison, pristine TiO₂ was prepared under similar condition without addition of EG and calcining the sample in air at 500 °C for 9 h.

1 % w/w of Pt was dispersed over C@TiO₂ composite by photodeposition method explained in detail in Chapter 4.

5.2.2 Characterization

Powder XRD patterns were recorded on a Philips diffractometer (model PW 1710), equipped with a graphite monochromator and Ni-filtered Cu-K_α radiation. The crystallite size was calculated from the XRD line width using the Scherrer equation. N₂- BET surface area was measured with a Micromeritics 3Flex analyser using nitrogen as the adsorbing gas. The elemental analysis of Ti present in the samples was evaluated using ICP-OES (*JobinVyon JY 2000*, France). Amount of carbon present in the sample was determined by using Euro vector elemental analyser (Euro EA 3000 series). Raman spectra were recorded using 532 nm lines

from a diode Nd: YAG laser (power 15 mW) focused to a spot size of $\sim 20 \mu\text{m}$. The scattered light was analyzed using an indigenously built 0.9 m single monochromator, coupled with a super notch filter and detected by a cooled charge couple device (CCD, Andor Technology). A resolution limited line width of 3 cm^{-1} was achieved at entrance slit width of $50 \mu\text{m}$. Optical properties of all samples was estimated by recording their diffuse reflectance UV-visible spectra using a spectrophotometer of JASCO model V-530, Japan, scanned in the range of 200-1000 nm at the scanning speed of 200 nmmin^{-1} . EXAFS measurements of the C@TiO₂ samples at the Ti K edge were carried out in fluorescence mode at the Scanning EXAFS Beamline (BL-9) at the INDUS-2 Synchrotron Source (2.5 GeV, 100 mA) at the Raja Ramanna Centre for Advanced Technology (RRCAT), Indore, India. The beam line uses a double crystal monochromator (DCM) in the photon energy range of 4-25 keV with a resolution of 10^4 at 10 keV. XPS experiments were recorded on an electron spectrometer (SPECS, Surface Nano Analysis GmbH, Germany) using Mg- K α X-rays ($h\nu=1253.6 \text{ eV}$) as the primary source of radiation with an overall energy resolution of the instrument of about 0.7 eV. The appropriate corrections for charging effects were made with the help of a C 1s signal appearing at 284.5 eV.

5.2.3 Photocatalytic activity

Photocatalytic activity of all these samples was evaluated for H₂ generation from aqueous methanol solutions (33 % v/v) by irradiating under sunlight and UV-Visible light. 50 mg of sample was suspended in 15 ml of water + methanol (33 % v/v) solution and irradiated under medium pressure mercury lamp (Hg, SAIC, India, 400 W) placed in an outer irradiation-type quartz cell surrounded with water circulation jacket to absorb IR irradiation. Photocatalytic H₂ production was quantified by gas chromatography (Shimadzu, GC 2010 plus) equipped with carboxen column (30 m length, 0.32 mm ID) and thermal Conductivity detector using Ar as the mobile phase.

Under sunlight, a mixture suspended with photocatalyst was irradiated for duration of 4 h during afternoon (11.00-15.00 IST) to evaluate the photocatalytic properties. Solar flux was measured using light meter LX 1108, Lutron Electronic. Flux was measured daily in the peak hours and average of lux recorded during 11.00-15.00 were used for AQE and SFE measurement.

5.3 Results and discussion

5.3.1 Characterization

Carbon and Ti present in C@TiO₂ sample were quantified by CHN and ICP-OES analysis as mentioned in Table 5.1. The amount of carbon varies from 0.14 to 14.7 wt % as estimated by CHN analyzer. The amount of carbon determined by CHN analyzer is lesser than the expected amount. ICP-OES technique was utilized to estimate amount of Ti present in C@TiO₂ composites (Table 5.1). Probably during synthesis there may be loss of EG from the as synthesized sample while washing with water. To confirm presence of water in C@TiO₂ samples, TGA-DTA-EGA were recorded.

Table 5.1 C and TiO₂ content determined in C@TiO₂ composite samples by ICP-OES and CHN analysis

Sample	TiO ₂ by ICP-OES (% w/w)	C from CHN analyzer (% w/w)
TiO ₂	99.94	-
C@TiO ₂ EG10	95.05	0.14
C@TiO ₂ EG14	93.57	0.36
C@TiO ₂ EG20	88.76	3.8
C@TiO ₂ EG25	92.15	3.8
C@TiO ₂ EG50	85.01	4.8
C@TiO ₂ EG75	79.23	8.3
C@TiO ₂ EG100	78.34	14.7

Thermogramme of C@TiO₂EG20 sample was recorded in air till 1000 °C shows mass loss in two steps (Fig. 5.1). The first step shows weight loss of 2.87 % in the range of 45.77-224.95 °C and second step shows weight loss of 5.05 % in the temperature range of 224.95-

479.67 °C. Total weight loss was 7.92 % from the sample. DTA shows that all the steps are exothermic in nature. Gases evolved at different stages were analyzed by FTIR coupled with TGA. FTIR spectrum of evolved gases recorded at 90 °C shows characteristic peaks of physically bonded water whereas FTIR spectrum recorded at 400 °C shows peak attributed to both H₂O and CO₂. Heating in presence of air oxidizes carbon to CO₂.

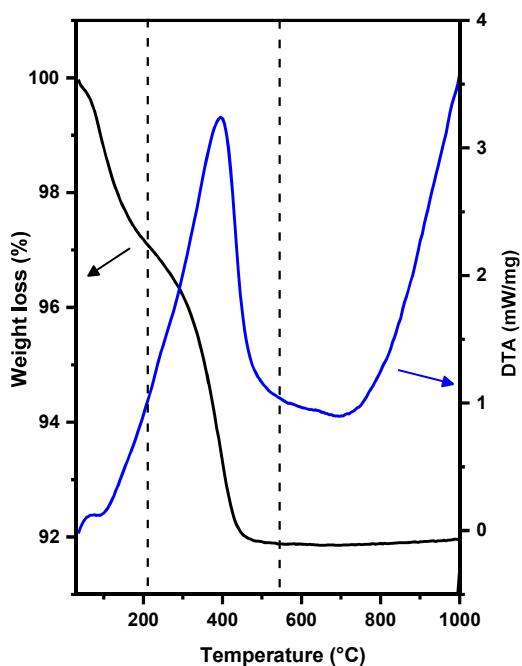


Fig. 5.1 TGA-DTA analysis of C@TiO₂EG20 sample in presence of air.

Fig. 5.2a shows XRD pattern of uncalcined sample where presence of broad peak centered at 25.78° is observed confirms amorphous nature of C@TiO₂EG20 sample before calcination. Fig. 5.2b shows XRD pattern of calcined samples at 500 °C in inert atmosphere. XRD pattern of C@TiO₂ samples exhibits peaks corresponding to anatase phase of TiO₂. Peak appearing at 2θ = 25.4°, 37.0°, 37.9°, 38.7°, 48.0°, 53.8°, 55.3°, 62.8° and 68.8° corresponding to (101), (103), (004), (112), (200), (105), (211), (204) and (116) planes of anatase phase of TiO₂ (JCPDS No: 21-1272). Peak broadening was observed with increase in carbon content. Crystallite size calculated by Scherrer equation is tabulated in Table 5.4. The crystallite size of TiO₂ was about 22.9 nm and it progressively decreases to 5.8 nm with

increase in carbon content. From, this it was inferred that presence of carbon might have inhibited the agglomeration of particles.

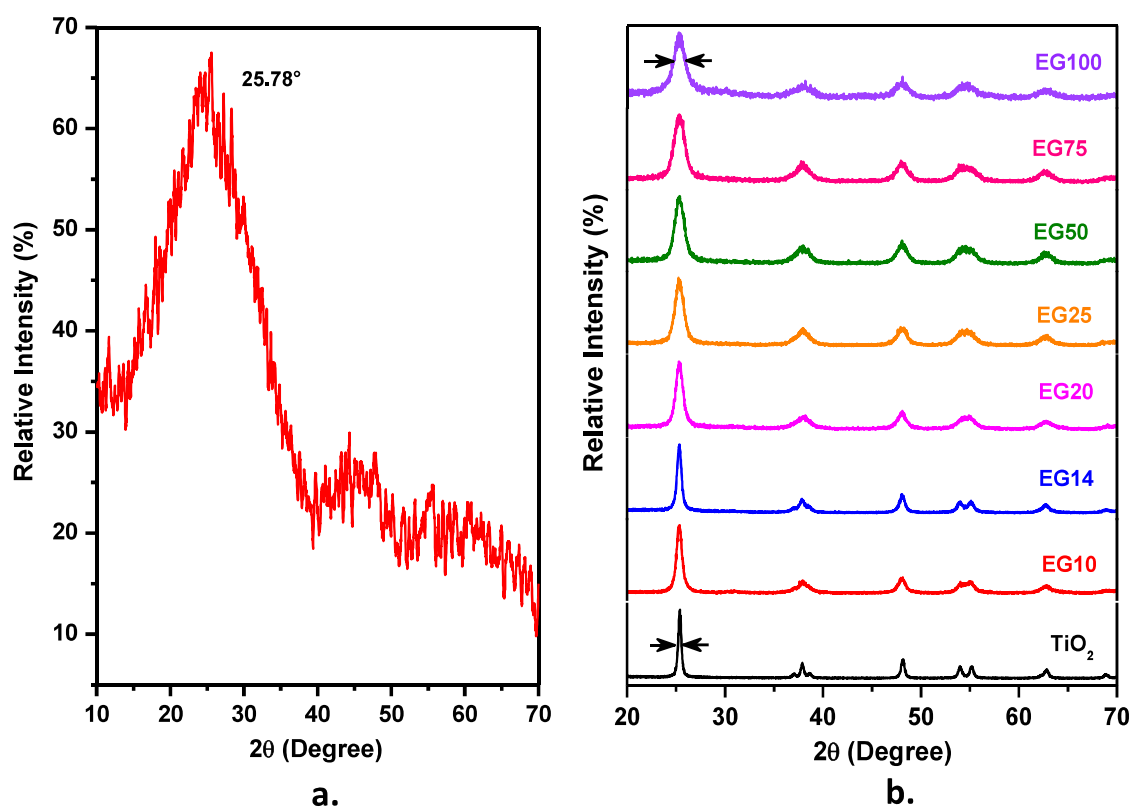


Fig. 5.2 XRD pattern of a. uncalcined C@TiO₂EG20 sample b. C@TiO₂EG (EG= 10, 14, 20, 25, 50, 75, 100) samples calcined in argon atmosphere at 500 °C for 9 h.

To know more about structural details FTIR and Raman spectra was recorded. Fig. 5.3 shows FTIR spectrum of uncalcined and calcined sample. Uncalcined sample shows band at 327 and 550 cm⁻¹ corresponds to Ti-O vibrations. The broad band around 550 cm⁻¹ corresponds to stretching vibration of Ti-O-Ti [272]. Peak at 1630 cm⁻¹ assigned to H-O-H bending vibration mode of water molecules [273] and broad band in the range of 3000-3500 cm⁻¹ attributes to the stretching vibration of hydroxyl group of physically adsorbed water or can be from ethylene glycol. Peak at 2866 and 2934 cm⁻¹ corresponds to alkyl (-CH₂) symmetric or asymmetric stretching of C-H bond of -CH₂ groups of ethylene glycol respectively [274]. 1456 cm⁻¹ corresponds to bending of -CH₂ group, 1150-1350 cm⁻¹

corresponds to the scissoring of C-H bonds of $-\text{CH}_2$ groups [274]. Peak at 1075 and 1550 cm^{-1} are ascribed to the presence of C-O [273] and $-\text{COO}^-$ group [275].

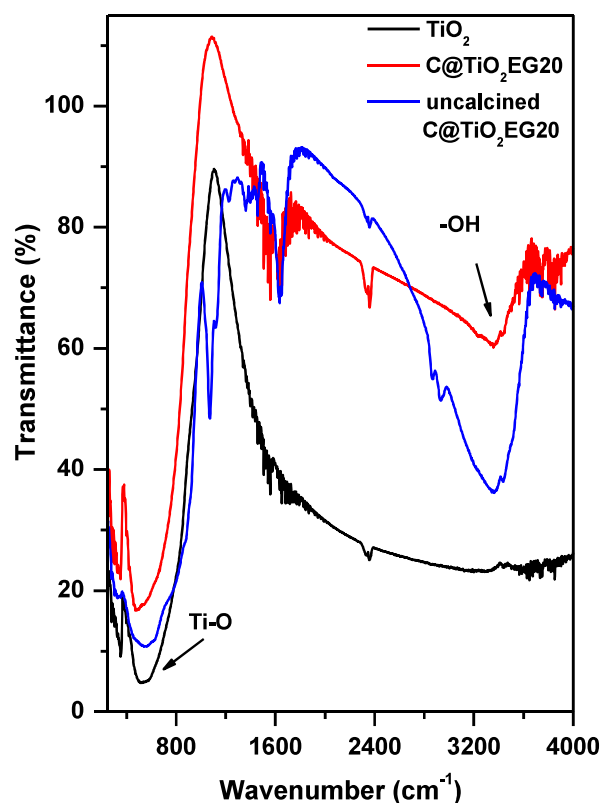


Fig. 5.3 FTIR spectra of uncalcined and calcined $\text{C@TiO}_2\text{EG20}$ sample compared with TiO_2 .

Pristine TiO_2 calcined at $500\text{ }^\circ\text{C}$ shows bands at 352 and 548 cm^{-1} corresponding to Ti-O vibration. Calcined sample did not show presence of 1075 , 1456 , $1150\text{--}1350$, 2866 and 2934 cm^{-1} bands. However, after carbon incorporation the FTIR spectrum has shown different features. IR spectrum of representative sample $\text{C@TiO}_2\text{EG20}$ is shown in Fig. 5.3. C@TiO_2 composite sample shows band at 351 cm^{-1} and a broad peak centered at 480 cm^{-1} . The peak observed at 550 cm^{-1} for bare TiO_2 was found to shift to 480 cm^{-1} in EG20 sample. Bands at 1630 and 3430 cm^{-1} attributed to $-\text{OH}$ group and peak at 1550 cm^{-1} corresponding to the $-\text{COO}^-$ group were found [275].

Raman spectra of C@TiO_2 samples show characteristic peaks of anatase phase of TiO_2 (Fig. 5.4) and graphitic carbon (Fig. 5.5). Anatase phase of TiO_2 shows six Raman active mode at 144 (E_g), 197 (E_g), 399 (B_{1g}), 513 (A_{1g}), 519 (B_{1g}) and 639 cm^{-1} (E_g). The two

peaks of doublet (513 and 519 cm^{-1}) merges to one peak at 516 cm^{-1} at room temperature [184]. E_g , 144 cm^{-1} is the most intense and sharp vibration mode and others are weak vibrations. E_g mode is very sensitive to crystal domain size and oxygen defects [276]. With increasing carbon content, progressive shift towards higher wave number and peak broadening were observed [277]. This confirms that the presence of carbon prevents the agglomeration of TiO_2 particles. Yang et al [266] observed a shift in E_g mode of anatase TiO_2 also in carbon hybridized TiO_2 samples and assigned it to both grain size and interaction between C and TiO_2 .

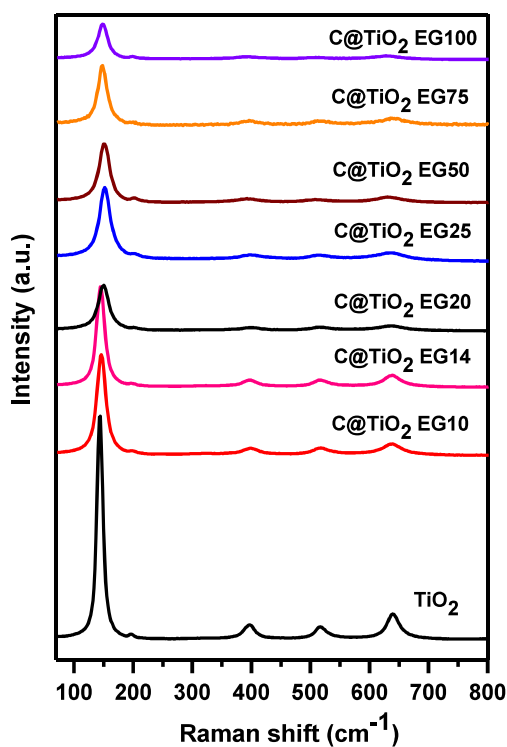


Fig. 5.4 Raman spectra of TiO_2 and C@TiO_2 samples.

Two bands were observed in all samples in frequency region of 1160 - 1760 cm^{-1} , called as D and G bands reported at ~ 1355 and 1575 cm^{-1} (Fig. 5.5) [278]. The G band reveals the presence of sp^2 hybridized carbon atoms in graphite like arrangement and D band corresponds to disorder sp^2 carbon atom in the structure. For $\text{C@TiO}_2\text{EG100}$ sample D and G bands observed at 1349 and 1595 cm^{-1} respectively, where G band has shifted to higher

wavenumber as compared to pure graphite indicating structural imperfection in the carbon [265,278].

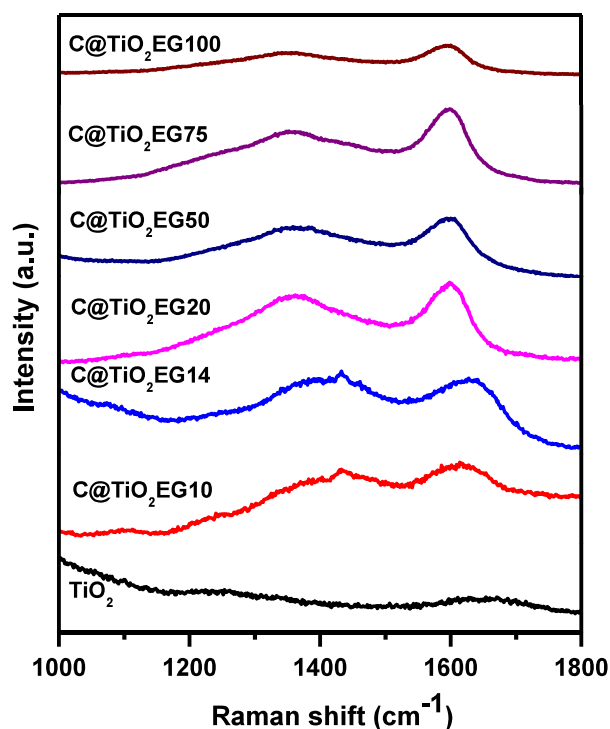


Fig. 5.5 Raman spectra of C@TiO₂ samples shows presence of D and G band.

Ratio of I_D/I_G suggests the degree of graphitization [279]. Lower the ratio more is the degree of graphitization. Intensity of G band is comparable to that of D band in case of C@TiO₂EG10 and 14 sample whereas on further increase in carbon content intensity of G band increases along with narrowing of the band. I_D/I_G ratio decreases marginally with increase in carbon content in the sample (Table 5.2). This implies degree of graphitization is increases with increase in carbon content of the sample.

Table 5.2 Ratio of I_D/I_G in C@TiO₂ samples

Sample	D band (cm ⁻¹)	G band (cm ⁻¹)	I_D/I_G
C@TiO ₂ EG10	1431	1610	1.07
C@TiO ₂ EG14	1406	1627	1.00
C@TiO ₂ EG20	1360	1598	0.97
C@TiO ₂ EG25	1362	1597	0.99
C@TiO ₂ EG50	1364	1597	0.98
C@TiO ₂ EG75	1356	1596	0.96
C@TiO ₂ EG100	1349	1595	0.99

Local structure around Ti ions was qualitatively analysed by recording XAS (EXAFS/XANES). Oxidation state of Ti ion was analyzed using XANES. The normalised XANES spectra recorded at Ti K edge is shown in Fig. 5.6. The absorption edge arises due to the transition of $1s$ electron into unoccupied $4p$ orbital. The absorption edge position is sensitive to the oxidation state of the absorbing atoms. The XANES spectra of TiO_2 show absorption edge at 4987.7 eV confirms the presence of Ti in +4 oxidation state. No shift in peak position was observed after carbon incorporation confirming the presence of Ti in +4 oxidation state in modified samples.

Being a transition metal, Ti shows spectral features immediately before the absorption edge called pre-edge spectral features. The pre-edge feature shown in Fig. 5.6 is marked as A, B and C, while the enlarged view of the pre-edge region is shown in the inset of the Fig. 5.6. These pre-edge features arise due to the transition of $1s$ electron into hybridized Ti $3d$ - O $2p$ states. In general TiO_2 is present in two polymorphs, anatase or rutile. The anatase phase of TiO_2 shows three strong pre-edge peaks and the rutile phase shows a weak peak and two separate strong peaks [280]. The pre-edge peak B and C is attributed to the $1s-2t_{2g}$ and $1s-3e_g$ transitions in octahedral field respectively [281]. The pre-edge peak A is attributed to exciton band or $1s-1t_{1g}$ transition from possible perturbation due to shakeup and shakeoff processes [282]. The presence of three pre-edge peaks in the present samples indicates that anatase phase is the major phase in these samples. The pre-edge peak intensity is directly related to the disorder of the coordination shell. Higher disorder produce intense peak and lower disorder produce small pre-edge peak intensity. With the analogy given above, the sample with 4.8 % w/w carbon (EG50) has maximum disorder as compared to bare TiO_2 . The intensity of pre-edge peak marked as B is higher in EG50 sample (Fig. 5.6). The peak intensities of spectral features denoted by E, F and G also depend on the relative presence of the anatase or rutile phase. In case of the Rutile phase peak F is strong, however for anatase

phase this peak is absent. Small hump type of shape at position F in the present samples indicates that small amount of rutile phase is also present in these samples along with the major anatase phase [280]. However, peak due to rutile phase is not observed in the XRD spectrum.

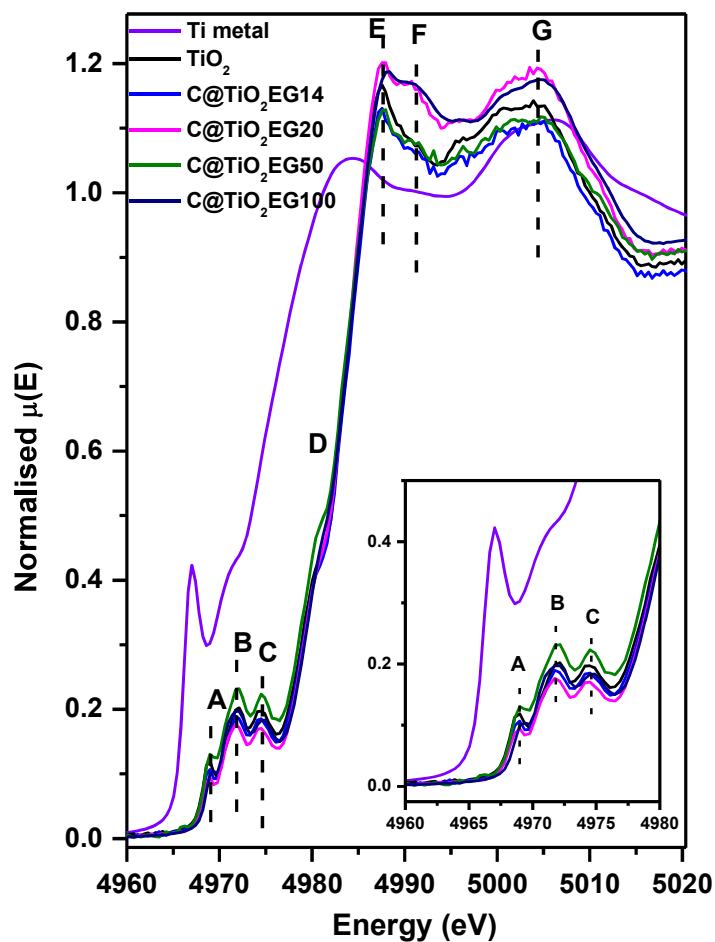


Fig. 5.6 Normalised XANES spectra of TiO₂ at Ti K-edge along with reference metal foil.

The $\chi(r)$ versus r plots generated (Fourier transform range $k = 2.0-9.5 \text{ \AA}^{-1}$) for all the samples from the $\mu(E)$ versus E spectra following the methodology described in Chapter 2 and shown for TiO₂ measured at Ti K edge in Fig. 5.7.

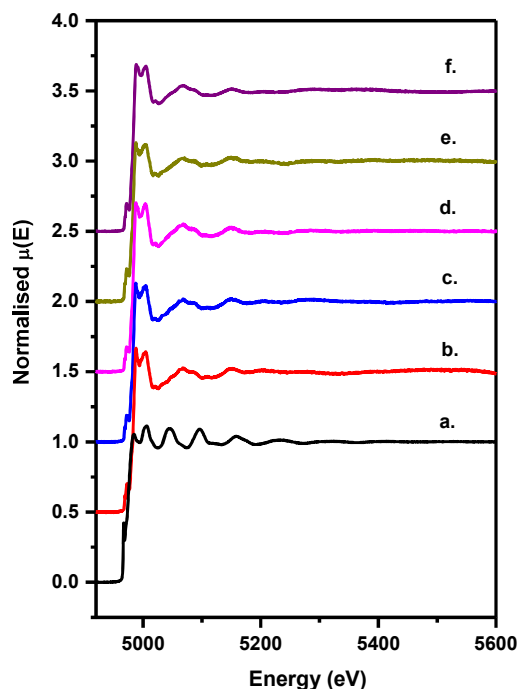


Fig. 5.7 Normalised EXAFS spectra of a. Ti metal, b. TiO₂, c. C@TiO₂EG14, d. C@TiO₂EG20, e. C@TiO₂EG50, f. C@TiO₂EG100 at Ti K-edge along with reference Ti metal

The structural parameters (atomic coordination and lattice parameters) of TiO₂ used for simulation of theoretical EXAFS spectra of the samples have been obtained from ref. [283,284] and the best fit $\chi(r)$ versus r plots of the samples have been shown in Fig. 5.8 along with the experimental data for all the samples. The bond distances and disorder (Debye-Waller) factors (σ^2), which give the mean square fluctuations in the distances, have been used as fitting parameters. The amplitude reduction factor (S_0^2) obtained from the standard sample is used as a constant in all the fittings. The best fit results of the above are summarized in Table 5.3. The first peak around 1.5 Å in Fig. 5.8(a) for the pristine TiO₂ has contributions from six oxygen atoms where 4 oxygen atoms are at a distance of 1.95 Å and 2 oxygen atoms are at 1.97 Å from the Ti atom. The second coordination peak which appears at 2.6 Å has contributions from four Ti-Ti paths at 2.95 Å. The coordination peak at 3.30 Å is again due to four Ti-Ti scattering paths at 3.78 Å distance. The number of peaks are same for all the samples, however their peak position and intensity are slightly different.

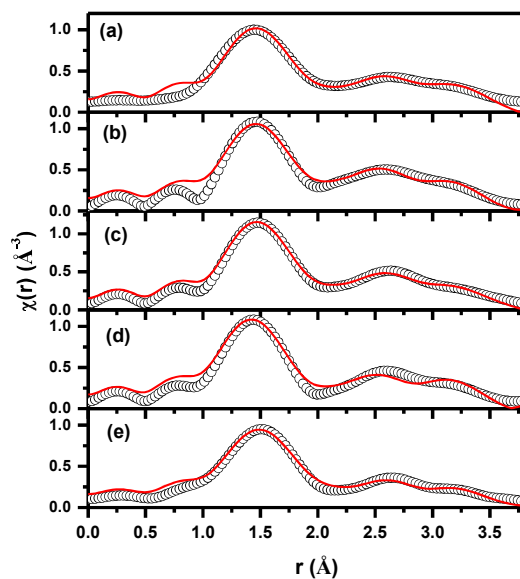


Fig. 5.8 Fourier transformed EXAFS spectra of TiO₂ at Ti K-edge (Scatter points) and theoretical fit (Solid line) (a) pristine TiO₂, (b) C@TiO₂EG14, (c) C@TiO₂EG20, (d) C@TiO₂EG50 and (e) C@TiO₂EG100.

Following inference is drawn from data given in Table 5.3.

- From the EXAF data, it is clear that carbon has been incorporated in the bulk as it is affected the r , N and σ^2 parameters beyond experimental error.
- The distortion in TiO₆ octahedra is progressively increasing with carbon content upto 4.8 wt %. From rise in intensity of pre-edge peak of EG50 sample also, it is confirmed that distortion is maximum in TiO₆ of EG50 sample.
- The bond length (r) of Ti-O linkages corresponding to square planar ($N=4$, Table 5.3) are decreasing while that of Ti-O linkages ($N=2$) in bipyramid are increasing with increase in carbon content, suggesting overall distortion in TiO₆ octahedra of anatase.
- Effect of carbon is observed in first co-ordinate only (Ti-O) bonds, whereas second co-ordinating sphere (Ti-Ti) is unaffected.
- Characteristics of TiO₂EG100 are similar to bulk pristine TiO₂, indicating that at higher content of carbon, the carbon has segregated as separate phase.
- Possibly carbon has affected local environment of Ti at square pyramid only.

Table 5.3 Bond distances, co-ordination number and disorder factor (σ^2) of C@TiO₂ samples

Paths	Parameters	TiO ₂	C@TiO ₂ EG14	C@TiO ₂ EG 20	C@TiO ₂ EG 50	C@TiO ₂ EG 100
Ti-O	r (Å)	1.95± 0.01	1.94±0.01	1.94±0.01	1.93±0.01	1.95±0.01
	N	4	4	4	4	4
	σ^2 (Å ²)	0.0068± 0.0005	0.0058± 0.0007	0.0046± 0.0006	0.0076± 0.001	0.0070± 0.0007
Ti-O	r (Å)	1.97±0.01	1.97±0.01	1.97±0.01	1.96±0.01	1.98±0.01
	N	2	2	2	2	2
	σ^2 (Å ²)	0.0068± 0.0005	0.0058± 0.0007	0.0046± 0.0006	0.0077± 0.001	0.0070± 0.0007
Ti-Ti	r (Å)	2.95±0.01	2.95±0.01	2.95±0.01	2.96±0.01	2.97±0.01
	N	4	4	4	4	4
	σ^2 (Å ²)	0.0049± 0.0005	0.0034± 0.0008	0.004± 0.0006	0.0052± 0.0008	0.0070± 0.0009
Ti-Ti	r (Å)	3.78±0.02	3.77±0.02	3.78±0.01	3.77±0.02	3.78±0.01
	N	4	4	4	4	4
	σ^2 (Å ²)	0.0033± 0.0007	0.0035± 0.0012	0.0036± 0.0011	0.0045± 0.0012	0.0070± 0.0013

Modification of surface properties due to incorporation of carbon is investigated by N₂-BET and XPS. Crystallite size, N₂-BET surface area, pore size and cumulative pore volume of C@TiO₂ as compared to pristine TiO₂ are tabulated in Table 5.4.

Table 5.4 Crystallite size, surface area, pore size and volume of C@TiO₂ samples

Sample	Crystallite size (nm)	Particle size by TEM (nm)	Surface area (m ² /g)	Pore volume (cm ³ /g)	BJH Pore size distribution
TiO ₂	22-23	8-20	19.9	0.03136	Distribution of pore size from 30-58 Å with maxima at 38 Å
C@TiO ₂ E G14	15-16		32.9	0.04756	Narrow distribution from 32- 46 Å with maxima at 36.34 Å
C@TiO ₂ E G20	8-9	5-11	99.8	0.13846	Binodal distribution 29-150 Å with maxima at 37 and 63 Å
C@TiO ₂ E G25	7-8		-	-	-
C@TiO ₂ E G50	7-8		78.6	0.05709	Narrow distribution in the range of 29- 47 Å with maxima at 37 Å
C@TiO ₂ E G75	6-7		-	-	-
C@TiO ₂ E G100	5-6	5-6	146.6	0.14606	Broad distribution of pore, Maxima at 33Å°

Fig. 5.9 shows that both pristine TiO_2 and C@TiO_2 samples show type IV adsorption isotherm. Composite samples have shown enhanced surface area as compared to $20 \text{ m}^2\text{g}^{-1}$ of pristine TiO_2 . It was observed that with increase in carbon content surface area and pore volume also increases. All the samples are mesoporous in nature as their pore diameter is in the range of 20-500 Å. $\text{C@TiO}_2\text{EG20}$ sample shows binodal distribution of pore size in the range of 29-150 Å with maxima at 37 and 63 Å whereas TiO_2 shows maxima around 38 Å with broad distribution of pore size from 30 to 58 Å. Sample with maximum carbon content of 14.7 % w/w (EG100) shows maximum surface area of $146 \text{ m}^2/\text{g}$ with cumulative pore volume of $0.14606 \text{ cm}^3/\text{g}$.

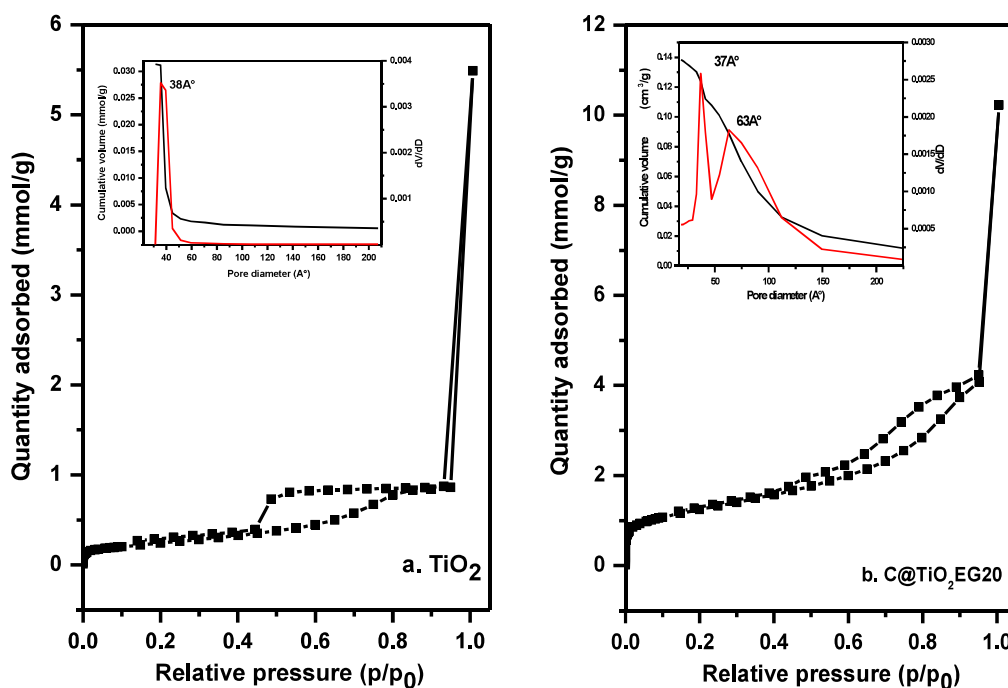


Fig. 5.9 N_2 -BET isotherms of a. TiO_2 and b. $\text{C@TiO}_2\text{EG20}$ sample with pore size distribution (shown in inset).

Low and high resolution TEM images with particle size distribution and SAED patterns are shown in Fig. 5.10 a, b and c for TiO_2 , $\text{C@TiO}_2\text{EG 20}$ and 100 respectively. Low resolution image of pristine TiO_2 shows agglomeration of faceted TiO_2 particles. HR-TEM images of all samples show lattice fringes with fringe width of 0.35 nm corresponding to 101 plane of anatase TiO_2 . Diffused rings with dotted pattern form SAED of TiO_2 and C@TiO_2

samples revealing nanocrystalline nature of these powders. These patterns were indexed and found to consist of anatase phase of TiO_2 in agreement with XRD results.

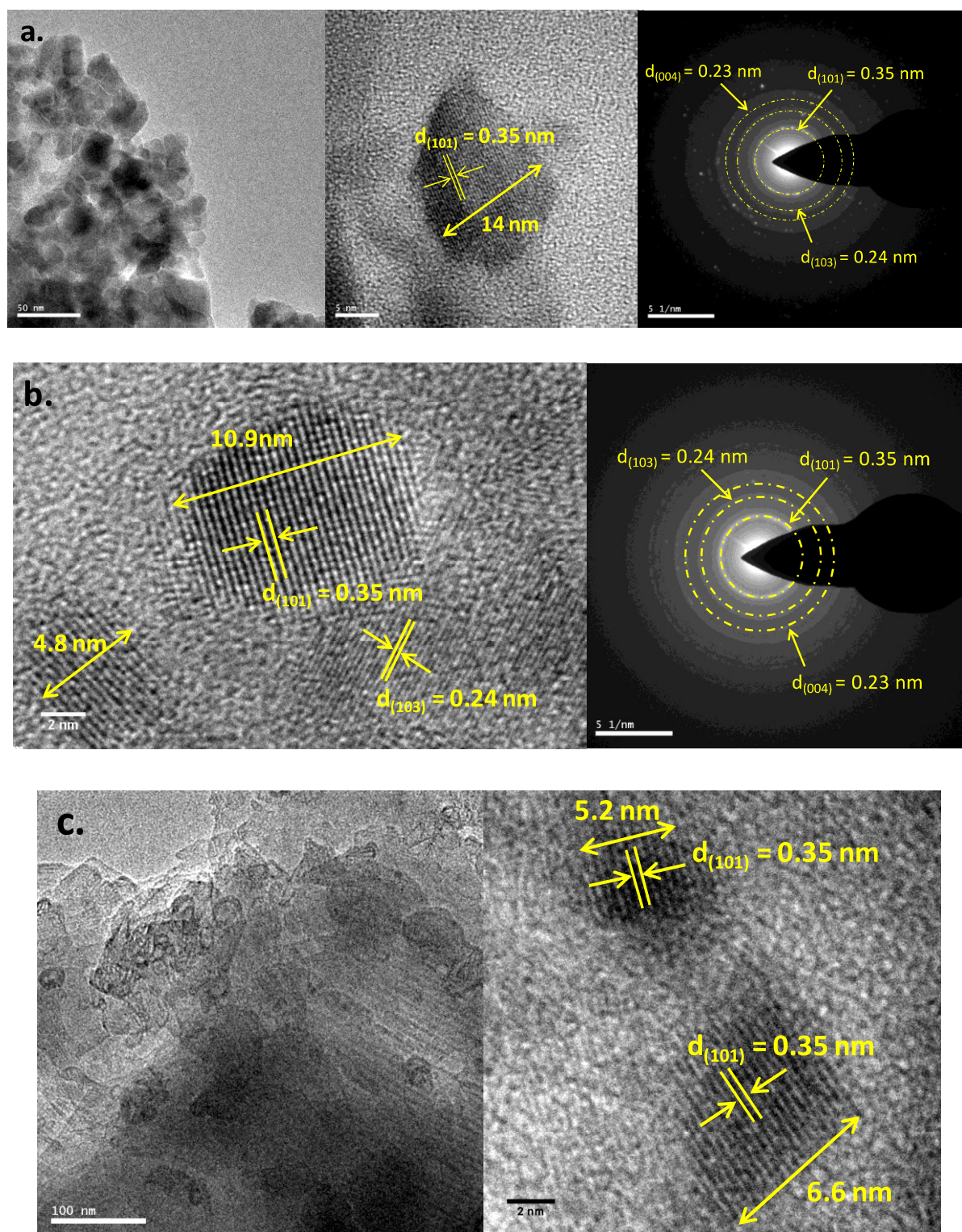


Fig. 5.10 Low and high resolution TEM images and SAED pattern of a. TiO_2 , b. C@TiO_2 EG20 c. C@TiO_2 EG100 samples

Fig. 5.11 shows the DRS spectrum of all samples. TiO_2 shows band gap at 3.2 eV. DRS spectrum of a composite sample is a result of an overlap of the band structures of both the carbon and TiO_2 . It was observed that with increase in carbon content, absorption in visible region increases, suggesting carbon has modified optical properties favourably. Hence C@TiO_2 samples are suitable to utilize visible region of sunlight.

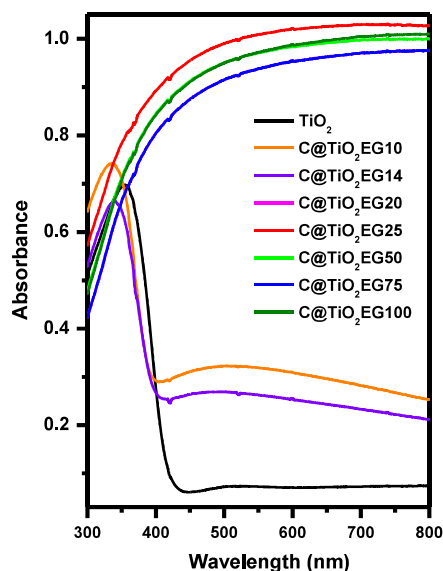


Fig. 5.11 Light absorption properties of C@TiO_2 samples as a function of carbon content recorded using DRS

XPS Survey scan of samples shows peak correspond to C, Ti and O elements with photoelectron peaks appearing at binding energies 529 (O 1s), 458 (Ti $2p_{3/2}$), 464 (Ti $2p_{1/2}$) and 285 eV (C 1s). Fig. 5.12a shows high resolution spectra of C1s of different samples. C1s spectra recorded for bare TiO_2 shows peak at binding energy 284.5 eV due to presence of adventitious carbon on the surface. Broadening of the C1s peak increased in sample with increase in carbon content of the sample. C1s spectrum of carbon incorporated samples was deconvoluted to give three distinct peaks. $\text{C@TiO}_2\text{EG25}$ shows peak at 284.05, 286.14, 290.39 eV associated with sp^2 hybridized graphitic carbon, C-O (or C-O-C) group and COOH species or π - π^* transition respectively [285]. No peak corresponds to Ti-C bond were found at 282.0 eV [286].

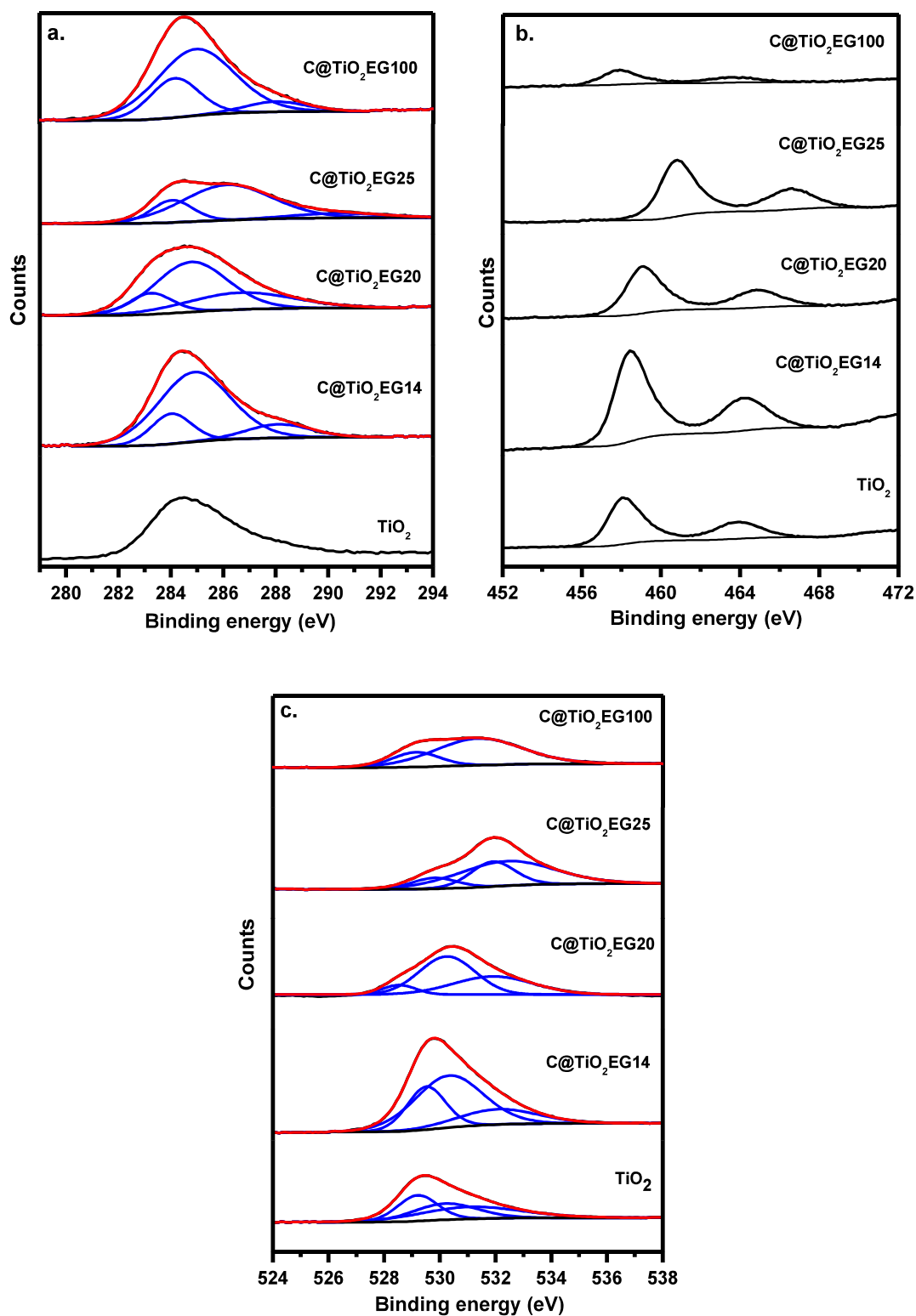


Fig. 5.12 High resolution spectra of a. C 1s, b. Ti 2p and c. O 1s of TiO_2 and C@TiO_2 samples.

High resolution spectra of Ti 2p shows peak at binding energy 457.9 eV and 463.8 eV corresponds to Ti $2p_{3/2}$ and $2p_{1/2}$ respectively as shown in Fig. 5.12b. Peak at binding

energy 458.16 eV assigned to Ti^{4+} state [192]. A systematic shift in Ti $2p_{3/2}$ and $2p_{1/2}$ towards higher binding energy with increase in carbon content is attributed to increasing interactions of Ti^{4+} ion with carbon as suggested by EXAFS studies also (Fig. 5.12b)

High resolution spectra of O 1s of TiO_2 shows presence of three peaks at binding energy corresponds to peak at 529.20, 530.19 and 531.08 eV ascribed to Ti-O, hydroxyl group and adsorbed H_2O molecules respectively. O 1s spectra of $C@TiO_2$ samples also deconvoluted into three peaks as shown in Fig. 5.12c. Peaks at binding energy 529.2, 531.5 and 532 eV corresponds to Ti-O, C=O and C-O (or C-O-C) respectively [279].

Atom % over the surface of sample was calculated and tabulated in Table 5.5. The atomic ratio of [O]/[Ti] significantly increased for EG100 due to hydroxylation of carbon along with Ti as evident from TG-DTA. As expected [C]/[Ti] and [C]/[O] concentration increases with increase in carbon content. This suggests that surface is becoming rich in carbon content. That will impart favourable light absorption properties to catalyst.

Table 5.5 Elemental compositions derived from XPS study of $C@TiO_2$ composite samples.

Sample	C (atom %)	O (atom %)	Ti (atom %)	[O]/[Ti]	[C]/[Ti]	[C]/[O]
TiO_2	-	82.79	17.20	4.8	-	-
$C@TiO_2EG14$	38.773	50.06	11.16	4.48	3.47	0.78
$C@TiO_2EG20$	46.756	44.17	9.08	4.86	5.15	1.06
$C@TiO_2EG25$	40.129	48.41	11.46	4.22	3.50	0.83
$C@TiO_2EG100$	62.629	34.24	3.13	10.92	19.99	1.82

5.3.2 Photocatalytic activity

Fig. 5.13a show photocatalytic activity of TiO_2 and $C@TiO_2$ samples under UV light illumination. Linear rise in H_2 yield with increase in illumination time was observed. Following trend in activity was observed: $C@TiO_2EG20$ (44.6 $\mu\text{mol/h}$) > $C@TiO_2EG25$ (26

$\mu\text{mol/h}$) > C@TiO₂EG50 (15 $\mu\text{mol/h}$) > TiO₂ (11.2 $\mu\text{mol/h}$) ~ C@TiO₂EG14 (11 $\mu\text{mol/h}$) > C@TiO₂EG10 (10 $\mu\text{mol/h}$) > C@TiO₂EG75 (5.6 $\mu\text{mol/h}$) > C@TiO₂EG100 (3.9 $\mu\text{mol/h}$). Maximum activity H₂ evolution activity was observed over C@TiO₂EG20 sample with carbon content of 3.8 % w/w @ 44.6 $\mu\text{mol/h}$ and AQE 1.6 %, ~ 4 times higher than pristine TiO₂. To further enhance the activity, 1 % w/w Pt was photodeposited over the C@TiO₂EG20 sample and the rate of H₂ generation was found to be 6405.4 $\mu\text{mol/h/g}$.

To check the performance of photocatalyst for actual application, rate of H₂ generation was evaluated under sunlight illumination (Fig. 5.13b). Following trend in activity was observed: C@TiO₂EG20 (9.7 $\mu\text{mol/h}$) > C@TiO₂EG25 (7.5 $\mu\text{mol/h}$) > C@TiO₂EG14 (6.8 $\mu\text{mol/h}$) > TiO₂ (4.1 $\mu\text{mol/h}$) > C@TiO₂EG50 (3.3 $\mu\text{mol/h}$) > C@TiO₂EG10 (2.8 $\mu\text{mol/h}$) > C@TiO₂EG75 (0.4 $\mu\text{mol/h}$) ~ C@TiO₂EG100 (0.4 $\mu\text{mol/h}$). Maximum activity was observed over C@TiO₂EG20 with rate of H₂ evolution of 9.7 $\mu\text{mol/h}$ with AQE of 0.86 % (Fig. 5.13b). After loading of Pt the H₂ yield increases by 14 times and maximum activity was observed over Pt/C@TiO₂EG20 (136 $\mu\text{mol/h}$) which is 33 times more than that compared to pristine TiO₂ sample. AQE was found to be 11.44 %.

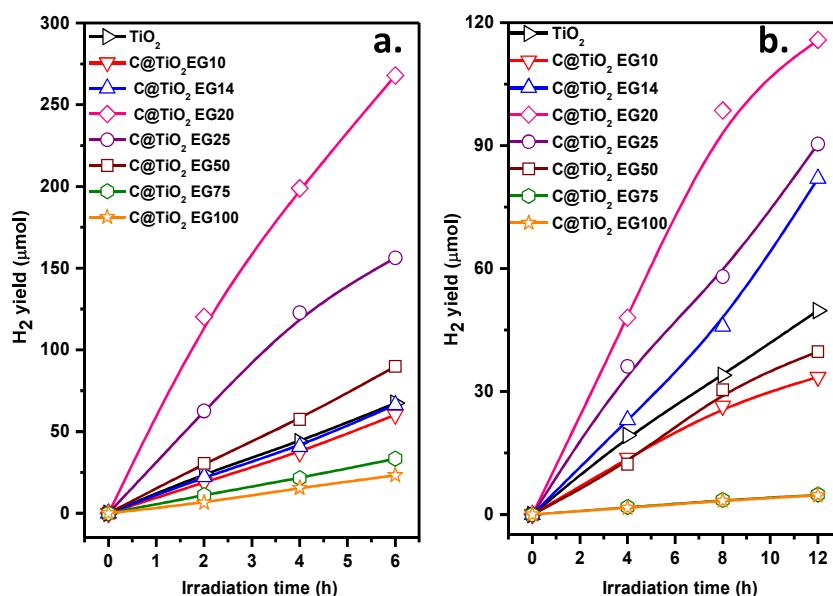


Fig. 5.13 H₂ yield generated over TiO₂ and C@TiO₂ samples under a. UV-visible and b. sunlight illumination.

Similar trend in activity was observed under both UV-Visible and sunlight illumination. Initially activity increases with increase in carbon content then reaches to an optimum value. On further addition of carbon H₂ yield found to decrease. Carbon plays an important role in determining the activity of the sample. Activity at high carbon content is low although high carbon content imparts high visible light absorption. This implies that the excess of carbon acts as optical filter restricting the light reaching to the photocatalytically active TiO₂. Hence low activity at higher carbon content was observed. This infers that it is important to optimize amount of carbon to get maximum H₂ generation.

The stability of the most active Pt/C@TiO₂EG20 sample was evaluated under sunlight for consecutive 8 days with irradiation time of 4 h per day (total 32 h of irradiation). After every 8 h of illumination sample solution was evacuated. Almost constant H₂ evolution was observed for 32 h under sunlight (Fig. 5.14).

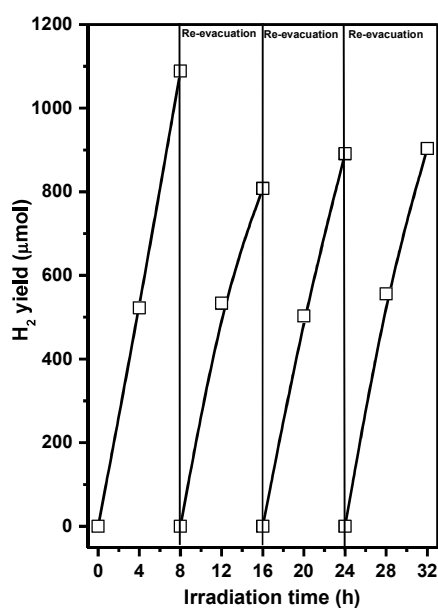


Fig. 5.14 Sustained H₂ generation over Pt C@TiO₂EG20 sample observed under sunlight for 32 h.

5.4 Conclusion

C coated TiO₂ composites were synthesized with varying amount of carbon 0.14 to 14.7 % w/w. Decrease in crystallite size was observed from 22.9 to 5.8 nm with increase in

carbon content. This shows that presence of carbon restricts growth of TiO₂ particles which is also confirmed by Raman spectroscopy. Presence of G and D band reveals the presence of sp² hybridized carbon atoms in graphite like arrangement and disorder sp² carbon atom in the structure respectively. Shift in D and G band was observed in C@TiO₂ composite which reveals structural imperfection or presence of nanocrystalline graphite. XAS reveals that the Ti exists in +4 oxidation state in bulk. Also local environment in Ti in TiO₆ octahedra is affected by carbon incorporation. Second co-ordination (Ti-Ti) is not affected due to carbon incorporation. XPS shows that with increase in carbon content surface hydroxylation increases also it shows presence of sp² hybridized carbon, C-OH and C=O group on the surface. Chemical composition on surface was derived using XPS reveals that surface has become richer in carbon as suggested by [C]/[Ti] and [C]/[O] ratio. Also systematic peak shift towards higher binding energy of Ti 2p shows growing interaction between Ti-C on surface with increase in carbon content. Surface area and pore volume increased, particle size decreased with increase in carbon content. Light absorption in visible region enhances with increasing the carbon content but at the same time increase in activity was not observed. Optimum amount of carbon is required to enhance the activity as excess of carbon might acts as optical filter. Highest H₂ generation @ 136 μmol/h/0.1g with AQE of 11.44 % was observed over Pt/C@TiO₂EG20 photocatalyst under sunlight. Enhanced surface area, favourable morphology, light absorption properties, interaction of C with Ti contributed positively to enhance the photocatalytic H₂ generation over C@TiO₂EG20 in sunlight having carbon content of 3.8 % w/w.

Performance of Most Active Photocatalyst, $\text{Cu}_{0.02}\text{Ti}_{0.98}\text{O}_{2-\delta}$ in Upscaled Photoreactors under Sunlight

6.1 Introduction

As explained in Chapter 1, photocatalytic water splitting has emerged as potential technique for production of H_2 from abundantly available water and renewable solar energy in presence of a photocatalyst [159,287–289]. Primarily, photocatalyst facilitates the absorption of solar energy and convert it into chemical energy. Photocatalytic water splitting can be achieved by suspending the powdered photocatalyst in water under sunlight illumination. The simplicity of this process has attracted researchers worldwide for large scale production of H_2 . The process has potential to provide a viable solution for the emerging energy crises and environmental concern. Main components of photocatalytic water splitting are photocatalyst in powder form, quartz/pyrex photoreactor, light source and sacrificial reagent in case of non-direct water splitting. Extensive research [97,110] took place throughout the globe with a common objective of designing visible light active, stable and efficient photocatalyst. However, the actual solution and desired efficiencies have not been achieved. The major issues associated with the process are faster recombination of photogenerated charge carrier e^-/h^+ and inability to use visible light which constitute the major portion of sunlight [37]. To overcome these problems development of photocatalyst with proper electronic, structural and optical properties are required. For electron economy, a sacrificial reagent is employed which can scavenge the holes produced and can prevent loss of electrons in the recombination reactions which are otherwise used to reduce the water to H_2 [290]. Use of methanol as sacrificial reagent is undesirable, as itself it is a fuel and

sacrificing a fuel to produce another fuel is meaningless. Thus, for commercialization, cheap sacrificial reagent such as glycerol which is a byproduct of biodiesel or any other organic compound with insignificant economic value can be used.

Results with respect to H₂ yield if compared are found to be different from different labs, as experimental condition varies from laboratory to laboratory. This implies that photocatalytic activity depends on experimental conditions such as light source, reaction cell or photoreactor, amount of catalyst loaded, amount and type of sacrificial reagent, configuration of lamp and photoreactor etc. Therefore, it is mandatory to study the effect of these parameters and optimize them in order to get maximum efficiency in H₂ production. Several studies were found in literature on the optimization of these parameters. Mangrulkar et al [285] has also studied the effect of the operational parameters and optimized them for better yield. Sreethawong et al [129] has also emphasized the importance of optimization of operational parameters for high H₂ production. Villa et al. [291] also studied the effect of several experimental parameters, such as pH, concentration of sacrificial reagent and catalyst loading for photocatalytic H₂ generation reaction over (Zn_{0.78}Cd_{0.22})S photocatalyst using formic acid as sacrificial reagent.

TiO₂ is an inert, chemically stable, robust conventionally known photocatalyst [36,37,243,292,293]. Although TiO₂ has gain much popularity as photocatalyst still its activity is low due to increased e⁻/h⁺ pair recombination and limited absorbance of visible light. Hence in the previous chapters attempt was made to improve the light absorption properties as well as electronic properties of TiO₂ by doping with Cu, forming *pn* junction composite with CuO and NiO and forming carbon-TiO₂ heterojunction. Among all the photocatalyst Cu_{0.02}Ti_{0.98}O_{2-δ} (referred as CuTi(2)) has shown enhancement in activity in sunlight and UV-Visible light with H₂ yield of 36 and 333.3 μmol/h/100mg with AQE of 3.6

and 20.8 %, respectively in absence of cocatalyst. Hence this low cost catalyst was chosen to study the enhancement of H₂ generation by modifying external parameters.

Along with the improvement of TiO₂ activity by structural modification using Cu²⁺ as substituent at Ti⁴⁺ site (which is already discussed in Chapter 3), studies were taken up to optimize the experimental parameters for effective utilization of photons falling on the system. Factors, such as photocatalyst loadings, ratio of water and sacrificial reagent, geometry of photoreactor with respect to light source in determining the overall photocatalytic hydrogen yield were evaluated. Also, efforts to substitute methanol by glycerol as sacrificial reagent were undertaken to make this process economical and ratio of water and glycerol optimized for efficient H₂ production. However, for practical application the H₂ yield over the photocatalyst must be monitored in sunlight. Sunlight is not constant throughout the day. This factor should be taken into account while commercializing the process. Hence effect of variable solar flux during the day on yield of H₂ generation was also studied. Therefore, it is necessary to monitor all the above mentioned factors before proceeding towards scaling-up the process. With this objective, in this chapter, detailed investigations on importance of various experimental parameters and also attempt to quantify their contribution towards photocatalytic H₂ yield using CuTi(2) as photocatalyst were discussed. For practical applications of Cu doped TiO₂ in scaled-up photocatalytic process, it is important to validate reproducibility in the properties (bulk and surface) of the sample, prepared in different batches following the same synthetic procedure. For this purpose, total of ~10 g of photocatalyst was prepared in two batches (BI and BII) of equal size (~5 g) under identical conditions. Sample from both the batches was thoroughly characterized by relevant techniques to establish the reproducibility of the synthesis procedure. Factors as mentioned above, responsible for determining the photocatalytic hydrogen yield were investigated using CuTi(2) photocatalyst. Experiments were carried out in systematic manner to delineate the

role of individual parameters under identical conditions. The results obtained from this study will provide valuable inputs for applying CuTi(2) photocatalyst for large scale solar hydrogen generation.

6.2 Experimental

6.2.1 Synthesis of CuTi(2) powder

Cu²⁺ (2 mole %) was substituted at Ti⁴⁺ site in TiO₂ lattice by adopting sol-gel method. Nanosized Cu_{0.02}Ti_{0.98}O_{2-δ} was prepared by mixing cupric acetate trihydrate and titanium isopropoxide in appropriate amount as explained in chapter 3. A total of ~10 g of sample was prepared in two batches of ~5 g each. Samples in two batches were named as CuTi(2)-BI and CuTi(2)-BII throughout the manuscript. Schematic of synthesis procedure is shown in Fig. 3.1.

6.2.2 CuTi(2)/ITO/PET Films

The required amount of CuTi(2) powder, titanium isopropoxide and ethanol taken in a molar ratio of 1:0.035:19.5 were homogenized by sonication for 30 min in an ice cold water bath. The homogeneous paste formed after sonication was coated on an indium tin oxide coated on polyethylene terephthalate (ITO-PET) films of geometrical area 21 cm² (0.7 cm x 30 cm) and surface resistivity ~100 Ωsq⁻¹ by doctor-blade technique. The area of film exposed in sunlight is same as its geometrical area referred as illumination area. To remove the hydrocarbons, prepared films were irradiated under UV light ($\lambda = 254$ nm) in a closed chamber in an ozone atmosphere. Ozone was formed by irradiation of dry oxygen for 2h. Total thickness of films inclusive of the ITO/PET supports was ~12 microns.

6.2.3 Characterization techniques

The samples prepared in two different batches are thoroughly characterized by relevant techniques. XRD patterns were recorded on a Philips diffractometer (model PW 1710), equipped with a graphite monochromator and Ni-filtered Cu-K α radiation. The crystallite size was calculated from the XRD line width using the Scherrer equation. XAFS measurements were carried out at Cu K-edge in fluorescence mode at the Scanning EXAFS Beamline (BL-9) at the INDUS-2 Synchrotron Source (2.5 GeV, 100 mA) at the Raja Ramanna Centre for Advanced Technology (RRCAT), Indore, India [144–146]. XAS includes both Extended X-Ray Absorption Fine Structure (EXAFS) and X-ray Absorption Near Edge Structure (XANES). The beamline uses a double crystal monochromator (DCM) in the photon energy range of 4-25 KeV with a resolution of 10^4 at 10 KeV. N $_2$ - BET surface area was measured with a Quantachrome Autosorb-1 analyser using nitrogen as the adsorbing gas. The elemental analysis of Cu and Ti present in the oxide samples was evaluated using ICP-OES (*JobinVyon* JY 2000, France). XPS experiments were recorded on an electron spectrometer (SPECS, Surface Nano Analysis GmbH, Germany) using Mg- K α X-rays ($h\nu=1253.6$ eV) as the primary source of radiation with an overall energy resolution of the instrument of about 0.7 eV. The appropriate corrections for charging effects were made with the help of a C 1s signal appearing at 284.5 eV. Diffuse reflectance UV-visible spectra was recorded using a spectrophotometer of JASCO model V-530, Japan, scanned in the range of 200-1000 nm at the scanning speed of 200 nmmin $^{-1}$. The microstructure was studied using a Zeiss Gemini Plus field emission scanning electron microscope (FESEM) operated at 5 kV. High resolution TEM images were recorded on FEI-Tecnai G-20 microscope with LaB $_6$ filament operating at 200kV equipped with Gatan CCD camera. Edinburgh Instruments FLSP 920 system equipped with a 450 W Xe lamp having a Peltier element cooled red sensitive

Hamamatsu R955 PMT was used to record PL with a resolution of 3 nm at room temperature. All emission spectra were corrected for the detector response.

6.2.4 Photocatalytic activity

Photocatalytic activity was evaluated over CuTi(2) photocatalyst to optimize different experimental parameters as mentioned in text under different illuminations: sunlight and UV-visible light sources. Photocatalytic activity was performed in a rectangular quartz reactor of dimensions (10 x 2.1 x 2.1 cm³, 81 ml, Chapter 2), equipped with a gas sampling port for analysis and an evacuation valve. In a typical analysis, a required amount of catalyst was suspended in aqueous sacrificial reagent solution, evacuated before irradiation to provide air free conditions as oxygen acts as an electron scavenger and, on photo-adsorption, blocks the active sites for the reaction [223]. Photocatalysts suspended in water-methanol mixtures were then irradiated under UV-visible light source. The reaction assembly used under UV-visible irradiation is shown in Chapter 2. The emission spectrum of UV-visible, medium-pressure Hg lamp is given in (Chapter 2). The evolved H₂ was quantified using a gas chromatograph (model Michro-1100, Netel, India) equipped with a thermal conductivity detector (TCD), a molecular sieve column with argon as the carrier gas was employed in the isothermal temperature mode at 50 °C oven temperature.

For solar applications, experiments were conducted under direct sunlight during the afternoon (10.00-16.00 IST) on the terrace of our institute in a photoreactor (the details of photoreactor is given in brief in Chapter 2). The emission spectrum of sunlight and image of upscaled photoreactor with dimensions is shown in Chapter 1 and Chapter 2 respectively. Instead of evacuating, reaction mixture in big reactors was purged with argon gas to remove air before irradiation under sunlight. Evolution of H₂ bubbles were observed during sunlight irradiation on Cu-TiO₂ photocatalysts. Solar flux was measured daily in the peak hours and the average recorded during 11.00-15.00 IST were used for optimization studies and for

calculations of AQE. The flux of both sunlight and medium pressure mercury lamp was measured using a silicon photodiode based light meter LX 1108, Lutron Electronic.

A standard deviation (SD) and relative standard deviation (RSD) [150] in hydrogen yield obtained by varying a particular factor keeping other parameters constant was calculated for each factor. The SD and RSD were calculated by using following formula:

(i) Mean (\bar{x})

Mean is calculated using the following formula:

$$Mean(\bar{x}) = \frac{x_1 + x_2 + x_3 + \dots + x_n}{n} \quad \dots 6.2$$

Where $X_1, X_2, X_3, \dots, X_n$ are the individual results (hydrogen yield obtained in individual results) and n is the number of results.

(ii) Standard Deviation (SD)

Standard deviation (SD) is calculated using the following formula:

$$SD = \sqrt{\frac{(x_1 - \bar{x})^2 + (x_2 - \bar{x})^2 + (x_3 - \bar{x})^2 + \dots + (x_n - \bar{x})^2}{(n-1)}} \quad \dots 6.3$$

Where $X_1, X_2, X_3, \dots, X_n$ are the individual results, \bar{x} is the mean and n is the number of results.

(iii) Relative standard deviation (RSD)

Relative standard deviation (RSD) is calculated using the following formula:

$$Relative\ standard\ Deviation\ (RSD) = \frac{SD \times 100}{\bar{x}} \quad \dots 6.4$$

Where \bar{x} is the mean, SD is standard deviation.

6.3 Results and discussion

6.3.1 Characterization

The present study is undertaken to establish the significance of different experimental parameters and to quantify their effect on H₂ yield. For this purpose, relatively large amount

of $\text{Cu}_{0.02}\text{Ti}_{0.98}\text{O}_{2-\delta}$, CuTi(2) sample was synthesized by sol-gel route in two batches of 5 g each. To establish that CuTi(2) sample produced in both the batches, was either chemically identical or similar, the sample from both the batches (abbreviated as CuTi(2)-BI and CuTi(2)-BII) was characterized for surface and bulk properties using different techniques. Fig. 6.1a shows XRD pattern of CuTi(2) sample synthesized in two different batches and both shows presence of single phase indexed as anatase TiO_2 phase in agreement with JCPDS card no: 21-1272. It crystallizes in the tetragonal space group with $a = 3.785(1) \text{ \AA}$, $c = 9.501(1) \text{ \AA}$, cell volume = $136.13(1) \text{ \AA}^3$ and $Z = 4$. Morphology and bulk characteristics of both the samples derived from different techniques are listed in Table 6.1. Surface area of CuTi(2) powder, synthesized under similar conditions was determined and found to be 73 and $60 \text{ m}^2\text{g}^{-1}$ for BI and BII respectively. Surface area recorded was within experimental error (RSD = 13.8 %) for both the batches. CuTi(2) from both batches were nearly of similar crystallite size (XRD) and particle size (6-13 nm) derived from FESEM and TEM as listed in Table 6.1. The local structure was probed using EXAFS Fig. 6.1b and it was revealed that the local environment around Ti and Cu cations was quite identical and Cu existed in +2 oxidation state in bulk CuTi(2) oxide prepared in both the batches as confirmed by characteristic peak observed in XANES pattern [inset of Fig. 6.1b, Table 6.1]. The $\text{Cu}^{2+}\text{-O}$ bond length was found to be $\sim 1.88 \text{ \AA}$ and 1.87 \AA , coordination number of 5.2(3) and 5.2(5) and distortion (σ) in lattice were obtained to be 0.006 and 0.008 in CuTi(2)BI and BII respectively, as mentioned in Table 6.1. The surface composition, oxidation states of different species on surface was analyzed using XPS and tabulated in Table 6.1. Fig. 6.1c shows high resolution spectra of Cu 2p, Ti 2p and O 1s. Cu shows presence of both +1 and +2 species in BI and BII with $\sim 0.8\text{-}0.85$ of Cu, 18.5-25.3 of Ti and 73.8-80.6 atom % of O species on surface. The composition with respect to Cu and Ti content present in bulk and surface did not differ much. DRS spectra (Fig. 6.1d) recorded in the region of 200-800 nm shows

identical optical characteristics of both samples with band gap at 2.92 eV. Photoluminescence properties of CuTi(2)-BI and BII were compared, along with TiO₂ as shown in Fig. 6.1e. TiO₂ shows a broad peak in the range of 350-540 nm with the maximum peak around 398 nm corresponding to band edge emission, along with other minor peaks due to emission from defects. However, Cu substitution in TiO₂ has shifted the band edge emission to lower wavelength of 372 nm. PL spectra recorded for CuTi(2) prepared in two batches was similar.

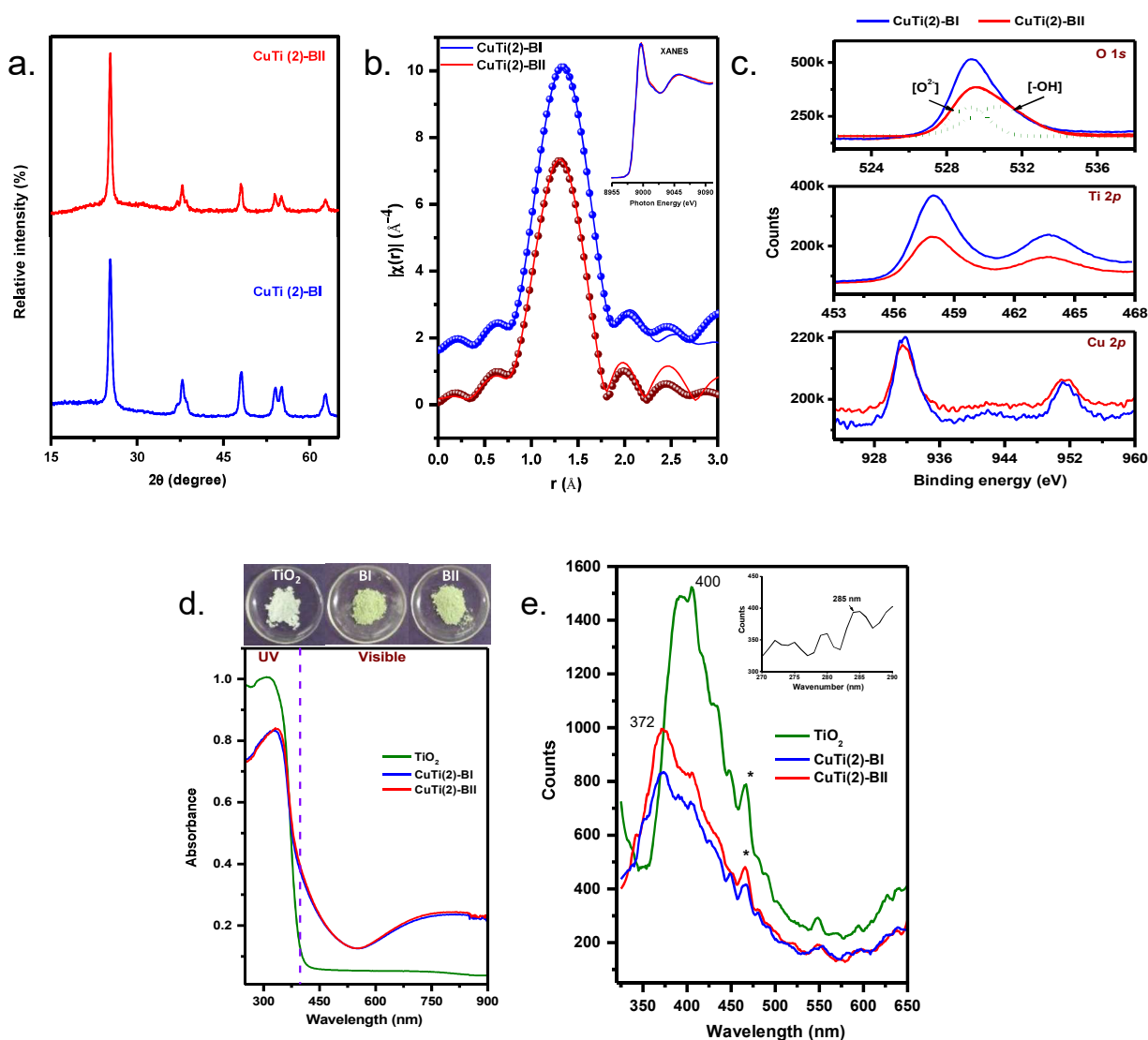
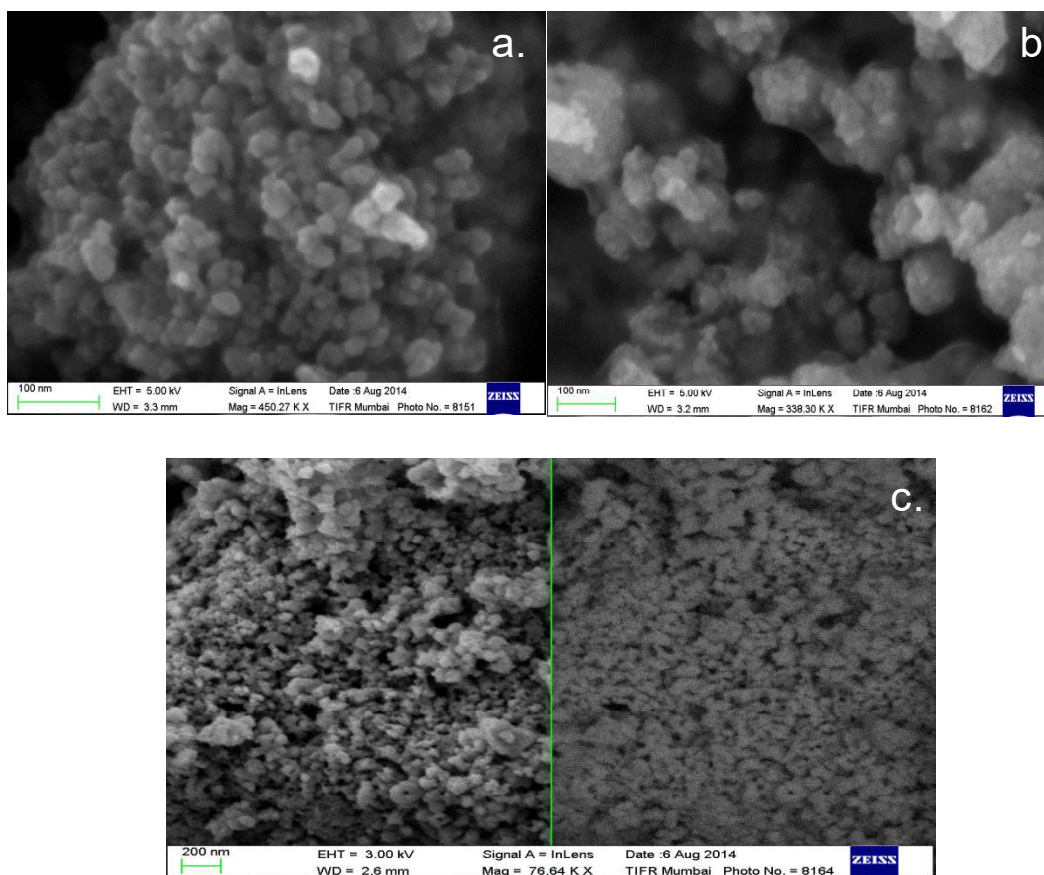


Fig. 6.1 a. XRD pattern of CuTi(2) synthesized in two different batches BI and BII, b. Experimental $\chi(r)$ versus r spectrum at Cu K edge of the CuTi(2)-BI and CuTi(2)-BII samples along with the best theoretical fits. Round circles are the experimental spectra data fitted with TiO₂ model as shown by solid continuous line. Inset shows XANES spectra of CuTi(2)-BI and CuTi(2)-BII samples obtained from both the batches recorded for Cu K-edge, c. XPS spectra recorded of Cu 2p, Ti 2p and O 1s for CuTi(2)-BI and BII samples, d. diffuse UV-visible

reflectance spectra (DRS) of CuTi(2) of BI and BII samples with pristine TiO₂, e. photoluminescence spectra of CuTi(2)-BI and BII along with TiO₂ recorded by exciting the sample at 285 nm and excitation spectra is given as inset. * artefact at 467 nm.

Surface morphology of sample was evaluated by FESEM and HR-TEM. Fig. 6.2 shows the FESEM images of two batches. FESEM shows uniform shape and nanosized particles of copper doped titanium dioxide in both batches. X-rays characteristic to Cu and Ti were observed in EDX and were quantified to reveal the bulk chemical composition. The bulk composition was further confirmed by ICP-OES and was found to be (Cu = 2 and Ti = 98 mol %) in both batches in agreement with the calculated results (Cu = 2.71 and Ti = 97.28, mol %, Table 6.1).



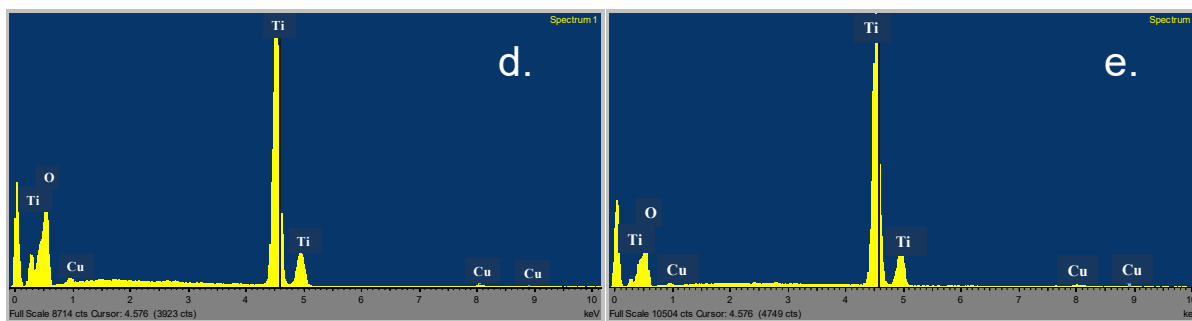


Fig. 6.2 FESEM images of CuTi(2) prepared from batch (a) BI (b) BII (c) Back scattered image of CuTi(2)BII, along with EDX of (d) CuTi(2)-BI and (e) CuTi(2)-BII.

HR-TEM images of CuTi(2)-BI are shown in Fig. 6.3. Fringe width of 0.35 nm shows presence of anatase TiO₂ particles in both the samples.

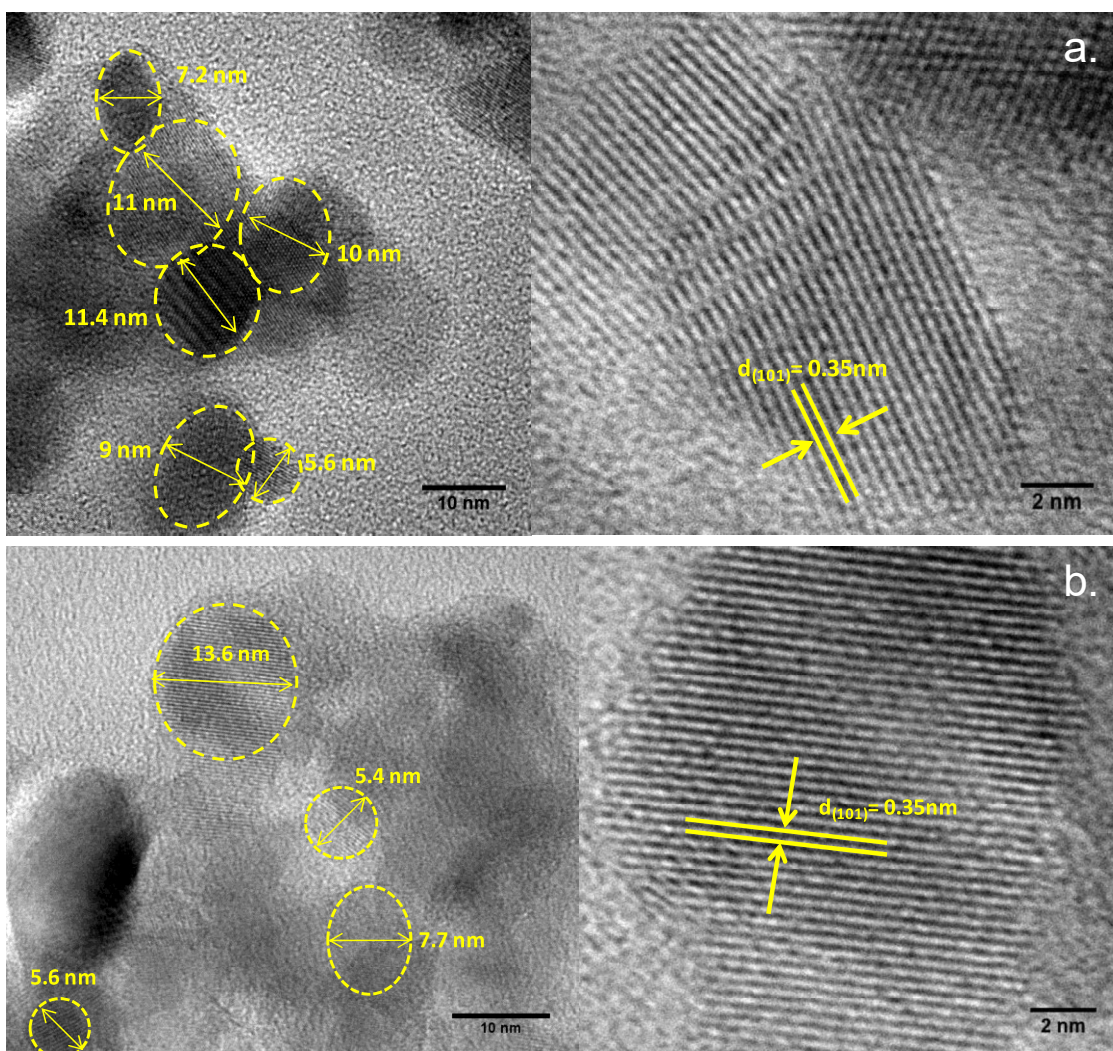


Fig. 6.3 Low and high resolution TEM images of (a) CuTi(2)-BI and (b) CuTi(2)-BII. Particle sizes are marked with yellow circles. Fringe width of 0.35 nm corresponds to anatase (d_{101}) TiO₂ phase.

From above, it was inferred that the bulk and surface properties of CuTi(2) nanopowders synthesized in different batches were found to be similar (within experimental error), infact some are identical (Table 6.1, RSD are nil for some parameters).

Table 6.1 Consistency of morphological and bulk properties of $\text{Cu}_{0.02}\text{Ti}_{0.98}\text{O}_{2-\delta}$, CuTi(2)-BI and BII nanopowders obtained from two different batches synthesized by sol-gel route.

S. No	Characterization	Batch-1 (BI)	Batch-2 (BII)	Expected values	Relative Standard Deviation, (RSD, %)
1.	Crystallite size calculated using Scherrer equation (nm)	12-13	12-13	-	NA
2.	N_2 -BET surface area (m^2g^{-1})	73	60	-	+/- 13.8
3.	Particle size from TEM (nm)	6-13	6-13	-	NA
4.	Chemical composition from EDX (mol %)	Ti: 97.82, Cu: 2.18	Ti: 97.75, Cu: 2.25,	Expected chemical composition Ti: 98.0, Cu: 2.0	Ti: 0.05% Cu: 2.23%
5.	Chemical composition from ICP-OES (mol %)	Ti: 97.28, Cu: 2.71	Ti: 97.28, Cu: 2.71	Expected chemical composition Ti: 98.0, Cu: 2.0	Nil
6.	Bond length $\text{Cu}^{2+}\text{-O}$ (\AA)	1.88(3)	1.87(2)	1.94	0.38
7.	Coordination Number from EXAFS	5.0(5)	5.2(5)	6	Nil
8.	Lattice distortion from EXAFS	0.005(2)	0.008(1)		20.2
9.	Bulk oxidation state from XANES	Cu^{2+}	Cu^{2+}	-	Nil
10.	Surface chemical composition from XPS (atom %)	Cu: 0.85 Ti: 25.3 O: 73.8	Cu: 0.79 Ti: 18.5 O: 80.6		Cu - 5.05, Ti - 21.96, O - 6.29
11.	Oxidation states of different species on surface from XPS	Cu: +1, +2 Ti: +4 O: -2	Cu: +1, +2 Ti: +4 O: -2	-	Nil
12.	Band gap calculated by Kubelka Munk Function (eV)	2.92	2.92		Nil

From Table 6.1 it can be inferred that for actual application, the deployment of photocatalyst prepared in different batches will not hamper the smooth running of the process. Or in other words, sol-gel route is simple and yields powders with reproducible

chemically identical oxides. For practical applications, synthetic procedure is a matter of concern - should be such which does not involve intricate steps highly sensitive or dependent on pH, temperature etc.- for yielding powders with identical bulk properties and surface morphology. Further optimization studies were carried out on this photocatalyst for the actual application in solar energy.

6.3.2 Photocatalytic activity

6.3.2.1 Optimization of experimental parameters for evaluation of photocatalytic activity under UV-visible light illumination

6.3.2.1.1 Optimization of amount of photocatalyst

Optimization of photocatalyst loadings is an important factor for H₂ generation. The amount of photocatalyst was varied from 50- 150 mg per 15 ml (3.3 to 10 mg/ml) of aqueous methanol solution by keeping other experimental conditions and illumination area constant. Reaction was carried out in 81 ml of reactor with illumination area of 20 cm². This experiment was performed under static condition. Fig. 6.4a shows effect of varying catalyst amount on H₂ yield. No reaction was observed with or without catalyst loading in presence of dark. This shows that reaction is solely photocatalytic in nature. A blank reaction of water and methanol mixture (without photocatalyst) was irradiated under UV-Visible lamp. No evolution of H₂ was observed. This implies that H₂ generated only in presence of photocatalyst and light. Fig. 6.4a depicted that with increase in catalyst amount H₂ yield increases and reaches an optimum value of 100 mg/ 15 ml. But the rise in H₂ yield is not proportional with catalyst loading amount. Initial rise in H₂ yield till maximum, can be attributed to increase in active sites with increase in catalyst loading amount. Maximum H₂ yield of 384.9 μmol/h was observed with 100 mg of photocatalyst. With further addition of photocatalyst, a decrease in H₂ evolution was observed. 150 mg catalyst loading has even

shown lesser activity than that observed with 50 mg of catalyst. This shows that with increase in catalyst amount a portion of the catalyst is hidden beneath the upper layer of catalyst and consequently reduces the optical path length or effective intensity of photons per unit length decreases. This infers that proper dispersion of photocatalyst and illumination area of reactor is playing an important role. The following trend was observed $100 > 75 \approx 50 > 150$ mg per 15 ml of solution in 81 ml capacity reactor.

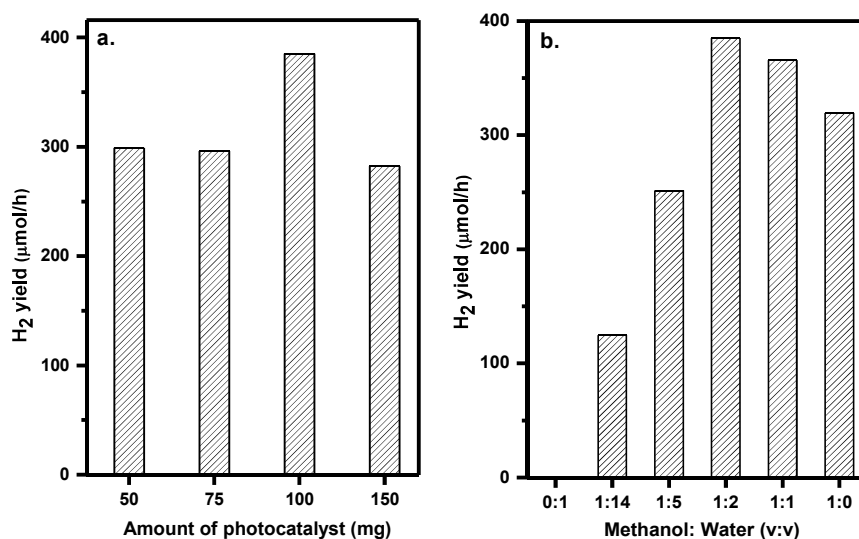


Fig. 6.4 a. Variation of hydrogen yield with change in a. photocatalyst loadings, (Experimental conditions: Reaction mixture containing constant water to methanol ratio (33% v/v, 15 ml) with suspended photocatalyst in different amounts evacuated and irradiated under UV-visible light in a photoreactor of 81 ml capacity providing an illumination area of 20 cm²), b. concentration of sacrificial reagent, methanol in water (v/v) evolved over CuTi(2) under UV-visible light. (Experimental conditions: 0.1 g of CuTi(2) photocatalyst suspended in reaction mixture containing varying concentration of water to methanol (total volume = 15 ml), evacuated and irradiated under UV-visible light in a photoreactor of 81 ml capacity providing an illumination area of 20 cm²).

6.3.2.1.2 Ratio of water and sacrificial reagent as methanol

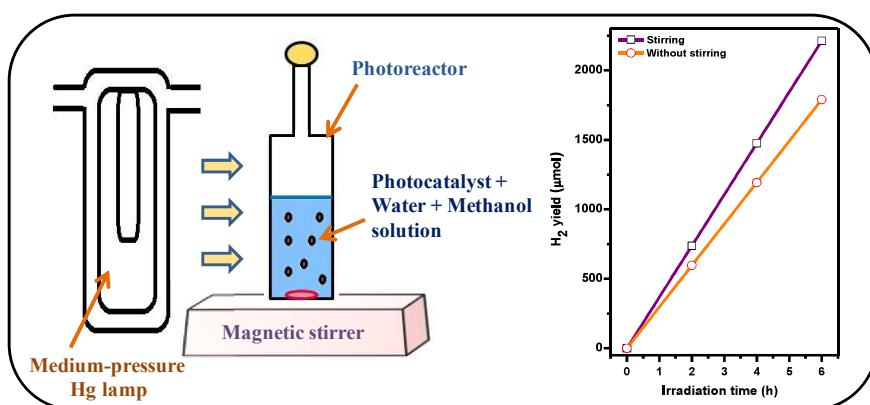
One of the factor which plays crucial role for uphill reaction of water splitting is fast rate of electron-hole pair recombination affecting adversely to photocatalytic efficiency of reaction. Hence, addition of a reducing agent which will get oxidized by holes, avert to recombination with electrons, helps to assist reduction of water for H₂ generation. The

reducing agent, here methanol, sacrifices itself for maintaining the inflow of photogenerated electrons or electron economy and therefore is referred as sacrificial reagent. To optimize the amount of methanol in the reaction mixture, H₂ yield was monitored over following v/v ratio of methanol: water, 0:1, 1:14, 1:5, 1:2, 1:1 and 1:0 v/v. Fig. 6.4b shows effect of varying ratio of water and sacrificial reagent on H₂ production under UV-visible irradiation. This mixture was irradiated under UV-visible lamp as mentioned in experimental section. Initially, increase in activity was observed with increase in methanol content and reaches an optimum value 1:2 v/v. Further addition of methanol content more than optimum value resulted into a lower H₂ yield. At high concentration probably, methanol may be blocking the surface active sites resulting into lower adsorption of water molecules on the surface thus deteriorating the photocatalytic activity.

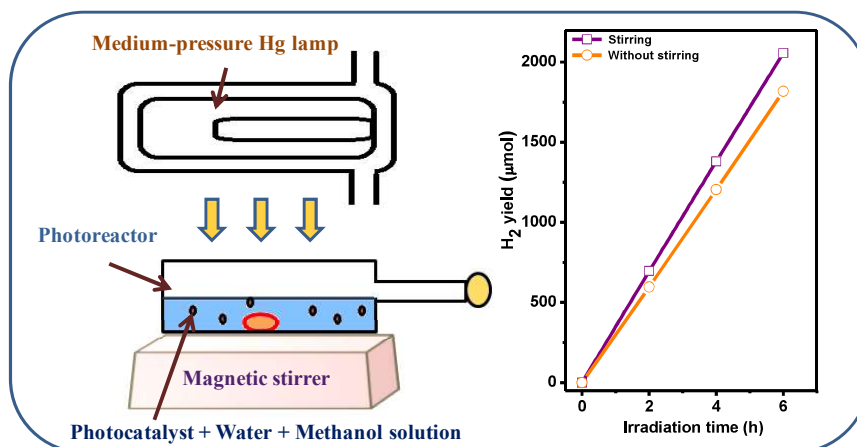
6.3.2.1.3 Configuration of lamp and reactor assembly

H₂ yield was monitored with different configuration and geometry of reactors and light sources. Two configurations of reactor with respect to light source were chosen. In first assembly, the reactor and light source are configured in horizontal positions, whereas in second both were placed vertically. Side views of both assemblies are depicted in Fig. 6.5. In vertical geometry it is expected that due to gravitational forces, the catalyst will settle down at the bottom and poor dispersion will affect the yield. To prevent the interference from catalyst dispersion in measurements, photocatalytic hydrogen yield was monitored under stirring conditions and was compared without stirring conditions using both the geometries. H₂ yield of 302.9 $\mu\text{mol/h}$ and 298.25 $\mu\text{mol/h}$ was obtained with horizontal arrangement and vertical arrangement without stirring respectively. H₂ yield of 342.79 $\mu\text{mol/h}$ (AQE of 12.36 %) and 368.73 $\mu\text{mol/h}$ (AQE of 10.02 %) was obtained with horizontal and vertical arrangement with stirring respectively. Flux observed for UV lamps used in two different

geometries were different and that explains reverse trend of AQE with respect to the hydrogen yield. 13 % and 23 % rise in H₂ yield was observed in horizontal and vertical geometry, respectively during stirring. This indicates that stirring has pronounced effect when reaction carried out in vertical geometry as it barely allow the catalyst to settle down and keep it in suspended form in a solution. Stirring is necessary in vertical geometry, whereas in horizontal geometry particles are well dispersed in solution and covers larger illumination area. The effective illumination area to which reaction mixture exposed was 7 cm² in case of vertical arrangement whereas in horizontal geometry it was 20 cm². This suggests horizontal geometry disperses photocatalyst in larger area and therefore results in covering larger illumination area as compared to that in vertical arrangement. Rather et al. [294] also reported five times enhancement in rate of photocatalytic H₂ evolution when illumination area was doubled in case of horizontal geometry.



a



b

Fig. 6.5 Role of different configurations in determining photocatalytic hydrogen yield. Pictorial representation of side view of a) Vertical geometry: Photoreactor and light source both are standing vertical and b) horizontal geometry: Photoreactor and light source are in horizontal position. Role of stirring for proper dispersion of photocatalyst in both geometries on hydrogen yield is also shown. (Experimental conditions: 0.1 g of photocatalyst was suspended in aqueous methanol solution (33 %, 15 ml), evacuated and irradiated under UV-visible light in respective geometries. The flux of radiation was recorded using silicon photodiode luxmeter in individual geometry to calculate the AQE achieved in both configurations).

6.3.2.2 Optimization of experimental parameters under sunlight illumination

In order to visualize the process for commercial production of photocatalytic H₂ from water, experiments were performed by illuminating the samples with actual sunlight on the terrace of our institute. For that purpose, first it was investigated that how hydrogen yield is affected with turbulence in solar flux on hourly basis during a year or a day. Also, affect of parameters such as loading of photocatalyst and use of cheaper sacrificial reagent like glycerol (instead of methanol) on H₂ production from sunlight were studied and are discussed below.

6.3.2.2.1 Effect of solar flux variations on H₂ yield

Solar energy reaching on earth surface is intermittent and variable in nature. It changes with time and season. The photon per square meter or intensity of radiation fluctuates throughout a year. Also photocatalytic H₂ yield strongly depends on incident

intensity of light source. Therefore it is mandatory to study the effect of variation of H₂ production with the variation of solar flux. The flux of sunlight varies during the day and also throughout year. To study the effect of variation of flux on photocatalytic activity, H₂ yield over CuTi(2) photocatalyst was monitored at different months and days.

Mumbai observes very high flux during May as compared to October month. The average flux values during these months were recorded and mentioned in Table 6.2.

Table 6.2 Flux of sunlight at different hours during months of May and October in Mumbai.

Time (IST)	October	May
	W/m ² §, *	W/m ²
10.30	108	260
12.15	121	322
14.20	95	235
16.10	57	249

§ Flux was measured using light flux meter based on silicon photodiode which has a photoresponse in UV-visible light (190-1100 nm). *1Wm⁻² = lux/683 at 550 nm

A fresh sample of the most active CuTi(2) photocatalyst was tested during different months to monitor the changes in hydrogen yield with variation in sunlight flux. For this, 100 mg of CuTi(2) photocatalyst was dispersed in aqueous methanol solution (33 % v/v) in 81 ml reactor with illumination area of 20 cm² and allowed to be illuminated under sunlight during 10:30 to 16:30 IST. Sunlight flux values increased almost three fold from October to May and as expected H₂ yield also increased from 36 μmol/h (AQE = 3.6 %) to 110 μmol/h (AQE = 3.13 %), respectively. Although the flux value increases three times but AQE nearly remains the same.

For monitoring hydrogen yield with hourly fluctuations of solar flux experiment, two extreme days were selected such that one is a bright sunny day and other is a cloudy day. Both the days, 100 mg of CuTi(2) photocatalyst was dispersed in aqueous methanol solution (33 % v/v) in 81ml reactor with illumination area of 20 cm² and allowed to be illuminated

under sunlight. Irradiation was carried out on first day at 10:40 till 17:40 IST and H₂ yield and flux were recorded after every one hour. On second day experiment was performed in a similar way except the irradiation time changed from 10:45 to 16:30 IST. Fig. 6.6 shows rate of H₂ generation as a function of hourly flux during the daytime.

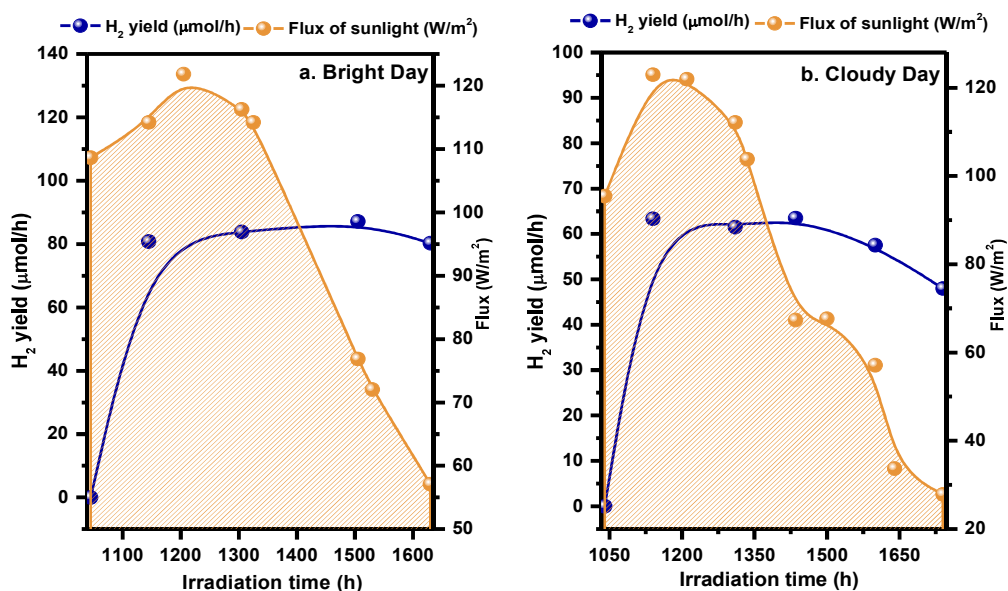


Fig. 6.6 Rate of hydrogen generation was monitored as a function of hourly fluctuations in solar flux during day time during 10:40 to 17:40 IST. Day-1 is bright sunny day and day-2 is a relatively cloudy day. (Experimental conditions: 0.1 g of CuTi(2) photocatalyst was suspended in aqueous methanol solution (33 %, 15 ml), evacuated and irradiated under direct sunlight. Rate of hydrogen evolved per hour was plotted as a function of solar flux. The solar flux was recorded using silicon photodiode luxmeter).

From the data obtained it was inferred that photocatalytic rate of H₂ generation/hour was highest and nearly constant during 11:00 to 15:00 IST in the afternoon. After 15:00 h, a noteworthy decline in H₂ generation rate was observed with decrease in sunlight flux. Same experiment was repeated on another day which was relatively cloudy and relative standard deviation (RSD) in H₂ yield was calculated to be +/- 3.82% and +/- 4.53% in time zone of 10.30 to 16.30 IST on bright and cloudy day respectively. Deviation of H₂ yield was more on cloudy days and beyond 16:30 h. These studies have provided a daily window of 11:00 to 15:00 h throughout the year, to be utilized for a commercial scaled up process. During this window, hydrogen generation with constant yield and maximum efficiency can be achieved

and will allow avoiding less efficient/productive hours of a day and consequently will be helpful in slashing the running cost and shaping the economics of process.

6.3.2.2.2 Effect of catalyst loading on H₂ yield by keeping illumination area constant

AQE is directly proportional to H₂ yield and inversely with illumination area. This implies AQE will increase only if H₂ yield increases at a constant illumination area. Therefore, in another set of experiments, illumination area was kept constant by fixing the reactor volume and solution volume (water + methanol) to 990 and 250 ml respectively, and varying concentrations of catalyst (g/l) were tested.

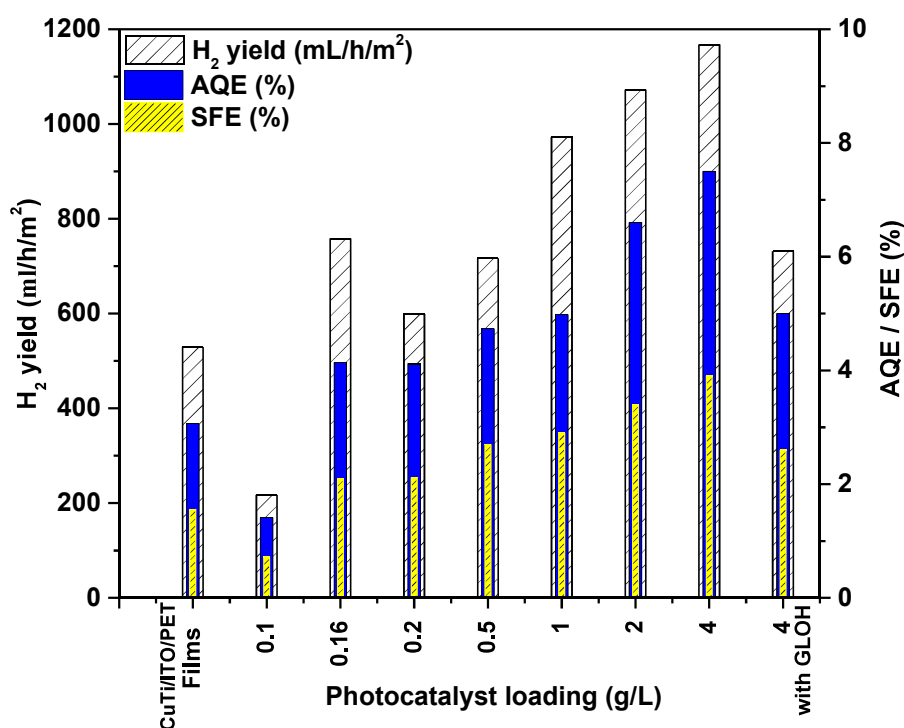


Fig. 6.7 Dependence of AQE of CuTi(2) photocatalyst on various factors such as 1. Concentration of CuTi(2) photocatalyst (0.1- 4 g/L) was optimized for a given reaction volume and illumination area (141 cm²). 2. Effect of different forms, powder or films on photoactivity was investigated by comparing H₂ yield over 25 mg of CuTi(2) powder with same amount of photocatalyst dispersed over ITO/PET films (illumination area over films = 0.7cm x 30 cm x 4 Nos = 84 cm²). 3. Effect of glycerol as sacrificial reagent on H₂ yield. Experiments were performed in a large sized reactor (~1 L) over CuTi(2) photocatalyst suspended in 250 ml of water + methanol (33 %) purged with argon gas and irradiated under direct sunlight. Experiment with Water + glycerol (15 %) was also performed. Blank ITO/PET films did not show any photocatalytic H₂ evolution.

AQE of $7.5 > 6.6 > 5.6 > 5.2 > 4.14 \approx 4.12 > 1.41$ % for $1 \text{ g} > 500 \text{ mg} > 250 \text{ mg} > 125 \text{ mg} > 50 \text{ mg} \approx 40 \text{ mg} > 25 \text{ mg}$ respectively of CuTi(2) photocatalyst under sunlight (Fig. 6.7) were achieved. Although, 1 g loading of catalyst has shown maximum H₂ yield of 735 $\mu\text{mol/h}$ with AQE of 7.5 %, it is important to understand that the rise in H₂ yield is non-linear with catalyst loading as shown in Fig. 6.7. In case of catalyst concentration upto 250 mg (1 g/L), the increase is considerable, whereas above that the rise in H₂ yield is very sluggish. Probably, the upper layer of photocatalyst shadows the lower layer and also blocks the penetration of light; hence under limited light illumination the contribution of lower layer towards H₂ yield was restricted. Shreethawong et al. [129] have also optimized the experimental conditions with respect to amount of photocatalyst and rationalized their results in terms of the availability of active sites on the TiO₂ surface and the penetration of photoactivating light into the suspension. The availability of active sites increases with the increase in photocatalyst concentration in the suspension, but the light penetration and the consequent photoactivated volume of the suspension shrink [295]. Thus, H₂ yield obtained over 50 mg of catalyst cannot be extrapolated to per g of catalyst.

From the above experiments, the maximum amount of H₂ was generated over 1g of CuTi(2) at the rate of 16 ml/h or 735 $\mu\text{mol/h}$ with 7.5 % of AQE and 3.9 % of SFE achieved in sunlight. Our results can be further extrapolated to suggest that H₂ at 1 L/h can be achieved photocatalytically, if the CuTi(2) photocatalyst is exposed to illumination area of 0.9 m² under above conditions. 1/20th of catalyst loadings i.e., 40-50 mg of CuTi(2) photocatalyst have also resulted in more than half of maximum H₂ yield, ca of 477 $\mu\text{mol/h/141cm}^2$ (or 0.758 L/h/m²) with 4.1 % of AQE and 2.1 % of SFE (Fig. 6.7). Lower loadings of photocatalyst are favourable as more and more water molecules can access the photocatalyst particles effectively under light illumination. Unlike high catalyst concentration where penetration of photoactivating light is blocked, in dilute catalyst concentrations all

photocatalyst particles realize maximum light illumination. Recently, Xiong et al. [296] have reported that addition of micrometer sized silica in the photocatalyst panel of $\text{Rh}_{2-y}\text{Cr}_y\text{O}_3/(\text{Ga}_{1-x}\text{Zn}_x)(\text{N}_{1-x}\text{O}_x)$ has improved the photoactivity. They found that addition of hydrophilic SiO_2 in between photocatalyst particles helped in providing interparticle voids, improved porosity of photocatalyst suitable for mass transfer of evolved gases at large scale. Also the access of water molecules by photocatalyst particles was improved by addition of inert silica.

However, we have also investigated the factors which limit the extrapolation of H_2 yield obtained over 50 mg of catalyst to 1 g of photocatalyst and is discussed in next section. This issue has not been properly surfaced in most of the manuscripts.

6.3.2.2.3 Variation of H_2 yield by varying illumination area

Effect of illumination area on photocatalytic activity was investigated by performing the activity tests in large sized tubular reactors by using a powder photocatalyst. For this purpose, photoreactors of different sizes were fabricated which can provide higher illumination area and can accommodate higher catalyst loadings. H_2 yield was monitored by changing area of illumination. In this 100 mg of photocatalyst is dispersed in 33 % aqueous solution of methanol and then irradiated in sunlight. H_2 yield enhanced from 110 to 183 and further to 251 $\mu\text{mol/h}$ when exposed to illumination area of 20, 32 and 45 cm^2 respectively (Table 6.3).

Table 6.3 Variation of H_2 yield with increase in illumination area

Sample	H_2 yield ($\mu\text{mol/h}$)	Illumination Area (cm^2)	AQE (η , %)
CuTi(2)	110	20	3.13
	183	32	3.23
	251	45	3.19

0.1 g catalyst suspended in water + methanol (33 % v/v, total volume of 15 ml) evacuated and irradiated under sunlight in reactor of capacity 81 ml with illumination area of 20 cm^2 .

*0.1 g catalyst suspended in water + methanol (33 % v/v, total volume of 15 ml) evacuated and irradiated under sunlight in up-scaled reactor of capacity 569 ml with illumination area of 32 cm^2 .

#0.1 g catalyst suspended in water + methanol solution (33 % v/v, total volume of 75 ml) evacuated and irradiated under sunlight in up-scaled reactor of capacity 569 ml with illumination area of 45 cm^2 .

Thus, illumination area (A), a geometrical factor, considerably affects the photocatalytic hydrogen yield. But there was no increment in efficiency (Table 6.3) of the photocatalyst, as the ratio of H₂ yield obtained at a given illumination areas (A) remains constant in the AQE and SFE calculations respectively.

6.3.2.2.4 Optimization of photocatalyst amount in upscaled ~2 L reactor

Not only increase in illumination area but proper dispersion of photocatalyst over given surface area is also mandatory. To further scale up the reaction, 2 L capacity reactor with circular geometry was designed for better stirring. The amount of photocatalyst is optimized by varying it from 50- 250 mg per 255 ml (3.3 – 10 mg/ml) of aqueous methanol solution by keeping other experimental conditions and irradiation area constant. Fig. 6.6 provided a time window of 11:00-15:00 IST found suitable for maximum and constant rate of H₂ generation. Hence all the sunlight experiments were carried out in 2 L of reactor with irradiation area of 172 cm² for duration of 4 h from 11:00-15:00 IST as a function of varying catalyst loadings (Fig. 6.8). Also, reaction mixture was stirred during the experiment to keep photocatalyst in dispersed form. Decreasing trend of activity for different catalyst loadings per 255 ml of solution was in concurrence with results obtained under UV-visible irradiation: 250 mg (507.12 μmol/h) > 100 mg (401.84 μmol/h) > 50 mg (231.34 μmol/h) as illustrated in Fig. 6.8. Under above stated conditions, H₂ yield increased with increase in catalyst loadings and reaches a maximum value of ~1 mg/ml (250 mg/ 255ml). As observed in above section, that H₂ yield is highly impropotional with catalyst loadings. The non linear rise in H₂ yield can be justified on the basis of availability of active sites on the surface of photocatalyst and the penetration of photoactivating sunlight in reaction mixture. In fact these results in conjunction with other literature reports suggest that lower catalyst loadings are more photoactivated under sunlight. The extrapolation of per g holds good provided illumination area of catalyst also increases proportionally. Photocatalytic hydrogen yield is proportional to

illumination area and not to catalyst loading. Thus, extrapolation of results without considering illumination area is inappropriate.

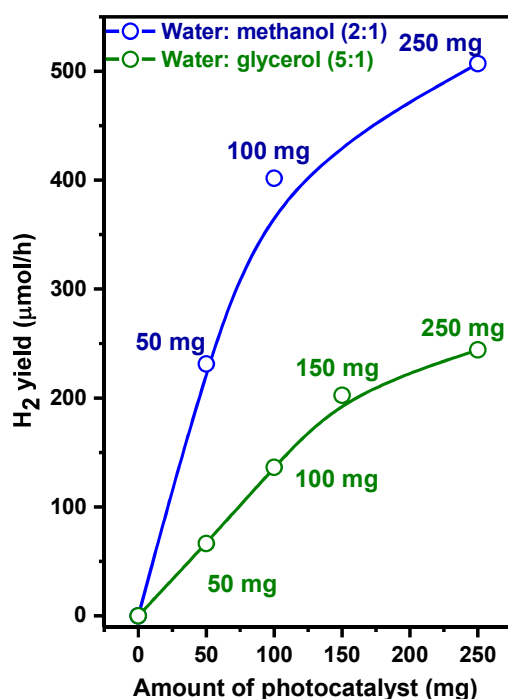


Fig. 6.8 Optimization of catalyst loadings in upscaled photoreactors under sunlight using constant concentration of methanol and glycerol as sacrificial reagents. (Experimental conditions: Different loadings of CuTi(2) was dispersed into ~255 ml of water + sacrificial reagent (methanol (33% v/v, 2:1 v/v) and glycerol (15%, 5:1 v/v) solution, purged with argon gas and irradiated under sunlight in upscaled reactor of 2L capacity with illumination area of 172 cm²).

6.3.2.2.5 Effect of loading of catalyst over ITO/PET film

Another attempt was made to enhance the efficiency further by spreading the minimum amount of photocatalyst over the maximum available illumination area. For this purpose, 6 mg of CuTi(2) was uniformly coated on 30 cms long and 0.7 cm wide ITO/PET films (total ~12 μ thickness) sized by a doctor blade technique. The performance of four such films with total area of 84 cm² and 24 mg of CuTi(2) photocatalyst was evaluated in 990 ml photoreactor with 250 ml of water + methanol solution under sunlight. For comparison, 25 mg of powder photocatalyst was also tested under identical conditions. CuTi(2) dispersed over ITO/PET films resulted in H₂ evolution at 198 μmol/h/84cm² (or 23,571 μmol/h/m² or

0.53 L/h/m²) was more than equivalent amount of powder form of catalyst (~136 μmol/h or 0.217 L/h/m²) as shown in Fig. 6.7. There was no H₂ evolution over blank ITO/PET films under identical conditions. Photocatalytic H₂ evolution over CuTi(2)/ITO/PET films was found to be highly efficient (AQE = 3.06 %) as compared to the equivalent amount of powders (AQE = 1.41 %). In addition to high efficiency obtained over very small amount of photocatalysts, other advantage it offers is easy recovery, handling and replacement of the catalyst after prolonged use. These are major issues which are of concern during scale- up of the hydrogen generation process.

6.3.3 Replacement of methanol by glycerol

Due to high rates of recombination reaction of photogenerated electrons and holes over photocatalyst, presence of sacrificial reagent becomes a necessity for efficient photocatalytic hydrogen generation from water splitting. Methanol is a precious organic molecule and itself can be used as fuel. Therefore, it becomes desirable to replace methanol by other organic compounds which have low commercial value. A candidate organic molecule as a sacrificial reagent for photocatalytic hydrogen production from water is glycerol. Glycerol is a by-product in soap manufacturing and more recently in biodiesel production [297]. Glycerol being renewable, safe, non-toxic, non inflammable with high boiling point qualifies it to be an appropriate compound employed for a large scale solar hydrogen production process. As a preliminary study, concentration of glycerol is optimized in 81 ml reactor over Pt/Cu_{0.06}Ti_{0.94}O_{2-δ} (referred as Pt/CuTi(6)). We have evaluated the photocatalytic H₂ yield generated over Pt/CuTi(6) catalyst from water in presence of glycerol as a sacrificial reagent and compared with water- methanol mixtures under UV-Visible illumination (Fig. 6.9). The amount of H₂ generated using a water-glycerol mixture (4:1 v/v) was 815 μmole in 4h as compared to 1320 μmole from water-methanol (2:1 v/v). Due to the high viscosity of glycerol, a lower amount of glycerol was taken as compared to methanol.

Further increase in the glycerol content in the water-glycerol mixture revealed a decrease in H₂ yield to 675 μmoles in 4 h. This result suggests that probably due to high viscosity the adsorption properties of water on photocatalyst decreases and results in lower H₂ yield. To compare the results with methanol performance of glycerol and methanol in up-scaled reactor (990 ml) reactor was also tested. With half the amount of glycerol, sunlight assisted H₂ was generated at 11.2 ml/h as compared to 16 ml/h with methanol (Fig. 6.7) over 1 g of CuTi(2) photocatalyst resulting in AQE of 5.0 % and SFE of 2.6 %.

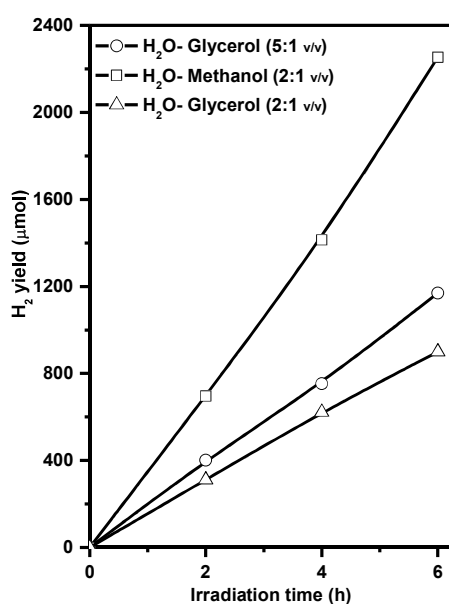


Fig. 6.9 Comparison of photocatalytic H₂ yield observed using glycerol and methanol as sacrificial reagents over Pt/CuTi(6) photocatalyst.

6.3.3.1 Optimization of catalyst loading in upscaled (2 L capacity) photoreactor by using glycerol as sacrificial reagent

Experiments were performed to optimize the catalyst loadings in presence of glycerol instead of methanol as a more practical solution for commercial photocatalytic hydrogen generation. In above section volume of glycerol was optimized to be in 1:5 v/v ratio with 5 being water. Fig. 6.8 shows the comparison of methanol and glycerol in determining the H₂ yield under sunlight illumination over different amount of photocatalyst loading. H₂ yield of 66.47, 136.39, 202.55 and 244.25 μmol/h was observed over 50, 100, 150 and 250 mg of

photocatalyst respectively. Photocatalytic activity with different catalyst loadings in presence of glycerol followed the same trend as with methanol. Hydrogen yields are much lower in case of glycerol. Thus, glycerol can replace the methanol at the cost of reduction of hydrogen yield by 50 %. At the same time it is pertinent to mention that the amount of glycerol (15 % v/v) used was half to that of methanol (33 % v/v).

6.3.4 Comparison of effect of different parameters on H₂ yield

Fig. 6.10 shows effect of different parameters on the H₂ yield. The bar graph shown presents the significance of each factor in determining the overall hydrogen yield. A relative standard deviation (RSD) in hydrogen yield obtained by varying a particular factor keeping other parameters constant was calculated for each factor. RSD for catalyst loadings and concentration of sacrificial reagent (v/v) are alike, suggesting any change in either factor will maximum affect hydrogen yield by ± 18 %. Among all factors, it is the hourly fluctuations in solar flux during the day that does not influence hydrogen yield considerably as revealed by minimum RSD of ~ 4 % on both type of days: bright sunny and cloudy. In other words, hydrogen generated at a uniform rate particularly in time window of 11.00 h to 15.00 h during the day. In vertical geometry, improper dispersion of photocatalyst limits the hydrogen yield significantly (RSD 14.9 %). However, in case of horizontal geometry, stirring of photocatalyst for dispersing the photocatalyst does not affect the hydrogen yield to a great deal. Other factors such as the very configuration of light source with respect to photoreactor and replacement of methanol by glycerol as sacrificial reagent, plays an important role in determining the hydrogen yield.

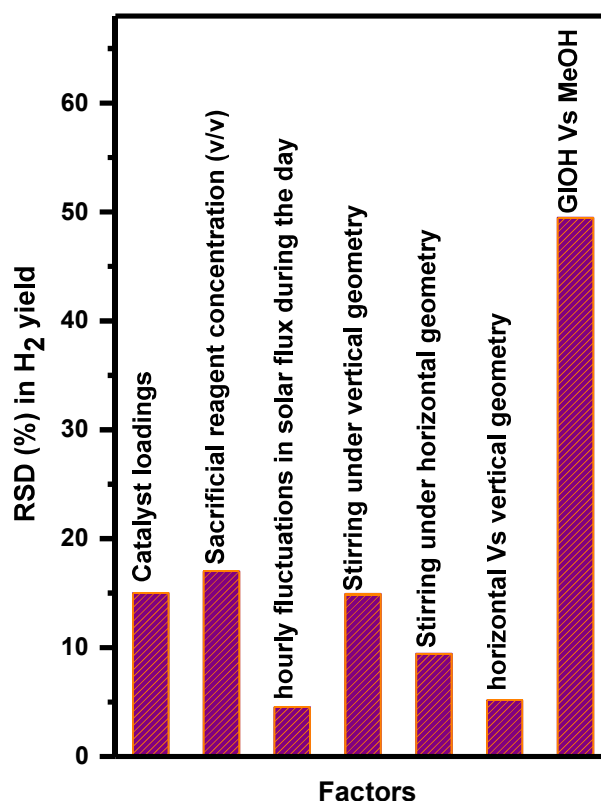


Fig. 6.10 A bar graph presenting relative standard deviation calculated in hydrogen yield by varying different factors.

6.3.5 Comparison of present work with reported results

To review our results, literature reports on copper modified TiO₂ systems were surveyed and the most relevant ones for H₂ evolution are listed in Table 6.4 [202,298–304]. Cu incorporated in TiO₂ in any form whether on surface by impregnation, or coupled with titania as Cu₂O or CuO or in form of cationic dopant substituting Ti⁴⁺ in titania lattice, results in enhancement of activity. Lalitha et al. [299] have reported highly efficient water splitting over Cu-TiO₂ prepared by an impregnation process (Table 6.4). Here, a comprehensive comparison of the doped Cu_xTi_{1-x}O_{2-δ} and composites, xCuO-yTiO₂ with varying amounts of Cu content under identical conditions is reported. Our results offer conversion rates under actual sunlight unlike most of the reports showing activity in UV light. Results are not extrapolated to per g instead more realistic extrapolation with respect to illumination area is

given. In the present work, 2 % Cu doping in TiO₂ results in solid solutions with improved photocatalytic and light absorption properties as compared to undoped samples.

Table 6.4 Comparison of present study with literature reports on various Cu-Ti-O systems for photocatalytic H₂ evolution under given experimental conditions.

S. No.	Authors	Type of photocatalyst	Source of light	H ₂ yield	Experimental conditions
1	C. Wang et al.[298]	Cu doped TiO ₂ films by RF magnetron sputtering	300 W Xenon lamp	810 μmol/h/g	100 ml of methanol+ H ₂ O (1:10 v/v)
2	Lalitha et al. [299]	0.5 wt % Cu-TiO ₂ calcined at 450 °C for 5 h	Sunlight	20,060 μmol/h	100 mg of photocatalyst in 5% glycerol + water
		2 wt % Cu ₂ O-TiO ₂ calcined at 450 °C	Sunlight	290 μmol/h	Pure water
3	T. Sreethawong et al. [300]	1.5 wt % Cu loaded (as cocatalyst) over mesoporous TiO ₂	300 W high-pressure Hg lamp	360 μmol/h	0.2 g of photocatalyst + 200 ml of distilled water + 20 ml of CH ₃ OH
4	S. S. Lee et al. [202]	6 mol % Cu-TiO ₂ composite nanofibre calcined at 450 °C	400 W high pressure Hg lamp (UV-visible source),	5800 μmol/h (UV-visible light)	0.5 g/L catalyst loading into 10 % (v/v) methanol aqueous solution
			360 W high pressure Na lamp (Visible lamp)	720 μmol/h (visible light)	
5	Z. Jin et al. [301]	1.0 wt % Eosin Y sensitized-CuO/TiO ₂	A 200 W halogen lamp equipped with a cutoff filter (λ > 420 nm)	10.56 μmol/h	20 mg of catalyst + 70 ml of 15 % diethanolamine-H ₂ O mixture.
6	H. J. Choi et al. [302]	10 % Cu loaded TiO ₂	UV lamps having intensity of 36 Wm ⁻² at 365 nm	13500 μmol/10h	2 g catalyst per 2.0 L of CH ₃ OH/H ₂ O (1:1) solution.
7	S. Xu et al. [303]	CuO /TiO ₂ nanotube (TNT) by hydrothermal method	400 W high pressure Hg lamp	71600 μmol/h/g	1 g/L catalyst concentration in 10% v/v methanol- water mixture
		CuO/TNT by wet impregnation		64200 μmol/h/g	
8	J. Yu et al. [304]	1.3 wt % CuO-TiO ₂	Four UV-LED (3 W, 365 nm)	2061 μmol/h/g	80 mg photocatalyst in 80 ml of 0.1 M glycerol aqueous solution

9	Present study	$\text{Cu}_{0.02}\text{Ti}_{0.98}\text{O}_{2-\delta}$	Medium pressure Hg lamp (UV-visible light)	333 $\mu\text{mol/h}$	100 mg in (33% methanol v/v solution), illumination area = 20 cm^2
		$\text{Cu}_{0.02}\text{Ti}_{0.98}\text{O}_{2-\delta}$	Sunlight	477 $\mu\text{mol/h}$ or 33829 $\mu\text{mol/h/m}^2$	50 mg in 250 ml (33% v/v methanol solution), illumination area = 141 cm^2
		$\text{Cu}_{0.02}\text{Ti}_{0.98}\text{O}_{2-\delta}$	Sunlight	507.12 $\mu\text{mol/h}$ or 29483.7 $\mu\text{mol/h/m}^2$	250 mg in (33% methanol v/v solution), illumination area = 172 cm^2
		$\text{Cu}_{0.02}\text{Ti}_{0.98}\text{O}_{2-\delta}$ /ITO/PET films	Sunlight	198 $\mu\text{mol/h}$ or 23571.43 $\mu\text{mol/h/m}^2$	Total of 24 mg dispersed on 4 ITO/PET films (0.7cm x 30 cm) in 250 ml (33 % v/v methanol solution), illumination area = 84 cm^2
		$\text{Cu}_{0.02}\text{Ti}_{0.98}\text{O}_{2-\delta}$	Sunlight	244.25 $\mu\text{mol/h}$ or 14200.6 $\mu\text{mol/h/m}^2$	250 mg in (16% glycerol v/v solution), illumination area = 172 cm^2
		$\text{Cu}_{0.02}\text{Ti}_{0.98}\text{O}_{2-\delta}$	Sunlight	735 $\mu\text{mol/h}$ or 52127.7 $\mu\text{mol/h/m}^2$	1 g in 250 ml (33% methanol v/v solution) illumination area = 141 cm^2
		$\text{Cu}_{0.02}\text{Ti}_{0.98}\text{O}_{2-\delta}$	Sunlight	492.2 $\mu\text{mol/h}$ or 34907.8 $\mu\text{mol/h/m}^2$	1 g in 250 ml (16 % glycerol v/v solution) illumination area = 141 cm^2

6.4 Conclusion

To develop low cost $\text{Cu}_{0.02}\text{Ti}_{0.98}\text{O}_{2-\delta}$ photocatalyst for its actual application in large scale sunlight driven photocatalytic hydrogen generation, it was essential to optimize different operational parameters and to quantify their effect on hydrogen yield. The reproducibility in yielding chemically similar $\text{Cu}_{0.02}\text{Ti}_{0.98}\text{O}_{2-\delta}$ powders by sol-gel process was established by relevant characterization techniques. Several operational parameters were investigated in order to finalize the conditions which are most favorable for photocatalytic

hydrogen yield. Concentration of methanol in water as sacrificial reagent was optimized and was found to be 33 % v/v. Further, addition of methanol resulted into a lower H₂ yield. At high concentration probably, methanol may be blocking the surface active sites resulting into lower adsorption of water molecules on the surface thus deteriorating the photocatalytic activity. Industrial waste, glycerol is a potential candidate to replace industrially important solvent methanol as sacrificial reagent. Increase in catalyst loadings in both small scale and upscaled photoreactors, resulted in non-linear rise further saturation in hydrogen yield. Thus, it is recommended to extrapolate hydrogen yield with respect to illumination area instead of per g of photocatalyst. Horizontal geometry a propos vertical provides better dispersion to the photocatalyst and results in higher photocatalytic hydrogen yield. Variation of flux of sunlight varies throughout a year. It was observed that sunlight flux values increased almost three fold from October to May and as expected H₂ yield also increased from 36 μmol/h (AQE = 3.6 %) to 110 μmol/h (AQE = 3.13 %), respectively. Variation in the rate of H₂ generation was studied with the solar flux at hourly basis on bright and cloudy day. From the data it was inferred that during time window of 11:00 to 15:00 h, hydrogen generation with constant yield and maximum efficiency can be achieved and will allow avoiding less efficient/productive hours of a day and consequently will be helpful in slashing the running cost and shaping the economics of process. Small amount of catalyst dispersed over ITO/PET film is found to be more beneficial than the powdered catalyst. Along with this dispersion of catalyst over film offers easy recovery, handling and replacement of the catalyst after prolonged use and will be helpful during scale- up of the hydrogen generation process. These optimization studies will be useful for further scale up of sunlight driven photocatalytic hydrogen production over low cost, visible light active Cu_{0.02}Ti_{0.98}O_{2-δ} photocatalyst.

g-C₃N₄ Decorated with Pt and Carbon Nanodots for Photocatalytic H₂ Generation

7.1 Introduction

As describe in the introduction chapter, g-C₃N₄ is a promising candidate for solar light application as its band gap is lower as compared to TiO₂. It fulfills thermodynamic criteria for water splitting, exhibits chemical and thermal stability, water resistivity and medium band gap of 2.7 eV [76,84,305]. Wang et al [76] first time demonstrated the photocatalytic activity of g-C₃N₄. Also performed DFT calculation to evaluate the structure of g-C₃N₄ and found that valence band is predominantly composed of nitrogen p_z orbitals while carbon p_z orbitals constitute conduction band. This implies that the nitrogen is the preferred sites for the oxidation of water whereas carbon atom offers reduction sites to give H₂. Regardless of its advantages its photocatalytic activity is poor due to high rate of electron- hole pair recombination and poor utilization of visible light. Hence various methodologies adopted to improve the light absorption and lower electron- hole pair recombination as discussed in Chapter 1. Cationic/ anionic doping [80,306,307], heterojunction formation [308–311], metal loading [312–314] to improve the band gap of g-C₃N₄ and effective separation of e⁻ and h⁺ pair, are commonly used methods to modify its properties.

Recently, g-C₃N₄ coupled with graphene [315], graphene oxide [316], carbon nanotubes [317], carbon nanodots [88] were used to improve electron-hole pair recombination and light absorption properties of g-C₃N₄. Carbon nanodots (CND) are chemically inert, shows high resistance to photobleaching, acts as electron reservoir for efficient separation of photogenerated electron-hole pairs when combined with

semiconductor and as photosensitizer [137]. These properties of CND help to improve photocatalytic activity of g-C₃N₄. Also similar π conjugated structure of both g-C₃N₄ and carbon dots may help in improving the photocatalytic activity of g-C₃N₄ [318]. Gao et al [319] performed DFT studies to understand the interaction between g-C₃N₄ and trigonal/hexagonal shaped CND and revealed that type II van der Waals heterojunction formed between CND/g-C₃N₄ which helps to reduce the band gap considerably and facilitate charge separation.

Juan Liu et al [88] reported the pure water splitting over carbon nanodot- carbon nitride nanocomposite under visible light irradiation. For optimum concentration of CND and g-C₃N₄ (4.8×10^{-3}) shows apparent quantum efficiency (AQE) 16 % and solar to fuel efficiency (SFE) 2 % at wavelength 420 nm. They proposed that this composite splits water into two steps two electron/ two electron pathway. CND catalyzes the decomposition of H₂O₂ into H₂O and O₂ thus helps in prevention of poisoning of catalyst by removing H₂O₂. Similarly, Li et al [320] reported carbon quantum dots (CQD) deposited onto g-C₃N₄ nanosheets (CNNS) and achieve maximum H₂ generation rate of 116 $\mu\text{mol/h}$ over optimized amount of CQD and CNNS. By photoluminescence and photoelectrochemical studies they proposed that CQD helps in trapping of electron and separation of electron and hole pair. Xia et al [321] demonstrated H₂ production @ 6.76 $\mu\text{mol/h/g}$ in near- IR at 808 nm over 10 % w/w carbon quantum dots/ g-C₃N₄ nanosheets (CQD/ CNNS) which was attributed to the synergistic effect on spectral and electronic coupling of CNNS and carbon quantum dots which is synthesized by hydrothermal method.

CQD coupled with g-C₃N₄ was also studied for dye and chemical degradation. Jian et al [322] reported synthesis of composite of CQD and proton functionalized g-C₃N₄ formed by electrostatic self assembly approach. Efficient photocatalytic activity for MB dye degradation and increase in photocurrent density in the composite than pure sample was attributed to the

efficient separation of e^- and h^+ and their low recombination rate. Zhang et al [318] reported phenol degradation over carbon dots decorated $g-C_3N_4$ samples which were synthesized by facile impregnation- thermal method. Fang et al [323] demonstrated both degradation of Rhodamine B under UV irradiation and photocatalytic hydrogen production under visible irradiation by using C-dots/ $g-C_3N_4$ hybrid. This hybrid was synthesized by calcination of mixture of C-dots and dicyandiamide, where C-dots were obtained from the combustion soot of an alcohol burner. All these studies suggest that heterostructure of CND and $g-C_3N_4$ is an effective way to enhance photocatalytic activity of $g-C_3N_4$ in visible region.

In the present chapter, $g-C_3N_4$ is synthesized using pyrolysis of urea. The light absorption and photocatalytic properties of bulk yellow coloured powder $g-C_3N_4$ were enhanced by co-dispersing carbon nanodots and Pt on its surface. $CNDs$ were synthesized by facile electrochemical oxidation of graphite rod. These CND are hydrothermally treated with ammonia to increase the hydrophilicity and to aid the interaction between CND and $g-C_3N_4$. Pt photodeposited over $CND/g-C_3N_4$ sample. For creation of active sites on surface, minute amounts (< 1 wt %) of CND were dispersed on $g-C_3N_4$ surface. Samples were characterized by relevant techniques to determine structural, electronic, surface and optical properties. In addition, XPS technique was used to verify the existence of CND on the surface. CHN analysis was carried out to confirm the composition of $g-C_3N_4$ samples. Direct water splitting was also achieved over the optimized $CND/g-C_3N_4$ sample under UV-visible light illumination. Further, photocatalytic activity of samples was evaluated under sunlight in upscaled photoreactors.

7.2 Experimental

7.2.1 Synthesis of g-C₃N₄ and CND decorated g-C₃N₄

g-C₃N₄ was synthesized by pyrolyzing urea (Sarabhai M Chemicals, India) in a covered alumina crucible and kept in a muffle furnace at 550 °C for 3 h at a heating rate of 5 °C/min inside fume hood. CND were synthesized by top-down approach using electrochemical oxidation of graphite rod [324]. A DC potential of 30 V was applied between two graphite rods, acted as cathode and anode, immersed in nanopure water with continuous stirring. After 120 h dark brown solution appeared, filtered and filtrate obtained was centrifuged at 15000 rpm for 1 h. The solution obtained was water soluble CND. Further CND solution was treated with NH₃ in an autoclave at 150 °C for 7 h to modify CND with NH₂ groups. The -NH₂/CND solution was mixed with urea and calcined inside a muffle furnace. Similarly, several samples with varying amounts of CND were synthesized viz. CND/g-C₃N₄-x wt % (x= 0.48, 0.62, 0.67, 0.75).

7.2.2 Synthesis of Pt/CND/g-C₃N₄ sample

3 % w/w Pt was loaded on CND/g-C₃N₄ by photo deposition method. A mixture of 25 ml of water, 5 ml of ethanol and 0.8 ml of H₂PtCl₆.6H₂O (0.02M) was added to a 100 mg of CND/g-C₃N₄ composite. The solution was evacuated and irradiated under UV-visible light for 2 h. Obtained sample was washed to remove chloride ion content and dried in an oven at 80 °C to remove moisture.

7.2.3 Characterization

Samples with different concentration of CND were synthesized and characterized by different techniques. Powder X- ray diffraction (XRD) patterns were recorded on a Philips diffractometer (model PW 1710), equipped with a graphite monochromator and Ni-filtered Cu-K_α radiation. Vibrational spectra of samples were recorded on Bomem (MB 102)

spectrometer in the mid-IR region (4000 to 200 cm^{-1}). ^{13}C MAS NMR spectra of sample recorded on AVANCE 400 MHz machine with a ^{13}C basic frequency of 100.57 MHz. TEM was recorded on FEI-Tecnai G-20 microscope operating at 200 kV. Amount of carbon, nitrogen and hydrogen present in the sample was determined by using Euro vector elemental analyser (Euro EA 3000 series). Amount of Pt present in the sample was quantified using ICP-OES (JobinVyon JY 2000, France). Thermo-gravimetry–evolved gas analysis (FTIR) were carried out in a Netzsch Thermobalance (Model No.: STA 409 PC Lux) coupled to Bruker FTIR system (Model No.: Tensor 27) via a heated Teflon capillary (1 m long, 2 mm i.d.). N_2 - Brunauer-Emmett-Teller surface area was measured with Micromeritics 3Flex analyzer using N_2 as the adsorbing gas. XPS experiments were recorded on electron spectrometer (SPECS, Germany) using $\text{Mg-K}\alpha$ X-rays ($h\nu= 1253.6$ eV) as the primary source of radiation with an overall energy resolution of the instrument of about 0.7 eV. The appropriate corrections for charging effect were made with the help of a C 1s signal appearing at 284.5eV. An optical characteristic of all samples was recorded using spectrophotometer of JASCO model V-530 (Japan) with an integrating sphere attachment. Samples were scanned in range of 200-800 nm at the scanning speed of 200 nm/min. BaSO_4 was used as reflectance standard. Photoluminescence studies were carried out at room temperature with a resolution of 3 nm, using Edinburgh Instruments' FLSP 920 system having a 450 W Xe lamp as the excitation source having a Peltier element cooled red sensitive Hamamatsu R955 PMT. All emission spectra were corrected for the detector response. Lifetime measurements were carried out by using a nanosecond hydrogen flash lamp as the excitation source and employing Time Correlated Single Photon Counting (TCSPC) technique. All the data were fitted with biexponential fitting. It gives two lifetime values τ_1 and τ_2 and corresponding amplitude, A_1 and A_2 respectively. Average lifetime (τ) was determined by using following equation [325]:

$$\tau = \frac{A_1 \times \tau_1^2 + A_2 \times \tau_2^2}{A_1 \times \tau_1 + A_2 \times \tau_2} \quad \dots 7.1$$

7.2.4 Photocatalytic activity

7.2.4.1 Direct water splitting under UV-visible irradiation

50 mg of sample was dispersed in pure water without sacrificial reagent, evacuated and irradiated under UV-Visible light (medium-pressure mercury lamp, SAIC, India, 400W). Yield of H₂ and O₂ was monitored using GC with He and Ar as carrier gas respectively.

7.2.4.2 Photocatalytic activity under UV-visible irradiation in presence of sacrificial reagent

H₂ generation reaction was also performed in presence of sacrificial reagent in 81 ml reactor with illumination area of 20 cm². For this, 50 mg of sample was dispersed in 15 ml of (10 % v/v) aqueous triethanolamine solution, evacuated and finally the solution was irradiated under a medium-pressure mercury lamp (Hg, SAIC, India, 400 W) with flux 14 x 10⁴ surrounded with water circulation jacket to absorb IR irradiation. The emission spectrum of lamp in UV-visible region and reaction assembly are shown in Chapter 2. AQE and SFE are calculated by using formula mentioned in Chapter 2.

7.2.4.3 Photocatalytic activity under sunlight in presence of sacrificial reagent

Photocatalytic activity of samples was evaluated under sunlight in a circular glass reactor (volume ~2 L) which is described in detail in Chapter 2. 80 mg of photocatalyst was dispersed in a 150 ml (10 % v/v) aqueous triethanolamine. This solution was purged with argon gas before irradiation to provide air free conditions as oxygen acts as e⁻ scavenger and on photoadsorption blocks the active sites for the reaction. This mixture then irradiated under sunlight for duration of 4 h during afternoon (11.00-15.00 IST). The hydrogen generated were analysed using a gas chromatograph (Schimadzu, Japan) equipped with a thermal

conductivity detector (TCD) and Carboxen column with argon as carrier. Solar flux was measured using light meter LX 1108, Lutron Electronic. Flux was measured daily in the peak hours and average of lux recorded during 11.00-15.00 IST were used for AQE and SFE measurement.

7.3 Results and discussion

7.3.1 XRD

Fig. 7.1 shows the XRD pattern of pristine $g\text{-C}_3\text{N}_4$, $\text{CND}/g\text{-C}_3\text{N}_4$ and $\text{Pt}/\text{CND}/g\text{-C}_3\text{N}_4$ samples. XRD of all samples shows two distinct peaks one at 12.9° and another broad peak at 27.7° corresponds to 100 and 002 planes (marked as *) ascribed to inplanar repeating units with a period of 0.688 nm and layered staking with inter-planar spacing of 0.323 nm of aromatic systems respectively. Inter-planar stacking distance of 0.323 nm reveals the graphitic nature of $g\text{-C}_3\text{N}_4$ [320]. Intensity of the peak at 27.7° varies in all samples. The more intense peak indicates that there is more regular repetition between graphitic layers [326].

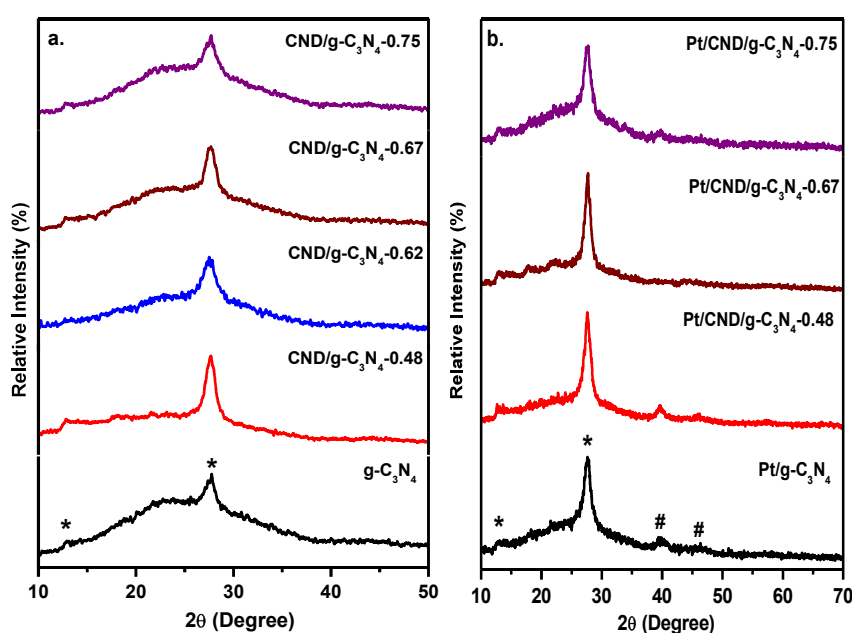


Fig. 7.1 Powder XRD patterns of a. $\text{CND}/g\text{-C}_3\text{N}_4$ b. $\text{Pt}/\text{CND}/g\text{-C}_3\text{N}_4$ samples.

XRD patterns of Pt dispersed samples show extra weak peaks (marked as # in Fig. 7.1b) at 39.62 and 46.02° corresponding to *111* and *200* plane of metallic platinum (JCPDS No. 88-2343). No shift in the peak position was observed. It can be inferred that presence of Pt and CND has not affected the structure of g-C₃N₄. However, as a result of irradiation under UV-visible light, in-plane and interplane crystallinity has improved, resulting in increased intensity of XRD peaks in ternary system (Fig. 7.1b).

7.3.2 FTIR

FTIR spectrum of g-C₃N₄, and CND/g-C₃N₄ were shown in Fig. 7.2.

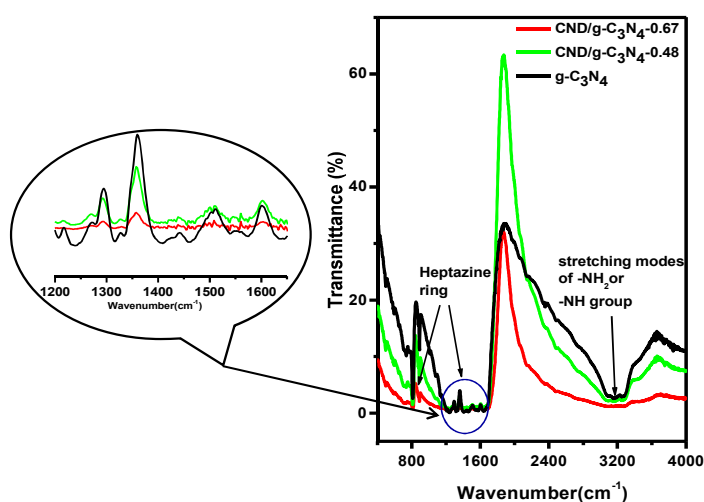


Fig. 7.2 FTIR spectrum of g-C₃N₄ and CND/g-C₃N₄ samples. Inset shows the vibration in the region of 1200-1800 cm⁻¹ arises due to stretching modes of CN heterocycle.

The observed vibrations are listed out in Table 7.1. Pristine g-C₃N₄ and CND/g-C₃N₄ have shown similar spectra which indicate that incorporation of CND has not altered the chemical structure as revealed by XRD results also.

Table 7.1 Characteristic vibrations of g-C₃N₄ and CND/g-C₃N₄ samples

IR frequency (cm ⁻¹)	Corresponding vibrations
810	Out of plane bending vibrations of heptazine rings [327]
890	Deforming mode of NH groups [327]
1236, 1334, 1432, 1579, 1640	Stretching modes of CN heterocycle [328]
3000-3600	Stretching modes of terminal NH ₂ or NH groups due to uncondensed amine group and OH stretching mode owing to adsorbed hydroxyl group [322]

7.3.3 ^{13}C MAS NMR analysis

The structure of $\text{g-C}_3\text{N}_4$ was further analyzed by ^{13}C MAS NMR. Fig. 7.3 shows ^{13}C MAS NMR spectrum of $\text{g-C}_3\text{N}_4$ and $\text{CND/g-C}_3\text{N}_4$. Spectrum shows two resonance peaks one at $\delta = 164.6$ and other at $\delta = 156.2$ ppm which is assigned to the $\text{CN}_2(-\text{NH}_x)$ and CN_3 group of $\text{g-C}_3\text{N}_4$ respectively [329,330]. With increasing carbon nanodot concentration extra peaks were observed. In case of $\text{CND/g-C}_3\text{N}_4-0.75$ peaks at $\delta = 28, 208.53$ ppm corresponds to C-C bonding (R_3CH) and C=O respectively were observed. No peak due to sp^2 hybridized C-C bond of graphitic carbon dots (110- 150 ppm) was observed. Reasons are obvious; one that CND are present on surface and does not form the integrated part of the chemical structure of $\text{g-C}_3\text{N}_4$, second amount of CND is below detection limit. NMR result confirms the heptazine ring structure of $\text{g-C}_3\text{N}_4$ and also indicates that CND is not incorporated in bulk $\text{g-C}_3\text{N}_4$.

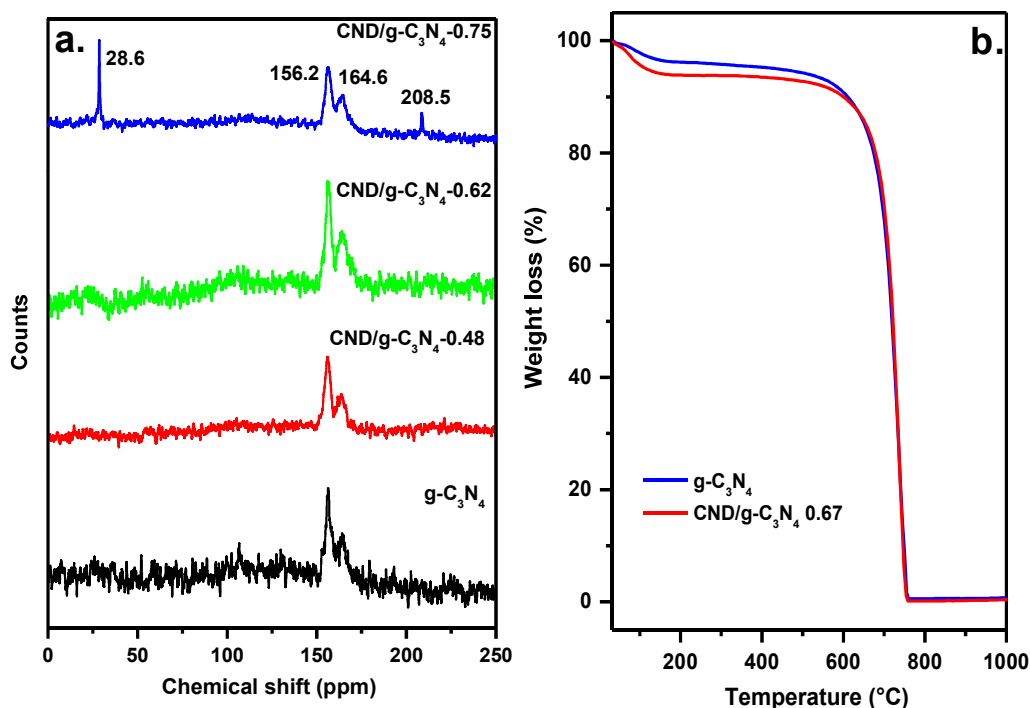


Fig. 7.3 a. NMR spectrum of $\text{g-C}_3\text{N}_4$, $\text{CND/g-C}_3\text{N}_4-0.48$, $\text{CND/g-C}_3\text{N}_4-0.62$ and $\text{CND/g-C}_3\text{N}_4-0.75$, b. thermogram of $\text{g-C}_3\text{N}_4$ and $\text{CND/g-C}_3\text{N}_4-0.67$ recorded till 1000 $^{\circ}\text{C}$ in air.

7.3.4 TGA-EGA

Thermogram of g-C₃N₄ and CND/g-C₃N₄ recorded upto 1000 °C in air and shown in Fig. 7.3b. TGA shows g-C₃N₄ is stable upto 600 °C, with further increase in temperature g-C₃N₄ starts to decompose. Thermal stability of g-C₃N₄ has not altered by incorporation of CND on g-C₃N₄.

7.3.5 Elemental analysis by CHN analyzer and ICP-OES

Elements C, H and N present in CND, -NH₂/CND, Pt/CND/g-C₃N₄ samples were determined using CHN analyzer and listed in Table 7.2. Atomic ratio of C/N was calculated and found to be 0.64 in g-C₃N₄ lower than the theoretical value of 0.75. H was also analyzed and found to exist in each sample along with C and N. Proportion of C, H, N is varying in all samples and was found to be in the range of 93-99 %. Rest was not analyzed or quantify the possibilities of existence of oxygen as impurity. The presence of H is attributed to the existence of uncondensed amino group, adsorbed water molecules on the surface as evidence by a broad peak in the region of 3000- 3600 cm⁻¹ of FTIR spectrum. CND/g-C₃N₄-0.75 shows highest oxygen content among the series which may be in the form of OH and C=O as seen in FTIR and NMR spectrum respectively. CND/g-C₃N₄ 0.67 has shown that the C, H, N was about 99.2 % with minimum impurities. This implies complete condensation in this sample. Fang et al [323] synthesized C- loaded over g-C₃N₄ and found the steady increase in C/N ratio with increase in amount of C-dots from 0.651 for pristine g-C₃N₄ to 0.654 for C-dot/g-C₃N₄ synthesized by adding 10 ml of 50 mg/L of C-dots to 10 g of dicyandiamide. Similarly here we have observed slight increase in carbon content in all CND/g-C₃N₄ samples. Also C/N ratio of used samples was determined and increase in C/N ratio was observed that may be due to adsorption of carbon or nitrogen species as a result of oxidation of triethanolamine used during photocatalytic reaction as sacrificial reagent. Pt content was

analyzed by ICP-OES. Amount of Pt was found to be around 2.8 % which is similar to the amount of Pt added by photodeposition method.

Table 7.2 Carbon, nitrogen, hydrogen content by CHN analysis.

Samples	C (wt %)	N (wt %)	H (wt %)	Atomic ratio of C/N from CHN analysis
g-C ₃ N ₄	33.4	60.7	3.0	0.641
CND/g-C ₃ N ₄ -0.48	32.7	59.0	2.8	0.647
CND/g-C ₃ N ₄ -0.67	33.6	62.5	3.1	0.627
CND/g-C ₃ N ₄ -0.75	32.2	57.7	3.1	0.651
Pt/CND/g-C ₃ N ₄ -0.48 used	34.6	57.5	3.2	0.702
Pt/CND/g-C ₃ N ₄ -0.67 used	33.7	57.5	3.4	0.684
Pt/g-C ₃ N ₄ used	33.4	57.5	3.1	0.678
CND	44.2	-	3.9	-
CND-NH ₂	29.75	12.9	Not detected	-

7.3.6 TEM

Morphology of g-C₃N₄ and CND/g-C₃N₄ was studied by TEM as shown in Fig. 7.4. Pristine g-C₃N₄ is a layered structure [331] and these layers are back folded at their edges as shown in Fig. 7.4a. HR-TEM image of CND/g-C₃N₄-0.67 shows CNDs are dispersed on the surface of g-C₃N₄ randomly and marked in white circle in Fig. 7.4b. They are crystalline in nature and nearly spherical in shape having diameter in the range of 4-7 nm. Lattice spacing of 0.22 nm were observed which corresponds to *100* in-plane lattice spacing of graphene [320]. This confirms that CND are successfully anchored on the layer of g-C₃N₄ to form CND/g-C₃N₄ composite. HR-TEM image of Pt/g-C₃N₄ were also recorded and it shows well dispersed small particles and also some agglomerates of Pt particles over g-C₃N₄. These particles are in the range of 2-4 nm and shows lattice spacing of 0.23 nm which corresponds to *111* plane of metallic Pt (Fig. 7.4c).

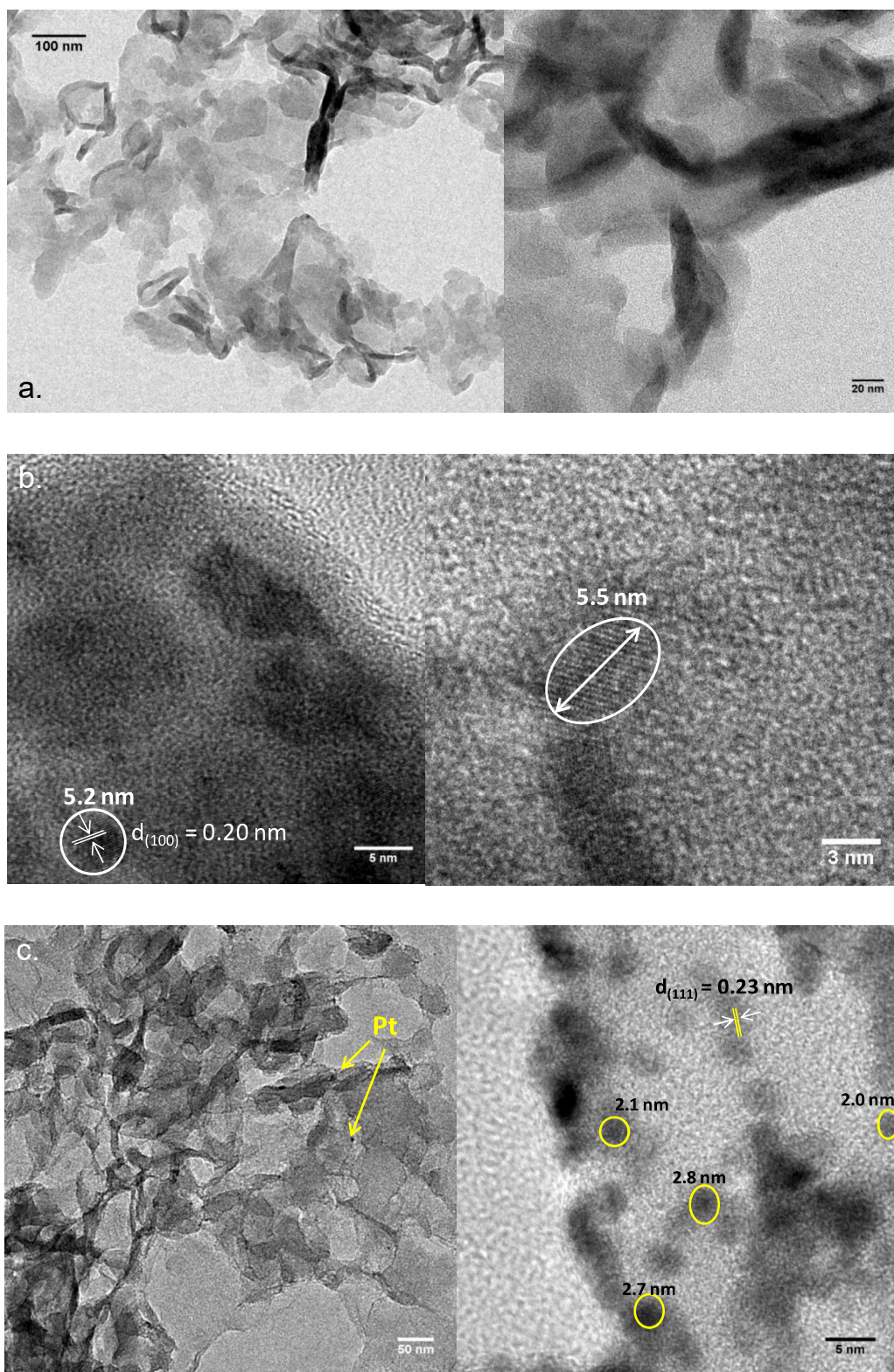


Fig. 7.4 Low and high resolution TEM images of a. g-C₃N₄, b. CND/g-C₃N₄-0.67 and c. Pt/g-C₃N₄.

7.3.7 Surface area

N_2 -BET surface area, mean pore size diameter and cumulative pore volume of pristine $g-C_3N_4$ is compared with composite of CND and $g-C_3N_4$ and tabulated in Table 7.3.

Table 7.3 Band gap, surface area, pore volume and pore size distribution of $CND/g-C_3N_4$

Sr No.	Sample	Surface area (m^2/g)	Pore volume (cm^3/g)	Pore size distribution
1	$g-C_3N_4$	74.1	0.280	Maxima at 28 and 41 Å
2	$CND/g-C_3N_4-0.48$	76.0	0.305	Broad distribution of pore size in the range of 50-256 Å centred at 172 Å
3	$CND/g-C_3N_4-0.62$	59.7	0.183	Maxima at 30 Å in the range of 21-116 Å

All the samples show type IV isotherm. Pristine $g-C_3N_4$ shows the surface area of 74 m^2/g whereas surface area of $CND/g-C_3N_4-0.48$ and 0.62 found to be 76 and 59 m^2/g respectively.

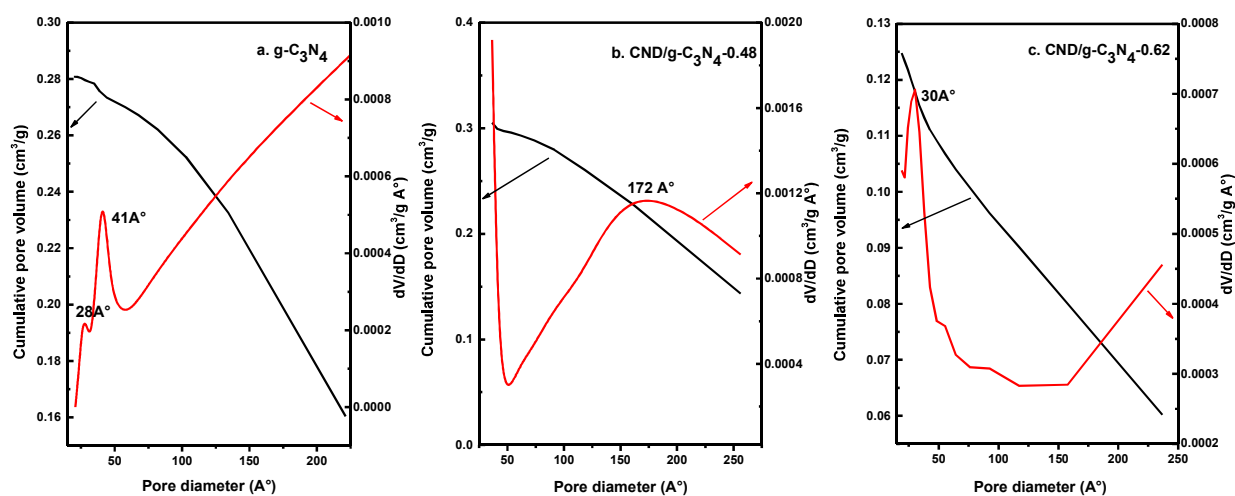


Fig. 7.5 Cumulative pore volume and pore size distribution of a. $g-C_3N_4$, b. $CND/g-C_3N_4-0.48$ and c. $CND/g-C_3N_4-0.62$ samples.

The pore size distribution and cumulative pore volume of the samples are shown in Fig. 7.5. $g-C_3N_4$ is mesoporous with maxima at 28 Å and 41 Å. However $CND/g-C_3N_4-0.48$ shows presence of small pores. Pore volume changes from 0.28 cm^3/g for $g-C_3N_4$ to 0.305 and 0.183 cm^3/g for $CND/g-C_3N_4-0.48$ and 0.62 respectively. Initially with increase in CND

concentration surface area as well as pore volume increases. On further increase in CND shows reduction in surface area and pore volume. Probably at higher concentration, CND is blocking the pores.

7.3.8 XPS

Chemical composition and oxidation state over the surface was probed by XPS analysis. XPS survey spectrum indicates peak corresponds to carbon, nitrogen and oxygen which appear at binding energies 284.5 eV (C 1s), 399 eV (N 1s) and 530 eV (O 1s) respectively. Fig. 7.6a shows high resolution scan of C 1s present in different samples which is deconvoluted into two peaks. First peak appears at 284.4 eV corresponds to graphitic carbon and second peak at 287.8 eV corresponds to sp^2 hybridized carbon atom attached to N (N-C=N) in g-C₃N₄ [320,323]. With increase in CND content, the area under the peak at binding energy 284.4 eV increases. This may be due to sp^2 hybridized graphitic carbon (C-C) of CND. Similar increase in peak intensity of 284 eV was observed with increase in CND concentration by Jian et al [322].

Table 7.4 mentions the ratio of both the ratio of carbon peak appearing at binding energy 284.4 and 287.8 eV. As expected the ratio increases with increase in CND content. This confirms the presence of CND on the surface of g-C₃N₄. Similar results were also observed by Li et al after modifying g-C₃N₄ nanosheet by carbon quantum dots [320]. In case of used samples this ratio is quite high. This can be attributed to adsorption of carbon on the surface as a result of decomposition of triethanolamine used as sacrificial reagent. This is in agreement with the result of CHN analysis which shows increase in carbon content of used sample.

A high resolution spectrum of N1s is deconvoluted into two peaks (Fig. 7.6b). One peak appears at 398.3 eV corresponds to sp^2 hybridized aromatic N in triazine ring (C=N-C) and other peak appears at 399.5 eV corresponds to tertiary N in N-(C)₃ or H-N-(C)₂ present in g-

C_3N_4 [320]. Also a weak peak at 404.3 eV attributed to charging effect or pi-excitation was observed [320].

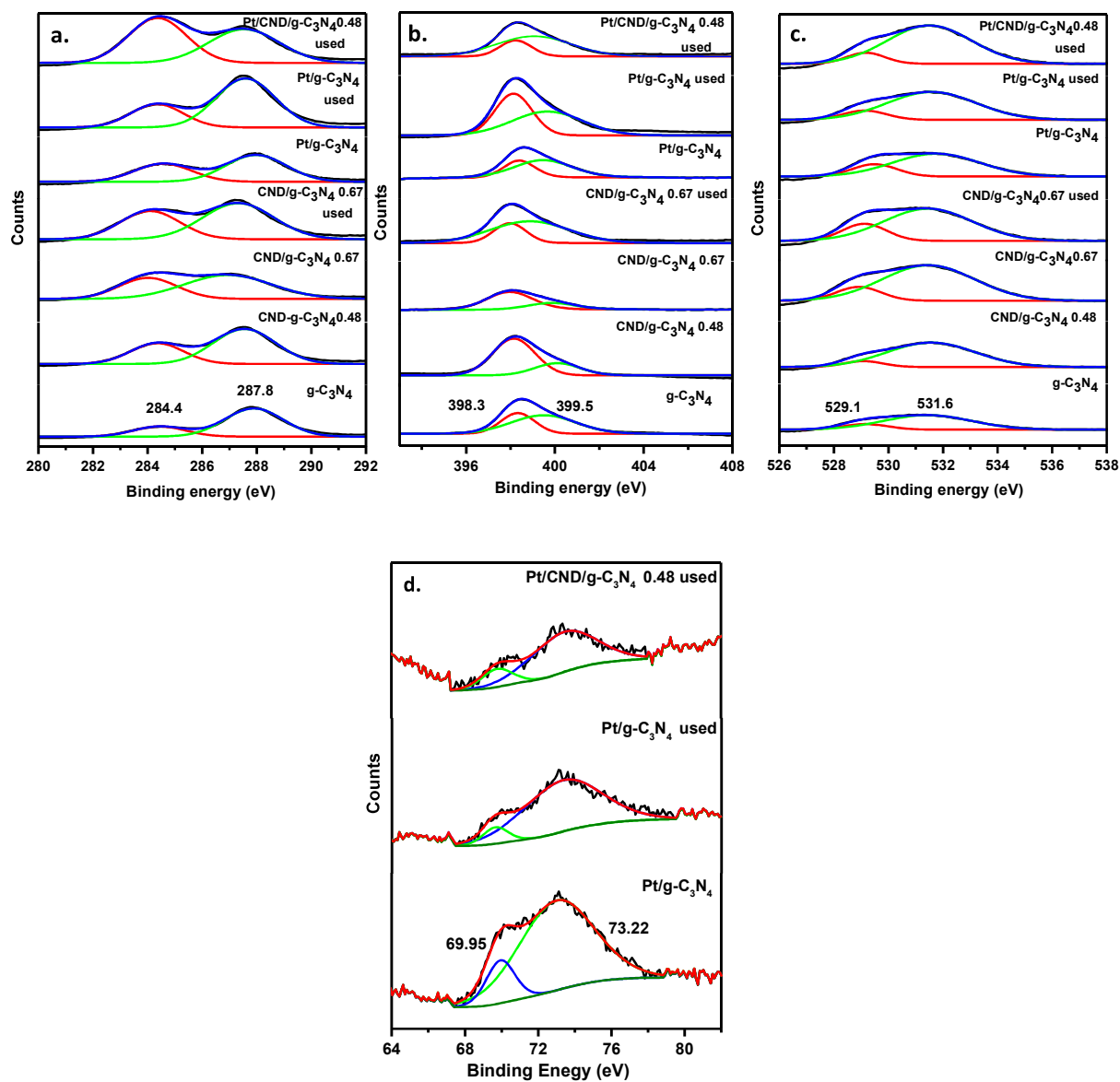


Fig. 7.6 Overlay of XPS spectra corresponding to a. C1s , b. N1s, c. O1s and d. Pt 4f.

Peak observed at 530 eV corresponds to O 1s which is deconvoluted into two peaks as shown in Fig. 7.6c. Peak at binding energy 529.1 and 531.6 eV were observed which can be attributed to HO-C=O and C-OH, respectively [322]. The peak due to Pt was deconvoluted into two different peaks which appear at binding energy of 73.2 and 69.95 eV associated with Pt 4f_{5/2} and Pt 4f_{7/2}, respectively (Fig. 7.6d). This confirms the existence of Pt in metallic

form. This data is in accordance with XRD and TEM results which also reveal existence of metallic Pt.

XPS spectrum of used sample shows spectrum similar to that of fresh sample. This confirms that the catalyst is stable after photocatalytic reaction. Elemental concentration on the surface was calculated and tabulated in Table 7.4. Atomic percent of C/N over the surface was also calculated and it is found to be different from that obtained by CHN analysis. This reveals that the surface characteristics are different from that of the bulk. In $\text{CND/g-C}_3\text{N}_4$ atomic ratio of C/N is greater than pristine $\text{g-C}_3\text{N}_4$ on the surface which indicates that surface is carbon rich which confirms the presence of CND on the surface of $\text{g-C}_3\text{N}_4$. However, in case of used sample C/N ratio decreases which indicated increase in N content in used sample that may be due to adsorption of N containing species as a result of decomposition of triethanolamine used during photocatalytic reaction.

Table 7.4 Elemental compositions derived from XPS study of $\text{g-C}_3\text{N}_4$ and $\text{CND/g-C}_3\text{N}_4$ and $\text{Pt/CND/g-C}_3\text{N}_4$

Sr No	Sample	Chemical composition (atom %)					Ratio of graphitic /sp ² hybridized carbon
		C	N	O	Pt	[C]/[N]	
1	$\text{g-C}_3\text{N}_4$	42.57	45.91	11.52	-	0.93	0.32
2	$\text{CND/g-C}_3\text{N}_4\text{-0.48}$	45.31	40.72	13.97	-	1.11	0.51
3	$\text{CND/g-C}_3\text{N}_4\text{-0.67}$	49.11	26.57	24.33	-	1.85	0.58
4	$\text{CND/g-C}_3\text{N}_4\text{-0.67}$ (used)	45.28	37.97	16.75	-	0.95	0.66
5	$\text{Pt/g-C}_3\text{N}_4$	43.82	40.65	15.53	*	1.07	0.64
6	$\text{Pt/g-C}_3\text{N}_4$ (used)	46.67	40.50	12.83	*	1.15	0.42
7	$\text{Pt/CND/g-C}_3\text{N}_4\text{-0.48}$ (used)	48.21	36.53	15.26	*	0.55	1.10

* Peak were very small hence didn't get detected by software while determination of chemical composition

7.3.9 DRS

UV-Visible absorption spectra of CND (black colour sample) and -NH₂ modified CND (light yellow colour sample) were recorded and shown in Fig. 7.7. It shows absorption in UV region. Peak observed at 227 nm corresponds to the π - π^* transition of aromatic sp^2 transition. Also a weak peak at 300 nm were observed which corresponds to n- π^* transition [324].

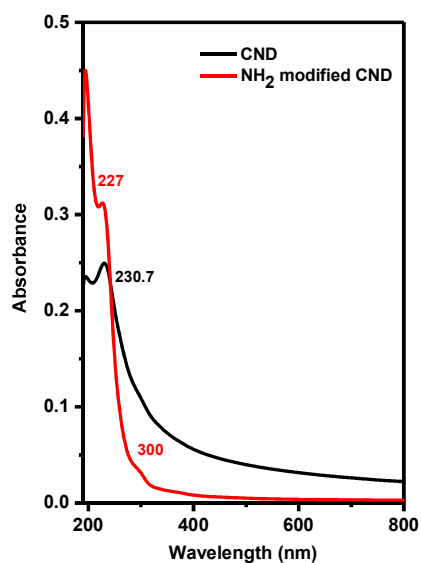


Fig. 7.7 Light absorption spectra of CND and -NH₂ modified CND

Optical properties of CND/g-C₃N₄ samples were investigated by recording its UV-visible DRS in the range of 200-800 nm. Fig. 7.8 shows DRS spectrum of g-C₃N₄, CND/g-C₃N₄ and Pt/CND/g-C₃N₄. Band gap of pristine g-C₃N₄ was found to be 2.79 eV. A slight red shift is observed with increase in concentration of CND. Moreover, CND/g-C₃N₄-0.48 and 0.67 shows enhanced visible absorption as compared to the pristine g-C₃N₄. But not much change in band gap was observed after addition of CND. DRS spectrum of Pt/CND/g-C₃N₄ didn't show much change in absorption edge but upward shift in baseline into visible region was observed due to presence of Pt. Light enhancement in the ternary composite of Pt, CND and g-C₃N₄ as compared to pristine sample will make it appropriate candidate for sunlight application.

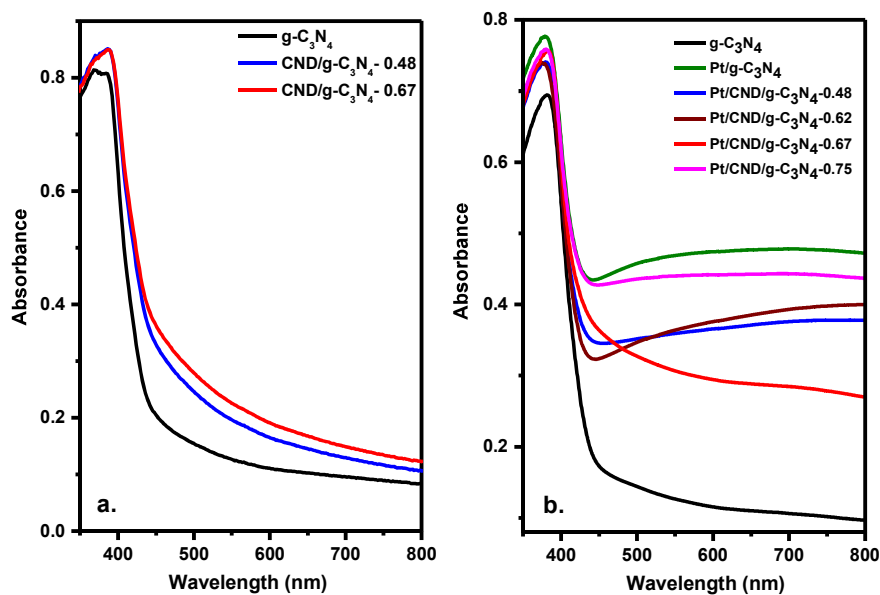


Fig. 7.8 DRS spectra of a. CND/g-C₃N₄ and b. Pt/CND/g-C₃N₄

7.3.10 Photoluminescence

Fig. 7.9a and b shows photoluminescence spectra of all the samples by exciting at 380 nm. PL spectra of g-C₃N₄ shows broad peak centred at 460 nm correspond to the band to band transition. No change in position of emission peak was observed after addition of CND or Pt.

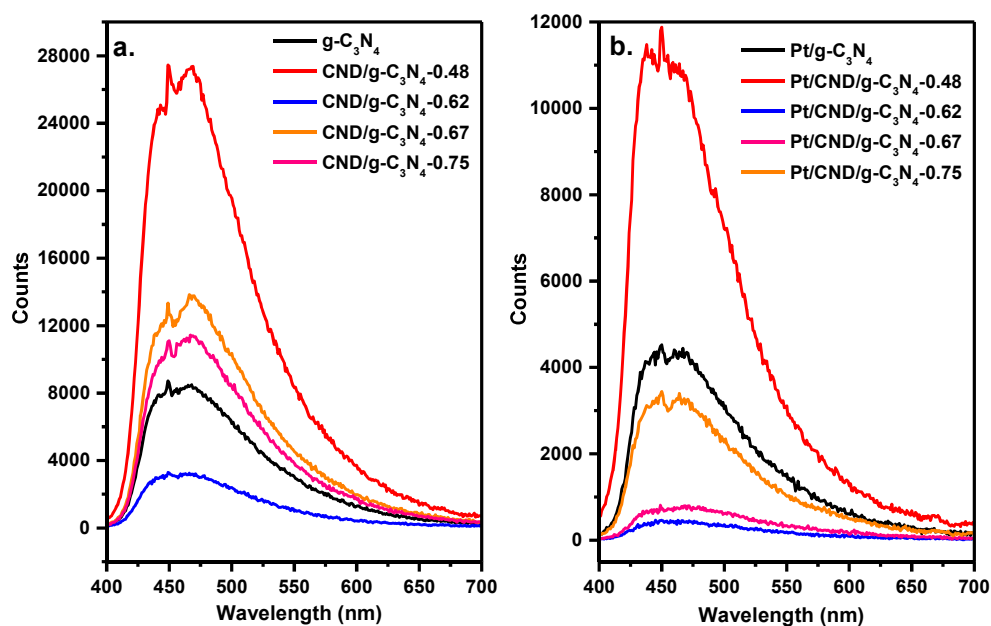


Fig. 7.9 Photoluminescence spectra of a. CND/g-C₃N₄ and b. Pt/CND/g-C₃N₄ samples.

Time resolved photoluminescence spectroscopy was performed to get more information about lifetime of charge carriers. Typical photoluminescence decay curves of g-C₃N₄, CND/g-C₃N₄-0.67, Pt/CND/g-C₃N₄-0.48 are shown in Fig. 7.10. Fluorescence intensity decays exponentially for all the samples. Decay data of g-C₃N₄, CND/g-C₃N₄ were fitted with biexponential fitting. Values of two lifetimes and their corresponding amplitude (A) and χ^2 are mentioned in Table 7.5. It was observed that with increase in CND content, contribution from shortest lifetime decreases while contribution from longest lifetime increases. CND/g-C₃N₄-0.67 shows increase in shortest lifetime as compared to g-C₃N₄ whereas longest lifetime is not much affected. CND/g-C₃N₄-0.75 shows decrease in τ_1 and τ_2 as compared to CND/g-C₃N₄-0.48. This implies that on increase in CND concentration beyond 0.67 wt % lifetime decreases as CND may acts as electron-hole recombination centre at higher concentration.

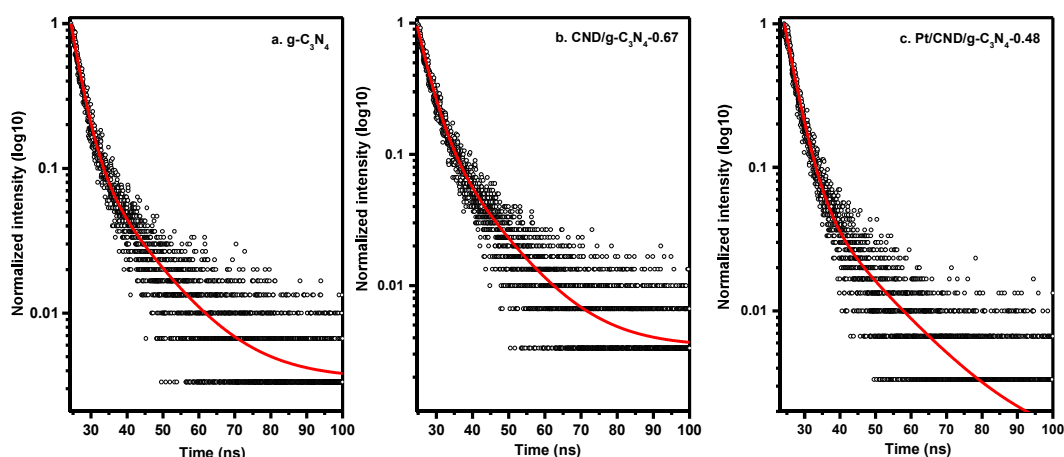


Fig. 7.10 Decay spectra of a. g-C₃N₄, b. CND/g-C₃N₄-0.67 and c. Pt/CND/g-C₃N₄-0.48

In case of Pt deposited samples, Pt/CND/g-C₃N₄-0.48 shows increase in both shortest and longest lifetime (τ_1 and τ_2) as compared to rest of the samples. Contribution from τ_1 is more as compared to τ_2 . This shows that presence of Pt and CND helps in enhancing the lifetime of charge carrier of g-C₃N₄. This prolonged lifetime will make charge carriers available for reaction, thus facilitates the photocatalytic reaction. While in case of Pt/CND/g-C₃N₄-0.67 and 0.75 both τ_1 and τ_2 decreases and their lifetimes are lower than the Pt/CND/g-

C₃N₄-0.48. The average lifetime of ternary system is as follows: Pt/CND/g-C₃N₄-0.48 > Pt/CND/g-C₃N₄-0.67 > Pt/CND/g-C₃N₄-0.75.

Table 7.5 Parameters derived from fitting of decay profile (upto 100 ns) of different samples using bi-exponential fitting decay equation CND/g-C₃N₄

Sample	τ_1 (ns)	A ₁	Relative percent age of τ_1 (%)	τ_2 (ns)	A ₂	Relative percent age of τ_2 (%)	χ^2	Average lifetime* (τ , ns)
g-C ₃ N ₄	2.78	0.848	58.95	12.34	0.133	41.04	0.98	6.70
CND/g-C ₃ N ₄ -0.48	2.63	0.826	47.2	9.17	0.265	52.79	0.98	6.08
CND/g-C ₃ N ₄ -0.67	3.22	0.785	55.99	11.55	0.172	44.00	0.98	6.88
CND/g-C ₃ N ₄ -0.75	2.16	0.763	39.80	8.06	0.309	60.19	0.98	5.71
Pt/g-C ₃ N ₄	2.5	0.895	60.08	11.35	0.131	39.92	0.98	6.03
Pt/CND/g-C ₃ N ₄ -0.48	3.17	0.88	70.08	15.61	0.076	29.92	0.98	6.89
Pt/CND/g-C ₃ N ₄ -0.67	2.08	0.769	44.35	7.69	0.261	55.65	0.99	5.2
Pt/CND/g-C ₃ N ₄ -0.75	2.01	0.744	41.99	7.41	0.279	58.01	0.98	5.14

* Average lifetime (τ) calculated using equation 7.1.

7.3.11 Photocatalytic activity

7.3.11.1 Direct water splitting under UV-visible illumination

50 mg of sample dispersed into water, evacuated and finally irradiated under 400 W UV-Visible lamp. The irradiation was carried for 20 h. After every 2 h hydrogen yield was monitored. Fig. 7.11a shows H₂ yield obtained over all the samples. Pristine g-C₃N₄ and CND/g-C₃N₄-0.48 has not shown any H₂ generation. But CND/g-C₃N₄-0.67 and 0.75 has shown considerable rise in H₂ yield compared to the pristine sample. No H₂ was observed over CND/g-C₃N₄-0.67 after 4 h of irradiation. But on further irradiation H₂ generation with the rate of 0.41 μ mol/h till 16 h and O₂ generation at 0.26 μ mol/h was observed. Ratio of H₂ and O₂ evolved was found to be 1.57:1. After 16 h, rise in H₂ generation was sluggish.

CND/g-C₃N₄-0.75 were activated for H₂ evolution after 6 h of illumination and on continuing the illumination H₂ generation rate of 0.16 μmol/h was observed for 16 h illumination. Following trend in photocatalytic activity was observed: CND/g-C₃N₄-0.67 > CND/g-C₃N₄-0.75 > CND/g-C₃N₄-0.48 ~ g-C₃N₄. Sample having optimum concentration of CND i.e. CND/g-C₃N₄-0.67 has shown highest H₂ generation among all the samples. H₂O₂ forms as an intermediate during water splitting reaction. Decomposition of H₂O₂ is catalyzed by the CND which otherwise proceeds with slow kinetics. Thus, CND/g-C₃N₄ samples show pure water splitting reaction while pristine g-C₃N₄ is inactive [88].

7.3.11.2 Activity evaluation under UV illumination and sunlight in presence of sacrificial reagent

To further enhance the photocatalytic activity, H₂ yield was monitored in presence of sacrificial reagent such as triethanolamine. CND decorated samples has shown better yield as compared to the pristine sample (Fig. 7.11b). Following trend in activity was observed: CND/g-C₃N₄-0.67 > CND/g-C₃N₄-0.62 > CND/g-C₃N₄-0.75 > g-C₃N₄ > CND/g-C₃N₄-0.48. Table 7.6 lists the rate of H₂ evolution under different conditions, light sources along with AQE and SFE values. With increase in CND concentration increase in H₂ yield was observed till 0.67 wt % on further increase in CND concentration H₂ yield decreases. Maximum activity was observed over CND/g-C₃N₄-0.67 with H₂ production rate of 4.25 μmol/h with AQE of 0.15 %. Increase in H₂ yield in CND/g-C₃N₄-0.67 as compared to pristine g-C₃N₄ can be attributed to the enhanced charge carrier lifetime and their separation evident by photoluminescence spectroscopy. The trend in activity is in agreement with photoluminescence results. The excess concentration than the optimum amount of CND acts as a recombination centre hence results into lower H₂ yield. Fang et al [323] also reported that excess concentration of CND acts as a electron recombination centre. It is also noteworthy, that all these samples did not respond in sunlight.

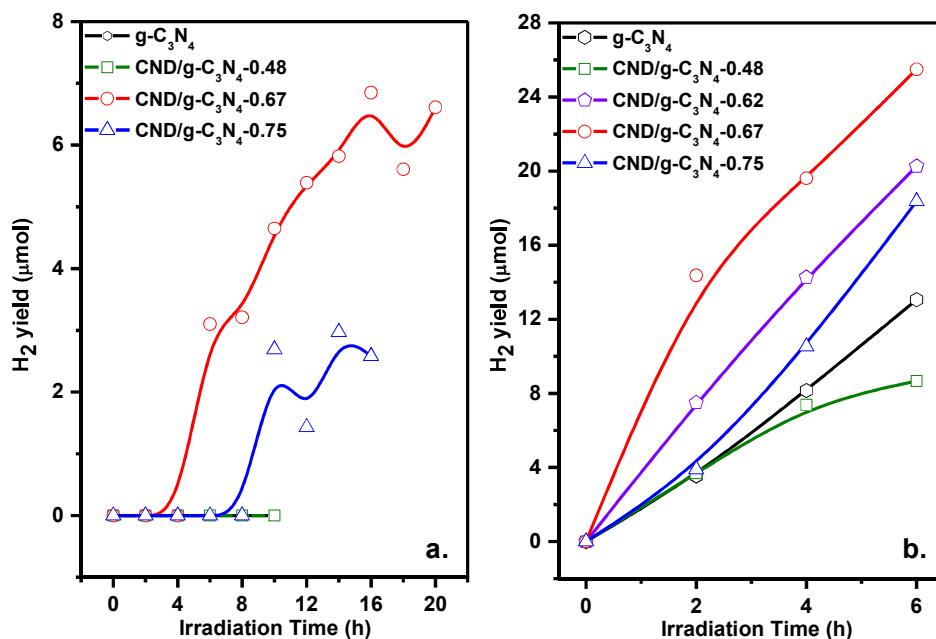


Fig. 7.11 Photocatalytic activity evaluation of g-C₃N₄ and CND/g-C₃N₄ under UV-visible irradiation in a. absence and b. presence of triethanolamine. (Experimental conditions: 50 mg of photocatalyst dispersed into water or aqueous triethanolamine solution (15 % v/v) and solution was evacuated, irradiated under UV-Visible light).

For practical application to harvest sunlight as well as to lower recombination of electron-hole pair, Pt metal was dispersed over CND/g-C₃N₄ sample. The activity of this ternary system was evaluated in both UV-visible and sunlight in presence of sacrificial reagent.

In UV-visible irradiation, almost comparable H₂ yield was observed over Pt/CND/g-C₃N₄-0.48 and 0.75 (Fig. 7.12). The sample CND/g-C₃N₄-0.67 which has performed better in UV light in both absence and presence of sacrificial reagent has shown poor activity (45.30 μmol/h) after dispersion of Pt. The following trend was observed over Pt dispersed samples: Pt/CND/g-C₃N₄-0.48 > Pt/CND/g-C₃N₄-0.75 > Pt/CND/g-C₃N₄-0.62 ~ Pt/g-C₃N₄ > Pt/CND/g-C₃N₄-0.67.

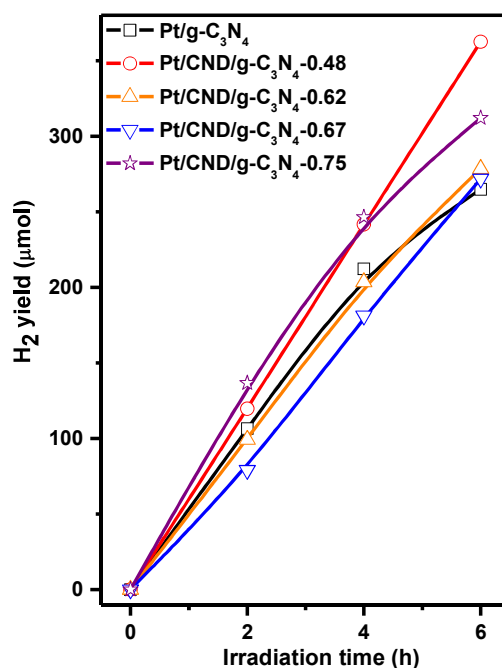


Fig. 7.12 Photocatalytic activity evaluation of Pt/g-C₃N₄ and Pt/CND/g-C₃N₄ under UV-Visible light. (Experimental conditions: 50 mg of photocatalyst dispersed into water and triethanolamine solution (15 % v/v) and mixture was evacuated and irradiated under UV-visible light)

However, under sunlight following trend was observed: Pt/CND/g-C₃N₄-0.48 > Pt/g-C₃N₄ > Pt/CND/g-C₃N₄-0.62 > Pt/CND/g-C₃N₄-0.75 ~ Pt/CND/g-C₃N₄-0.67 (Fig. 7.13a). Highest H₂ yield @ 398.28 μmol/h was observed over Pt/CND/g-C₃N₄-0.48 which is 1.7 times than that over Pt/g-C₃N₄. AQE and SFE of Pt/CND/g-C₃N₄-0.48 were found to be 4.0 and 2.04 % respectively. Pristine g-C₃N₄ has not shown any activity under similar conditions. Increased H₂ generation over Pt/CND/g-C₃N₄-0.48 can be due to prolonged lifetime of charge carrier confirmed by lifetime measurements using PL spectroscopy (Table 7.5).

To reconfirm the visible light activity of Pt/CND/g-C₃N₄-0.48, it was tested exclusively under visible light lamp and yielded H₂ @ 33.61 μmol/h in 2 L reactor in (Fig. 7.13b). Photocatalytic activity results shows that presence of CND, Pt has positive effect in enhancing the photocatalytic activity of g-C₃N₄. Among all samples, Pt/CND/g-C₃N₄-0.48 is most active which has optimum concentration of CND and proper dispersion of Pt.

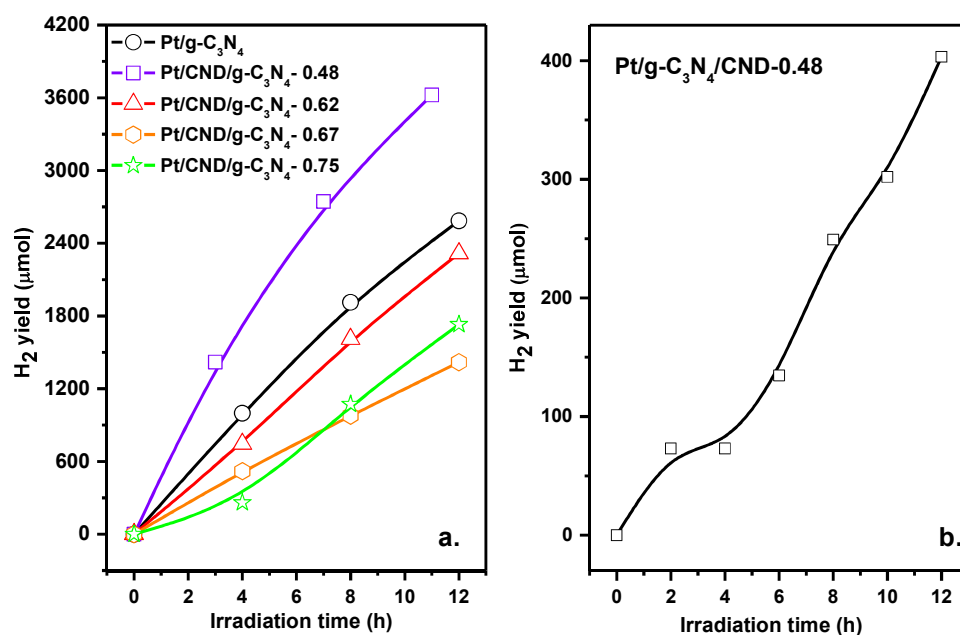


Fig. 7.13 Photocatalytic activity evaluation over a. Pt/g-C₃N₄ and Pt/CND/g-C₃N₄ under sunlight and b. Pt/CND/g-C₃N₄-0.48 under visible light. (Experimental conditions: 80 mg of photocatalyst dispersed into 150 ml of solution of water and triethanolamine (15 % v/v) and this solution was purged with argon gas and irradiated under sunlight from 11:00 to 15:00 IST or visible light).

Table 7.6 H₂ yield, AQE and SFE obtained under different conditions using Pt/CND/g-C₃N₄ samples.

Sample	Activity (μmol/h) in presence of sacrificial reagent		AQE (%) (UV-Visible)	SFE (%)	AQE (%) (Sunlight)
	UV-Visible light	Sunlight			
g-C ₃ N ₄	2.18	0	0.08	0	0
CND/g-C ₃ N ₄ -0.48	1.44	0	0.05	0	0
CND/g-C ₃ N ₄ -0.62	3.38	0	0.12	0	0
CND/g-C ₃ N ₄ -0.67	4.25	0	0.15	0	0
CND/g-C ₃ N ₄ -0.75	3.06	0	0.11	0	0
Pt/g-C ₃ N ₄	44.14	234.67	1.58	1.76	3.46
Pt/CND/g-C ₃ N ₄ -0.48	60.42	398.28	2.16	2.04	4.00
Pt/CND/g-C ₃ N ₄ -0.62	46.43	193.49	1.66	0.97	1.90
Pt/CND/g-C ₃ N ₄ -0.67	45.30	123.50	1.62	0.74	1.44
Pt/CND/g-C ₃ N ₄ -0.75	52.01	139.11	1.86	0.70	1.38

Very little literature is available on H₂ generation over CND coupled g-C₃N₄. Table 7.7 shows the comparison of available data with our results. Yet no one has reported photocatalytic H₂ generation over ternary system of Pt coupled with CND decorated g-C₃N₄

in presence of actual sunlight. Among all reports, catalysts used in this study has shown comparatively better performance in the terms of H₂ yield in presence of triethanolamine as sacrificial reagent, although it is important to mention here that experimental conditions used for activity evaluation are different. Liu et al [88] evaluated the photocatalytic activity of CND/g-C₃N₄ for pure water splitting by illuminating the sample under solar simulator and found maximum activity for 0.48 wt % CND/g-C₃N₄ with SFE of 2.0 %. But we didn't find the similar activity over CND/g-C₃N₄ samples. The catalyst synthesized in this study was active under UV-visible light for pure water splitting reaction but not found to be active under sunlight as well as visible light illumination to split pure water. To improve the activity further Pt and triethanolamine as sacrificial reagent is used. Maximum H₂ generation was observed for Pt/CND/g-C₃N₄-0.48 with AQE of 4.0 % and SFE of 2.04 % in sunlight in presence of sacrificial reagent.

Table 7.7 Comparison of present study with literature reports on various CND/g-C₃N₄ system for photocatalytic H₂ evolution under stated experimental conditions.

Sr No.	Author	Photocatalyst	Source of light	H ₂ Yield	Reaction conditions	AQE or SFE
1	Juan Liu et al [88]	Carbon nanodot-carbon nitride (C ₃ N ₄) nanocomposite	Solar simulator	46 μmol/h	80 mg of photocatalyst dispersed in water	AQE= 16 % at 420 nm, SFE 2.0 %
2	Shun Fang et al [323]	Carbon dots modified g-C ₃ N ₄ hybrid	350 W Xenon arc lamp equipped with a UV-cutoff filter (≥420 nm)	218 μmol/h/g	50 mg of the photocatalyst was suspended in 80 ml of triethanolamine aqueous solution (10 vol %)	Not given
3	Kui Li et al [320]	CQD deposited over g-C ₃ N ₄ nanosheets by hydrothermal method	300 W Xe arc lamp with an ultra-violet cutoff filter (λ > 420nm)	116.1 μmol/h	50 mg of CNNS/CQDs dispersed into 100 ml water and 10 vol % triethanolamine	Not given

4	Xinyuan Xia et al [321]	Heterostructure of g-C ₃ N ₄ nanosheets (CNNS) with CQDs synthesized by one-step hydrothermal method	1000 W xenon Lamp (UV-Vis) equipped with a cut-off filter (Vis, $\lambda \geq 420$ nm) or an 808 nm laser beam (MDL-III-808)	219.5 $\mu\text{mol/h/g}$ (UV-Vis), 50.5 $\mu\text{mol/h/g}$ (Visible) and 6.76 $\mu\text{mol/h/g}$ (near IR region at 808 nm)	10 mg of photocatalysts suspended in 10 ml aqueous Solution containing 20 vol% methanol (20%)	AQE= 0.034 % (at 800 nm)
5.	Present work	CND/g-C ₃ N ₄ -0.67	UV-visible light (400 W medium pressure Hg lamp)	0.41 $\mu\text{mol/h}$ (absence of sacrificial reagent)	50 mg of photocatalyst dispersed in 15 ml of pure water	-
			UV-visible light (400 W medium pressure Hg lamp)	4.25 $\mu\text{mol/h}$	50 mg of photocatalyst dispersed in 15 ml of 10% aqueous triethanolamine solution	AQE = 0.15 %
		Pt/CND/g-C ₃ N ₄ -0.48	UV-visible light (400 W medium pressure Hg lamp)	60.42 $\mu\text{mol/h}$	50 mg of photocatalyst dispersed in 15 ml of 10 % aqueous triethanolamine solution	AQE = 2.16%
			Sunlight	398.28 $\mu\text{mol/h}$	80 mg of photocatalyst dispersed in 150 ml of 10 % aqueous triethanolamine solution	AQE = 4.0%, SFE = 2.04%
			Visible light	33.61 $\mu\text{mol/h}$	aqueous triethanolamine solution	-

7.4 Conclusion

-NH₂ modified CND synthesized from electrochemical oxidation of graphite were anchored over g-C₃N₄. Further Pt was dispersed on the CND decorated g-C₃N₄ to improve the H₂ yield. XPS shows that the peak due to graphitic carbon increases as the CND concentration increases which reveals presence of CND on the surface. CND/g-C₃N₄-0.67 composite was found to be active for pure water splitting reaction in presence of UV-visible light with H₂ generation @ 0.41 μmol/h and O₂ @ 0.26 μmol/h for 16 h. The ternary system Pt/CND/g-C₃N₄ was found to be more active than individual CND/g-C₃N₄ and Pt/g-C₃N₄ system. Most active sample Pt/CND/g-C₃N₄-0.48 has shown H₂ @ 398.28 μmol/h with AQE of 4.0 % and SFE of 2.04 % in presence of sacrificial reagent under sunlight and 33.61 μmol/h under visible light. Our results have shown that optimum concentration of CND and proper dispersion of Pt has resulted in minimum rate of recombination which is confirmed by lifetime estimation of charge carriers using PL spectroscopy.

**Role of Metal (M = Pt, Pd, Au, Ag and Cu) Dispersion in
Improvement of Photocatalytic Properties of g-C₃N₄**

8.1 Introduction

As explained in previous chapter, g-C₃N₄ is a promising candidate for solar H₂ generation due to suitable band edge for reduction and oxidation of water and stability. However its photocatalytic activity is poor owing to high rate of recombination of electron-hole pair and medium band gap which leads to low absorption in visible region of solar spectrum [73,285,313,314]. Hence in previous chapter attempt was made to enhance the photocatalytic activity by dispersing CND on g-C₃N₄ surface. Another strategy to improve light absorption and charge separation properties of g-C₃N₄ is by forming effective metal-semiconductor heterojunction. As explained in Chapter 1, Schottky barrier is formed at the interface of metal and semiconductor and the barrier acts as driving force for the separation of electron-hole pair [334]. The height of schottky barrier depends on work function of metal. This barrier enhances with increase in work function of metal thus helping in better separation of photogenerated charge carriers [335]. Along with this metal nanoparticles shows surface plasmon effect which stimulate the light absorption properties and also provides surface active sites for the reaction [336]. There are many methods for the deposition of metal over semiconductor such as photodeposition method, wet impregnation method, chemical reduction, electrodeposition, atomic-layer deposition, sputtering and physical mixing [337]. Among all these methods photodeposition is an attractive method because it allows deposition of metal at the active centres and energy from light is sufficient

to reduce metal salt into metal nanoparticles. This method is also useful to deposit metal particle selectively on a particular plane of faceted nanoparticles [338].

Maeda et al [339] deposited Ru, Rh, Pd, Ir, Au and Pt as cocatalyst over g-C₃N₄ synthesized by photodeposition method. Among all the samples maximum H₂ generation of 7.3 μmol/h was observed over Pt/g-C₃N₄ in presence of triethanolamine under 300 W Xenon lamp illumination. Li et al [340] synthesized Au, Pt, Pd nanoparticles supported over mesoporous g-C₃N₄ nanorods for reduction of 4-nitrophenol using H₂ generated from reduction of water. Ag photodeposited over g-C₃N₄ was studied by Li et al for degradation of Rhodamine B dye under visible light illumination [341]. Some researchers have also demonstrated enhancement of photocatalytic H₂ generation after coloaded of two different metals [342].

In this chapter the role of different metals in the enhancement of solar driven photocatalytic H₂ generation over g-C₃N₄ is investigated under sunlight. For this, ~ 3(% w/w) Pt, Pd, Au, Ag and Cu was deposited over g-C₃N₄ surface by photodeposition method using respective metal precursor. Optical, electronic properties of samples were studied by relevant techniques. Time resolved photoluminescence was recorded in order to reveal the effect of metal deposition on lifetime of charge carriers. Photocatalytic properties of these samples were evaluated in water-triethanolamine solution under sunlight and UV-Visible light irradiation.

8.2 Experimental Methods

8.2.1 Synthesis of metal/g-C₃N₄ samples

Graphitic carbon nitride (g-C₃N₄) was synthesized by pyrolysis of urea (CO(NH₂)₂) at 550 °C for 3 h at a heating rate of 10 °C/min. The sequence of decomposition of urea is

mentioned in detailed in Chapter 2. Then obtained powder was washed with distilled water and dried at 80 °C.

(~ 3% w/w) Pt, Pd, Au, Ag and Cu loaded on g-C₃N₄ by photodeposition method using AR grade precursors such as H₂PtCl₄.6H₂O, PdCl₂, AuCl₃, AgNO₃ and CuSO₄.5H₂O respectively. For this, powdered g-C₃N₄ was dispersed in aqueous ethanol solution (20 % v/v) and to the dispersed solution appropriate amount of aqueous solution of metal salt was added. The mixture was evacuated to remove air and then irradiated under UV-Visible (medium pressure mercury UV-Visible lamp, 400 W) source for 3 h. The solid product was filtered, washed with distilled water and dried in oven at 80 °C. However, for Cu loading, irradiation was continued for 8 h to ensure complete reduction of Cu²⁺ to Cu⁰.

8.2.2 Characterization

Powder X- ray diffraction (XRD) patterns were recorded on a Philips diffractometer (model PW 1710), equipped with a graphite monochromator and Ni-filtered Cu-K_α radiation. Vibrational spectra of samples were recorded on a Bomem (MB 102) spectrometer in the mid-IR region (4000 to 200 cm⁻¹). TEM was recorded on FEI-Tecnai G-20 microscope operating at 200 kV. Light absorption properties of all samples were recorded in range of 200-800 nm at a scanning speed of 200 nm/min using JASCO model V-530 (Japan) spectrophotometer and BaSO₄ as reflectance standard. Photoluminescence studies were carried out at room temperature with a resolution of 3 nm, using Edinburgh Instruments' FLSP 920 system having a 450 W Xe lamp as the excitation source having a Peltier element cooled red sensitive Hamamatsu R955 PMT. All emission spectra were corrected for the detector response. Lifetime measurements were carried out by using a nanosecond hydrogen flash lamp as the excitation source and employing Time Correlated Single Photon Counting (TCSPC) technique. All the data were fitted with biexponential fitting. It gives two lifetime

values τ_1 and τ_2 and corresponding amplitude, A_1 and A_2 respectively. Average lifetime (τ) was determined using equation 7.1 [325].

8.2.3 Photocatalytic activity

Photocatalytic activity of all the samples was evaluated under UV-Visible light and sunlight. Sample was suspended in water + triethanolamine (10 % v/v) solution in a quartz reactor having illumination area of 20 cm². The resultant solution was evacuated and irradiated under medium pressure mercury lamp (Hg, SAIC, India, 400W) surrounded with water circulation jacket to absorb IR irradiation. Similarly, photocatalytic tests were also performed by irradiating sample under sunlight in a reactor having volume of 2 L. Instead of evacuation of reactant solution it was purged with inert gas to remove air as volume of reactor was large. Sunlight illumination was carried out for duration of 4 h during 11.00-15.00 IST under sunlight. Photocatalytic H₂ production was quantified by gas chromatography (Shimadzu, GC 2010 plus) equipped with carboxen column (30 m length, 0.32 mm ID) and thermal conductivity detector using argon as the mobile phase. Solar flux was measured in the peak hours using light meter LX 1108 (Lutron Electronic) during 11.00-15.00 IST and average of lux recorded were used for AQE and SFE measurement. Calculation of AQE and SFE is described in detail in Chapter 2.

8.3 Results and discussion

8.3.1 XRD

Fig. 8.1 a shows the XRD pattern of g-C₃N₄ and metal/g-C₃N₄. XRD spectrum of g-C₃N₄ exhibited major diffraction peaks at $2\theta = 27.72^\circ$ and 12.91° which corresponds to *002* and *100* crystalline planes (mentioned as * in Fig. 8.1a) attributed to interlayer stacking of aromatic systems with interlayer spacing of 0.321 nm and in-plane structural repeating unit with distance of 0.685 nm, respectively [331]. All metal/g-C₃N₄ exhibited similar XRD

pattern as that of pristine g-C₃N₄ except Au/g-C₃N₄ which shows additional diffraction peaks at $2\theta = 38.23^\circ$ (marked as # in Fig. 8.1a) which corresponds to *111* plane of Au metal (JCPDS No. 04-0784). It can be inferred from the spectra that deposition of metal has not hampered the structure of g-C₃N₄ as no shift in the peak position was observed.

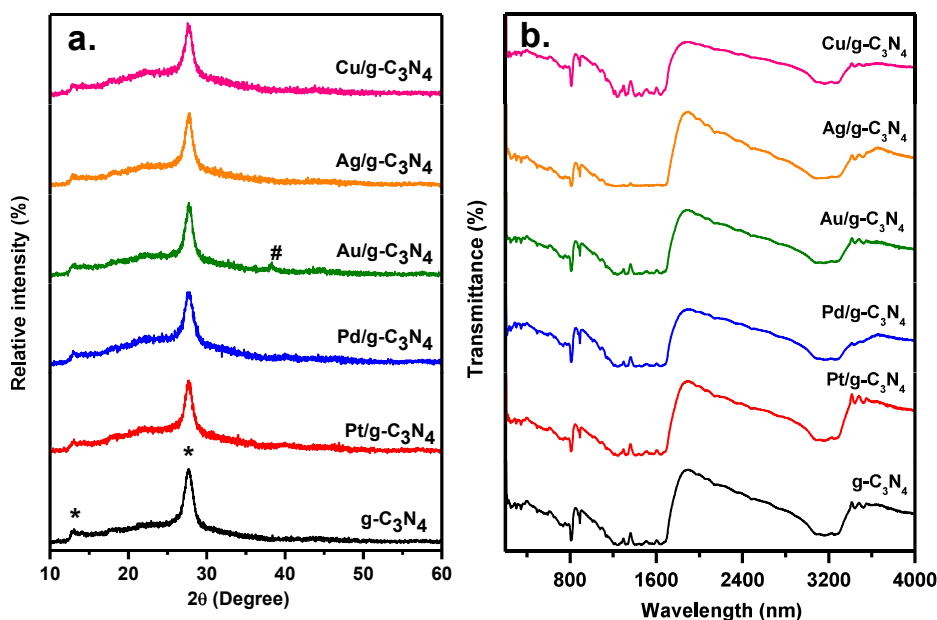


Fig. 8.1 a. XRD pattern and b. FTIR spectra of g-C₃N₄ and metal/g-C₃N₄ samples.

8.3.2 FTIR

Fig. 8.1b shows FTIR spectrum of g-C₃N₄ and metal/g-C₃N₄. The sharp band at 812 cm⁻¹ attributed to the out of plane bending vibration of heptazine rings. Peak observed at 890 cm⁻¹ corresponds to deformation modes of NH group [327]. The broad band in the range of 2900- 3500 cm⁻¹ assigned to stretching vibration modes for OH and amine group (-NH₂ or -NH) [342]. Absorption band at 1636 cm⁻¹ corresponding to C=N stretching vibration mode and peaks at 1247, 1329, 1423 and 1569 cm⁻¹ assigned to aromatic C-N stretching [327]. Metal/g-C₃N₄ samples exhibits the similar FTIR spectra as that of pristine g-C₃N₄ sample. This signifies that presence of metal has not hampered the structure of g-C₃N₄. This is in accordance with the XRD result.

8.3.3 ICP-OES

Metal content in all metal/g-C₃N₄ samples was quantified by using ICP-OES technique and tabulated in Table 8.1. Metal content was found to be nearly 2 wt%. It is lesser than the amount of metal targeted for loading. Probably some metal was lost in solution.

Table 8.1 Metal content of g-C₃N₄ and metal/g-C₃N₄ sample.

Sample	Metal content by ICP-OES (wt%)
Pt/g-C ₃ N ₄	2.1
Pd/g-C ₃ N ₄	1.7
Au/g-C ₃ N ₄	1.1
Ag/g-C ₃ N ₄	2.1
Cu/g-C ₃ N ₄	1.4

8.3.4 TEM

Morphology and the dispersion of metal over g-C₃N₄ were analyzed by TEM. Low resolution TEM images of g-C₃N₄ shows layered structure and these layers are back folded as shown in Fig. 7.4a. Metal particles are clearly discerned because of difference in electron density between metal and g-C₃N₄. The loading of metal by photodeposition method exhibits more or less spherical Pt, Au and Pd particles (Fig. 8.2a, b, c). HR-TEM of Pt/g-C₃N₄ shows distribution of Pt particles with lattice fringes of 0.23 nm belongs to the *111* plane of metallic Pt. High resolution image of Au/g-C₃N₄ and Pd/g-C₃N₄ shows lattice fringes with fringe width of 0.23 nm and 0.22 nm belonging to *111* plane of Au and Pd respectively. This signifies the crystalline nature of Pt, Au and Pd. SAED pattern of Au/g-C₃N₄ and Pd/g-C₃N₄ is shown in b and c and both shows diffused rings revealing nanocrystalline nature of sample. The rings in SAED pattern of Au/g-C₃N₄ were indexed for metal Au. The line scanning recorded over Au/g-C₃N₄ sample and the green line indicates where the line scanning was performed. The position marked as 1 in Fig. 8.2d shows presence of Au particle over g-C₃N₄.

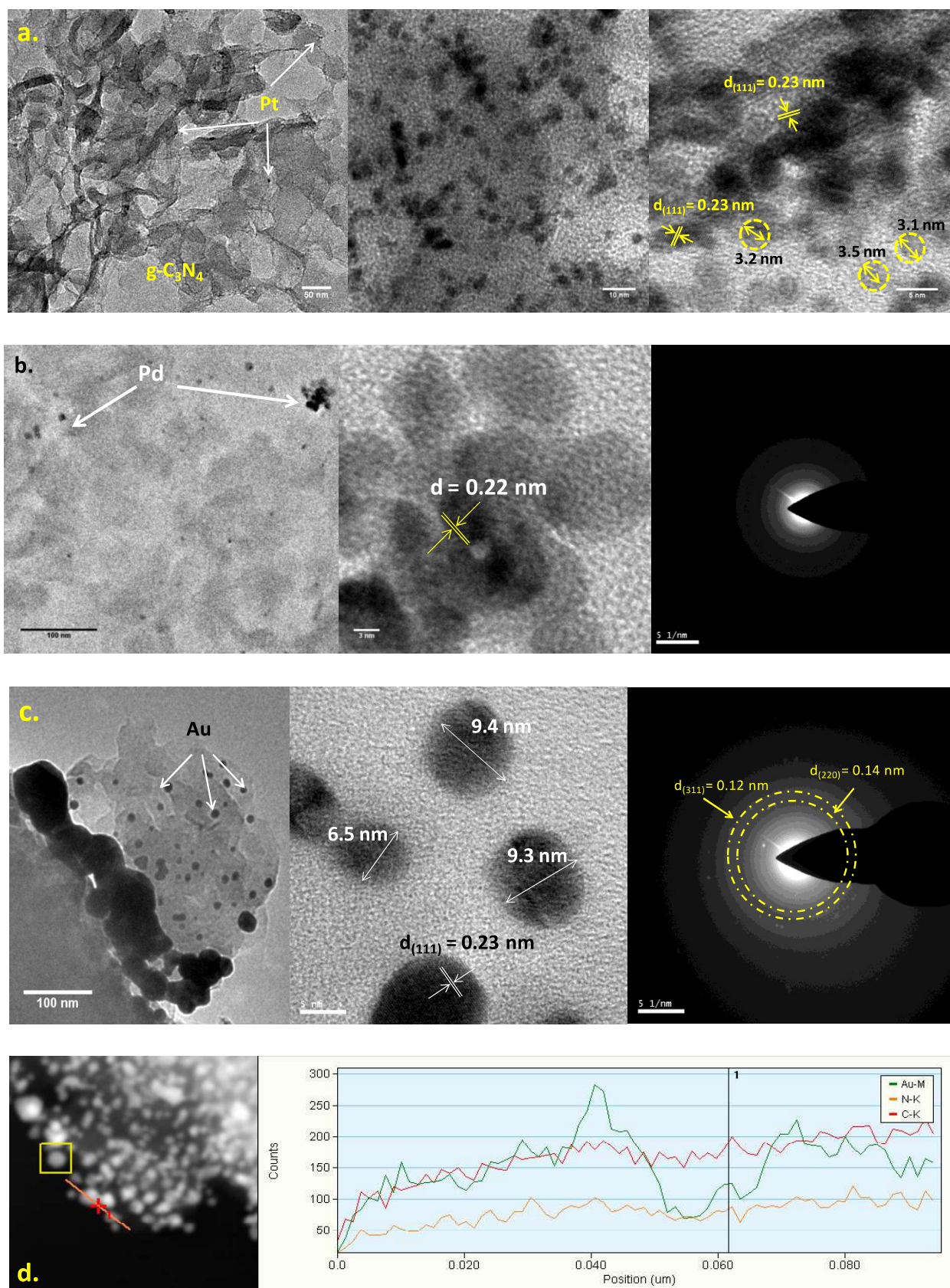


Fig. 8.2 a. Low and high resolution TEM images and SAED pattern of a. Pt/g-C₃N₄, b. Pd/g-C₃N₄. c. Au/g-C₃N₄ and d. EDX line scanning of Au/g-C₃N₄

8.3.5 DRS

Fig. 8.3a shows the DRS spectrum of $g\text{-C}_3\text{N}_4$, $\text{Pt}/g\text{-C}_3\text{N}_4$, $\text{Pd}/g\text{-C}_3\text{N}_4$, $\text{Au}/g\text{-C}_3\text{N}_4$, $\text{Ag}/g\text{-C}_3\text{N}_4$ and $\text{Cu}/g\text{-C}_3\text{N}_4$. DRS spectrum of pristine $g\text{-C}_3\text{N}_4$ is compared with metal deposited samples. Presence of metal has extended absorption in the visible region as compared to pristine sample. $g\text{-C}_3\text{N}_4$ shows optical absorption edge around 440 nm which is in accordance with previous reports [327]. An extra absorption peak was found in visible region at 488, 565 and 686 nm for $\text{Ag}/g\text{-C}_3\text{N}_4$, $\text{Au}/g\text{-C}_3\text{N}_4$ and $\text{Cu}/g\text{-C}_3\text{N}_4$ respectively. These peaks are due to the surface plasmon resonance (SPR) effect of metal nanoparticles. These positions matches with the literature report [341,343,344]. The position of SPR maxima depends on particle size, shape/aspect ratio, interparticle interactions, dielectric properties and local environment of the nanoparticles [343]. DRS spectrum of $\text{Pt}/g\text{-C}_3\text{N}_4$ and $\text{Pd}/g\text{-C}_3\text{N}_4$ shows absorption in all wavelengths of visible region as compared to the pristine $g\text{-C}_3\text{N}_4$. This indicates that Pt and Pd deposited samples absorb all the light falling on it which is also evidenced by the black colour of the Pt and Pd/ $g\text{-C}_3\text{N}_4$ samples. From Fig. 8.3a it can be inferred that metal/ $g\text{-C}_3\text{N}_4$ enhances light absorption in visible region which results into increased number of photogenerated charge carriers hence improved photocatalytic activity.

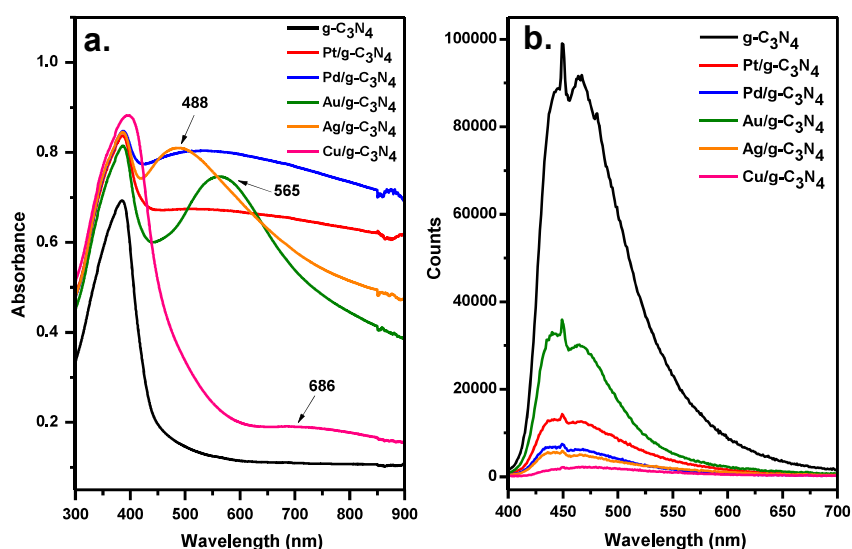


Fig. 8.3 a. UV-visible DRS and b. photoluminescence spectra of $g\text{-C}_3\text{N}_4$ and metal/ $g\text{-C}_3\text{N}_4$ samples.

8.3.6 Photoluminescence spectroscopy

Photoluminescence spectroscopy provides information on electron and hole pair recombination. Emission spectra of samples were recorded by irradiating the sample at 380 nm and depicted in Fig. 8.3b. A broad peak at 450 nm corresponds to band to band transition. This transition arises due to $n-\pi^*$ transition [345]. Addition of metal does not alter the position of emission peak in comparison with pristine $g-C_3N_4$. High intensity of peak in PL spectrum indicates higher rate of recombination and vice versa. From the spectra it can be inferred that presence of metal decreases the e^-/h^+ pair recombination as decrease in intensity of emission peak of metal/ $g-C_3N_4$ samples was observed as compared to pristine sample.

To further probe the role of different metal to reduce recombination rate, life time of all the samples were measured. Excitation and emission wavelengths for all samples were monitored at 380 nm and 450 nm, respectively. Time resolved photoluminescence data was fitted with biexponential fitting and lifetime of charge carrier were evaluated using equation 7.1. The fitted data is shown in Fig. 8.4.

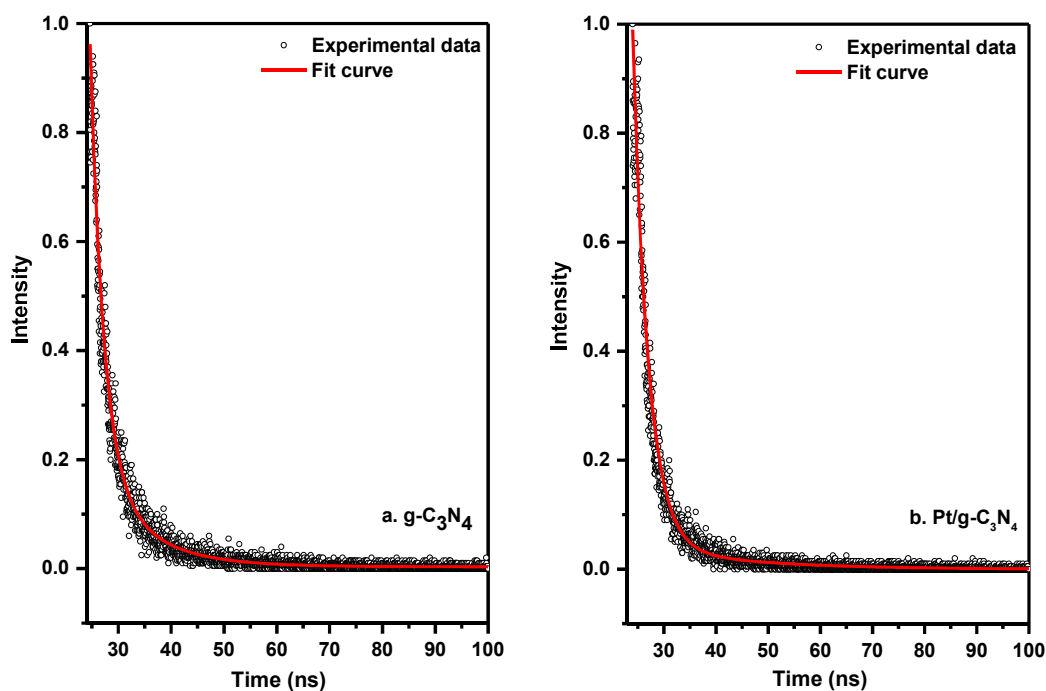


Fig. 8.4 Biexponential fitting of decay curve of a. $g-C_3N_4$ and b. Pt/ $g-C_3N_4$

Radiative lifetimes and their contribution in the decay process along with average life time are listed in Table 8.2. Two lifetimes were observed. Short lifetime increases from 2.54 ns for g-C₃N₄ to 2.95, 2.58, 2.56 for Pt, Pd and Ag deposited samples respectively. Au/g-C₃N₄ and Cu/g-C₃N₄ shows decrease in short lifetime as compared to g-C₃N₄ to 1.91 ns and 2.06 ns respectively. The longest life time increases from 9.52 ns for g-C₃N₄ to 19.88, 16.88 and 10.08 ns for Pt/g-C₃N₄, Ag/g-C₃N₄ and Cu/g-C₃N₄ respectively. For Au/g-C₃N₄ and Pd/g-C₃N₄ longest life time decreases to 7.13 and 7.21 ns respectively.

Among all the samples Pt/g-C₃N₄ has shown maximum average lifetime of 7.15 ns as compared to pristine sample. This implies that loading of metal over g-C₃N₄ enhances the radiative lifetime due to formation of Schottky barrier at the interface which helps in delaying the recombination reaction.

Table 8.2 Lifetime measurement by biexponential fitting (upto 100 ns)

Sample	Lifetime τ_1 (ns)	A ₁	%	Lifetime τ_2 (ns)	A ₂	%	χ^2	Average lifetime (ns)
g-C ₃ N ₄	2.54	0.86	54.7	9.52	0.19	45.29	0.97	5.76
Pt/g-C ₃ N ₄	2.95	0.95	75.40	19.88	0.05	24.6	0.97	7.15
Pd/g-C ₃ N ₄	2.58	0.89	71.01	7.21	0.13	28.99	0.97	3.96
Au/g-C ₃ N ₄	1.91	0.76	37.45	7.13	0.34	62.55	0.98	5.17
Ag/g-C ₃ N ₄	2.56	0.89	72.97	16.88	0.05	27.03	0.97	6.75
Cu/g-C ₃ N ₄	2.06	0.91	65.03	10.08	0.10	34.97	0.98	4.85

8.3.7 Photocatalytic activity

8.3.7.1 Activity under UV-visible illumination

The potential of metal/g-C₃N₄ samples for H₂ generation was evaluated by irradiating the sample under different light sources. Fig. 8.5a shows photocatalytic H₂ generation over metal/g-C₃N₄ from an aqueous triethanolamine solution under UV-Visible light irradiation. It was observed that amount of H₂ evolved increased linearly with increase in irradiation time. Among all samples the pristine g-C₃N₄ has shown lowest activity i.e. H₂ generation @ 1.84 μ mol/h. After loading of metal like Pt, Pd, Au, Ag and Cu enhancement in the yield was

examined. This reveals that metal incorporation enhances the photocatalytic activity. Following order for photocatalytic H₂ generation was observed: Pt/g-C₃N₄ (44.14 μmol/h) > Au/g-C₃N₄ (23.35 μmol/h) > Ag/g-C₃N₄ (4.89 μmol/h) > Pd/g-C₃N₄ (3.56 μmol/h) > Cu/g-C₃N₄ (2.12 μmol/h) ~ g-C₃N₄ (1.84 μmol/h). Maximum H₂ yield @ 44.14 μmol/h was obtained over Pt/g-C₃N₄ which is ~ 24 times more as compared to pristine g-C₃N₄. The AQE of Pt/g-C₃N₄ is found to be 1.58 %. (Table 8.3)

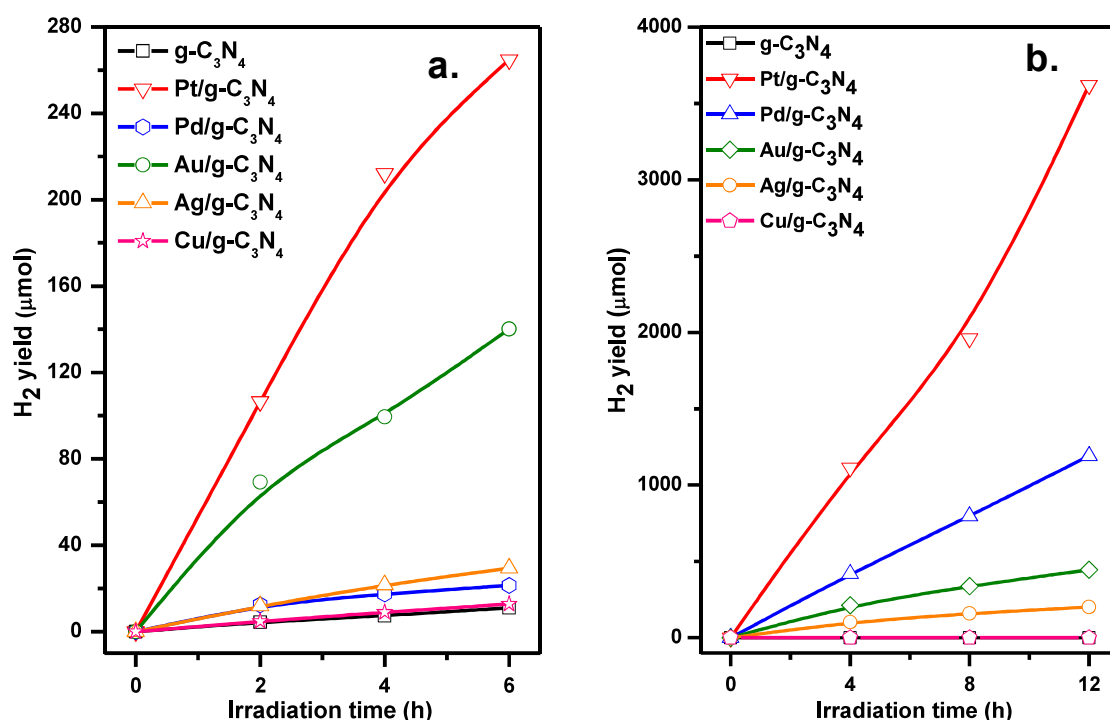


Fig. 8.5 Photocatalytic H₂ generation evaluated over g-C₃N₄ and metal/g-C₃N₄ under a. UV-Visible (Experimental condition: 50 mg of sample dispersed in 15 ml of water + triethanolamine solution (10 % v/v), evacuated and irradiated under UV-Visible lamp (400 W medium pressure Hg lamp)) and b. sunlight illumination (Experimental condition: 80 mg of sample dispersed in 150 ml of water + triethanolamine solution (10 % v/v), purged with argon gas and irradiated under sunlight from 11:00 to 15:00 IST).

8.3.7.2 Activity under sunlight illumination

In similar way for practical application, performance of metal/g-C₃N₄ samples was evaluated under sunlight in 2 L capacity photoreactor. Amount of H₂ generated monitored with illumination time and shown Fig. 8.5b. Highest H₂ yield @ 234.67 μmol/h obtained over 80 mg of Pt/g-C₃N₄ with AQE and SFE of 3.46 and 1.76 % respectively. Pristine g-C₃N₄ and

Cu/g-C₃N₄ has not shown any activity in sunlight whereas sample loaded with (3% w/w) Pt, Pd and Au has shown remarkable amount of H₂ production while pristine g-C₃N₄ sample was inactive under sunlight. The order of solar assisted H₂ generation is as follows: Pt/g-C₃N₄ (234.67 μmol/h) > Pd/g-C₃N₄ (99.23 μmol/h) > Au/g-C₃N₄ (37.04 μmol/h) > Ag/g-C₃N₄ (16.81 μmol/h) > Cu/g-C₃N₄ (0 μmol/h) ~ g-C₃N₄ (0 μmol/h).

Table 8.3 H₂ yield, AQE and SFE calculated over different metal/g-C₃N₄ samples with different irradiation sources

Sample	Activity (μmol/h)		AQE (η, %) (UV-visible)	AQE (η, %) (Sunlight)	SFE (%)
	UV-Visible light	Sunlight			
g-C ₃ N ₄	1.84	0	0.07	0	0
Pt/g-C ₃ N ₄	44.14	234.67	1.58	3.46	1.76
Pd/g-C ₃ N ₄	3.56	99.23	0.13	1.13	0.58
Au/g-C ₃ N ₄	23.35	37.04	0.84	0.58	0.30
Ag/g-C ₃ N ₄	4.89	16.81	0.17	0.19	0.09
Cu/g-C ₃ N ₄	2.12	0	0.08	0	0

8.4 Relation between work function of metal and H₂ yield

Work function of metal is in following order Pt > Pd > Au > Cu > Ag [332]. Work function of g-C₃N₄ is 4.34 eV lower as compared to all of these noble metals [346]. After absorption of light by metal/g-C₃N₄ electron from valence band of g-C₃N₄ gets excited to conduction band. These electrons from the conduction band then transfer to the metal where the reduction of water takes place to produce H₂. Nearly same trend was observed for photocatalytic activity under sunlight except for Cu. Ag/g-C₃N₄ has shown better activity as compared to Cu/g-C₃N₄ though Cu has higher work function than Ag. Among all these samples Pt/g-C₃N₄ shows highest activity for H₂ generation which can be ascribed to larger work function of Pt among Pd, Au, Ag and Cu. Schottky barrier is enhances if the work function of metal is high. Presence of Schottky barrier results into electron-hole pair

separation thus prolongs the life time of photo-generated charge carriers as evidenced by the photoluminescence spectroscopy.

Pt/g-C₃N₄ exhibited highest activity due to following reasons (i) increase in light absorption due to SPR effect, (ii) reduction of charge carrier lifetime as a result of formation of Schottky barrier, (iii) acts as cocatalyst by providing surface active sites and lowering overpotential for reaction.

8.5 Conclusion

Reduction of recombination rate due to formation of Schottky barrier evidence by photoluminescence studies and enhancement of visible light absorption properties of sample as a result of surface plasmon resonance which is seen in DRS spectrum has contributed positively for enhancement of H₂ yield over metal/g-C₃N₄ sample as compared to pristine g-C₃N₄ sample. Among all the metals Pt, Pd and Au has exhibited significant rise in H₂ yield as compared to the pristine g-C₃N₄ sample under sunlight.

Conclusion and Scope of the Work in Future

H₂ generation by splitting water into H₂ and O₂ can solve near future energy crises. There are many methods to split water by using renewable energy such as solar energy. One of the attractive methods is photocatalytic water splitting. In this method photocatalyst absorbs light falling on it and use this energy to break water molecule into H₂ and O₂. Extensive efforts have taken place in recent past to develop novel materials but still the required efficiency for commercialization of the process is not yet achieved.

In this work two different kinds of photocatalyst were selected on the basis of stability and low cost, one is metal oxide based such as TiO₂, UV light absorber with band gap of 3.2 eV and other is organic nitride based semiconductor, g-C₃N₄ having a band gap of 2.7 eV. The inherent problem with the two systems is poor light absorption as well as high recombination of photogenerated charge carriers which leads to low activity in sunlight. With the aim to improve the photocatalytic efficiency of these systems various strategies such as band gap engineering by cationic doping, forming *pn* junction to reduce the recombination rate, decorating with carbon to form carbon-semiconductor heterostructure to improve mobility of charge carriers as well as light absorption and forming noble metal-semiconductor heterojunctions for efficient separation of charge carriers were adopted.

The light absorption and rate of electron-hole pair recombination of pure TiO₂ was improved by doping Cu into the lattice of TiO₂, forming *pn* junction with CuO and NiO and heterojunction with carbon. In case of g-C₃N₄ photocatalytic properties were improved by decorating it with carbon nanodots and forming heterojunction with metal like Pt, Pd, Au, Ag and Cu.

Sol-gel method was adopted to incorporate Cu into TiO₂ lattice, form composite of CuO-TiO₂, NiO-TiO₂ and C@TiO₂. The amount of Cu was varied from 2-50 mol %. No separate phase of CuO was formed till 10 mol % Cu addition. On further rise in Cu content different phase of CuO was observed which inferred that TiO₂ lattice can tolerate Cu upto 10 mol %. The elemental analysis quantified from ICP-OES was in agreement with the expected composition. In another study, NiO-TiO₂ composites were prepared to create *pn* junctions in different samples having varied ratio of NiO:TiO₂ phase with NiO from 15-65 mol %. Along with formation of NiO and TiO₂ another phase of NiTiO₃ was co-formed. To evaluate the contribution of NiTiO₃ in photocatalytic activity of the composite sample, a nearly pure phase of NiTiO₃ was synthesized by solid state as well as sol gel route. Presence of NiTiO₃ may hamper the formation of *pn* junction. Hence gel drying temperature and calcination temperature was optimized to attain a composite with minimum impurity of NiTiO₃ phase. The optimum condition of synthesis of NiO-TiO₂ with the desired composition was found at gel drying temperature of 90 °C and finally calcining at 600 °C. Sol gel method is useful to form *pn* junction in the bulk as this methods allows mixing of precursors at molecular level. Another strategy to modify the catalytic, electronic and morphological properties of TiO₂ was by incorporating carbon. C@TiO₂ composites were synthesized by sol-gel method by mixing ethylene glycol and titanium tetrabutoxide and allowed to form organic-inorganic polymer which on calcination in inert atmosphere at 500 °C forms C@TiO₂ composite. By using this method carbon content was altered from 0.14 to 14.7 wt % in the composite as confirmed using CHN analysis.

For g-C₃N₄ synthesis, thermal decomposition of urea was carried out in a crucible covered with lid. Carbon nanodots (CND) were dispersed on its surface to improve the light absorption properties and acts as electron reservoir. CND were obtained from electrochemical oxidation of graphite rod and further treated with ammonia. CND of 4-7 nm were decorated

over g-C₃N₄ surface by heating a mixture of urea and NH₂ modified CND solution at 550 °C. In another approach, metals like Pt, Pd, Au, Ag and Cu was dispersed over g-C₃N₄ by photodeposition method. By this method small nanoparticles of Pt in the range of 2-8 nm can be deposited on the surface of g-C₃N₄. Photodeposition method also provides an additional advantage of depositing metal at the active sites of the catalyst.

Optical, surface and electronic properties of all these samples were characterized by X-ray diffraction (XRD), Fourier transform Infrared spectroscopy (FTIR), Raman spectroscopy, Nuclear Magnetic Resonance Spectroscopy (NMR), X-ray absorption spectroscopy (EXAFS/XANES), N₂-BET surface area, high resolution transmission electron microscopy (HRTEM)/ selected area electron spectroscopy (SAED), X-ray photoelectron spectroscopy (XPS), inductively coupled plasma- optical emission spectroscopy (ICP-OES), diffuse reflectance UV-visible spectroscopy (DRS) and photoluminescence spectroscopy (PL).

In all samples anatase phase of TiO₂ is the major phase. Anatase phase is photocatalytically more active as compared to the rutile phase of TiO₂. XRD spectrum of Cu doped TiO₂ system has not shown any peak of CuO phase which confirms the incorporation of Cu in TiO₂ lattice. Whereas XRD pattern of composite of CuO-TiO₂ shows both the phases of CuO and TiO₂ which is also evident from the SAED pattern of composite samples. Phase identification by XRD reveals presence of crystalline cubic NiO and tetragonal anatase and rutile phase of TiO₂ along with rhombohedral NiTiO₃ phase in NiO-TiO₂ samples. XRD pattern of C@TiO₂ composite exhibits line belongs to anatase phase of TiO₂. Decrease in crystallite size from 22.9 to 5.8 nm with increase in carbon content was estimated using Scherrer equation. This reveals that presence of carbon restricts growth of TiO₂ particles which is also evident by Raman spectroscopy. Structural characterization by Raman spectroscopy was further reveals presence of characteristic peaks of anatase phase in TiO₂

modified samples. In Cu doped and CuO composite samples and C@TiO₂ samples, E_g peak (144 cm⁻¹) of anatase phase of TiO₂ shows shift towards higher wavenumber (upto 148 cm⁻¹) and considerable increase in FWHM with increase in Cu or C content in the samples. This can be attributed to increased nanocrystallinity of the samples with an increase in Cu and C content. Raman spectra of C@TiO₂ shows characteristics G and D band which reveals the presence of sp² hybridized carbon atoms in graphite like arrangement and disorder sp² carbon atom in the structure respectively. The shift in D and G band was observed in C@TiO₂ composite which indicates structural imperfection in the carbon or presence of nanocrystalline graphite. EXAFS of Cu doped and C@TiO₂ sample revealed that the disorder in lattice is increases with increase in the amount of Cu and carbon respectively. Distorted structures are more open and flexible with improved charge carrier dynamics and favourable photocatalytic properties.

XRD spectrum of g-C₃N₄ sample exhibits two characteristic peak at 12.9 and 27.7° corresponds to *100* and *002* planes ascribed to inplanar repeating units with a period of 0.68 nm and layered staking with inter-planar spacing of 0.32 nm of aromatic systems respectively. After dispersion of CND and metal particles, structural as well as thermal properties were unaltered as evident from the XRD, FTIR and TG/DTA spectra.

Surface and morphological features were studied using N₂-BET surface area and HR-TEM respectively. Both modified TiO₂ and g-C₃N₄ samples shows type IV adsorption-desorption isotherm. Cu-Ti oxides shows enhanced porosity and surface area (60-70 m²g⁻¹) and exhibited nanosized particles of 7-15 nm lower than pristine TiO₂. NiO-TiO₂ (1:1) (referred as NTC11) having minimal amount of NiTiO₃ shows presence of monodisperse, nanosized faceted particles, having higher surface area, better porosity and pore volume as compared to pristine TiO₂ sample. In case of NiO-TiO₂ (0.35:65) (referred as NTC36) sample where NiTiO₃ phase was dominant shows presence of large particles with low surface area of

19 m²/g. In case of C@TiO₂ samples surface area enhances from 20 to 147 m²/g and pore volume increases from 0.0314 to 0.1461 cm³/g with increase in carbon content. Among all the TiO₂ modified samples presence of carbon has shown enhanced surface area which is important in heterogeneous catalysis. Cu existed in +2 and +1, Ti in +4 and O as O²⁻ and OH⁻ ions was confirmed on surface by XPS of Cu_{0.02}Ti_{0.98}O_{2-δ} oxide. XPS shows presence of Ni, Ti in +2 and +4 state respectively. Surface concentration of [Ni]/[Ti] was ascertained to be 0.95 by XPS, close to the expected value of 1.0 in case of most active composition, NTC11 (NiO:TiO₂ in 1:1) among NiTi oxides. This revealed that, the composite character of bulk in NTC11 is extended upto surface and Ni and Ti metal ions are homogeneously distributed over the surface of NTC11. XPS spectra of C@TiO₂ samples shows that hydroxylation increases with increase in carbon content and also presence of sp² hybridized carbon, C-OH and C=O group on the surface. In case of CND/g-C₃N₄, XPS shows that the content of graphitic carbon increases with the increases in CND concentration, thus confirming the presence of dispersed CND on the surface of parent g-C₃N₄. XPS spectrum of Pt/g-C₃N₄ sample confirms the existence of metallic Pt on the surface.

Photoluminescence (PL) spectra reveal the course of electron and hole produced after absorption of light. *pn* nanojunctions formation in NTC11 is evident by enhanced life times of charge carriers monitored by time resolved photoluminescence. Photoluminescence spectroscopy of metal/g-C₃N₄ and CND/g-C₃N₄ shows the enhancement of life time of charge carriers as compared to the pristine g-C₃N₄ sample. Reduction of recombination rate in metal/g-C₃N₄ due to formation of Schottky barrier is evident by photoluminescence studies.

Optical properties of the samples were recorded using UV-visible diffuse reflectance spectroscopy. Cu in both doped as well as in composite form, NiO modified TiO₂ and C@TiO₂ composite has shown enhancement towards higher wavelengths in visible light as compared to pristine TiO₂. Also the calculation of valence band offset (ΔE_v) and conduction

band offset (ΔE_c) at NiO and TiO₂ heterojunction in NiO:TiO₂ (1:1) reveals type-II band alignment at the interface and the effective forbidden gap was deduced to be 3.2 (E_{g, TiO_2}) - $\Delta E_v = 3.6 (E_{g, NiO}) - \Delta E_c = 2.67$ eV. Thus, a composite of *pn* oxides offers lower band gap energy of 2.67 eV as compared to both pure oxides TiO₂ and NiO. In case of CND/g-C₃N₄ not much change in absorption was observed but after addition of Pt light absorption into visible region was enhanced. Surface plasmon resonance effect exhibited by metal nanoparticles enhances visible light absorption of metal/g-C₃N₄ sample as compared to the pristine sample.

All the samples prepared were active under UV-visible light. But to evaluate the potential of photocatalyst for practical application activity was carried out in sunlight. Evolution of bubbles during sunlight irradiation was observed and rate and size of bubbles varied with the different photocatalysts. The photocatalytic activity studies have shown that 2 mol% Cu-TiO₂ (360 $\mu\text{mol/h/g}$) was most active among doped samples and 20 mol% CuO-TiO₂ (255 $\mu\text{mol/h/g}$) among composite CuO-TiO₂ samples as compared to pristine TiO₂ (249 $\mu\text{mol/h/g}$) evaluated under sunlight in presence of methanol as sacrificial agent. It was observed that CuO reduces to photocatalytically more active Cu₂O by photogenerated e^- on surface of composites as evident by the XPS spectra of used CuTi sample. Cu₂O plays a crucial role in photoreduction of water molecules on the surface of the CuTi photocatalyst. From reduction potentials values, reduction of cupric to cuprous ion is more favourable than water reduction. Under light illumination, photogenerated e^- reduces Cu^{+2} to Cu^{+1} at the surface. Cu₂O formed on the surface with band gap of 2.2 eV, absorbs visible light photons to generate e^- s which are transferred from CB of Cu₂O to CB of TiO₂ and reduces water molecules to evolve H₂. Also presence of adsorbed $>\text{C}=\text{O}$ species in used CuTi(2) catalyst suggests oxidation of methanol to higher oxidation products on the surface of photocatalyst is

taking place. Surface composition of used oxide by XPS shows that its surface is enriched in Cu^{+1} indicating the predominance of $\text{Cu}_2\text{O-TiO}_2$ type of oxides instead of CuO-TiO_2 .

In case of NiO-TiO_2 composite, presence of NiTiO_3 was found to be derogatory for H_2 yield. Among all composites of NiO-TiO_2 , maximum H_2 yield @ 169 $\mu\text{mol/h/g}$ was observed over NiO: TiO_2 (1:1) having minimum amount of NiTiO_3 phase. H_2 yield @ 537 $\mu\text{mol/h/g}$ with 5.4 % AQE was observed after photodepositing 1 % (w/w) Pt over this sample. The linear rise in H_2 yield with time was observed. No deterioration in photocatalytic activity was found during long term activity evaluation of 60 h under sunlight. The enhanced hydrogen generation in NiO-TiO_2 composites was a result of formation of *pn* junctions in these composites, at which the separation of photogenerated e^- and h^+ was facilitated, leading to suppression of the recombination reaction and efficient reduction of water molecules. Maximum activity was observed over C@TiO_2 sample having carbon of 3.8 w/w %, which was ~ 4 times higher than the rate observed over pristine TiO_2 under UV-Visible illumination. After Pt loading rate of H_2 generation observed was 7689.5 $\mu\text{mol/h/g}$ and 2721.6 $\mu\text{mol/h/g}$ (AQE 11.44 %) under UV-Visible and sunlight illumination respectively. Almost constant H_2 evolution was observed after irradiating the sample under sunlight illumination for 32 h under sunlight irradiation. This high photocatalytic activity can be attributed to improved light penetration, absorption properties and high surface area.

Pristine $\text{g-C}_3\text{N}_4$ has not shown any activity under sunlight illumination. $\text{CND/g-C}_3\text{N}_4$ composite was found to be active for pure water splitting reaction in presence of UV-visible light but not found to be active under sunlight as well as visible light illumination. Maximum H_2 evolution rate of 398.28 $\mu\text{mol/h}$ or 4978.5 $\mu\text{mol/h/g}$ with AQE of 4.0 % and SFE of 2.04 % was observed over $\text{Pt/CND/g-C}_3\text{N}_4$ -0.48 in presence of sacrificial reagent under sunlight illumination. Enhanced life time of charge carrier and light absorption properties which result into enhancement of photocatalytic activity of ternary system of Pt, CND and $\text{g-C}_3\text{N}_4$.

Among all the metals (Pt, Pd, Au, Ag and Cu) Pt, Pd and Au has exhibited significant rise in H₂ yield as compared to the pristine g-C₃N₄ sample under sunlight. Maximum H₂ generation @ 2692.7 μmol/h/g was observed over Pt/g-C₃N₄ sample. Fig. 9.1 shows the comparison of activity of best modified sample in all systems in presence of cocatalyst under sunlight illumination. H₂ yield is expressed in terms of L/h/m² of illumination area.

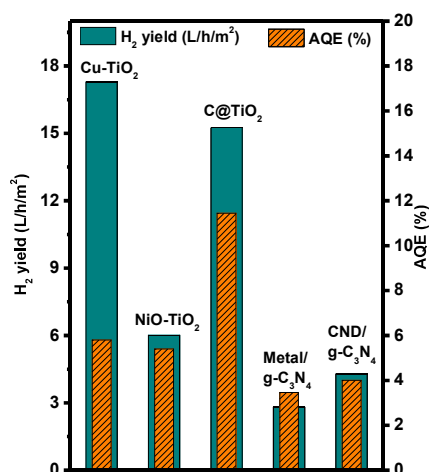


Fig. 9.1 Photocatalytic H₂ generation expressed in terms of L/h/m² and AQE of the system evaluated in presence of Pt as cocatalyst and sacrificial reagent and under sunlight illumination.

Improved light absorption, surface area and charge carrier lifetime favoured the photocatalytic properties in the modified samples as compared to the pristine sample and thus make them more suitable candidates as photocatalysts for water splitting reaction. TiO₂ modified by Cu²⁺ ions is an efficient low cost visible light photocatalyst that can be targeted for large scale H₂ production under sunlight.

Future Scope

Two low cost catalysts developed from the present thesis, Cu doped TiO₂ and C@TiO₂ composites are established as potential low cost sunlight active photocatalysts with 7.5 and 11% AQE, can be employed for large scale photocatalytic hydrogen generation under sunlight. For, this photoreactors will be coupled with compound parabolic collectors (CPC) to enhance the solar flux falling on the reactors. The fabrication of CPC coupled photoreactors

with provision of water cooling and to accommodate with the varying sunlight angle will be designed. Attempts would also be there to replace costly commercially important methanol with organics which are cheap and thrown as waste from industries. We already shown the efficacy of glycerol, an industrial waste, as substitute for methanol in our studies (Chapter-6).

For fundamental studies, the systems developed in this work can be further explored for energy and environment related problems such as reduction of CO₂ to methane or removal of organic pollutants under sunlight. There is a scope of improvisation of photocatalytic properties of TiO₂ and g-C₃N₄ by other strategies such as core shell structures and with respect to the nature of carbon to further facilitating charge separation and enhance charge carrier mobility. Also, the functional group on the surface can be altered to further enhance its properties for better adsorption of reactant molecules. For example it is possible to decorate the surface of carbon with amino group to facilitate the adsorption of dye having acidic group and hence its degradation. It was observed that after addition of Pt as co-catalyst rate of H₂ generation significantly rises. But Pt is very costly hence studies can be undertaken to lower down the price of photocatalyst for its commercial use by replacing costly Pt with comparatively cheap cocatalyst like MoS₂.

References

- [1] BP Energy Outlook 2017 edition, available online at <https://www.bp.com/content/dam/bp/pdf/energy-economics/energy-outlook-2017/bp-energy-outlook-2017.pdf>, (2017).
- [2] https://en.wikipedia.org/wiki/Energy_policy_of_India.
- [3] C. A. Grimes, O. K. Varghese, S. Ranjan, Hydrogen Generation by Water Splitting, Springer, New York, NY, USA. (2008).
- [4] P. Chowdhury, G. Malekshoar, A. K. Ray, Inorganics. 5 (2017) 34.
- [5] <https://www.esrl.noaa.gov/gmd/ccgg/trends/global.html>.
- [6] M. E. Mann, Earth Will Cross the Climate Danger Threshold by 2036, Sci. Am. available.
- [7] Rising global temperatures and CO₂, <http://www.climatecentral.org/gallery/graphics/co2-and-rising-global-temperatures>, Clim. Cent.
- [8] <http://rredc.nrel.gov/solar/spectra/am1.5/>.
- [9] T. Hisatomi, J. Kubota, K. Domen, Chem. Soc. Rev. 43 (2014) 7520–7535.
- [10] I. Dincer, C. Zamfirescu, Sustainable Energy Systems and Applications, Springer Science & Business Media: New York, NY, USA, 2011.
- [11] <http://www.iea.org/Textbase/npsum/solar2011SUM.pdf>, (2015).
- [12] <http://www.indiaenergyportal.org/subthemes.php?text=solar>.
- [13] BP Statistical Review of World Energy June 2017, Available online at <https://www.bp.com/content/dam/bp/en/corporate/pdf/energy-economics/statistical-review-2017/bp-statistical-review-of-world-energy-2017-full-report.pdf>, (2017).
- [14] M. A. Green, K. Emery, Y. Hishikawa, W. Warta, E. D. Dunlop, Prog. Photovolt Res. Appl. 23 (2015) 805–812.
- [15] F. E. Osterloh, Chem. Soc. Rev. 42 (2013) 2294–2320.
- [16] T. Hisatomi, J. Kubota, K. Domen, Chem. Soc. Rev. 43 (2014) 7520–7535.
- [17] <https://hypertextbook.com/facts/2005/MichelleFung.shtml>.
- [18] I. Dincer, C. Acar, Int. J. Hydrogen Energy. 40 (2015) 11094–11111.
- [19] A. Steinfeld, Sol. Energy. 78 (2005) 603–615.
- [20] A. M. Banerjee, A. R. Shirole, M. R. Pai, A. K. Tripathi, S. R. Bharadwaj, D. Das, P. K. Sinha, Appl. Catal. B Environ. 127 (2012) 36–46.
- [21] I. Akkerman, M. Janssen, J. Rocha, R. H. Wijffels, Int. J. Hydrogen Energy. 27 (2002) 1195–1208.
- [22] A. Kudo, Y. Miseki, Chem. Soc. Rev. 38 (2009) 253–278.
- [23] Z. Li, W. Luo, M. Zhang, J. Feng, Z. Zou, Energy Environ. Sci. 6 (2013) 347–370.
- [24] F. E. Osterloh, B. A. Parkinson, MRS Bull. 36 (2011) 17–22.
- [25] A. J. Bard, M. A. Fox, Acc. Chem. Res. 28 (1995) 141–145.
- [26] J. Verne, Available at <http://www.literature-web.net/verne/mysteriousisland>, (1874).
- [27] G. Ciamician, The photochemistry of the future, Science 36 (1912) 385–394.
- [28] P.J. Boddy, J. Electrochem. Soc. 115 (1968) 199–203.
- [29] A. Fujishima, K. Honda, Nature. 238 (1972) 37–38.
- [30] G. C. Bond, Principles of catalysis, Second Edition, The Chemical Society, 1972.
- [31] D. I. Kondarides, Available at <https://www.eolss.net/Sample-Chapters/C06/E6-190-16-00.pdf>.
- [32] Available at <https://goldbook.iupac.org/html/P/PT07446.html>, PAC, 2007, 79, 293 (Glossary of terms used in photochemistry, 3rd edition (IUPAC Recommendations 2006)) on page 384, (2006).
- [33] T. Takata, C. Pan, K. Domen, Sci. Technol. Adv. Mater. 16 (2015) 033506 (18pp).

- [34] L. Li, P. A. Salvador, G. S. Rohrer, *Nanoscale*. 6 (2014) 24–42.
- [35] C. Acar, I. Dincer, C. Zamfirescu, *Int. J. Energy Res.* 38 (2014) 1903–1920.
- [36] K. Nakata, A. Fujishima, *J. Photochem. Photobiol. C Photochem. Rev.* 13 (2012) 169–189.
- [37] X. Chen, S. Shen, L. Guo, S. S. Mao, *Chem. Rev.* 110 (2010) 6503–6570.
- [38] S. Y. Tee, K. Y. Win, W. S. Teo, L. Koh, S. Liu, C. P. Teng, M. -Y. Han, *Adv. Sci.* 4 (2017) 1600337 (24pp).
- [39] F. Fresno, R. Portela, S. Suárez, J. M. Coronado, *J. Mater. Chem. A*. 2 (2014) 2863–2884.
- [40] T. Hisatomi, K. Takanabe, K. Domen, *Catal. Letters*. 145 (2015) 95–108.
- [41] B. A. Pinaud, J. D. Benck, L. C. Seitz, A. J. Forman, Z. Chen, T. G. Deutsch, B. D. James, K. N. Baum, G. N. Baum, S. Ardo, H. Wang, E. Miller, T. F. Jaramillo, *Energy Environ. Sci.* 6 (2013) 1983–2002.
- [42] M. G. Kibria, Z. Mi, *J. Mater. Chem. A*. 4 (2016) 2801–2820.
- [43] K. Maeda, K. Domen, *J. Phys. Chem. Lett.* 1 (2010), 2655–2661.
- [44] S. Chen, T. Takata, K. Domen, *Nat. Rev. Mater.* 2 (2017) 1–17.
- [45] K. Domen, A. Kudo, T. Onishi, *J. Catal.* 102 (1986) 92–98.
- [46] H. Kato, A. Kudo, *Chem. Phys. Lett.* 295 (1998) 487–492.
- [47] T. Takata, Y. Furumi, K. Shinohara, A. Tanaka, M. Hara, J. N. Kondo, K. Domen, *Chem. Mater.* 9 (1997) 1063–1064.
- [48] Y. Miseki, H. Kato, A. Kudo, *Chem. Lett.* 35 (2006) 1052–1053.
- [49] S. Ogura, M. Kohno, K. Sato, Y. Inoue, *Appl. Surf. Sci.* 121/122 (1997) 521–524.
- [50] K. Sayama, K. Yase, H. Arakawa, K. Asakura, A. Tanaka, K. Domen, T. Onishi, *J. Photochem. Photobiol. A Chem.* 114 (1998) 125–135.
- [51] T. Takata, K. Shinohara, A. Tanaka, M. Hara, J. N. Kondo, K. Domen, *J. Photochem. Photobiol. A Chem.* 106 (1997) 45–49.
- [52] H. Kato, K. Asakura, A. Kudo, *J. Am. Chem. Soc.* 125 (2003) 3082–3089.
- [53] Y. Inoue, *Energy Environ. Sci.* 2 (2009) 364–386.
- [54] S. Y. Tee, K. Y. Win, W. S. Teo, L. Koh, S. Liu, C. P. Teng, *Adv. Sci.* 4 (2017) 1600337.
- [55] X. Chen, S. Shen, L. Guo, S.S. Mao, Semiconductor-based photocatalytic hydrogen generation, *Chem. Rev.* 110 (2010) 6503–6570. doi:10.1021/cr1001645.
- [56] J. Sato, N. Saito, H. Nishiyama, Y. Inoue, *J. Phys. Chem. B*. 107 (2003) 7965–7969.
- [57] J. Sato, H. Kobayashi, N. Saito, H. Nishiyama, Y. Inoue, *J. Photochem. Photobiol. A Chem.* 158 (2003) 139–144.
- [58] J. Sato, N. Saito, H. Nishiyama, Y. Inoue, *Chem. Lett.* (2001) 868–869.
- [59] K. Ikarashi, J. Sato, H. Kobayashi, N. Saito, H. Nishiyama, Y. Inoue, *J. Phys. Chem. B*. 106 (2002) 9048–9053.
- [60] J. Sato, H. Kobayashi, K. Ikarashi, N. Saito, H. Nishiyama, Y. Inoue, *J. Phys. Chem. B*. 108 (2004) 4369–4375.
- [61] J. Sato, N. Saito, H. Nishiyama, Y. Inoue, *J. Phys. Chem. B*. 105 (2001) 6061–6063.
- [62] J. Sato, N. Saito, H. Nishiyama, Y. Inoue, *J. Photochem. Photobiol. A Chem.* 148 (2002) 85–89.
- [63] L. Liao, Q. Zhang, Z. Su, Z. Zhao, Y. Wang, Y. Li, X. Lu, D. Wei, G. Feng, Q. Yu, X. Cai, J. Zhao, Z. Ren, H. Fang, F. Robles-Hernandez, S. Baldelli, J. Bao, *Nat. Nanotechnol.* 9 (2014) 69–73.
- [64] S. M. Gupta, M. Tripathi, *Chinese Sci. Bull.* 56 (2011) 1639–1657.
- [65] M. Landmann, E. Rauls, W. G. Schmidt, *J. Phys. Condens. Matter.* 24 (2012) 195503 (6 pp).
- [66] L. Kavan, M. Gratzel, S. E. Gilbert, C. Klemenz, H. J. Scheel, *J. Am. Chem. Soc.* 118

- (1996) 6716–6723.
- [67] A. Scalfani, J. M. Herrmann, *J. Phys. Chem.* 100 (1996) 13655–13661.
- [68] H. Yan, J. Yang, G. Ma, G. Wu, X. Zong, Z. Lei, J. Shi, C. Li, *J. Catal.* 266 (2009) 165–168.
- [69] J. F. Reber, K. Meier, *J. Phys. Chem.* 88 (1984) 5903–5913.
- [70] M. A. Holmes, T.K. Townsend, F. E. Osterloh, *Chem. Commun.* 48 (2012) 371–373.
- [71] M. -Y. Tsang, N. E. Pridmore, L. J. Gillie, Y. -H. Chou, R. Brydson, R. E. Douthwaite, *Adv. Mater.* 24 (2012) 3406–3409.
- [72] K. Maeda, K. Teramura, D. Lu, N. Saito, Y. Inoue, K. Domen, *Angew. Chemie - Int. Ed.* 45 (2006) 7806–7809.
- [73] T. Jafari, E. Moharreri, A. Amin, R. Miao, W. Song, S. Suib, *Molecules.* 21 (2016) 900.
- [74] J. Sato, N. Saito, Y. Yamada, K. Maeda, T. Takata, J. N. Kondo, M. Hara, H. Kobayashi, K. Domen, Y. Inoue, *J. Am. Chem. Soc.* 127 (2005) 4150–4151.
- [75] G. Hitoki, A. Ishikawa, T. Takata, J. N. Kondo, M. Hara, K. Domen, *Chem. Lett.* 31 (2002) 736–737.
- [76] X. Wang, K. Maeda, A. Thomas, K. Takanabe, G. Xin, J. M. Carlsson, K. Domen, M. Antonietti, *Nat. Mater.* 8 (2009) 76–80.
- [77] M. Ahmed, G. Xinxin, *Inorg. Chem. Front.* 3 (2016) 578–590.
- [78] D. J. Martin, K. Qiu, S.A. Shevlin, A. D. Handoko, X. Chen, Z. Guo, J. Tang, *Angew. Chem. Int. Ed.* 53 (2014) 9240–9245.
- [79] Y. Meng, G. Xin, D. Chen, *Optoelectron. Adv. Mater. Rapid Commun.* 5 (2011) 648–650.
- [80] S. C. Yan, Z. S. Li, Z. G. Zou, *Langmuir.* 25 (2009) 10397–10401.
- [81] G. Zhang, J. Zhang, M. Zhang, X. Wang, *J. Mater. Chem.* 22 (2012) 8083–8091.
- [82] Y. Zhang, J. Liu, G. Wu, W. Chen, *Nanoscale.* 4 (2012) 5300–5303.
- [83] J. Liu, T. Zhang, Z. Wang, G. Dawson, W. Chen, *J. Mater. Chem.* 21 (2011) 14398–14401.
- [84] Z. Zhao, Y. Sun, F. Dong, *Nanoscale.* 7 (2015) 15–37.
- [85] K. Maeda, K. Teramura, K. Domen, *J. Catal.* 254 (2008) 198–204.
- [86] X. Chen, L. Liu, P.Y. Yu, S. S. Mao, *Science.* 331 (2011) 746–750.
- [87] C. Zhao, H. Luo, F. Chen, P. Zhang, L. Yi, K. You, *Energy Environ. Sci.* 7 (2014) 1700–1707.
- [88] J. Liu, Y. Liu, N. Liu, Y. Han, X. Zhang, H. Huang, Y. Lifshitz, S. -T. Lee, J. Zhong, Z. Kang, *Science.* 347 (2015) 970–974.
- [89] J. Sun, G. Chen, Y. Li, R. Jin, Q. Wang, J. Pei, *Energy Environ. Sci.* 4 (2011) 4052–4060.
- [90] K. Maeda, M. Higashi, D. Lu, R. Abe, K. Domen, *J. Am. Chem. Soc.* 132 (2010) 5858–5868.
- [91] C. Pan, T. Takata, M. Nakabayashi, T. Matsumoto, N. Shibata, Y. Ikuhara, K. Domen, *Angew. Chemie - Int. Ed.* 54 (2015) 2955–2959.
- [92] J. W. Jo, J. H. Kang, K. Kong, S. Y. Lee, H. Park, Y. Lee, T. Buonassisi, K. K. Gleason, J. S. Lee, *Proc. Natl Acad. Sci. USA.* 112 (2015) 13774–13778. doi:10.1073/pnas.1509674112.
- [93] W. Wang, J. Chen, C. Li, W. Tian, *Nat. Commun.* 5:4647 (2014) 1–8.
- [94] M. G. Kibria, F. A. Chowdhury, S. Zhao, B. AlOtaibi, M. L. Trudeau, H. Guo, Z. Mi, *Nat. Commun.* 6:6797 (2015) 1–8.
- [95] L. Yuan, C. Han, M. Yang, Y. Xu, *Int. Rev. Phys. Chem.* 35 (2016) 1–36.
- [96] S. I. Mogal, M. Mishra, V. G. Gandhi, R. J. Tayade, *Mater. Sci. Forum.* 734 (2012) 364–378.

- [97] M. Ni, M. K. H. Leung, D. Y. C. Leung, K. Sumathy, *Renew. Sustain. Energy Rev.* 11 (2007) 401–425.
- [98] L. S. Yoong, F. K. Chong, B. K. Dutta, *Energy*. 34 (2009) 1652–1661.
- [99] R. Dholam, N. Patel, M. Adami, A. Miotello, *Int. J. Hydrogen Energy*. 34 (2009) 5337–5346.
- [100] D. Jing, Y. Zhang, L. Guo, *Chem. Phys. Lett.* 415 (2005) 74–78.
- [101] M. I. Zalas, M. Laniecki, *Sol. Energy Mater. Sol. Cells*. 89 (2005) 287–296.
- [102] F. Zuo, L. Wang, T. Wu, Z. Zhang, D. Borchardt, P. Feng, *J. Am. Chem. Soc.* 132 (2010) 11856–11857.
- [103] R. Niishiro, S. Tanaka, A. Kudo, *Appl. Catal. B Environ.* 150–151 (2014) 187–196.
- [104] T. Ohno, T. Tsubota, Y. Nakamura, K. Sayama, *Appl. Catal. A Gen.* 288 (2005) 74–79.
- [105] J. Hong, X. Xia, Y. Wang, R. Xu, *J. Mater. Chem.* 22 (2012) 15006–15012.
- [106] W. J. Youngblood, S. -H. A. Lee, K. Maeda, T. E. Mallouk, *Acc. Chem. Res.* 42 (2009) 1966–1973.
- [107] W. Fan, Q. Zhang, Y. Wang, *Phys. Chem. Chem. Phys.* 15 (2013) 2632–2649.
- [108] X. Wang, C. Li, *J. Photochem. Photobiol. C Photochem. Rev.* 33 (2017) 165–179.
- [109] C. Li, J. Yuan, B. Han, W. Shangguan, *Int. J. Hydrogen Energy*. 36 (2011) 4271–4279.
- [110] S. J. A. Moniz, S. A. Shevlin, D. J. Martin, Z. -X. Guo, J. Tang, *Energy Environ. Sci.* 8 (2015) 731–759.
- [111] Z. Zhang, J. Yates, John T, *Chem. Rev.* 112 (2012) 5520–5551.
- [112] M. Kong, Y. Li, X. Chen, T. Tian, P. Fang, F. Zheng, X. Zhao, *J. Am. Chem. Soc.* 133 (2011) 16414–16417.
- [113] J. Schneider, D. W. Bahnemann, *J. Phys. Chem. Lett.* 4 (2013) 3479–3483.
- [114] H. Ahmad, S. K. Kamarudin, L. J. Minggu, M. Kassim, *Renew. Sustain. Energy Rev.* 43 (2015) 599–610.
- [115] Y. K. Kho, A. Iwase, W. Y. Teoh, L. Mädler, A. Kudo, R. Amal, *J. Phys. Chem. C*. 114 (2010) 2821–2829.
- [116] K. Maeda, A. Xiong, T. Yoshinaga, T. Ikeda, N. Sakamoto, T. Hisatomi, M. Takashima, D. Lu, M. Kanehara, T. Setoyama, T. Teranishi, K. Domen, *Angew. Chem. Int. Ed.* 49 (2010) 4096–4099.
- [117] R. Marschall, *Adv. Funct. Mater.* 24 (2014) 2421–2440.
- [118] H. Wang, L. Zhang, Z. Chen, J. Hu, S. Li, Z. Wang, J. Liu, X. Wang, *Chem. Soc. Rev.* 43 (2014) 5234–5244.
- [119] C. Shifu, Z. Sujuan, L. Wei, Z. Wei, *J. Hazard. Mater.* 155 (2008) 320–326.
- [120] L. Liu, W. Yang, W. Sun, Q. Li, J. K. Shang, *ACS Appl. Mater. Interfaces*. 7 (2015) 1465–1476.
- [121] Q. Zhang, Z. Hai, A. Jian, H. Xu, C. Xue, S. Sang, *Nanomaterials*. 6 (2016) 138.
- [122] F. Meng, J. Li, S. K. Cushing, M. Zhi, N. Wu, *J. Am. Chem. Soc.* 135 (2013) 10286–10289.
- [123] X. Zhou, G. Liu, J. Yu, W. Fan, *J. Mater. Chem.* 22 (2012) 21337–21354.
- [124] K. L. Kelly, E. Coronado, L. L. Zhao, G. C. Schatz, *J. Phys. Chem. B*. 107 (2003) 668–677.
- [125] Q. Zhang, W. Li, C. Moran, J. Zeng, J. Chen, L. -P. Wen, Y. Xia, *J. Am. Chem. Soc.* 132 (2010) 11372–11378.
- [126] D. Chen, L. Zou, S. Li, F. Zheng, *Sci. Rep.* 6 (2016) 20335.
- [127] Q. Li, B. Guo, J. Yu, J. Ran, B. Zhang, H. Yan, J. R. Gong, *J. Am. Chem. Soc.* 133 (2011) 10878–10884.
- [128] Q. Wang, T. Hisatomi, Y. Suzuki, Z. Pan, J. Seo, M. Katayama, T. Minegishi, H. Nishiyama, T. Takata, K. Seki, A. Kudo, T. Yamada, K. Domen, *J. Am. Chem. Soc.*

- 139 (2017) 1675–1683.
- [129] T. Sreethawong, T. Puangpetch, S. Chavadej, S. Yoshikawa, *J. Power Sources*. 165 (2007) 861–869. doi:10.1016/j.jpowsour.2006.12.050.
- [130] K. Lalitha, J. K. Reddy, P. M. V. Sharma, V. D. Kumari, M. Subrahmanyam, *Int. J. Hydrogen Energy*. 35 (2010) 3991–4001.
- [131] O. M. Alfano, D. Bahnemann, A. E. Cassano, R. Dillert, R. Goslich, *Catal. Today*. 58 (2000) 199–230.
- [132] K. Villa, X. Domènech, S. Malato, M. I. Maldonado, J. Peral, *Int. J. Hydrogen Energy*. 38 (2013) 12718–12724.
- [133] D. Jing, H. Liu, X. Zhang, L. Zhao, L. Guo, *Energy Convers. Manag.* 50 (2009) 2919–2926.
- [134] A. R. West, *Solid state chemistry and its applications*, John Wiley and Sons, 1984.
- [135] H. Chu, Y. H. Lin, T. K. Tseng, Photocatalytic degradation of volatile organic compounds, in: S. C. Esteves, A. C. Varghese, K. C. Worrilow (Eds.), *Clean Room Technol. ART Clin.*, CRC Press, Taylor and Francis Group, 2017: pp. 133–156.
- [136] W. Jia, D. Jia, Methods of phosphor synthesis and related technology, in: W.M. Yen, S. Shionoya, H. Yamamoto (Eds.), *Pract. Appl. Phosphors*, CRC Press, Taylor and Francis Group, 2007: pp. 41–51.
- [137] P. Roy, P. -C. Chen, A. P. Periasamy, Y. -N. Chen, H. -T. Chang, *Mater. Today*. 18 (2015) 447–458.
- [138] B. D. Cullity, *Elements of X-ray diffraction*, Addison-Wilson Publishing Comp. Inc., USA, 1959.
- [139] H. P. Klug, L. E. Alexander, *X-ray diffraction procedures*, Wiley-Interscience Publication, New York, 1974.
- [140] L. V. Azaroff, M. J. Buerger, *The Powder Method in X-ray Crystallography*, McGraw-Hill Book Comp., New York, 1958.
- [141] WinPLOT, J Rodriguez-Carvajal, Laboratoire Leon Brillouin (CEA-CNRS), April 2005 (LLB-LCSIM), (n.d.).
- [142] http://web.archive.org/web/20110722032112/http://xafs.org/Tutorials?action=AttachFile&do=view&target=Newville_xas_fundamentals.pdf.
- [143] <http://www.chem.ucalgary.ca/research/groups/faridehj/xas.pdf>.
- [144] <http://www.rrcat.gov.in>.
- [145] D. C. Konigsberger, R. Prince, *X-Ray Absorption: Principles, Applications, Techniques of EXAFS, SEXAFS and XANES*, Wiley, New York, 1988.
- [146] M. Newville, B. Ravel, D. Haskel, J. J. Rehr, E. A. Stern, Y. Yacoby, *Phys. B Condens. Matter*. 208–209 (1995) 154–156.
- [147] M. Bizarro, S. E. Rodil, Physicochemical Characterization of Photocatalytic Materials, in: A. Hernández-Ramírez, I. Medina-Ramírez (Eds.), *Photocatalytic Semiconductors: Synthesis, Characterization, and Environmental Applications*, Springer, 2015: pp. 103–154.
- [148] S. Brunauer, P.H. Emmett, E. Teller, *J. Am. Chem. Soc.* 60 (1938) 309–319.
- [149] K. S. W. Sing, *Pure Appl. Chem.* 54 (1982) 2201–2218.
- [150] D. A. Skoog, F. J. Holler, T. A. Nieman, *Principles of Instrumental Analysis*, 5th Editio, Thomson Brooks/Cole, 1998.
- [151] W. F. Pickering, *Modern analytical chemistry*, Marcel Dekker, Inc., New York, 1971.
- [152] P. Atkins, J. De Paula, *Elements of Physical chemistry*, 5th Editio, Oxford University Press, 2009.
- [153] E. R. Andrew, A. Bradbury, R. G. Eades, *Nature*. 183 (1959) 1802–1803.
- [154] I. J. Lowe, *Phys. Rev. Lett.* 2 (1959) 285–287.

- [155] J. Tang, Z. Zou, J. Ye, *J. Phys. Chem. B.* 107 (2003) 14265–14269.
- [156] K. K. Rohatgi-Mukherjee, *Fundamentals of Photochemistry*, New Age International Publishers, New Delhi, 2007.
- [157] R. W. Cahn, P. Haasen, E. J. Kramer, *Material Science and Engineering: Characterisation of Materials*, VCH Publisher Inc., New York, 1991.
- [158] D. B. William, C. B. Carter, *Transmission Electron Microscopy*, Plenum Press, New York, 1996.
- [159] M. R. Pai, A. M. Banerjee, A. K. Tripathi, S. R. Bharadwaj, *Functional Materials: Preparations, Processing and Applications*, in: S. Banerjee, A. K. Tyagi (Eds.), Elsevier, USA, 2012: pp. 579–606.
- [160] A. A. Ismail, D. W. Bahnemann, *Sol. Energy Mater. Sol. Cells.* 128 (2014) 85–101. doi:10.1016/j.solmat.2014.04.037.
- [161] X. Chen, L. Liu, F. Huang, *Chem. Soc. Rev.* 44 (2015) 1861–1885.
- [162] M. Scarisoreanu, I. Morjan, R. Alexandrescu, C. T. Fleaca, A. Badoi, E. Dutu, A. M. Niculescu, C. Luculescu, E. Vasile, J. Wang, S. Bouhadoun, N. Herlin-Boime, *Appl. Surf. Sci.* 302 (2014) 11–18.
- [163] X. H. Liu, Y. Deng, Y. Zhang, Y. Zhou, *Adv. Mater. Res.* 887–888 (2014) 388–394.
- [164] A. Naldoni, M. Allieta, S. Santangelo, M. Marelli, F. Fabbri, S. Cappelli, C. L. Bianchi, R. Psaro, V. D. Santo, *J. Am. Chem. Soc.* 134 (2012) 7600–7603.
- [165] C. W. Li, M. W. Kanan, *J. Am. Chem. Soc.* 134 (2012) 7231–7234.
- [166] H. S. Park, D. H. Kim, S. J. Kim, K. S. Lee, *J. Alloy. Compd.* 415 (2006) 51–55.
- [167] M. Sahu, P. Biswas, *Nanoscale Res. Lett.* 6 (2011) 441.
- [168] W. Shu-Xin, M. Zhi, Q. Yong-Ning, H. Fei, J. Li-Shan, Z. Yan-Jun, *Acta Phys.-Chim. Sin.* 19 (2003) 967–969.
- [169] J. Morales, J. P. Espinos, A. Caballero, A. R. Gonzalez-Elipe, J. A. Mejias, *J. Phys. Chem. B.* 109 (2005) 7758–7765.
- [170] I. Ganesh, P. P. Kumar, I. Annapoorna, J. M. Sumliner, M. Ramakrishna, N. Y. Hebalkar, G. Padmanabham, G. Sundararajan, *Appl. Surf. Sci.* 293 (2014) 229–247.
- [171] H. Fan, L. Yang, W. Hua, X. Wu, Z. Wu, S. Xie, B. Zou, *Nanotechnology.* 15 (2004) 37.
- [172] M. Hara, T. Kondo, M. Komoda, S. Ikeda, J. N. Kondo, K. Domen, M. Hara, K. Shinohara, A. Tanaka, *Chem. Comm.* 0 (1998) 357–358.
- [173] B. Choudhury, M. Dey, A. Choudhury, *Int. Nano Lett.* 3 (2013) 25.
- [174] J. Arana, J. M. Dona-Rodriguez, J. A. H. Melian, E. T. Rendon, O. G. Diaz, *J. Photochem. Photobiol. A.* 174 (2005) 7–14.
- [175] A. D. Paola, G. Marci, L. Palmisano, M. Schiavello, K. Uosaki, S. Ikeda, B. Ohtani, *J. Phys. Chem. B.* 106 (2002) 637–645.
- [176] A. Manivel, S. Naveenraj, P. S. Sathish Kumar, S. Anandan, *Sci. Adv. Mater.* 2 (2010) 51–57.
- [177] C. -Y. Tsai, H. -C. Hsi, T. -H. Kuo, Y. -M. Chang, J. -H. Liou, *Aerosol Air Qual. Res.* 13 (2013) 639–648.
- [178] H. Liu, X. Yu, H. Yang, *Chem. Eng. J.* 243 (2014) 465–472.
- [179] S. Wang, K. K. Meng, L. Zhao, Q. Jiang, J. S. Lian, *Ceram. Int.* 40 (2014) 5107–5110.
- [180] N. R. Khalid, E. Ahmed, Z. Hong, M. Ahmad, Y. Zhang, S. Khalid, *Ceram. Int.* 39 (2013) 7107–7113.
- [181] G. Li, N. M. Dimitrijevic, L. Chen, T. Rajh, K. A. Gray, *J. Phys. Chem. C.* 112 (2008) 19040–19044.
- [182] A. Singhal, M. R. Pai, R. Rao, K. T. Pillai, I. Lieberwirth, A. K. Tyagi, *Eur. J. Inorg. Chem.* 2013 (2013) 2640–2651.
- [183] R. Lo'pez, R. Go'mez, M. E. Llanos, *Catal. Today.* 148 (2009) 103–108.

- [184] T. Ohsaka, F. Izumi, Y. Fujiki, *J. Raman Spectrosc.* 7 (1978) 321–324.
- [185] M. J. Šćepanović, M. Grujić-Brojčin, Z. D. Dohčević-Mitrović, Z. V. Popović, *Sci. Sinter.* 41 (2009) 67–73.
- [186] J. F. Xu, W. Ji, Z. X. Shen, W. S. Li, S. H. Tang, X. R. Ye, D. Z. Jia, X. Q. Xin, *J. Raman Spectrosc.* 30 (1999) 413–415.
- [187] M. Rashad, M. Rusing, G. Berth, K. Lischka, A. Pawlis, *J. Nanomater.* 2013 (2013) pp 6, Article ID 714853. doi:10.1155/2013/714853.
- [188] A. Gaur, B. D. Shrivastava, S. K. Joshi, *J. Phys. Conf. Ser.* 190 (2009) 12084.
- [189] H. Irie, K. Kamiya, T. Shibanuma, S. Miura, D. A. Tryk, T. Yokoyama, K. Hashimoto, *J. Phys. Chem. C* 113 (2009) 10761–10766.
- [190] P. Steiner, V. Kinsinger, I. Sander, B. Siegwart, S. Hufner, C. Politis, R. Hoppe, H. P. Muller, *Z. Phys. B - Condens. Matter.* 67 (1987) 497–502.
- [191] N. S. McIntyre, M. G. Cook, *Anal. Chem.* 47 (1975) 2208–2213.
- [192] B. Erdem, R. A. Hunsicker, G. W. Simmons, E. D. Sudol, V. L. Dimonie, M. S. El-Aasser, *Langmuir.* 17 (2001) 2664–2669.
- [193] H. Eskandarloo, A. Badiei, M. A. Behnajady, G. M. Ziarani, *Photochem. Photobiol.* 91 (2015) 797–806.
- [194] S. Xu, D. D. Sun, *Inter. J. Hyd. Energ.* 34 (2009) 6096–6104.
- [195] D. A. Palmer, P. Bénézeth, Solubility of copper oxides in water and steam, in: *Proc. 14th Int. Conf. Prop. Water Steam, Kyoto, Japan, 2004*: p. 491.
- [196] V. Datsyuk, M. Kalyva, K. Papagelis, J. Parthenios, D. Tasis, A. Siokou, I. Kallitsis, C. Galiotis, *Carbon* 46 (2008) 833–840.
- [197] L. Chen, T. Horiuchi, T. Osaki, T. Mori, *Appl. Catal. B Environ.* 23 (1999) 259–269.
- [198] H. Praliaud, S. Mikhailenko, Z. Chajar, M. Primet, *Appl. Catal. B Environ.* 16 (1998) 359–374.
- [199] G. Colo'n, M. Maicu, M. C. Hidalgo, J. A. Navi'ó, *Appl. Catal. B Environ.* 67 (2006) 41–51.
- [200] X. Lin, F. Huang, W. Wang, Y. Wang, Y. Xia, J. Shi, *Appl. Catal. A Gen.* 313 (2006) 218–223.
- [201] A. M. Banerjee, M. R. Pai, A. Arya, S. R. Bharadwaj, *RSC Adv.* 5 (2015) 61218–61229.
- [202] S. S. Lee, H. Bai, Z. Liu, D. D. Sun, *Appl. Catal. B Environ.* 140–141 (2013) 68–81.
- [203] K. Y. Song, Y. T. Kwon, G. J. Choi, W. I. Lee, *Bull. Korean Chem. Soc.* 20 (1999) 957–960.
- [204] Y. Xu, D. Liang, M. Liu, D. Liu, *Mater. Res. Bull.* 43 (2008) 3474–3482.
- [205] J. Li, L. Liu, Y. Yu, Y. Tang, H. Li, F. Du, *Electrochem. Commun.* 6 (2004) 940–943.
- [206] X. Zhang, Q. Liu, *Appl. Surf. Sci.* 254 (2008) 4780–4785.
- [207] J. Zhang, S. Z. Qiao, L. Qi, J. Yu, *Phys. Chem. Chem. Phys.* 15 (2013) 12088–12094.
- [208] M. Miyauchi, Y. Nukui, D. Atarashi, E. Sakai, *ACS Appl. Mater. Interfaces.* 5 (2013) 9770–9776.
- [209] J. Cao, B. Xu, H. Lin, S. Chen, *Chem. Eng. J.* 228 (2013) 482–488.
- [210] V. R. Choudhary, A. M. Rajput, A. S. Mamman, *J. Catal.* 178 (1998) 576–585.
- [211] I. Hotovy, J. Huran, L. Spiess, S. Hascik, V. Rehacek, *Sensors Actuators B Chem.* 57 (1999) 147–152.
- [212] X. Li, X. Zhang, Z. Li, Y. Qian, *Solid State Commun.* 137 (2006) 581–584.
- [213] C. -J. Chen, C. -H. Liao, K. -C. Hsu, Y. -T. Wu, J. C. S. Wu, *Catal. Commun.* 12 (2011) 1307–1310.
- [214] K. -j. Zhang, W. Xu, X. -j. Li, S. -j. Zheng, G. Xu, J. -h. Wang, *Trans. Nonferrous Met. Soc. China.* 16 (2006) 1069–1075.
- [215] H. Lin, H. Ye, B. Xu, J. Cao, S. Chen, *Catal. Commun.* 37 (2013) 55–59.

- [216] T. Sreethawong, S. Ngamsinlapasathian, S. Yoshikawa, *Chem. Eng. J.* 192 (2012) 292–300.
- [217] Y. Ku, C. -N. Lin, W. -M. Hou, *J. Mol. Catal. A Chem.* 349 (2011) 20–27.
- [218] J. Yu, W. Wang, B. Cheng, *Chem. Asian J.* 5 (2010) 2499–2506.
- [219] H. Hu, W. Xiao, J. Yuan, J. Shi, M. Chen, W. Shang Guan, *J. Environ. Sci.* 19 (2007) 80–85.
- [220] R. Liu, H. Yoshida, S. Fujita, M. Arai, *Appl. Catal. B Environ.* 144 (2014) 41–45.
- [221] E. P. Melián, M. N. Suárez, T. Jardiel, J. M. D. Rodríguez, A. C. Caballero, J. Araña, D. G. Calatayud, O. G. Díaz, *Appl. Catal. B Environ.* 152–153 (2014) 192–201.
- [222] L. Li, B. Cheng, Y. Wang, J. Yu, *J. Colloid Interface Sci.* 449 (2015) 115–121.
- [223] M. R. Pai, J. Majeed, A. M. Banerjee, A. Arya, S. Bhattacharya, R. Rao, S. R. Bharadwaj, *J. Phys. Chem. C.* 116 (2012) 1458–1471.
- [224] R. A. Spurr, H. Myers, *Anal. Chem.* 29 (1957) 760–762.
- [225] E. A. Kraut, R. W. Grant, J. R. Waldrop, S. P. Kowalczyk, *Phys. Rev. Lett.* 44 (1980) 1620–1623.
- [226] P. E. Blöchl, *Phys. Rev. B.* 50 (1994) 17953–17979.
- [227] G. Kresse, J. Furthmüller, *Phys. Rev. B.* 54 (1996) 11169–11186.
- [228] J. P. Perdew, K. Burke, M. Ernzerhof, *Phys. Rev. Lett.* 77 (1996) 3865–3868.
- [229] H. J. Monkhorst, J. D. Pack, *Phys. Rev. B.* 13 (1976) 5188–5192.
- [230] M. Methfessel, A. T. Paxton, *Phys. Rev. B.* 40 (1989) 3616–3621.
- [231] P. E. Blöchl, O. Jepsen, O. K. Andersen, *Phys. Rev. B.* 49 (1994) 16223–16233.
- [232] D. J. Taylor, P. F. Fleig, R. A. Page, *Thin Solid Films.* 408 (2002) 104–110.
- [233] M. A. Ruiz-Preciado, A. Kassiba, A. Gibaud, A. Morales-Acevedo, *Mater. Sci. Semicond. Process.* 37 (2015) 171–178.
- [234] T. -I. Chang, J. -L. Huang, H. -P. Lin, S. -C. Wang, H. -H. Lu, L. Wu, J. -F. Lin, *J. Alloys Compd.* 414 (2006) 224–229.
- [235] Y. M. Chiang, D. Birnie, W. D. Kingery, *Physical Ceramics: Principles of Ceramic Science and Engineering*, New York: John Wiley & Sons Inc, 1996.
- [236] Y. Ni, X. Wang, J. Hong, *Mater. Res. Bull.* 44 (2009) 1797–1801.
- [237] M. R. Mohammadi, D. J. Fray, *Solid State Sci.* 12 (2010) 1629–1640.
- [238] N. Mironova-Ulmane, A. Kuzmin, J. Grabis, I. Sildos, V. I. Voronin, I. F. Berger, V. A. Kazantsev, *Solid State Phenom.* 168–169 (2011) 341–344.
- [239] K. P. Lopes, L.S. Cavalcante, A. Z. Simões, J. A. Varela, E. Longo, E. R. Leite, *J. Alloys Compd.* 468 (2009) 327–332.
- [240] P. H. M. De Korte, G. Blasse, *J. Solid State Chem.* 44 (1982) 150–155.
- [241] Y. -J. Lin, Y. -H. Chang, W. -D. Yang, B. -S. Tsai, *J. Non. Cryst. Solids.* 352 (2006) 789–794.
- [242] E. Wang, T. He, L. Zhao, Y. Chen, Y. Cao, *J. Mater. Chem.* 21 (2011) 144–150.
- [243] J. Schneider, M. Matsuoka, M. Takeuchi, J. Zhang, Y. Horiuchi, M. Anpo, D.W. Bahnemann, *Chem. Rev.* 114 (2014) 9919–9986.
- [244] J. Yan, G. Wu, N. Guan, L. Li, Z. Li, X. Cao, *Phys. Chem. Chem. Phys.* 15 (2013) 10978–10988.
- [245] T. Ahmad, K. V. Ramanujachary, S. E. Lofland, A. K. Ganguli, *Solid State Sci.* 8 (2006) 425–430.
- [246] T. Sreethawong, Y. Suzuki, S. Yoshikawa, *Int. J. Hydrogen Energy.* 30 (2005) 1053–1062.
- [247] K. S. Kim, R. E. Davis, *J. Electron Spectros. Relat. Phenomena.* 1 (n.d.) 251–258.
- [248] M. A. van Veenendaal, G. A. Sawatzky, *Phys. Rev. Lett.* 70 (1993) 2459–2462.
- [249] Y. Qu, W. Zhou, Z. Ren, S. Du, X. Meng, G. Tian, K. Pan, G. Wang, H. Fu, *J. Mater. Chem.* 22 (2012) 16471–16476.

- [250] K. S. Kim, N. Winograd, *Surf. Sci.* 43 (1974) 625–643.
- [251] K. M. Parida, S. K. Mahanta, S. Martha, A. Nashim, *Int. J. Energy Res.* 37 (2013) 161–170.
- [252] P. Liao, E. A. Carter, *Chem. Soc. Rev.* 42 (2013) 2401–2422.
- [253] M. C. Toroker, E. A. Carter, *J. Mater. Chem. A* 1 (2013) 2474–2484.
- [254] M. C. Toroker, D. K. Kanan, N. Alidoust, L. Y. Isseroff, P. Liao, E. A. Carter, *Phys. Chem. Chem. Phys.* 13 (2011) 16644–16654.
- [255] S. Hufner, *Adv. Phys.* 43 (1994) 183–356.
- [256] F. Reinert, P. Steiner, S. Hufner, H. Schmitt, J. Fink, M. Knupfer, P. Sandl, E. Bertel, *Z. Phys. B Condens. Matter.* 97 (1995) 83–93. doi:10.1007/BF01317591.
- [257] W. -L. Jang, Y. -M. Lu, W. -S. Hwang, W. -C. Chen, *J. Eur. Ceram. Soc.* 30 (2010) 503–508.
- [258] P. Kuiper, G. Kruizinga, J. Ghijsen, G. A. Sawatzky, H. Verweij, *Phys. Rev. Lett.* 62 (1989) 221–224.
- [259] Y. Huang, Q. Zhang, J. Xi, Z. Ji, *Appl. Surf. Sci.* 258 (2012) 7435–7439.
- [260] X. Yu, J. Zhang, Z. Zhao, W. Guo, J. Qiu, X. Mou, A. Li, J. P. Claverie, H. Liu, *Nano Energy.* 16 (2015) 207–217.
- [261] Y. Yang, D. Ni, Y. Yao, Y. Zhong, Y. Ma, J. Yao, *RSC Adv.* 5 (2015) 93635–93643.
- [262] F. Dong, S. Guo, H. Wang, X. Li, Z. Wu, *J. Phys. Chem. C* 115 (2011) 13285–13292.
- [263] D. Xu, Z.-H. Huang, F. Kang, M. Inagaki, T. -H. Ko, *Catal. Today.* 139 (2008) 64–68.
- [264] Z. Zhang, Y. Zhou, Y. Zhang, X. Sheng, S. Zhou, S. Xiang, *Appl. Surf. Sci.* 286 (2013) 344–350.
- [265] L. -W. Zhang, H. -B. Fu, Y. -F. Zhu, *Adv. Funct. Mater.* 18 (2008) 2180–2189.
- [266] Y. Yang, Y. Yao, L. He, Y. Zhong, Y. Ma, J. Yao, *J. Mater. Chem. A* 3 (2015) 10060–10068.
- [267] S. K. Parayil, H. S. Kibombo, C. -M. Wu, R. Peng, J. Baltrusaitis, R. T. Koodali, *Int. J. Hydrogen Energy.* 37 (2012) 8257–8267.
- [268] M. A. Nawi, I. Nawawi, *Appl. Catal. A Gen.* 453 (2013) 80–91.
- [269] C. Lin, Y. Song, L. Cao, S. Chen, *Nanoscale.* 5 (2013) 4986–4992.
- [270] F. Dong, H. Wang, Z. Wu, *J. Phys. Chem. C* 113 (2009) 16717–16723.
- [271] Y. Li, D. S. Hwang, N. H. Lee, S. J. Kim, *Chem. Phys. Lett.* 404 (2005) 25–29.
- [272] P. Cheng, J. Qiu, M. Gu, Y. Jin, W. Shangguan, *Mater. Lett.* 58 (2004) 3751–3755.
- [273] D. T. Dam, J. -M. Lee, *Electrochim. Acta.* 108 (2013) 617–623.
- [274] M. Wei, H. Zhou, Y. Konishi, M. Ichihara, H. Sugiha, H. Arakawa, *Inorg. Chem.* 45 (2006) 5684–5690.
- [275] S. Wei, R. Wu, J. Jian, J. Hou, F. Chen, A. Ablat, Y. Sun, *RSC Adv.* 5 (2015) 40348–40351.
- [276] A. Li Bassi, D. Cattaneo, V. Russo, C. E. Bottani, E. Barborini, T. Mazza, P. Piseri, P. Milani, F. O. Ernst, K. Wegner, S. E. Pratsinis, *J. Appl. Phys.* 98 (2005) 74305.
- [277] H. C. Choi, Y. M. Jung, S. Bin Kim, *Vib. Spectrosc.* 37 (2005) 33–38.
- [278] A. C. Ferrari, J. Robertson, *Phys. Rev. B.* 61 (2000) 14095–14107.
- [279] B. Sambandam, A. Surenjan, L. Philip, T. Pradeep, *ACS Sustain. Chem. Eng.* 3 (2015) 1321–1329.
- [280] P. C. Angelome, L. Andrini, M. E. Calvo, F. G. Requejo, S. A. Bilmes, G. J. A. A. Soler-Illia, *J. Phys. Chem. C* 111 (2007) 10886–10893.
- [281] M. Sahoo, A. K. Yadav, S. N. Jha, D. Bhattacharyya, T. Mathews, N. K. Sahoo, S. Dash, A. K. Tyagi, *J. Phys. Chem. C* 119 (2015) 17640–17647.
- [282] L. X. Chen, T. Rajh, Z. Wang, M. C. Thurnauer, *J. Phys. Chem. B.* 101 (1997) 10688–10697.
- [283] P. Ballirano, R. Caminiti, *J. Appl. Cryst.* 34 (2001) 757–762.

- [284] W. H. Baur, A. A. Khan, *Acta Crystallogr. B* 27 (1971) 2133–2139.
- [285] P. A. Mangrulkar, A. V. Kotkondawar, S. Mukherjee, M. V. Joshi, N. Labhsetwar, D. D. Sarma, S. S. Rayalu, *Energy Environ. Sci.* 7 (2014) 4087–4094.
- [286] H. Wang, Z. Wu, Y. Liu, *J. Phys. Chem. C* 113 (2009) 13317–13324.
- [287] A. Kudo, *Int. J. Hydrogen Energy*. 31 (2006) 197–202.
- [288] M. Ge, J. Cai, J. Iocozzia, C. Cao, J. Huang, X. Zhang, J. Shen, S. Wang, S. Zhang, K.-Q. Zhang, Y. Lai, Z. Lin, *Int. J. Hydrogen Energy*. 42 (2017) 8418–8449.
- [289] D. Kandi, S. Martha, K. M. Parida, *Int J Hydrog. Energy*. 42 (2017) 9467–9481.
- [290] T. Kawai, T. Sakata, *Nature*. 286 (1980) 474–476.
- [291] K. Villa, X. Domènech, U.M. García-Pérez, J. Peral, *RSC Adv.* 6 (2016) 36681–36688.
- [292] Q. Hu, J. Huang, Q. Li, C. Wang, G. Li, J. Chen, Y. Cao, *Int J Hydrog. Energy*. 42 (2017) 5478–5484.
- [293] X. Chen, S. S. Mao, *Chem Rev.* 107 (2007) 2891–2959.
- [294] R. A. Rather, S. Singh, B. Pal, *J. Catal.* 346 (2017) 1–9.
- [295] I. K. Konstantinou, T. A. Albanis, *Appl. Catal. B Environ.* 49 (2004) 1–14.
- [296] A. Xiong, G. Ma, K. Maeda, T. Takata, T. Hisatomi, T. Setoyama, J. Kubota, K. Domen, *Catal. Sci. Technol.* 4 (2014) 325–328.
- [297] F. Yang, M. A. Hanna, R. Sun, *Biotechnol. Biofuels.* 5:13 (2012).
- [298] C. Wang, Q. Hu, J. Huang, C. Zhu, Z. Deng, H. Shi, L. Wu, Z. Liu, Y. Cao, *Appl. Surf. Sci.* 292 (2014) 161–164.
- [299] K. Lalitha, G. Sadanandam, V. D. Kumari, M. Subrahmanyam, B. Sreedhar, N. Y. Hebalkar, *J. Phys. Chem. C*. 114 (2010) 22181–22189.
- [300] T. Sreethawong, S. Yoshikawa, *Catal. Commun.* 6 (2005) 661–668.
- [301] Z. Jin, X. Zhang, Y. Li, S. Li, G. Lu, *Catal. Commun.* 8 (2007) 1267–1273.
- [302] H. -J. Choi, M. Kang, *Inter. J. Hyd. Energ.* 32 (2007) 3841–3848.
- [303] S. Xu, A. J. Du, J. Liu, J. Ng, D. D. Sun, *Inter. J. Hyd. Energ.* 36 (2011) 6560–6568.
- [304] J. Yu, Y. Hai, M. Jaroniec, *J. Colloid Interface Sci.* 357 (2011) 223–228.
- [305] G. Dong, Y. Zhang, Q. Pan, J. Qiu, *J. Photochem. Photobiol. C Photochem. Rev.* 20 (2014) 33–50.
- [306] Y. Zhou, L. Zhang, J. Liu, X. Fan, B. Wang, M. Wang, W. Ren, J. Wang, M. Li, J. Shi, *J. Mater. Chem. A* 3 (2015) 3862–3867.
- [307] J. S. Kim, J. W. Oh, S. I. Woo, *Int. J. Hydrogen Energy*. 42 (2017) 5485–5495.
- [308] J. -X. Sun, Y. -P. Yuan, L. -G. Qiu, X. Jiang, A. -J. Xie, Y. -H. Shen, J. -F. Zhu, *DaltonTrans.* 41 (2012) 6756–6763.
- [309] J. Wang, J. Huang, H. Xie, A. Qu, *Int. J. Hydrogen Energy*. 39 (2014) 6354–6363.
- [310] S. -W. Cao, Y. -P. Yuan, J. Fang, M. M. Shahjamali, F. Y. C. Boey, J. Barber, S. C. J. Loo, C. Xue, *Int. J. Hydrogen Energy*. 38 (2013) 1258–1266.
- [311] X. Xu, G. Liu, C. Random, J. T. S. Irvine, *Int. J. Hydrogen Energy*. 36 (2011) 13501–13507.
- [312] W. -J. Ong, L. -L. Tan, S. -P. Chai, S. -T. Yong, *Dalt. Trans.* 44 (2015) 1249–1257.
- [313] S. Samanta, S. Martha, K. Parida, *Chem Cat Chem.* 6 (2014) 1453–1462.
- [314] L. Ge, C. Han, J. Liu, Y. Li, *Appl. Catal. A Gen.* 409–410 (2011) 215–222.
- [315] Q. Xiang, J. Yu, M. Jaroniec, *J. Phys. Chem. C*. 115 (2011) 7355–7363.
- [316] G. Liao, S. Chen, X. Quan, H. Yu, H. Zhao, *J. Mater. Chem.* 22 (2012) 2721–2726.
- [317] A. Suryawanshi, P. Dhanasekaran, D. Mhamane, S. Kelkar, S. Patil, N. Gupta, S. Ogale, *Int. J. Hydrogen Energy*. 37 (2012) 9584–9589.
- [318] H. Zhang, L. Zhao, F. Geng, L. -H. Guo, B. Wan, Y. Yang, *Appl. Catal. B Environ.* 180 (2016) 656–662.
- [319] G. Gao, Y. Jiao, F. Ma, Y. Jiao, E. Waclawik, A. Du, *Phys. Chem. Chem. Phys.* 17

- (2015) 31140–31144.
- [320] K. Li, F. -Y. Su, W. -D. Zhang, *Appl. Surf. Sci.* 375 (2016) 110–117.
- [321] X. Xia, N. Deng, G. Cui, J. Xie, X. Shi, Y. Zhao, Q. Wang, W. Wang, B. Tang, *Chem. Commun.* 51 (2015) 10899–10902.
- [322] X. Jian, X. Liu, H. Yang, J. Li, X. Song, H. Dai, Z. Liang, *Appl. Surf. Sci.* 370 (2016) 514–521.
- [323] S. Fang, Y. Xia, K. Lv, Q. Li, J. Sun, M. Li, *Appl. Catal. B Environ.* 185 (2016) 225–232.
- [324] H. Ming, Z. Ma, Y. Liu, K. Pan, H. Yu, F. Wang, Z. Kang, *Dalt. Trans.* 41 (2012) 9526–9531.
- [325] J. R. Lakowicz, *Principles of Fluorescence Spectroscopy*, Third Edition, Springer, New York, USA, (2006).
- [326] D. J. Martin, *Investigation into High Efficiency Visible Light Photocatalysts for Water Reduction and Oxidation*, (2014). doi:10.1007/978-3-319-18488-3.
- [327] W. -J. Ong, L. -L. Tan, S. -P. Chai, S. -T. Yong, *Dalt. Trans.* 44 (2015) 1249–1257.
- [328] L. Ge, F. Zuo, J. Liu, Q. Ma, C. Wang, D. Sun, L. Bartels, P. Feng, *J. Phys. Chem. C.* 116 (2012) 13708–13714.
- [329] Y. Cui, Z. Ding, X. Fu, X. Wang, *Angew. Chem. Int. Ed.* 51 (2012) 11814–11818.
- [330] Y. -P. Yuan, L. -S. Yin, S. -W. Cao, L. -N. Gu, G. -S. Xu, P. Du, H. Chai, Y. -S. Liao, C. Xue, *Green Chem.* 16 (2014) 4663–4668.
- [331] F. Dong, L. Wu, Y. Sun, M. Fu, Z. Wu, S. C. Lee, *J. Mater. Chem.* 21 (2011) 15171–15174.
- [332] S. Sun, S. Liang, *Nanoscale.* 9 (2017) 10544–10578.
- [333] J. Wen, J. Xie, X. Chen, X. Li, *Appl. Surf. Sci.* 391 (2017) 72–123.
- [334] X. -H. Li, M. Antonietti, *Chem. Soc. Rev.* 42 (2013) 6593–6604.
- [335] B. Gupta, A. A. Melvin, T. Matthews, S. Dash, A. K. Tyagi, *Renew. Sustain. Energy Rev.* 58 (2016) 1366–1375.
- [336] W. Hou, S. B. Cronin, *Adv. Funct. Mater.* 23 (2013) 1612–1619.
- [337] K. Wenderich, G. Mul, *Chem. Rev.* 116 (2016) 14587–14619.
- [338] R. Li, H. Han, F. Zhang, D. Wang, C. Li, *Energy Environ. Sci.* 7 (2014) 1369–1376.
- [339] K. Maeda, X. Wang, Y. Nishihara, D. Lu, M. Antonietti, K. Domen, *J. Phys. Chem. C.* 113 (2009) 4940–4947.
- [340] X. -H. Li, X. Wang, M. Antonietti, *Chem. Sci.* 3 (2012) 2170–2174.
- [341] Z. Li, J. Wang, K. Zhu, F. Ma, A. Meng, *Mater. Lett.* 145 (2015) 167–170.
- [342] S. Liang, Y. Xia, S. Zhu, S. Zheng, Y. He, J. Bi, M. Liu, L. Wu, *Appl. Surf. Sci.* 358 (2015) 304–312.
- [343] A. Tanaka, K. Teramura, S. Hosokawa, H. Kominami, T. Tanaka, *Chem. Sci.* 8 (2017) 2574–2580.
- [344] P. A. DeSario, J. J. Pietron, T. H. Brintlinger, M. McEntee, J. F. Parker, O. Baturina, R. M. Stroud, D. R. Rolison, *Nanoscale.* 9 (2017) 11720–11729.
- [345] V. N. Khabashesku, J. L. Zimmerman, J. L. Margrave, *Chem. Mater.* 12 (2000) 3264–3270.
- [346] L. Bi, D. Xu, L. Zhang, Y. Lin, D. Wang, T. Xie, *Phys. Chem. Chem. Phys.* 17 (2015) 29899–29905.